Durham E-Theses

Flat-Plate Solar Collectors for Water Heating with Improved Heat Transfer for Application in Climatic Conditions of the Mediterranean Region

IORDANOU, GRIGORIOS

How to cite:

Use policy

Flat-Plate Solar Collectors for Water Heating with Improved Heat Transfer for Application in Climatic Conditions of the Mediterranean Region

Grigorios Iordanou

School of Engineering and Computing Science
Durham University

2009

Flat-Plate Solar Collectors for Water Heating with Improved Heat Transfer for Application in Climatic Conditions of the Mediterranean Region

Grigorios Iordanou

School of Engineering and Computing Science
Durham University

A thesis submitted in fulfilment of the requirements of the Council of the University of Durham for the Degree of Doctor of Philosophy (PhD)

2009

Στον θείο μου Παναγιώτη

Ἡ περὶ τῆς ἀληθείας θεωρία τῇ μὲν χαλεπὴ τῇ δὲ ῥᾳδία. σημεῖον δὲ τὸ μήτ' ἀξίως μηδένα δύνασθαι θιγεῖν αὐτῆς μήτε πάντας ἀποτυγχάνειν, ἀλλ' ἕκαστον λέγειν τι περὶ τῆς φύσεως, καὶ καθ' ἕνα μὲν ἢ μηθὲν ἢ μικρὸν ἐπιβάλλειν αὐτῇ, ἐκ πάντων δὲ συναθροιζομένων γίγνεσθαί τι μέγεθος.

ΑΡΙΣΤΟΤΕΛΗΣ

The verification of truth could be easy on the one hand and difficult on the other. Evident to that is the fact that not everyone can have the knowledge to accomplish it, yet not everyone fails. Everybody talks about nature and each individual could contribute nothing or something to this research, yet if all this tiny information is gathered it results to significant amount of information.

ARISTOTLE

Abstract

The aim of this research project is to improve the thermal performance of passive flat plate solar collectors using a novel cost effective enhanced heat transfer technique. The project work focuses on the process of energy conversion from the collector to the working fluid. This is accomplished by employing an aluminium grid placed in the channels of a collector to induce a gradient of heat capacitance.

This novel technique is tested both theoretically by means of simplistic designs using Computational Fluid Dynamics (CFD) and experimentally using two unglazed collectors. One collector has the aluminium net inserted in its channels and it is tested against an identical conventional collector in order to have a direct comparison at the same time. The obtained CFD data and the experimental findings are coupled and show a good agreement. All the obtained results are validated with the literature.

The results both theoretical and experimental demonstrate an enhancement in the heat transfer coefficient by 9 % resulting to an increase in the output temperature of the working fluid in the collector with the metallic insertion. Other parameters such as the Nusselt and Raleigh numbers supported these findings.

Three novel expressions that correlate the Nusselt and the Rayleigh number, for different heat fluxes, were developed using data from CFD and experimental results. These correlations can be applied on any flat plate collector with an aluminium grid in its pipes, in order to predict its performance. Furthermore an existing lumped parameters model that predicts the output temperature of a collector was simplified and improved.

Acknowledgements

I would like to thank my supervisor, Dr. Khamid Mahkamov, for all his support and assistance throughout the duration of this doctorate degree at Durham. I would also like to thank many technicians who have provided their advice and knowledge during the experimental part of this research, in particular to Tony Collinson for his excellent work on the collectors. Special thanks to my colleagues Giovanni Airoldi, Chin Lim, Nick Stannard, Blanca Cocho Martinez and Pavlos Trichakis for their valuable contribution throughout the project work. Above all I would like to thank my parents for giving me, once again, the opportunity to carry out a degree by supporting me financially and morally all these years.

Declaration

I hereby declare that this thesis is a record of work carried out by myself, that it has not been the subject of any previous application for a degree, and that all sources of information have been acknowledged.

Contents

List of Figures

List of Tables

List of Graphs

Nomenclature

A_c Gross collector area
A_e Edge area of collector
A_p Aperture area
b_o Incidence angle modifier coefficient
C_b Tube-plate bond conductance
C_p Specific heat of working fluid
D Outer diameter of tube
D_i Inner diameter of tube
F Fin efficiency of straight insulated-fins with rectangular cross section
f Darcy friction factor
F_R Collector heat removal factor
F' Collector efficiency factor
G_T Total intensity of incident solar radiation on tilted collector surface.
h_{fi} Forced convection heat transfer coefficient inside of tubes
h_w Wind convection coefficient
I Intensity of incident radiation
k Thermal conductivity
k_b Thermal conductivity of back insulation
k_e Thermal conductivity of edge insulation
L Characteristic length
L_b Thickness of back insulation
L_e Thickness of edge insulation
L_{eq} Equivalent length
m Parameter of the fin-air arrangement
n Number of tubes
Nu Nusselt number
P Pressure
Pr   Prandtl number
Q Heat transfer rate
q radiation flux
U_c Heat transfer rate due to convection
U_r Heat transfer rate due to radiation
U_b Back heat loss from collector
U_e Edge heat loss from collector
Q_u Useful gain from collector
Q_{loss} Overall heat loss from collector
Q_t Top heat loss from collector
r Reflection of radiation
R_b Geometric factor

S	Absorbed radiation per unit area of absorber plate
S_c	Absorbed radiation per unit area based on the gross collector area
T	Temperature
T_a	Ambient temperature
T_b	Fin base temperature
T_f	Local fluid temperature
$T_{f\,ref}$	Reference fluid temperature
T_{fm}	Mean fluid temperature
T_i	Fluid temperature at collector inlet
T_o	Fluid temperature at collector exit
T_{pm}	Mean plate temperature
U	Mean fluid velocity inside of tubes
U_L	Overall loss coefficient of the collector based on the gross collector area
V	Wind speed
W	Distance between the centres of adjacent tubes
u_i	Velocity vector
E	Specific energy,
k_{eff}	Effective thermal conductivity
τ_{eff}	Effective stress tensor
u_j	Average velocities
U^*	Mean velocity,
E	Empirical constant
k_p	Turbulent kinetic energy at point P,
y_p	Distance from point P to the wall.
C_μ	Model constant
G_k	Production of kinetic energy
C_2	Inertial resistance factor
E_f	Total fluid energy
E_s	Total solid medium energy
k_f	Fluid thermal conductivity
k_s	Solid thermal conductivity
D_p	Mean particle diameter
L	Bed depth
IR	Infrared
AR	Anti reflecting coatings
Q	Heat
Q	Heat flux
k	Thermal conductivity coefficient
h_f	Convection heat transfer coefficient
h_f	Head loss
∇T	Temperature gradient
A_s	Surface area
ΔT	Temperature difference
T_a	Ambient temperature
T_b	Local base temperature
T_s	Surface temperature

T_p Plate temperatures
T_f Fluid temperature
v   Mean flow velocity
Di Inner pipe diameter
Re Reynolds Number
u Velocity of flow in the boundary layer
U(x)   Outer stream velocity
τ   Shear stress
y   Height of the boundary layer
f   Friction factor
λ Coefficient of flow
L   Pipe length
V   Average flow velocity
D Tube diameter
g   Acceleration due to gravity
ΔP   Pressure drop
S   Absorbed radiation
I   Intensity of radiation
ρ_g Diffuse reflectance of ground
R_b Ratio of beam radiation
ρ_d Reflectance for diffuse radiation
Q_u Useful energy output of a collector
Q_u Useful energy gain
A_c Gross collector area
S Unit area of absorber
U_L Heat transfer coefficient
T_{pm} Mean absorber plate temperature
Q_{loss} Overall heat loss from collector
$h_{c,p\text{-}c}$ Convection coefficient between the plate and the cover
$h_{r,p\text{-}c}$ Radiation coefficient from the plate to the cover
$h_{r,c\text{-}a}$ Radiation coefficient from the cover to the air
$q_{r\ p\text{-}s}$ Net radiant energy transfer between the collector and the sky
h_w Wind convection coefficient
Nu Nusselt number
Ra Rayleigh number
Pr   Prandtl number
L   Plate spacing
β' Volumetric coefficient of expansion of air
v   Kinematic viscosity
U_b Back heat loss
ε_p Emittance of the absorber plate for infrared radiation
F Standard fin efficiency
F' Collector efficiency factor
W Distance between the tubes
D_i Inner diameter of the tube
q'_{tube} Useful gain of the tube

q'_u	Useful gain
q'_{fin}	Useful gain of the fin
h_{fi}	Forced-convection heat transfer coefficient inside of tubes
C_b	Bond conductance
$\dot{m}$	Total collector flow rate
n	Number of tubes
F_R	Heat removal factor
T_o	Output temperature
n_i	Collector's efficiency
G_T	Irradiance on tilted plates
$K_{\tau\alpha}$	Incidence angle modifier
θ	Angle of incidence of beam radiation
b_o	Incident angle modifier coefficient
SDHWS	Solar domestic hot-water system
TPCT	Two-phase closed thermosiphon
ICSSWH	Integrated Collector Storage Solar Water Heater'
CPC	Compound parabolic concentrator
PVT	Photovoltaic Thermal
PV	Photovoltaic
HPVT	Hybrid photovoltaic thermal

GREEK

α	Absorbptance
β	Collector slope
β_v	Volumetric coefficient of expansion of air
δ	Thickness of absorber plate
ε	Emittance
η	Instantaneous efficiency of solar collector
v	Kinematic viscosity
θ	Angle of incidence of solar radiation
σ	Stefan-Boltzmann constant
τ	Transmittance
$(\tau\alpha)$	Transmittance-absorbptance product
κ	Von Karman constant
ε	Dissipation rate
τ_w	Wall shear stress.
α	Permeability
γ	Porosity of the medium
ρ_f	Density of the fluid
ρ_s	Density of the solid
ε	Emissivity
μ	Dynamic fluid viscosity
δ	Thickness of the boundary layer

Subscript

b	Beam radiation
b	Back
c	Cover
c1	Cover 1 (inner cover)
d	Diffuse radiation
e	Edge
g	Ground-reflected radiation
i	Incidence radiation
n	Normal incidence
p	Absorber plate
r	Reflected radiation
t	Top
⊥	Perpendicular component of radiation
‖	Parallel component of radiation

CHAPTER 1

Introduction

1.1 Flat plate solar water collectors

In recent years solar energy has been strongly promoted as a viable energy source. One of the simplest and most direct applications of this energy is the conversion of solar radiation into heat. Hence way that the domestic sector can lessen its impact on the environment is by the installation of solar flat plate collectors for heating water. Although it should be said that some of these collectors have been in service for the last 40-50 years without any real significant changes in their design and operational principles.

A typical flat-plate collector consists of an absorber in an insulated box together with transparent cover sheets (glazing). The absorber is usually made of a metal sheet of high thermal conductivity, such as copper or aluminium, with integrated or attached tubes. Its surface is coated with a special selective material to maximise radiant energy

absorption while minimising radiant energy emission. The insulated box reduces heat losses from the back and sides of the collector [1].

The research in this thesis is concerned with improvements of the efficiency of the flat plate solar collector using cost effective heat transfer techniques. This is examined by the design of collector models utilising Computational Fluid Dynamics (CFD) packages and by the design and construction of an experimental test rig. The use of a model involving lumped parameters enables the accuracy of the computer model results to be evaluated and the experimental data to be recorded. The use of partially porous medium inside the channels of the collector is a means of enhancing the heat transfer.

The proposed CFD design employs an elliptical geometry consisting of two vertical cylindrical pipes with two adiabatic semi-circles at the top and bottom. In one vertical pipe a net is introduced that models the role of the porous medium.

The experimental work involves tests conducted on the rig equipped with two types of unglazed solar collector panels and artificial insolation. The first type used is similar to the conventional design, whilst the second one has a metallic porous material inserted in all its pipes. The porous medium used in this panel is made of an aluminium wire mesh which is folded and placed in each pipe to provide reasonably evenly spaced porosity along the length of the channel.

Having established the context of the research, the thesis will feature the structure of the study and explain how the different aspects of the work interconnect; by examining

the background work and its relevance to the challenges present when utilising solar energy in solar water collectors.

1.2 History and Utilisation of Solar Energy

Humans have always used the rays of the sun to gather their energy needs. In the energy needs of today with increasing environmental concern, alternatives to the use of non-renewable and polluting fossil fuels have to be investigated. One such possibility is solar energy, which has become increasingly popular in recent years.

Solar energy is the radiation produced by nuclear fusion reactions in the core of the sun. This radiation travels to Earth through space in the form of energy called photons. Even though only 30% of the solar power actually reaches the Earth, every 20 minutes the sun produces enough power to supply the Earth with its needs for an entire year.

Unfortunately the atmosphere and clouds absorb a large amount of this sunlight. So the amount of light that reaches any point on the ground depends on the time of day, the day of the year, the amount of cloud cover, and the latitude at that point, with the solar focus directly dependent on three of these factors.

The history of using the sun for energy goes way back to the Ancient Greeks and Romans as their buildings were constructed such that the rays of the sun provided light and heat for indoor spaces. The Greek philosopher Socrates wrote, "In houses that look toward the south, the sun penetrates the entrance in winter." Romans advanced this art by

covering the openings to south facing building with glass, in order to retain the heat of the winter sun.

The history of utilising solar energy in recent times dates from 1861 when Mouchout developed a steam engine powered entirely by the sun and in 1883 American inventor Charles Fritts described the first solar cells made of selenium wafers [2].

Throughout the 20th century, scientists developed large cone-shaped collectors that could boil ammonia for refrigeration. In the United States, John Ericsson designed the "parabolic trough collector" a technology which functions more than a hundred years later on the same basic design [2].

Albert Einstein was awarded the 1921 Nobel Prize in physics for his research on the photoelectric effect; a phenomenon central to the generation of electricity through solar cells [3].

In 1953 AT&T laboratory scientists developed the first silicon solar cell capable of generating an electric current. In 1956, solar photovoltaic (PV) cells were very expensive and electricity from solar cells cost about $300 per watt.

The Arab oil embargo in 1973 confirmed the degree to which the western economy depended upon there, being a cheap and reliable flow of oil. In the 1970s it was thought that through massive investment in funding and research, solar photovoltaic costs could drastically reduced, such that eventually solar cells could become competitive with fossil fuels [4].

By the 1990s, the reality was that the costs of solar energy had dropped as predicted and the huge PV market growth in Germany and Japan from the 1990s to the present has boosted the solar industry. Furthermore, such large PV productions are creating steadily lowering costs. Meanwhile, the heating of water by solar energy is an increasingly cost-effective means of lowering gas and electricity demand [4].

Due to the nature of solar energy, two components are required in order to have a functional solar energy generator. These two components are a collector and a storage unit. The collector collects the radiation that falls on it and converts it to other forms of energy (electricity, heat). Whilst the storage unit is required because of the non-constant nature of solar energy, as during cloudy days the amount of energy produced by the collector will be quite small. The storage unit can hold the energy produced during the periods of maximum radiation and release it when it is needed or the productivity drops.

Methods of collecting and storing solar energy vary depending on the use of the solar generator. In general, there are three types of collectors (flat -plate collectors, focusing collectors, and passive collectors) and many forms of storage units.

1.3 The Structure of the Thesis

The thesis consists of eight Chapters, dedicated to research and to the examination of flat plate solar water collectors and their features. The current Chapter contains information regarding the utilisation of solar energy over the years, as well as analyses of how each chapter is formed and an outline of the research undertaken within that chapter.

- *Chapter 2* contains a literature review; an overview of solar water heating and different solar water heaters and collectors. An extensive description of absorber coatings and glazing for flat plate solar collectors. Various designs and improvements in Solar Water Systems are also included in this chapter.

- *Chapter 3* focuses on the theory behind the research; thermodynamics, heat transfer modes, different modes of fluid flow, heat transfer enhancement techniques and mathematical models that portray the operation and performance of the collector.

- *Chapter 4* includes a background work on Computational Fluid Dynamics (CFD), the CFD codes three main elements, various examples of CFD applications in solar collectors systems and heat transfer and finally the Governing equations of flow and heat transfer in passive solar collectors.

- *Chapter 5* presents the work conducted using Computational Fluid Dynamics (CFD); the model geometry constructed in Fluent's pre-processor program Gambit. This chapter assesses the suitability of CFD packages to model a section of a solar collector and the methods of enhancing heat transfer. It also includes prior research on different designs that assisted the numerical work.

- *Chapter 6* is concerned with the experimental work; explains the design and construction of the experimental test rig and the various experimental setups. The techniques used for temperature, fluid flow and pressure measurements are also described in detail. Various graphs created from the numerical data recorded during the experiments are illustrated and analysed.

- *Chapter 7* focuses on the evaluation of the lumped parameters model; a correlation combining experimental results and mathematical formulae. An arithmetical solution is presented using all the different data. Then detailed analysis is performed on the model of lumped parameters in order to achieve a better understanding of this concept. An attempt is then made to provide a simplified and improved version.

- *Chapter 8* contains the conclusions and recommendations of the research conducted; the evaluation of the design, manufacturing, and tests of the sections of the solar collectors. From the results obtained in Chapters 5, 6 and 7 it is shown to be feasible to utilise porous medium using aluminium net inside the channels of the collector. The final chapter of this thesis examines possible further work.

- *Chapter 9* lists all the references used in the thesis.

- Appendices contain supplementary information such as types of solar water systems, tables with experimental results and charts that can be used to predict the performance of the collector when utilised in conjunction with the experimental data and the lumped parameters model. Furthermore there are information concerning the apparatus and components used in the experiments.

CHAPTER 2

Literature Review

2.1 Overview of Solar Water Heating

Solar energy can be utilised as a form of heat, such as solar water heating and as electricity, such as solar photovoltaic. Solar water heating systems are commonly referred to in industry as Solar Domestic Hot Water (SDHW) systems and it is a technology that is not entirely new.

In the 19th century, people used a stove to heat water by burning pieces of wood or coal. In cities, the wealthier heated their water with gas manufactured from coal. In many areas, wood, coal or gas could not be easily obtained and hence such fuels were often expensive [5].

To avoid these problems, a much easier and safer way to heat water was created. This was achieved by placing outside a black painted metal tank full of water to absorb solar energy. The disadvantage was that even on clear hot days it usually took from morning to early afternoon for the water to get hot. As the sun went down, the tank rapidly lost its heat because it had no insulation [5].

In 1891, Clarence Kemp patented the old design of metal tanks exposed to the sun by adding a metal panel to the tank, shown below in Figure 2.1a, in order to increase the efficiency of the solar tank [5].

In the beginning of the 20th century, inventors designed improved systems, but still the heating and the storage unit were one, and both were exposed to the weather and the cold nights.
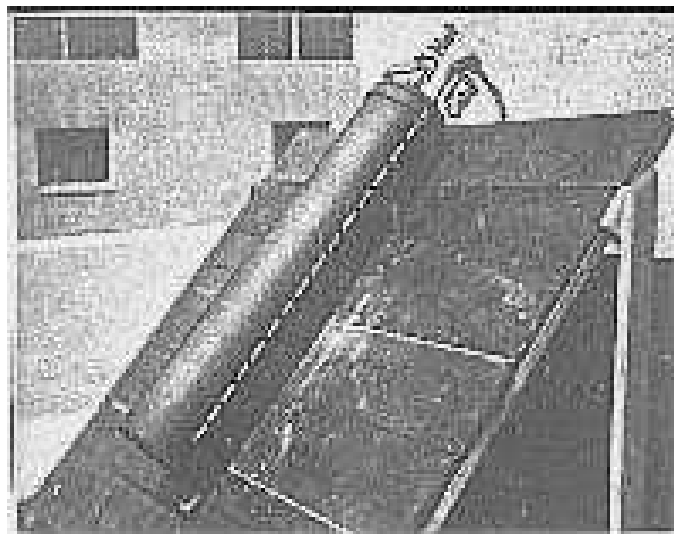
Figure 2.1a A prototype Solar Water Collector [5].

In 1909, William Bailey began selling the Day and Night solar water heater, which provided an insulated indoor water storage tank, supplied by a separate solar collector located outside the house and facing south. The collector consisted of a coiled pipe inside a glass covered box which had to be mounted below the storage tank. This allowed the hot water to circulate from the collector to the storage tank by natural convection [6].

In Japan a simple solar water heater was created consisting of a basin with its top covered by glass; by the 1960s more than 100,000 collectors of this type were in use.

In Australia the number of sales grew as a consequence of the two increases in oil prices.

Figure 2.1b Solar water collector with separated storage tank [6].

In the late 1980s, the Australian solar water heater market began to drop as the discovery of natural gas to previously fuel-short regions, such as the Northern Territory and Western Australia, affected the market for solar water heaters. However exports still account for more than 50% of the sales made by Sol-Hart, Australia's leading manufacturer of solar water heaters [4].

In the mid 50's Israeli engineer, Levi Yissar, suggested the use of solar energy for heating up domestic water with Israelis responding by the mass purchasing of solar water heaters. By 1983, 60% of the population heated their water from the sun. When the price of oil dropped in the mid 1980s, the Israeli government required its inhabitants to heat their water with the sun. Today, more than 90% of Israeli households own solar water heaters [4].

The history of Solar Water Collectors in Greece started when the first collectors were imported from Israel in the mid 70's. The Greek Solar Industry

Association was established in 1978 and the promotion of solar systems started around the same period. The technology of the Solar Water Heaters was largely accepted by the market and small units of $2m^2$ were installed in order to cover the needs of a household. In 2001 Greece held the first place in Europe for m^2 installed per capita and the 2nd place in the world [7]. This is shown on Graph 2.1a.
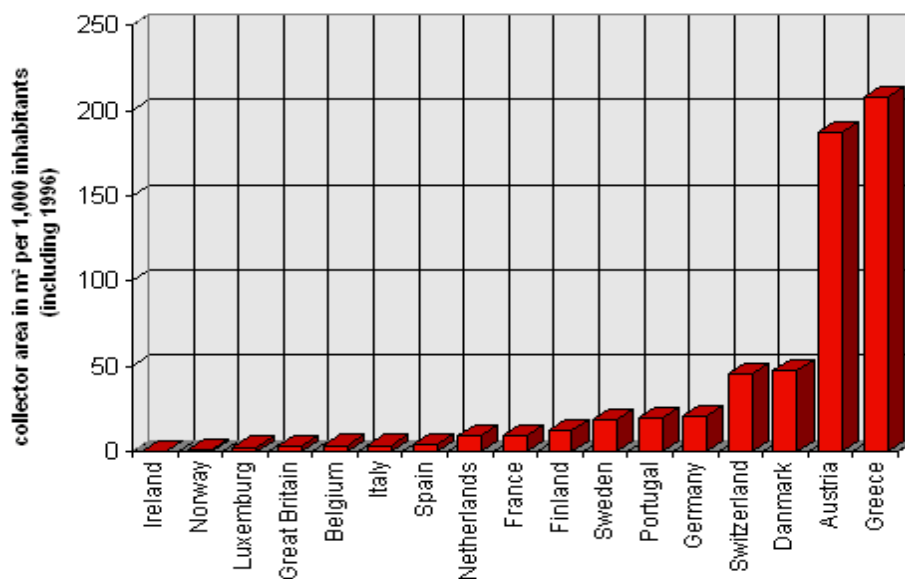
Graph 2.1a Solar Collectors in m^2 installed per capita [7].

2.2 Solar Water Heaters and Collectors

The solar collector is the key element in solar energy systems. It absorbs the solar radiation and converts it into a useable form of energy that can be applied to meet a specific demand. More sophisticated systems have also been developed for higher temperatures.

There are a number of different design models for collectors but generally they are either stationary or concentrating. The stationary type includes: Flat Plate Collectors, Evacuated Tube Collectors and Compound Parabolic Collectors. The

Concentrating type includes: Parabolic and Cylindrical Trough Collectors, Parabolic

Dish Reflector and Heliostat Field Collector [8].

2.2.1 Flat Plate Collectors

Flat-plate collectors are the most common for residential water-heating and space-heating installations. A typical flat-plate collector consists of an absorber, transparent cover sheets and an insulated box. The absorber is usually a sheet of high-thermal-conductivity metal with tubes or ducts either integral or attached. Its surface is painted
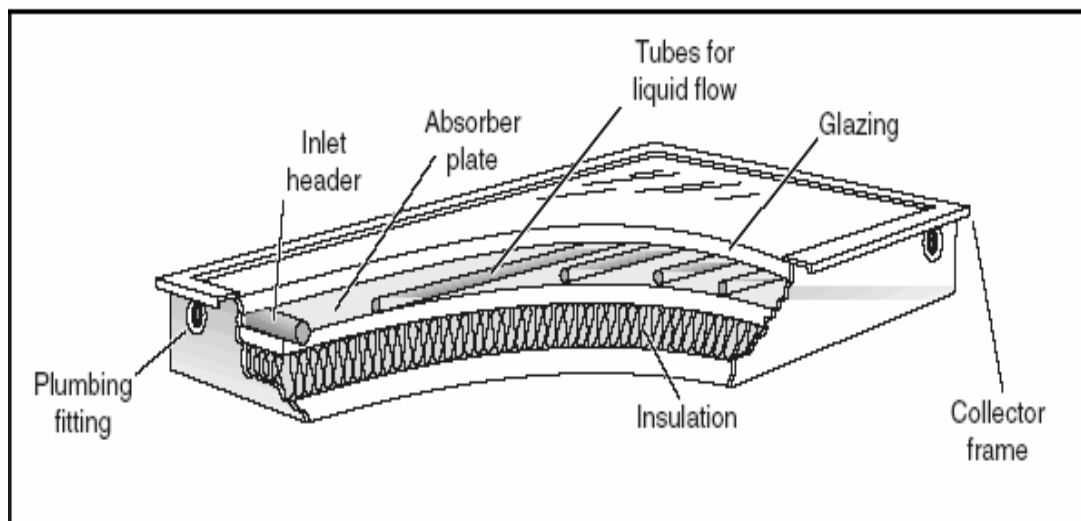
Figure 2.2a Flat plate solar water collector [9].

or coated to maximise radiant energy absorption and in some cases to minimise radiant emission. The insulated box provides structure and sealing and reduces heat loss from the back or sides of the collector [9]. The cover sheets, called *glazing,* allow sunlight to pass through to the absorber but insulate the space above the absorber to

prevent cool air from flowing into this space. However, the glass also reflects a small part of the sunlight, which does not reach the absorber.

The collector can reach temperatures up to 200°C when no liquid flows through it and therefore all the materials used must be able to resist such heat. The absorber is usually made of metallic materials such as copper, steel or aluminium. The collector housing can be made of plastic, metal or wood, and the glass front cover must be sealed so that heat does not escape, and the collector itself is protected from dirt, insects or humidity.

The collector housing is highly insulated at the back and sides to reduce the heat losses. Although there are still some collector heat losses due to the temperature difference between the absorber and ambient air that results to convection and radiation losses. The convection losses are caused by the angle of inclination and the spacing between the glass cover and the absorber plate, while the radiation losses are caused by the exchange of heat between the absorber and the environment.

The absorber plate which covers the full aperture area of the collector must perform three functions: absorb the maximum possible amount of solar irradiance, transfer this heat into the working fluid at a minimum temperature difference and lose a minimum amount of heat back to the surroundings.

Solar irradiance passing through the glazing is absorbed directly onto the absorber plate. Surface coatings that have a high absorbptance for short-wavelength light are used on the absorber. Paint or plating is used and the resulting black surface will typically absorb over 95% of the incident solar radiation. The second function of the absorber plate is to transfer the absorbed energy into a heat-transfer fluid at a

minimum temperature difference. This is achieved by conducting the absorbed heat to tubes that contain the heat-transfer fluid. The heat-transfer fluid may be either water or water with antifreeze liquid. Transferring the heat absorbed on the absorber surface into the fluid gives rise to heat losses. Liquid collector absorber plates consist of a flat sheet of metal with tubes spaced 10 cm apart and attached to it. The sheet of metal absorbs most of the solar irradiance and acts as a carrier to bring the absorbed heat into the fluid. In an efficient system the absorber sheet is made of a material with high thermal conductivity. The tubes are not spaced far too apart otherwise a much lower temperature will occur halfway between them.

Since the temperature of the absorber surface is above ambient temperature, the surface re-radiates some of the heat it has absorbed back to the surroundings. This loss mechanism is a function of the emittance of the surface for low-temperature, long-wavelength radiation. Many coatings that enhance the absorption of sunlight (short-wavelength radiation) also enhance the long wavelength radiation loss from the surface. A good coating will produce an absorber surface that is a good absorber of short-wavelength solar irradiance but a poor emitter of long-wavelength radiant energy

Normally the absorber is covered with one or more transparent cover sheets to reduce convective heat loss. However convective loss is not completely eliminated because a convective current exists between the absorber and the cover sheet, so transferring heat from the absorber to the cover sheet. External convection then produces a net heat loss from the absorber as it cools the cover sheet.

2.2.2 Further features of solar water collectors

The collector performance test data are associated with the collector temperature rises above ambient divided by the solar irradiance. The collector temperature used for flat-plate collector performance correlation is normally the temperature of the heat-transfer fluid entering the collector, not the average fluid temperature.

The use of fluid inlet temperature makes the application of the performance correlation easier in design studies; it also makes the correlation considerably more dependent on the flow rate of the heat-transfer fluid. Every correlation using fluid inlet temperature must specify the fluid flow rate at which the measurements were made. The recommended test flow rate for a liquid collector is 0.02 kg/hr [10].

Since a flat-plate collector can collect both beam (direct) and diffused solar radiation, the total solar irradiance is used as the basis for flat-plate collector performance calculations. The aperture irradiance is the total solar irradiance measured in the plane of the collector, which includes the cosine loss of the beam component as the collector is tilted from the horizontal, as well as some ground reflection [1].

Flat-plate collectors cost less than other types of collectors (i.e. concentrating, evacuated tube collectors), as they do not operate using a tracking system. In addition, today there are much more flat-plate than other types of collectors being produced. Due to their potential to produce more low-temperature energy for a given cost, flat-plate collectors have been considered for use as pre-heaters for concentrating collectors in high-temperature industrial process heat systems.

2.3 Solar Air Collectors

Solar air collectors operate similarly to liquid collectors at the difference that air is circulated through the collector to cause of heat transfer. Air collectors are simple flat-plate collectors used primarily for space heating.
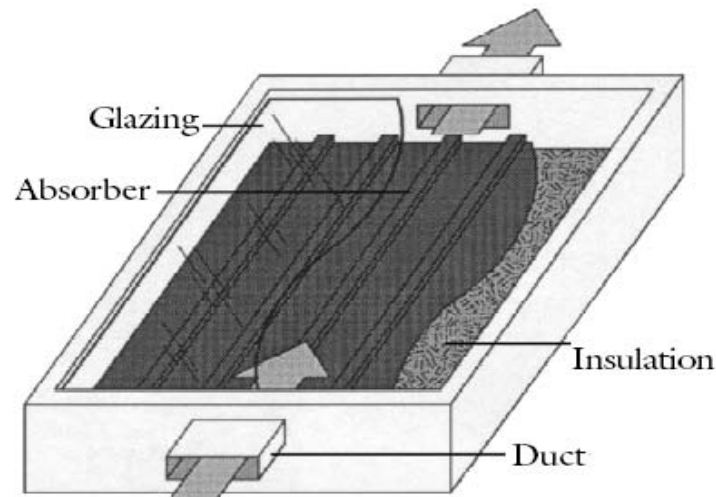
Figure 2.3a Flat Plate Air Collector [9].

The absorber plates in air collectors can be metal sheets, layers of screen, or non-metallic materials. Air collector absorber plates can be unfilled or wavy to create air turbulence that helps the heat to pass from the plate. The air flows through the absorber by natural convection or it is forced by a fan.

As air conducts heat slower than liquid does, less heat is transferred between the air and the absorber than in a liquid collector. The disadvantage of this design is that it can also increase the amount of power needed for fans and hence increase the costs of operating the system [1].

2.4 Evacuated Tube –Heat Pipe Collectors

The Evacuated Tube Collector as shown in Figure2.4a[1] consists of rows of parallel transparent glass tubes, each of which contains an absorber tube covered with a selective coating. When evacuated tubes are manufactured, air is evacuated from the space between the two tubes so forming a vacuum.

Figure 2.4a Evacuated tube collector.

Conductive and convective heat losses are eliminated because there is no air to conduct heat or to cause convective losses. There can still be some radiant heat loss (heat energy will move through a space from a warmer to a cooler surface, even across a vacuum); but this loss is small and of little consequence compared with the amount of heat transferred to the liquid in the absorber tube [11].

Evacuated tube collectors can be classified in two main groups:

1. Direct flow tubes: the heat transfer fluid flows through the absorber,

2. Heat pipe tubes: tubes with heat transfer between the absorber and heat transfer fluid of the collector.

---

1 Source: Apricus Solar Ltd.

The direct flow collectors as shown in Figure 2.4b[2] consist of a group of glass tubes. Inside each tube there is a flat or curved aluminium plate which is attached to a metal (usually copper) or glass pipe depending on the configuration.
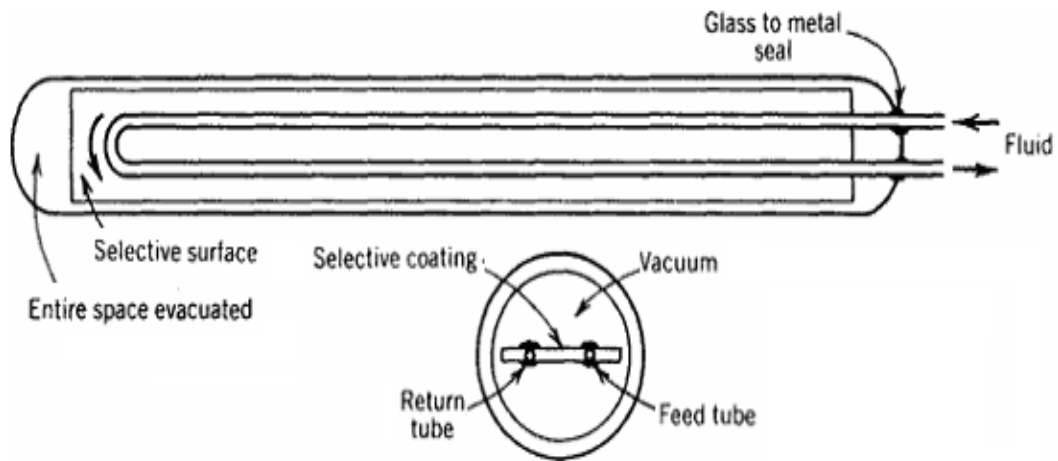
Figure 2.4b Direct evacuated tube Flow collector.

The aluminium plate is generally coated with a selective coating. The heat transfer fluid is water and circulates through the pipes, one for the inlet fluid and one for the outlet fluid. In an evacuated-tube collector, sunlight enters through the outer glass tube, strikes the absorber tube and is transformed into heat. The heat is transferred to the liquid flowing through the absorber tube.

The heat pipe as shown in Figure 2.4c[3] is similar to the direct flow tube type. In this case there is a change of the state of the liquid. Inside the heat pipe there is a small quantity of purified water and some special additives. Due to the vacuum of the tube, the water boils at a lower temperature, typically 30 °C, so when the heat pipe is heated above 30ºC the water vaporises. This vapour rapidly rises to the top of the heat pipe transferring heat into the condenser.

---

2 Source : Power From The Sun.net
3 Source : Power From The Sun.net

As the heat is lost at the condenser, the vapour condenses to form a liquid and returns to the bottom of the heat pipe and the process starts again.
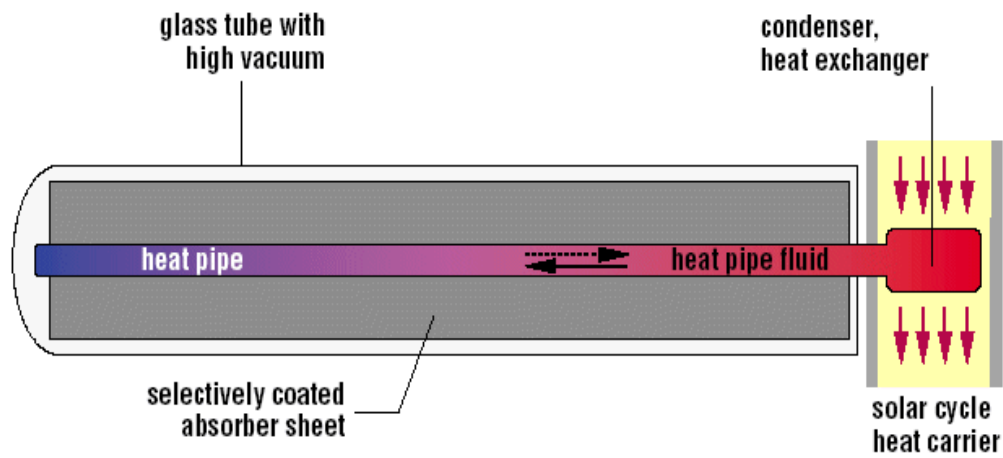
Figure 2.4c An evacuated tube collector with heat pipe.

2.5 Stationary Concentrating Collectors

Stationary concentrating collectors as illustrated in Figure 2.5a[4] use compound parabolic reflectors and flat reflectors for directing solar energy to an absorber or aperture through a wide acceptance angle.
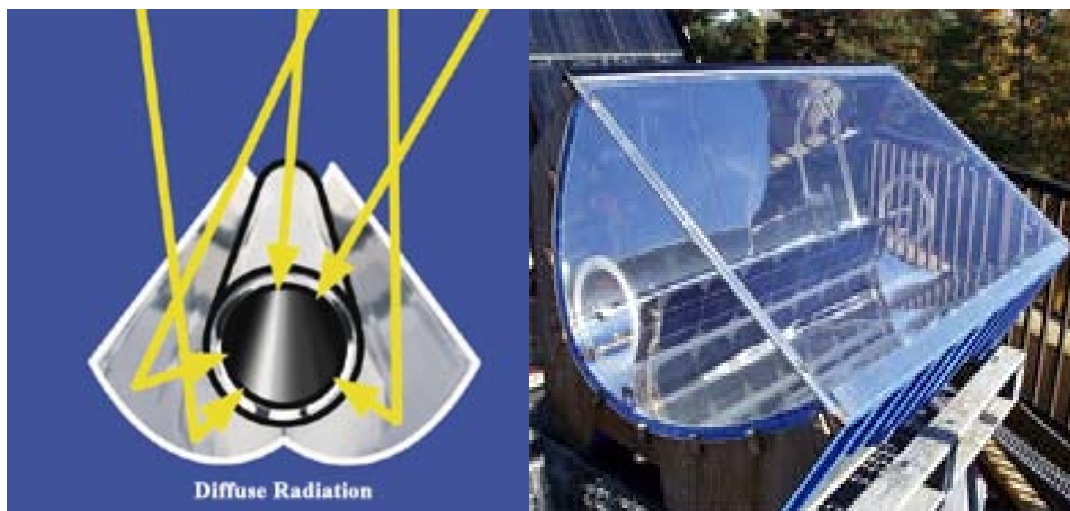
Figure 2.5a Stationary concentrating collectors.

---

4 Source: Paradigma solar heating systems

The wide acceptance angle for these reflectors eliminates the need for a sun tracker. These collectors are more useful as linear or trough-type concentrators. The acceptance angle is defined as the angles through which a source of light can be moved and still connect at the absorber [12].

2.6 Concentrating Solar Collectors

Concentrating solar collectors are used when higher temperatures are required. Solar energy which is falling onto a large reflective surface is reflected onto a much smaller area before it is converted into heat. Most concentrating collectors can only concentrate the parallel insolation coming directly from the sun's beam and hence must follow (track) the sun's direction across the sky. Three types of solar concentrators are in common use; central receivers, parabolic dishes and parabolic troughs [13].

2.6.1 Central Receiver System

A central receiver system illustrated consists of a large field of independently movable flat mirrors (heliostats) and a receiver located at the top of a tower [13].

Figure 2.6a A Central Receiver System [13].

Each heliostat moves about two axes throughout the day to keep the sun's rays reflected onto the receiver at the top of the tower. The amount of energy coming out of the sun rays when concentrated at one point (the tower in the middle) produces a range of temperatures between 550°C to 1500°C. This thermal energy can be used for heating water or molten salt, which saves the energy for a later use. The water changes to steam which is used to move the turbine-generator; hence thermal energy is converted into electricity.

2.6.2 Parabolic Dish

A parabolic dish is a combination of a satellite-dish, a receiver and a Stirling Engine [14]. It concentrates the incoming solar radiation to a point and generates electricity in the range of 5 KW to 25 KW; therefore it's used as a stand alone generator.
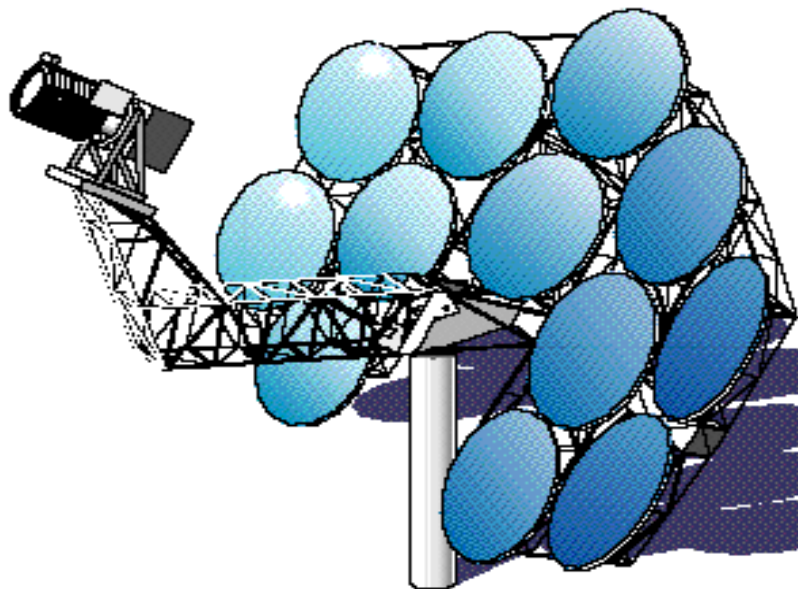
Figure 2.6b Two-axis tracking parabolic dish collector [14].

Solar Dishes use a parabolic mirror to concentrate solar energy at its focal point. Then a receiver, mounted at the focal point, converts the energy of the sun's

rays into heat. The heat gained produces a temperature of between 650 ℃ to 800 ℃ and this is used to drive a Stirling Engine that generates electricity.

2.6.3 Parabolic Trough Collectors

A parabolic trough collector shown in Figure 2.6c[5] has a linear parabolic-shaped reflector that focuses the sun's radiation onto a linear receiver tube located along the trough's focal line. The collector tracks the sun along one axis from east to west during the day to ensure that the sun is continuously focused on the receiver.
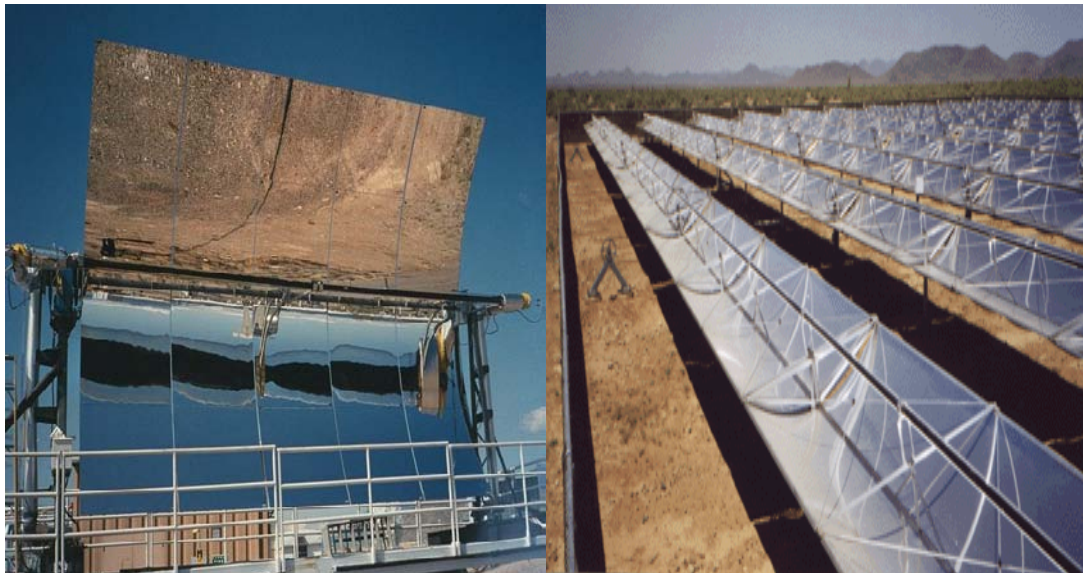
Figure 2.6c Parabolic trough collectors.

Mechanical drives slowly rotate the troughs during the day to keep the reflected sunlight focused onto the pipe receivers. The fluid flowing in the tube is heated in the range of 300 °C to 400 °C [15]. The working fluid is heated as it circulates through the receivers and returns to a series of heat exchangers at a central

5 Source: Physics Forums.com

location where the fluid is used to generate high-pressure superheated steam. The steam is then fed to a conventional steam turbine/generator to produce electricity. The solar trough generators operating today have gas-fired backup heaters so electricity can be generated during cloudy periods or at night [16].

2.7 Absorber Coatings

The electromagnetic radiation emitted by the sun displays a wide range of wavelengths. This can be divided into two major regions with respect to the capability of ionizing atoms in radiation-absorbing matter: ionizing radiation (X-rays and gamma-rays) and non-ionizing radiation (UVR, visible light and infrared radiation).

Solar radiation is commonly divided into various regions or bands of wavelength as seen in Figure 2.7a[6]. Ultraviolet radiation is that part of the electromagnetic spectrum between 100 and 400 nm [17].
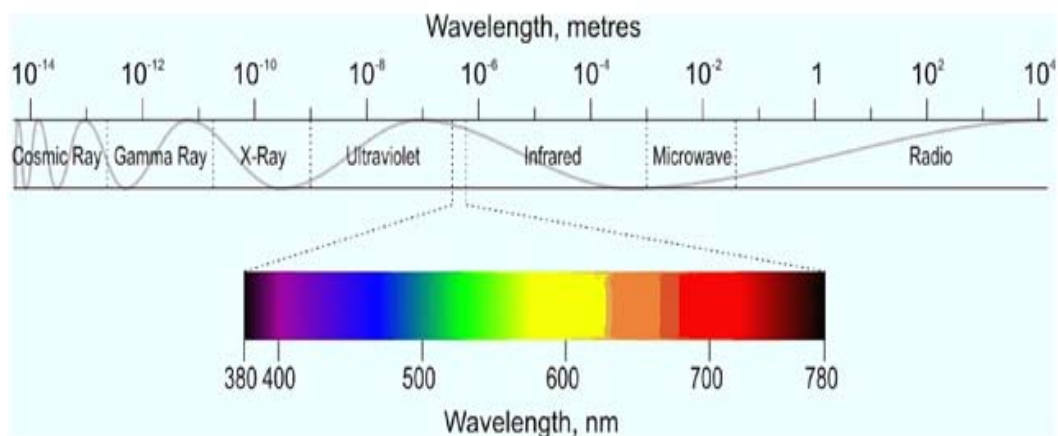
Figure 2.7a Solar radiation wavelength bands.

---

6 Source: Lighting Industry Federation Ltd.

Spectrally selective surfaces for solar absorbers have been studied since the 1950s, when the idea of using wavelength separation was introduced by Tabor [18]. Spectrally selective solar surfaces are used for the conversion of solar radiation into thermal energy.

Since then numerous studies have been conducted using different types of absorber coatings. Four cases were reviewed of how proper design of radiative surface properties could be used for heating and cooling purposes.

Surfaces were manufactured by mechanically operated grinding for about 15 min when producing a whole sheet 2 m long and 0.12 m wide. The grinding process did not produce any environmentally harmful waste [19].

Further experimental studies showed that by altering the composition of the grinding pad and locating the best grinding parameters for the advanced pad then a higher absorbptance α could be produced [20]. High solar performance Zr–ZrO_2 cermet solar coatings were designed, so achieving a solar absorbptance of 0.96 and an emittance ε of 0.05 at 80 °C for deposited films [21].

A series of metal–aluminium nitride (M–AlN) cermet materials for solar selective coatings were deposited by a novel direct current, magnetron sputtering technology. Aluminium nitride was used as the ceramic component in the cermets and stainless steel [22].

Electrochemically deposited thin films of black chromium or black nickel are widely used for efficient conversion of solar thermal energy. These films can provide absorber-reflector tandems with good selective properties [23].

An electrolyte was proposed for the deposition of black cobalt selective absorber coating on copper plate [24]. The emittance and absorbance increased with increasing deposition time or thickness. Nickel pigmentation was applied to anodically oxidised surfaces in order to produce selective coatings on aluminium substrates to be used as absorber plates in high efficiency solar collectors [25].

Solar selective surfaces are generally composed of two thin film layers. The first layer closest to the substrate, which is often glass, is a thin film of metal such as Cu, Al, Au, or Ag and provides the high IR reflectance property of the selective surface. The second layer often consists of a combination of metal and dielectric materials in a two-phase form which is often referred to as a cermet.

Selective surfaces were produced of comparable performance to reactively sputtered and vacuum deposited surfaces with high temperature stability by deposition of carbon and silica onto copper-coated substrates [26]. Today's selective surfaces have good optical properties: 90 %< α<98% and 3 %< ε<10%.

For collectors operating at a high temperature range and upper medium temperature range, selective absorber coating is worthwhile because it reduces radiation losses significantly.

The ability of the collector to absorb solar energy and keep it from being lost is illustrated by the Hottel-Whillier Bliss efficiency curves [27].

These curves show that the greater the temperature difference between the collector outlet water (Tout) and the ambient air (Ta), the lower the operating efficiency due to heat loss. The wavelength of a radiation emitted from a surface is proportional to the temperature of the surface (Planck's Law).

An ideal selective surface for solar collectors should absorb electromagnetic radiation (light) in the visible range and emit a small amount of radiation back in the infra red range. So the maximum amount of energy from the incoming sunlight is used to heat water.
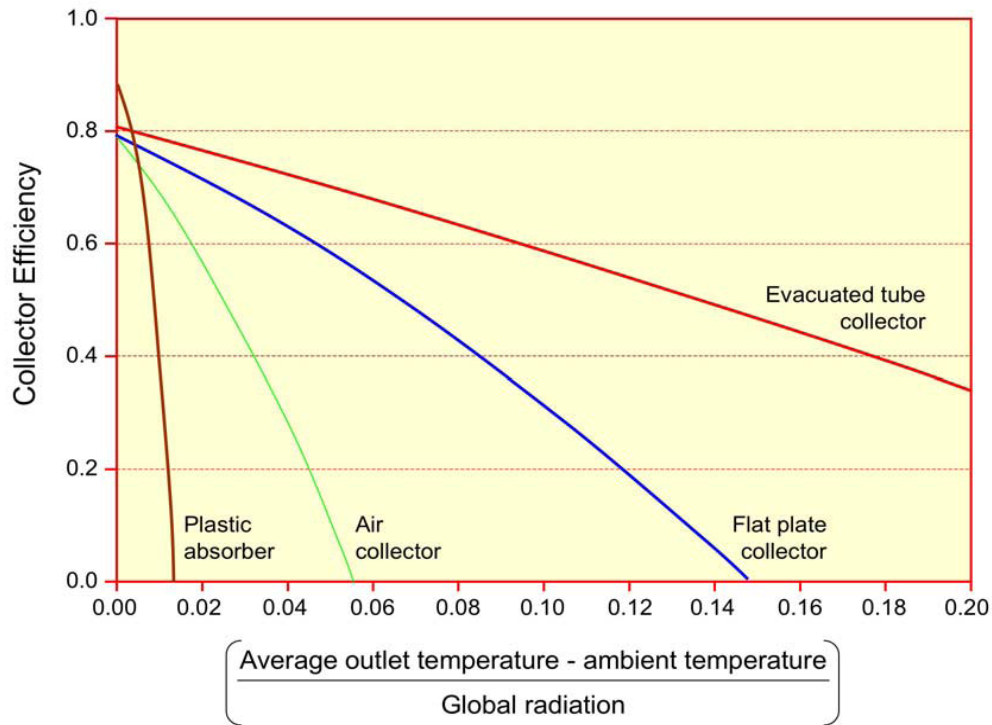
Figure 2.7b Hottel - Whillier Bliss efficiency curves [27].

In selective coating a thin layer of a selective material (i.e. black chrome or black nickel) is applied by electrolysis onto the surface. A layer of this kind has the property that it absorbs solar energy about the same as that of a black non-selective surface.

The difference is that it is a poor emitter of energy at the temperature of the base metal. Therefore, a selectively coated absorber under sunlight will get hotter than a simple matt black one.

Selective coatings enable the collector to operate better in weak sunlight. Water temperatures in collectors coated with black chrome can rise above 80 ºC after a few hours of sunlight. The temperature that drops over the night, or the heat loss after cloudy spells, are relatively small [28]. This is a result of the coating's high absorbptance and low emittance. A collector with a selective coating is illustrated in Figure 2.7c[7].

Figure 2.7c Selective coating on solar collector.

The absorber coating on glazed solar collector absorber plates must be able to withstand stagnation temperatures and they must be stable and resilient to endure the weather exposure of unglazed collectors. The most secure paint and primer bonding is obtained in high quality collectors by using an electrostatic painting process. Common methods for selective surfaces are used in the production of absorber plates: Oxide, Chemical, Electroplated and Vapour deposited [29].

---

7 Source: Sun Earth Inc.

2.8 Glazing

Glass is a good material for glazing flat plate solar collectors as it transmits almost 90% of the received shortwave solar radiation. Types of plastics can also be used as covers as few of them can endure ultraviolet radiation for a long time.

Polycarbonate rigid sheet, polycarbonate rigid film and corrugated sheets are plastic products available on the market. The benefit of using plastics is that they cannot be broken by hail or stones and they are flexible and light [30].

A design of the solar window was developed with the expectation to improve the performance of the solar energy collectors at high solar radiation incidences [31]. The solar window was composed of two transparent plastic sheets of acrylic ribbed together. One of the inner surfaces of the solar window has triangular projection pairs separated from the adjacent projection pair by a distance equal to the width of the triangular projection pair at the top.

A transparent cover plate often made of glass reflects around 8% to 10% of the incident solar radiation, so resulting in a reduction in the overall efficiency of the collector.

Antireflective coatings on glass sheets are also a possibility for increasing the efficiency of solar energy systems by reducing the reflection of the incoming light. Studies have shown that the transmittance of glass can be increased by 4% if the glass is equipped with antireflection surfaces and also in return the efficiency of the solar collector can also be increased [32].

An effective antireflective coating on glass panels was developed for solar applications [33]. The coating solution was prepared by a sol-gel technique. The sol-gel technique is based on hydrolysis of liquid precursors (i.e. metal chlorides) and formation of colloidal sols. A gel is a state where both liquid and solid are dispersed in each other, which presents a solid network containing liquid components which is applied on the glass by dip-coating. Thus, the sol evolves towards the formation of a gel-like dysphasic system containing both a liquid phase and solid phase whose morphologies range from isolated particles to continuous polymer networks.

A wide band antireflective effect leads to an increase of solar transmission from 90% for an ordinary glass up to 96% for an antireflective coated glass. If constant thermal losses are assumed, a 5% increase in solar transmittance could result in as much as a 10% improvement in energy collection efficiency.

Other types of antireflective coatings (AR) were tested including various sol-gels applied to glass and to an embossed treatment of sheet acrylic [34].

Recently, a silica low-reflection coating via a dip-coating process has been developed. The value of the film refractive index that leads to a minimum of reflection on the surface of the glass cover was achieved. A comparison has been made between an uncoated flat-plate solar collector glass cover and one with a porous sol-gel antireflective coating [35].

2.9 Designs and Improvements in Solar Water Systems

Flat plate solar collectors used in modern domestic hot water systems have not changed significantly in the past twenty years. These types of absorbers typically have high heat losses through convective and radiative heat transfer. A number of designs

have been investigated in order to reduce heat losses in flat plate collectors and improve their efficiency.

In the 60's a method in order to estimate the performance of solar water heaters circulating to a storage tank by thermosyphon was investigated. Two absorber and tank systems were tested and the results compared with those estimated from the theoretical method [36].

The method described above was improved by the development of a computer model incorporating a collector efficiency factor and expanding solar radiation and air temperature as Fourier series in time [37].

In the mid 70's more comprehensive studies to evaluate the thermal performance of a thermosyphon system were conducted. An experimental test rig, incorporating a system having five thermocouples on the bottom surface of the water pipes and six thermocouples on the bottom surface of the absorber plate was designed and tests performed. Thermocouples were also placed in the storage tank [38, 39].

In the 80's the long term performance, transient response, system modelling and operation characteristics of a thermosyphon system with vertical or horizontal storage tank were investigated. Its performance was maximised when the daily collector volumetric flow was approximately equal to the daily load flow [40].

The use of an optical element consisting of three specularly reflective surfaces and an infra red reflective surface facing towards the absorber of a flat plate solar collector has been described [41]. By incorporating a panel of such optical elements in between the absorber and the window of the flat plate solar water collector, the radiation and convection heat losses were reduced.

When the enhancement of solar water heater associated with mirrors is considered and then the difference has to be made between any geometrical-optical enhancement and the actual benefit in terms of the collector output. The collector output depends on parameters that are considerably different from the geometrical enhancement [42].

In contrast to previous approaches, i.e. repair the winter damage caused by placing the collector at a smaller than optimal tilt angle, a reduction of the overall height of a thermosyphon solar water heater by lowering the collector tilt angle and attaching a mirror to the elevated storage tank was proposed [43].

Approximations that are often made were reinvestigated in order to treat the reflection of diffused radiation. It was concluded that by ignoring this diffused component, the net enhancement caused by the use of a plane reflector would, in general, be overestimated.

In a flat plate solar collector energy losses occur by natural and forced convection, as well as by radiation. To minimise these loses the collector is thermally insulated on its sides and bottom [44]. The upper surface has most of the thermal losses.

An alternative way of minimising the energy loss is through the addition of a wind barrier alongside the collector's perimeter [45]. The barrier reduces the wind velocity over the solar collector by creating a re-circulation zone behind it and so it is more efficient in minimising energy loss than the traditional addition of a second glass cover.

The efficiency of solar collectors is related to the flow distribution through the parallel riser tubes. The sensitivity of the flow distribution to the collector design parameters focusing on junction pressure losses and continuous energy losses due to friction. The relation of these parameters is responsible for the different flow distributions in such a collector system [46].

An experimental study was conducted in a water solar flat plate collector with laminar flow conditions to analyse the flow distribution through the collector [47]. It was concluded that the flow distribution depends on the relation between energy loss in the risers and the energy losses in the manifolds. To obtain a homogeneous flow distribution the influence of the energy losses in the risers must control the system.

The contamination of solar collector surfaces by dust can be a source of considerable loss of solar power. The general problems of collector surface maintenance have been reviewed in recent years [48]. Studies have been conducted upon the effect of dust accumulation on the performance of solar collectors [49].

A computerised microscope system has been developed for studying the physics of dust particles that stick to various kinds of surfaces, such as those of solar collectors [50]. The device enables the particle size distribution of dust on a surface to be obtained together with the calculation of the fraction of surface area covered by dust and the reduction of optical efficiency.

A cleanliness level of 90% relative to a perfectly clean surface will, for many kinds of collectors, imply an annual loss in profits of 10%.

A bifacial collector shown in Figure 2.9a incorporates two stationary concentrators with a flat plate absorber mounted above them [51]. This design achieved higher efficiencies than other flat plate collectors under low irradiation conditions.
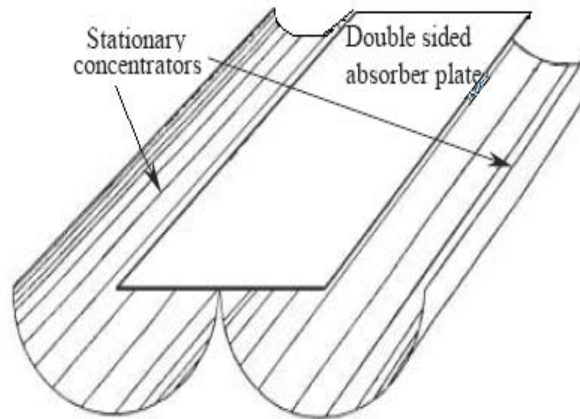
Figure 2.9a A Bifacial Collector [51].

A collector design was presented for domestic solar water heating [52]. The use of a double sided absorber with low emissivity selective surface coupled with high reflectance stationary concentrators reduced the radiative and conductive losses through the back of the collector. The main source of heat loss in this design is through the glass cover. The net heat losses were 30% – 70% lower then conventional systems.
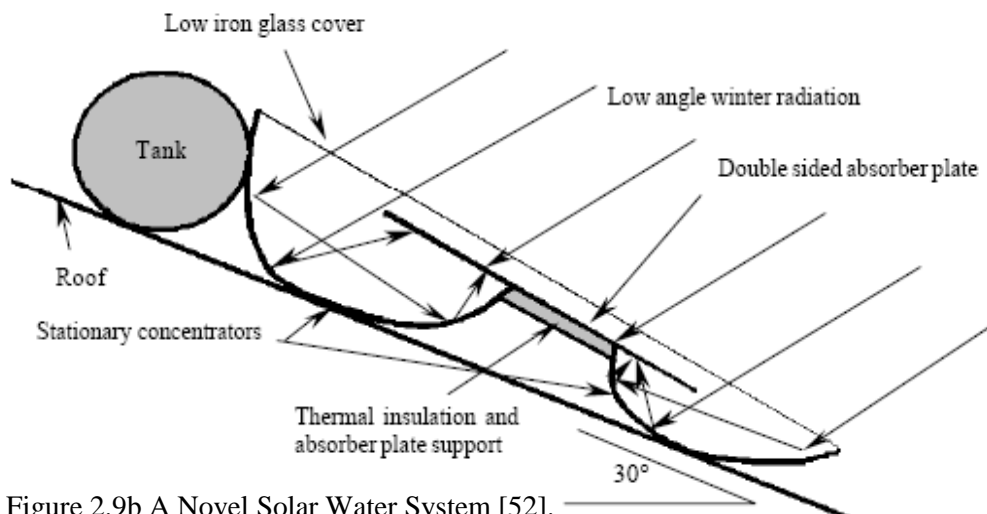
Figure 2.9b A Novel Solar Water System [52].

Although many types of conventional collectors are available on the market, their investment costs are still relatively high A simulation model of a large-area plastic solar collector installed in Almeria, Spain was developed. The model was validated and found to fit well to experimental data [53].

Advances in polymer technology resulted in the development of suitable materials to withstand long exposure under the sunlight. Experimental studies on the performance of a rubber product as an absorber plate showed it can be used as an alternative to conventional ones [54].

An experimental and theoretical evaluation of the performance of a tar solar water heater and its comparison with that of a conventional type collector was investigated [55]. Results showed that the conventional collector was more efficient than the tar type during most of the hours of daylight, but that the tar collector had the added advantage of better conservation of energy in late afternoon and evening.

The reverse flat plate collector shown in Figure 2.9c has an inverted absorber plate with a stationary concentrating reflector beneath [56].
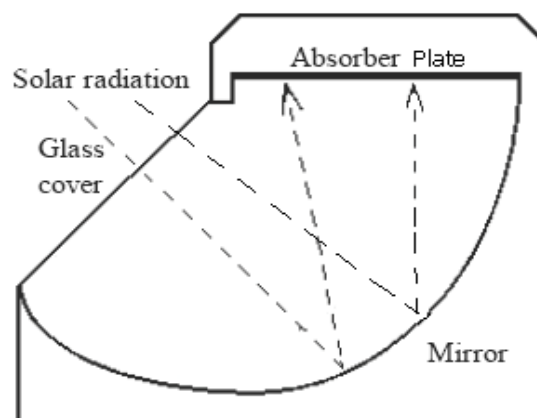
Figure 2.9c Inverted Absorber Plate [56].

This design reduces considerably the convective heat losses, but there are still heat loss paths through the insulation above the collector and the conduction of heat through the air cavity. This design allows modifications on the shape of the concentrating mirror. The drawback of this collector is its large size ensuing difficulties carrying it and mount it on a typical roof.

Another type of stationary collector is the integrated collector where the collection and the storage tank is one unit. A rectangular built in storage water system was investigated initially by Tanishita [57]. However, these rectangular shaped systems have a low solar gain and poor heat transfer during winter in northern latitudes.

A triangular built-in-storage solar water heater, as seen in Figure 2.9d, has been studied under winter conditions. The system resulted in higher solar gain and enhanced natural convection, leading to a higher water temperature. A comparative study of the triangular water heater with a rectangular one was also made [58].
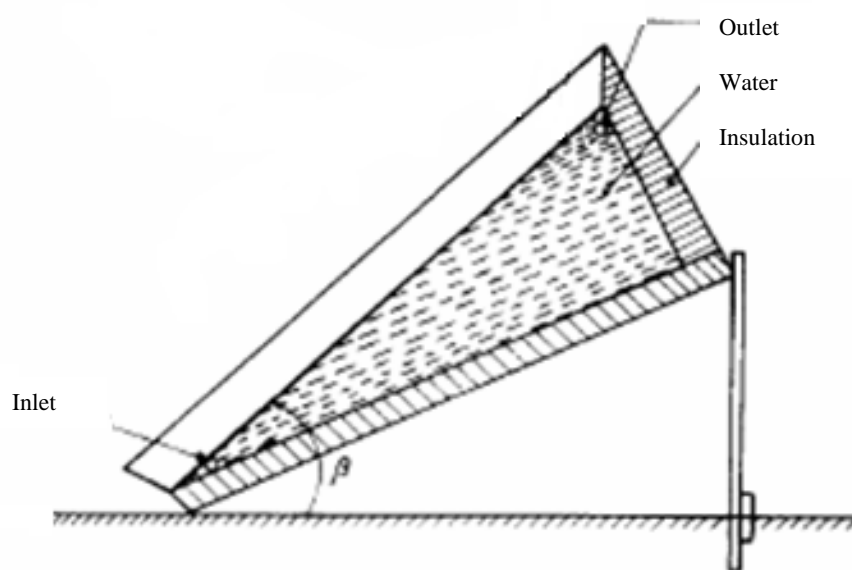
Figure 2.9d A triangular built-in-storage solar water heater [58].

An 'Integrated Collector Storage Solar Water Heater' (ICSSWH) system, as seen in Figure 2.9e, that incorporates two cylindrical vessels, an outer absorbing vessel and an inner storage vessel, has been developed [59]. The space between the two vessels contains a small pool of water which when heated evaporates and consequently condenses on the surface of the colder surface of the inner vessel, thus transferring thermal energy to the store.
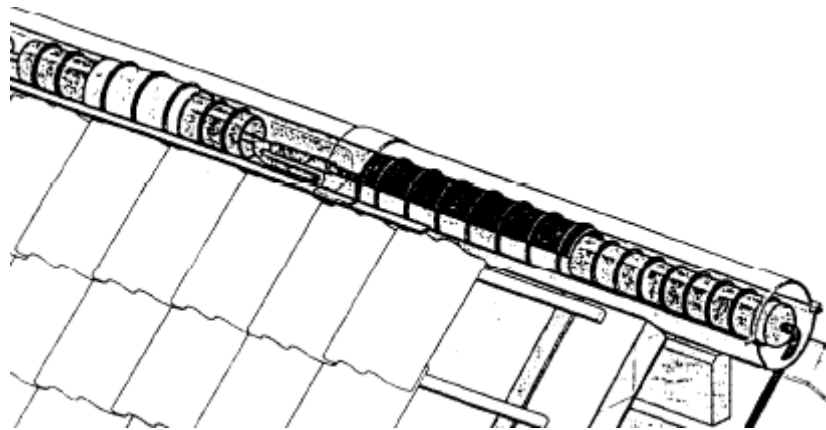
Figure 2.9e A novel Integrated Collector Storage Solar Water Heater [59].

An analysis and experimental data were presented for a solar water heater of the integrated collector–storage type as seen in Figure 2.9f.

Figure 2.9f An Integrated collector–storage system [60].

One of the storage tank walls is coated on its outer surface to enable it to act as a solar absorber plate. Its design incorporates a device that automatically lowers the heat-loss coefficient of the system during night time. This overcame one of the basic problems associated with solar water heaters of this sort [60].

A new configuration, shown in Figure 2.9g, was developed recently for the design of a compact ''Solar Domestic Hot-Water System'' (SDHWS) with Two-Phase Closed Thermosyphon (TPCT) modules assembled in parallel [61].
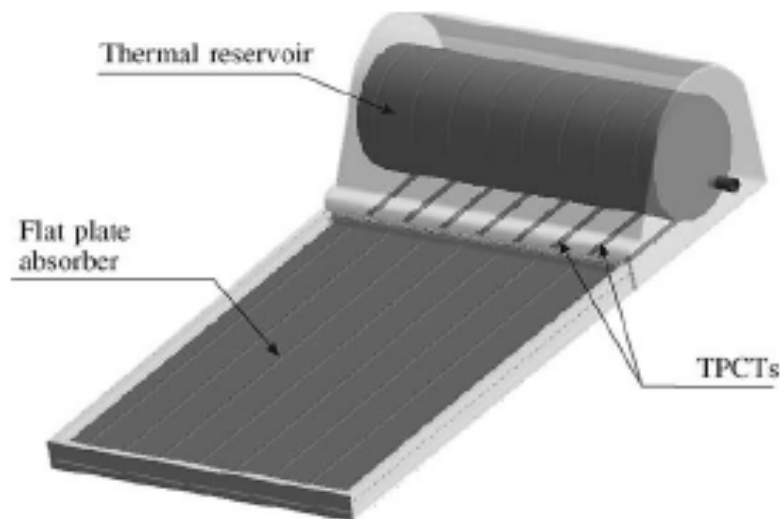
Figure 2.9g TPCT module [61].

Each individual module has a TPCT coupled with a flat plate absorber in the evaporator and with the thermal reservoir in the condenser. The main advantages of solar heating systems using TPCT's are better thermal efficiency, antifreezing natural protection and thermal diode working characteristics.

An inverted absorber 'Integrated Collector Storage Solar Water Heater' ICSSWH mounted in the tertiary cavity of a compound parabolic concentrator with a secondary cylindrical reflector using several types of transparent baffles at different locations within the collector cavity was experimentally investigated [62].

It was concluded that the collector performance increased by using transparent glass baffles in the collector cavity. By employing full baffles or baffles located at the wrong position resulted in unnecessary surfaces at which extra reflections and absorption of incident radiation occurred thus cancelling any thermal benefits of reduced fluid motion.
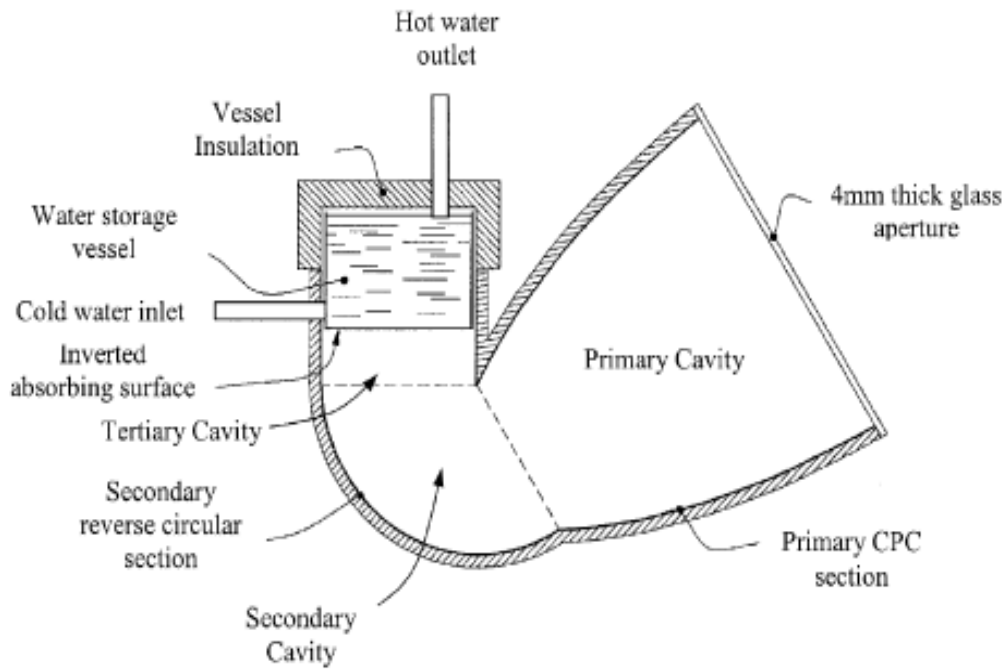
Figure 2.9h An inverted absorber ICSSWH [62].

The cylindrical solar water heater listed in Figure 2.9i was designed and manufactured in Bahrain.

Figure 2.9i A cylindrical solar water heater [63].

It consisted of a cylindrical tube of length 0.8 m, outer diameter 0.14 m and thickness 6 mm, made from high quality glass. A copper coil tube in the shape of spiral rings, with the tube having inner and outer diameters of 2 mm and 3.18 mm, respectively [63]. The tube was painted black to allow incident solar energy to reach the cylinder wall. Due to its circular shape it is not necessary for this system to be directed at the sun, whereas the flat plate collector should always be directed at the sun, with a certain tilted angle to maintain the maximum efficiency.

Another type of Solar Collector that has emerged in recent years is the Photovoltaic Thermal (PVT) panel. This enables the radiation to be converted into both heat and electricity.

The basic concept PVT panel consists of a photovoltaic (PV) laminate that is joined to a sheet-and-tube type solar thermal absorber. Prototypes were designed, built and tested in order to increase thermal absorption [64, 65]. The resulting PVT panel produced was by direct lamination of the PV subsystem onto the sheet-and-tube substrate. This resulted in a good thermal performance, with basically the same production steps as for conventional PV panels.

Other designs considered the modelling of a hybrid PVT collector coupled with a compound parabolic concentrator (CPC). In this design, several CPC troughs are combined in a single PVT collector panel [66].

A similar system to that of the Photovoltaic Thermal panel is the Hybrid Photovoltaic Thermal (HPVT) solar system which provides a simultaneous conversion of solar radiation into electricity and heat [67, 68]. Although in these systems the PV modules are mounted together with the heat recovery units, a

circulating fluid cools them during their operation as PV cells operate better at low temperatures

Figure 2.9j Front and back side of a PVT [67].

An experimental model of a HPVT system of a bifacial PV module was constructed and studied. Electric energy production with this configuration was enhanced [69].

The hybrid system implemented with a bifacial module produces approximately 40% more electrical energy than a conventional PVT system without any noticeable increase in the cost of the system.

If the solar plane collector is made transparent in the spectral region of a working PV module, i.e. for photon energies larger than the band gap of the module's

absorber–semiconductor and absorbing for smaller photon energies, a bifacial PV module can be used in a PVT hybrid system.

Figure 2.9k A bifacial PV module [69].

Studies focused on the actual collectors and the improvement of the convectional heat transfer between the metal parts and the water has also been conducted by researchers. Among numerous techniques available for the intensification of heat transfer extending the heat transfer area in single pipes or flat-plate solar collectors using internal fins, appeared to be a hopeful method according to the results obtained from several past investigations. For both laminar and turbulent flows, the finned tubes demonstrated substantially higher heat transfer coefficients when compared with corresponding smooth (un-finned) tubes[113,114].

An experimental set-up was designed to study the heat transfer performance in the entrance region as well as in the fully-developed region. The tube and the fin assembly were cast from aluminium to avoid any thermal contact resistance. The length of the test section was 15.2 m. The inner diameter of the tube was 70 mm. The

tube contained six equally spaced fins of height 15 mm. Air was used as the working fluid in all experiments. The enhancement of heat transfer rate due to integral fins was found to be very significant over the entire range of flow rates studied in this experiment. Heat transfer coefficient, based on inside diameter and nominal area of finned tube exceeded un-finned tube values [115].

Laminar flow in internally finned tubes by assuming constant and uniform heat flux in tube and fin surfaces has been analysed. Using 22 fins extended to about 80% of the tube radius, they showed that an enhancement as high as 20 times that of un-finned tube could be realised [116].

A theoretical study investigated the effects on collector efficiency of a solar water heater with fins attached as shown in Figure 2.9l. The theoretical prediction showed that the higher collector efficiency was obtained under the suitable designing and operating parameters. Considerable improvement in collector performance was obtained by employing water recycle operation with fins attached, instead of employing a single-pass flat-plate device [117].
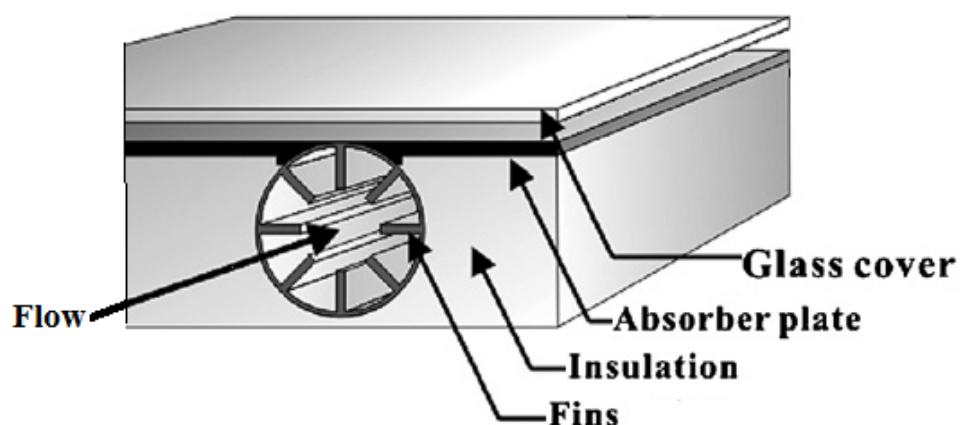
Figure 2.9l Solar water heater with internal fins [117].

To summarise the types of the collectors described in this chapter, Table 2.9a was created to point up their performance.

Collector Types	Operational Collection Efficiency
Collector with internal fins (Theoretical)	60% - 72%
Bifacial type collectors	50% - 68%
Intergraded solar systems (ICSSWH)	46% - 63%
Plastic Collectors	42% - 52%
Tar Collector	40% - 50%
Convectional Collector	40% - 46%
Cylindrical Collectors	38% - 42%

Table 2.9a Collector types and their efficiencies.

The efficiency ranges depended on the ambient temperatures and the time of the day that the experiments took place. Other studies focused only in investigating the collectors theoretically and therefore the resulting efficiencies were based upon the data used.

2.10 Conclusions

After reviewing all the systems available and the techniques incorporated in order to improve their efficiency, it was concluded that in many of the systems the alterations and modification were focused only at changing the original shape of a solar collector (i.e. intergraded and bifacial collectors), resulting to bulky, expensive, unsuitable for domestic purposes systems, that are efficient but unattractive for the market. Collectors produced by polymer plastic are very expensive as they need to have a large area to absorb sufficient heat. Customers are preoccupied in buying a collector made of plastic since it is not nature friendly. The same principle would apply to the collector utilised tar that instead of copper fins. The cylindrical type collector had the

lowest efficiency since its aperture area is small. Increasing its area would definitely increase its efficiency but also its manufacturing costs.

The highest efficiency (theoretical) occurred in the collector utilised internal fins in its pipes. This technique has been employed and experimentally tested to single pipes with larger diameter in order to fit a number of fins internally. Since commercial collectors have an internal diameter of 8 mm it is practically difficult almost impossible[8] to fit a sufficient number of internal fins thick enough to enhance the heat transfer between the copper and the water; the internal fins will also increase the collector's manufacturing, cost since copper is more expensive, compare to other metals like aluminium for instance.

The question rose at that point was what could be carried out aiming to improve the efficiency in a flat plate collector without changing its original shape and without increasing its manufacturing costs. Also the majority of the research reviewed was focused in increasing the heat transfer by gathering more radiation from the sun.

At this point the research scope was to investigate the area of the convective heat transfer since the highest possible efficiency was achieved in the systems that incorporated this method (i.e. internal fins in the pipes). Therefore the plan was to identify methods to improve the collector's efficiency based on the convective heat transfer theory and how they affect the fluid flow inside the pipes. Keeping the manufacturing costs low was also a factor that needed to be taken into account.

---

[8] Sun systems manufacturing quote.

CHAPTER 3

Theoretical Background

This chapter deals with the theory behind the modes of heat transfer and background work on the convective heat transfer enhancement techniques, since the research scope was focused in this area. Another important issue that investigated in this chapter was the existing mathematical model that portrays the operation of a collector and can predict its performance. The theoretical background would form the platform of the research techniques that will be used this project, since they will be based on physical phenomena, thermodynamic principles and existing mathematical models and will be correlated and cross examined with the experimental and the numerical work (simulations).

3.1 Heat Transfer

Heat transfer is the thermal energy exchange between bodies when there is a temperature difference between them. Thermal energy is transferred from the higher temperature, to the lower temperature. Temperature is a measure of the amount of energy molecules a body holds. In SI units, heat is typically denoted by the symbol Q and it is expressed in joules (J). The rate of heat transfer q is measured in watts (W), which are joules per

second. The rate of heat transfer per unit area, heat flux, is measured in watts per area (W/m^2).

3.2 Heat Transfer Modes

Heat transfer processes are classified into three modes: conduction, convection and radiation. Conduction occurs when there is a temperature gradient across a body. It is an energy transfer across a system due to random molecular movement. Higher temperatures are related with higher molecular energies, hence when they collide with molecules of lower energy and conduction occurs.

Conduction process is illustrated below in Figure 3.2a[1]. A metal for instance has one surface at a high temperature T_1 and one at a lower temperature T_2.
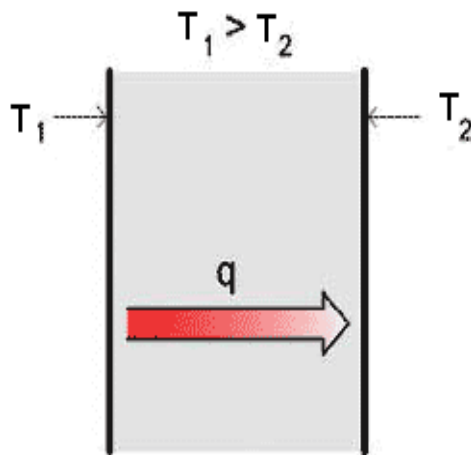
Figure 3.2a Conduction process.

In engineering, the conduction rate is described by the Fourier equation:

$$q = -kA\nabla T \qquad (3.2.1)$$

[1] Source: Home foam insulation.

where q is the heat flow in W, k is the thermal conductivity of the material in W/mK, A is the cross-sectional area in the heat flow direction in m^2. ∇T denotes the temperature gradient in K/m and is given by:

$$\text{Σφάλμα! Δεν έχει οριστεί σελιδοδείκτης.} \nabla T = \frac{\partial T}{\partial x} i + \frac{\partial T}{\partial y} j + \frac{\partial T}{\partial z} k \quad (3.2.2)$$

In tube shaped walls it is convenient to use the radial direction given by:

$$q_r = -kA_r \frac{dT}{dr} \quad (3.2.3)$$

The second heat transfer process is convection as shown in Figure 3.2b [2]where the motion of fluids (gas or liquid) is used to transfer heat. This type of heat transfer consists of two mechanisms: diffusion and energy transferred by mass or macroscopic motion of the fluid. The convection heat transfer occurs when a cool fluid flows past a warm body.
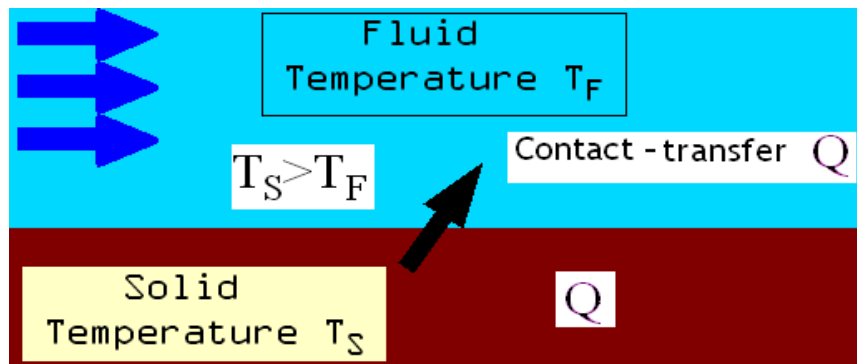
Figure   3.2b   Convection   heat

When heat conducts into a fluid it causes a volumetric expansion. This results in a gravity-induced pressure gradient, the expanded fluid displaced and thereby transferring

---

[2] Source: Wikimedia commons.

heat. The warm fluid is replaced by a cooler one, which can then extract more heat away from the surface. The rate of heat transfer from a surface by convection is given by:

$$q = hA_s \Delta T$$
(3.2.4)

where h is the convection heat transfer coefficient measured in W/m^{2}K and describes how effectively a fluid transfers heat by convection. A_s is the surface area of the object, ΔT is the temperature difference between the surface temperature T_s and the fluid temperature T_f.

The convection heat transfer can be natural (free) convection where the fluid motion is created by the warm fluid itself. The density of fluid decreases as it is heated and it becomes lighter than the cold fluid. Forced convection occurs when the flow is caused by external means, such as pumps.

The third process is radiation where the transmission of energy is achieved without the presence of a body. Radiation travels at the speed of light and it is emitted by any matter with temperature above 0 K. This is represented in Figure 3.2c[3]
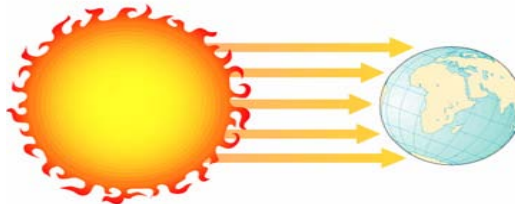
Figure 3.2c Radiation from the Sun.

---

[3] Source: Wyckoff schools.

This mode of heat transfer as shown in Figure 3.2d[4], takes place when the emitted radiation strikes another body and it is absorbed. For example, solar radiation is absorbed by bodies and it is why objects are warmer in the sun than in the shade.
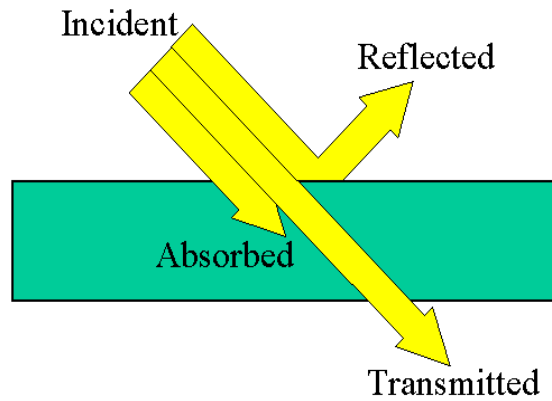
Figure 3.2d Radiation process.

The electromagnetic radiation emitted by bodies is propagated as a result of a temperature difference and it is called thermal radiation. The emissive power of a surface is given by

$$E = \sigma \varepsilon T_s^4 \ (\text{W/m}^2)$$

(3.2.5)

where ε is emissivity, ($\varepsilon = 1$ is black body), σ is the Stefan Boltzman constant equal to 5.67 x 10^{-8} W/m^{2}K^4, T_s is the temperature of the surface. The above equation is derived from the Stefan Boltzman law and it describes heat emission.

Emissivity depends on the surface material and the surface texture. It ranges from $0 \leq \varepsilon \leq 1$, providing a measure of how efficiently a surface emits energy relative to $\varepsilon = 1$.

---

[4] Source: Remote Sensing Project.

The rate of radiation heat exchange between a surface and a large surrounding area is called the Stefan Boltzman law of thermal radiation and it is given by the following expression:

$$q = \sigma A(T_s^4 - T_a^4) \qquad (3.2.6)$$

where A is the surface area, T_s is the temperature of the surface and T_a is the ambient temperature. This law only relates to blackbodies.

3.3 Modes of Fluid Flow

When considering fluid flow in pipes, there are three flow patterns: Laminar, Transitional and Turbulent. Laminar flow as shown in Figure 3.3a[5] appears at lower flow rates through small pipes. The name is derived from the fluids moving in arranged layers or laminate.The fluid particles flow in concentric cylinders, where the outer particles, do not move due to the frictional resistance between the fluid and the pipe wall.
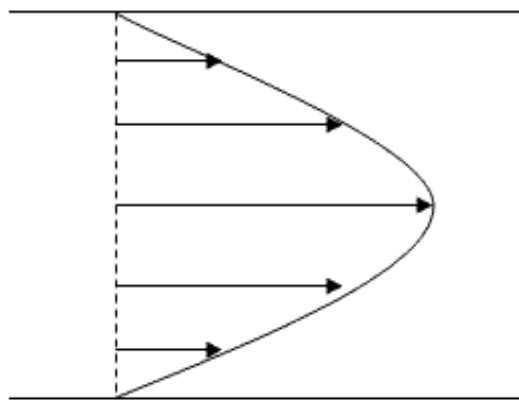
Figure 3.3a Laminar flow.

The next cylinder flows against the outer motionless fluid cylinder, which exhibits less frictional resistance than the pipe wall. The others are moving at increasing velocities at the centre of the pipe. Due to this trend laminar pipe flow yields a parabolic velocity profile.

When the flow shows evidence of both laminar and turbulent flow or a mixture then it is called Transitional flow. The edges of the fluid flow are in a laminar state, whilst the centre of the flow continues to be turbulent. Alike to turbulent flows, transitional flows are not easy to measure accurately. Each of these flows behaves in a different way in terms of their frictional energy loss.

A flow is Turbulent when the fluid particles have an irregular motion towards the direction of flow. The fluid travels in random paths with no clear pattern and no definite layers. Turbulent flows are by nature chaotic and they are characterised by constant changes in their behaviour. Turbulent flow usually occurs in larger diameter pipes at high flow rates and it has a velocity profile as shown in Figure 3.3b[5].
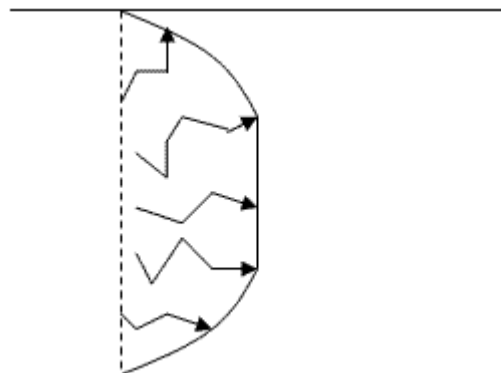
Figure 3.3b Turbulent flow.

The flow velocity profile for turbulent flow is fairly flat across the centre section of a pipe and then it drops rapidly very close to the walls. The average flow velocity is approximately equal to the velocity at the centre of the pipe.

This produces eddies in the flow, which in turn produces a better fluid mix and causes boundary layer separation. This can lead to improved heat transfer rates due to the fluid mixing and the reduced boundary layer effects.

3.4 Reynolds number

Osborne Reynolds proved experimentally that a dimensionless parameter called the Reynolds number provides a quantitative explanation of a flow. The nature of a flow depends on the mean flow velocity v, the pipe diameter D, the density ρ and the fluid viscosity μ. The equation for the Reynolds number is given below and is a ratio of the fluid dynamic forces and the fluid viscous forces.

$$Re = \frac{vD\rho}{\mu} \qquad (3.4.1)$$

The viscous forces occur because of the internal friction of the fluid. The dynamic or inertia forces represent the natural resistance of the fluid to motion. In a low Reynolds number the inertia forces are insignificant compared with the viscous forces, whilst in a high Reynolds number flow the viscous forces are small compared to inertia forces.

The flow in pipes is regarded as being laminar if the related Reynolds number is less than 2300 and it is turbulent if the Reynolds number is greater than 4000. Between

these two values there is the critical zone where the flow is transitional and it can be either laminar or turbulent or the flow can change between the two. It is essential to know the type of flow in a pipe when considering friction losses and obtaining the appropriate friction factors.

3.5 Boundary Layer and Friction Factor

When a fluid flows through a pipe its molecules interact with the pipe wall and slow down. These molecules consequently delay the flow just above them. This creates a thin layer of fluid near the pipe wall in which the velocity changes from zero at the inner surface of the pipe to the free stream value, a small distance away from it. This layer is called the boundary layer because it is developed at the boundary of the fluid.
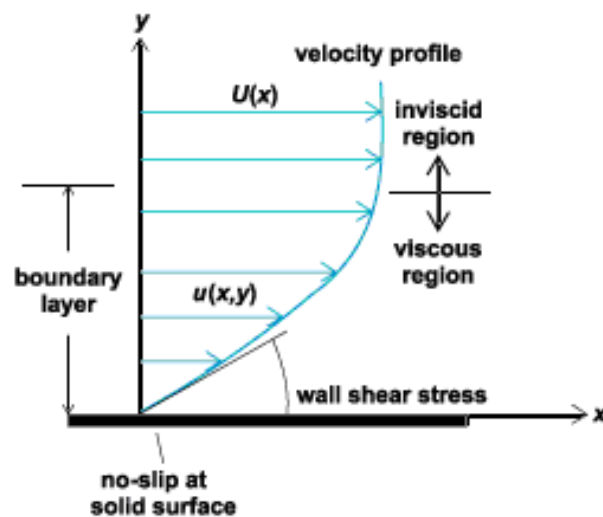
Figure 3.5a Boundary layer occurrence inside a pipe.

For the boundary layer to be thin the Reynolds number of the body needs to be large, 10^3 or more. Under these conditions the flow outside the boundary layer is effectively inviscid, i.e. it is assumed to have no viscosity.

The fluid has zero velocity relative to the boundary, i.e. no-slip condition where $u(x, 0) = 0$, as shown in Figure 3.5a[6], where u is the velocity of flow in the boundary layer and $U(x)$ is the outer (inviscid) stream velocity.

The fluid in the boundary layer is undergoing shear forces. In the boundary layer at any point, the shear stress τ is proportional to the local velocity gradient. The shear stress is conveyed on top of the boundary as a result of this loss of velocity and can be expressed as:

$$\tau_w = \mu \frac{\partial u}{\partial y}\bigg|_{y=0} \qquad (3.5.1)$$

where μ is the dynamic viscosity of the fluid, u is the velocity of the fluid along the boundary and y is the coordinate perpendicular to the boundary. The value of the shear stress at the wall is very important as it affects the heat transfer between the wall and the working fluid. Since τ approaches zero asymptotically at the outer edge of the boundary layer, the thickness of a boundary layer δ is normally defined randomly as the point where $u = 0.99U$.

The term head loss is used to express the resistance to flow created by the roughness of the pipe. The diameter of the pipe, the resistance through various valves and

---

[6] Source: Answers.com

fittings, the viscosity of the fluid, the roughness of the pipe walls, the changes of height inside the system and the distance the fluid is transferred, are all factors that affect the head loss in pipes.

Darcy introduced the idea of relative roughness where the ratio of the internal roughness of a pipe to the internal diameter of a pipe will affect the friction factor for turbulent flow. In a relatively smooth pipe the turbulence along the pipe walls has less overall effect.

The Darcy Equation is a theoretical equation that predicts the frictional energy loss in a pipe based on the velocity of the fluid and the resistance due to friction.

The Darcy-Weisbach friction factor is a dimensionless number used in internal flow calculations with the Darcy-Weisbach equation. It expresses the linear relationship between the mean flow velocity and the pressure gradient.

The Darcy-Weisbach equation listed below is regarded as the best empirical relation for pipe flow resistance. The head loss for fluid flow is directly proportional to the length of pipe, the square of the fluid velocity, and a term accounting for fluid friction called the friction factor. The head loss is inversely proportional to the diameter of the pipe.

$$h_f = \frac{fLV^2}{2Dg} \qquad (3.5.2)$$

where, h_f is the head loss(energy loss per length of pipe, bends, fittings), f is the friction factor, L is the pipe length, V is the average flow velocity, D is the pipe diameter and g is the acceleration of gravity ρ is the fluid density.

In terms of pressure drop, it is:

$$\Delta P = f\, \frac{L}{D}\, \frac{\rho V^2}{2} \qquad (3.5.3)$$

For laminar flows the friction factor f or coefficient of flow λ is a result of Poiseuille's Law and states that λ equals to *64/Re*. For rough pipes and hence turbulent flow, it is necessary to use the Moody chart to obtain the friction factor f. That may require a reiteration where a flow rate is guessed, f estimated and then a new flow rate calculated. Another way is by solving equations such as the Colebrook-White, or the Swamee-Jain equation. The Swamee-Jain equation listed below allows f to be found directly for the full flow in a circular pipe.

$$f = \frac{0.25}{\left\{ \log \left[\dfrac{e}{3.7D} + \dfrac{5.74}{Re^{0.9}} \right] \right\}^2} \qquad (3.5.4)$$

3.6 Heat Transfer Enhancement Techniques

The flow distribution through the finned tubes of a collector clearly affects the operational efficiency of the collector system. Therefore, the more uniform the flow through the tubes, then the higher efficiency of the collector, and vice versa [70, 71]. The flow distribution can be evaluated by temperature measurements at various points of the collector [72].

A numerical and experimental investigation of the flow and temperature distribution in a 12.5 m2 solar collector panel with an absorber consisting of 16 parallel connected horizontal fins was performed. [73]. The fluid flow through the *ith* tube (counted from the top) was characterised by a parameter β_i, defined as follows:

$$\beta_i = \frac{Q_i}{Q_o} \qquad (3.6.1)$$

Q_i is the volume flow rate through the *ith* tube, while Q_o is the overall volume flow rate for all the tubes. A relative flow non-uniformity parameter Φ was introduced to quantify the flow misdistribution.

$$\Phi = \sqrt{\frac{\Sigma_{i=1}^{16}(\beta_i - 1/16)^2}{16}} \cdot \left(\frac{1}{16}\right)^{-1} \cdot 100\% \qquad (3.6.2)$$

The relative flow non-uniformity parameter was similar to the root-mean square or standard deviation, except it was divided by the mean value (1/16).

Due to of the absorber tube wall having a higher temperature than the fluid inside, small corrections are made to the temperature measurements to get the fluid temperatures. The corrections were determined based on the difference between the measured solar collector fluid outlet temperature and the mean of the measured absorber tube wall temperatures as seen below:

$$T_{fluid,i} = T_{wall,i} - \left(\frac{\sum_{i=1}^{16} T_{wall,i} \cdot Q_i}{Q_o} - T_{outlet} \right) \qquad (3.6.3)$$

where $T_{fluid,i}$ is the fluid temperature in *ith* tube (°C); $T_{wall,i}$ is the temperature of the *ith* tube wall (°C); T_{outlet} is the outlet temperature from the collector (°C); Q_i is the volume flow rate through the *ith* tube (l/min); while Q_o is the overall volume flow rate for all the tubes (l/min). The results showed that the buoyancy driving force will decrease the flow
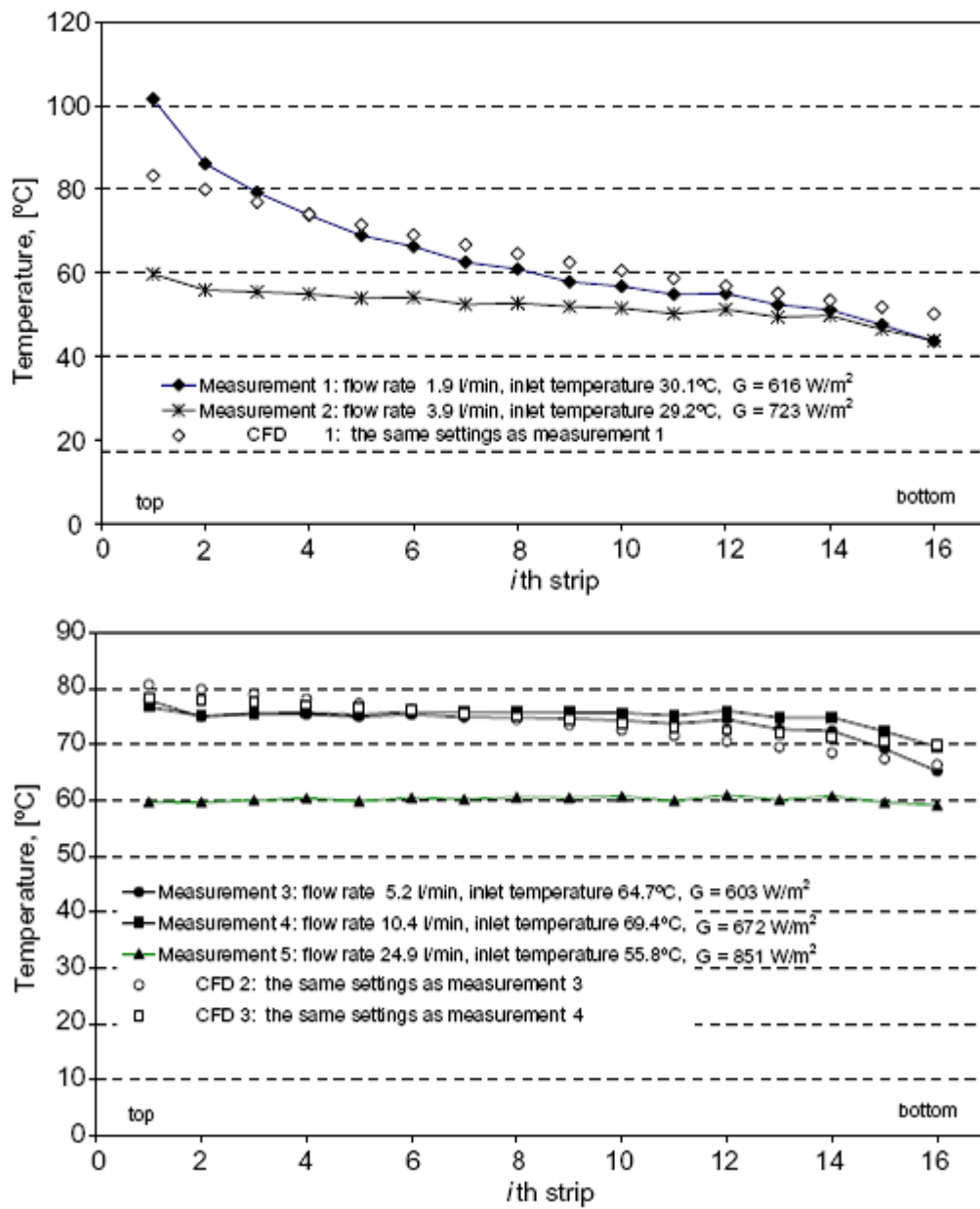
Figure 3.6a Fluid temperature at different flow rates [73].

rate in the upper tubes and increase the flow rate in the bottom tubes. When the inlet flow rate was 2.5 l/min, the collector tilt angle and temperature of inlet flow had a significant influence on the flow and temperature distribution through the absorber tubes.

A similar study described above, was developed using a 3-D mathematical model for solar flat plate collectors based on setting mass and energy balances on finite volumes. The model was validated experimentally with a commercial collector [74]. In Figure 3.6b the absorber temperatures contours are shown with uniform and non-uniform flow ($\Phi = 0.0612$) for a flow rate of 162 kg/h. Φ in this case was given by:

$$\Phi = \sqrt{\frac{\Sigma_{i=1}^{10}(\beta_i - 1/10)^2}{10}} \qquad (3.6.4)$$
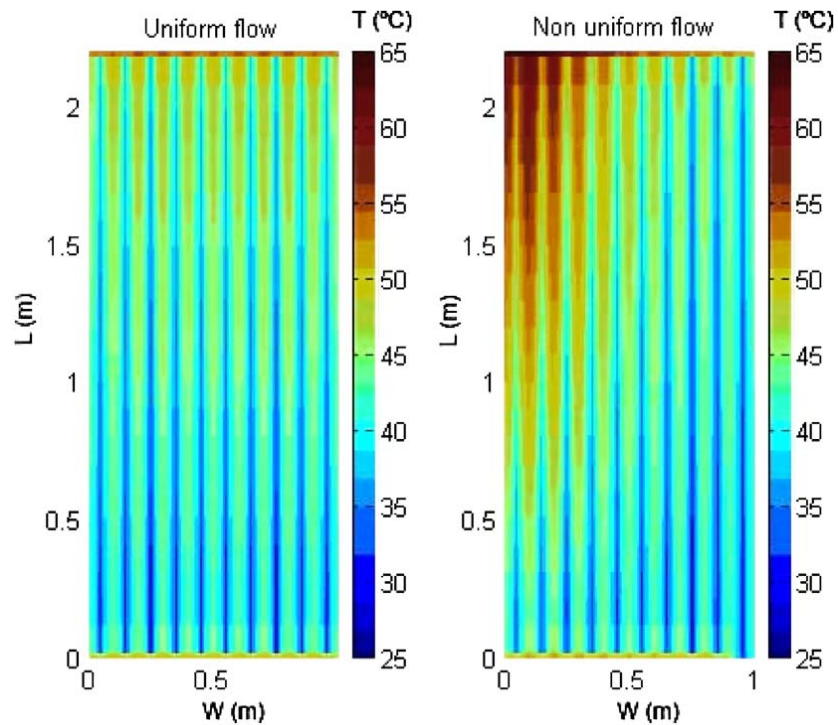
Figure 3.6b Temperature contours for uniform and non-uniform flow [74].

In the case of a uniform flow, the increase of temperature experienced by the fluid in each riser was practically the same in all of them. The outlet temperature difference between risers is less than 0.4 $^{\circ}$C.

Below in Figure 3.6c the fluids temperatures along the risers for the case of Φ = 0.0612 is demonstrated. In this case, the differences between risers are higher than 20 $^{\circ}$C, showing the non uniform flow in each of the pipes.
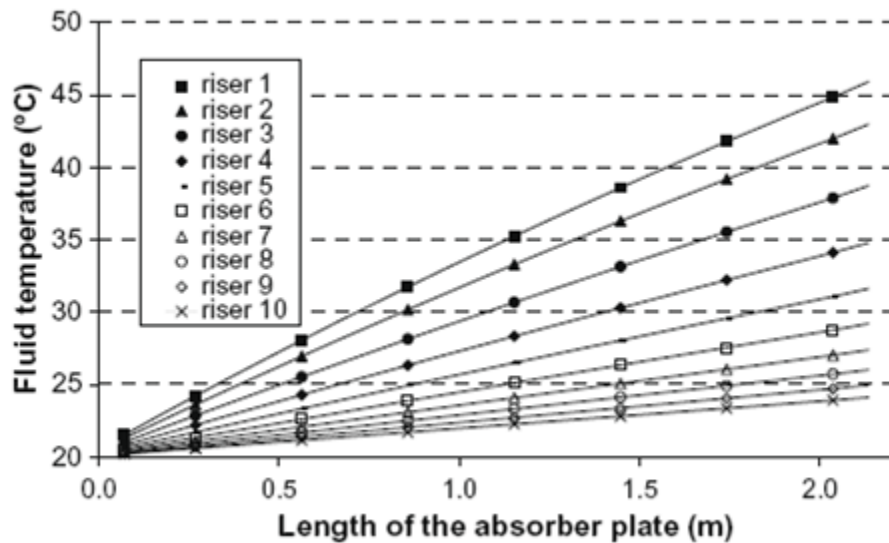
Figure 3.6c Fluid temperature in the tubes [74].

Very close to the walls of the pipe the viscosity of the fluid reduces its velocity and a fairly thin boundary layer is developed in which the fluid is virtually stationary. However, the velocity increases slowly to reach the free-stream velocity not much further away. Outside the boundary layer the fluid behaves as if it had no viscosity. The boundary layer insulates the body and provides a resistance to heat transfer. The thicker

the boundary layer, the higher the conduction length. Hence the higher the resistance to heat transfer, and the lower the heat transfer coefficient [75].

Heat transfer enhancement methods can be classified into two categories: (a) passive methods requiring no direct application of external power or (b) active methods, which require external power [76]. One passive method that is used to enhance heat transfer between the working liquid and the metal part of the collector is the application of a metal porous medium placed in the channels of the heat exchangers [77, 78].

A study that dealt with a Casson (Casson fluid is a shear thinning liquid which is assumed to have an infinite viscosity at zero rates of shear, a yield stress below which no flow occurs and a zero viscosity at an infinite rate of shear) fluid flow in a tube which was filled with a homogeneous porous medium, showed clearly how the flow was affected by the presence of porous medium [79].

Two cases of permeability have been considered, namely (i) permeability has a constant value K_o, and (ii) permeability varies in the radial direction according to:

$$K(r) = K_o \left(\frac{1-r}{r} \right) \qquad (3.6.5)$$

where K_o, is the permeability factor and r the radius. The last case showed that at the centre of the tube the permeability decreases in the radial direction with permeability zero at the solid wall.

Figure 3.6 d (a) and (b) shows the velocity distribution for cases (i) and (ii), respectively, for different values of K_o. In both cases it could be seen that the velocity distribution approached a similar velocity profile as K_o reached to the value 15. For lower values of K_o, the profile is flat and is comparably less flat in case (ii). This was because there was more flow in case (ii) due to variable permeability.
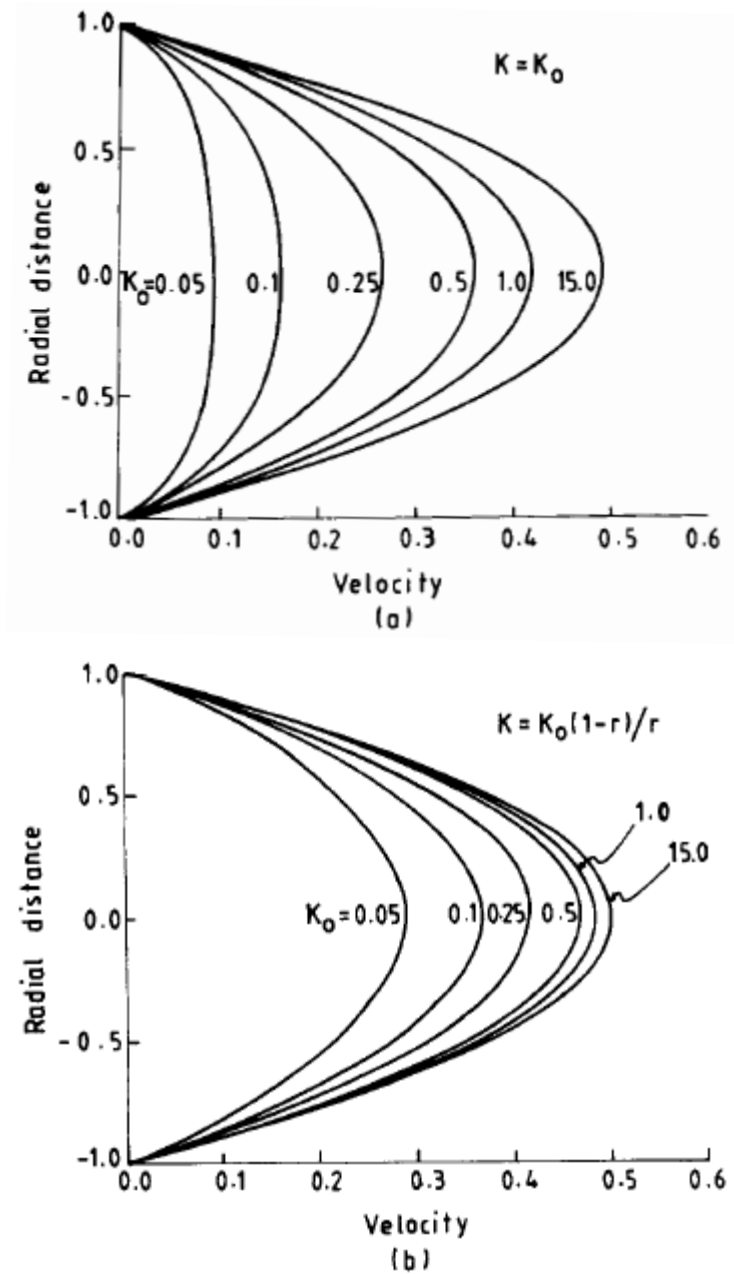
Figure 3.6d Velocity distribution for different values of K_o [79].

Metal foams are a type of porous material (such as copper, aluminium, lead, zinc, cobalt, iron, cadmium) having low density and large surface area which improves energy absorption and heat transfer in thermal applications, such as heat exchangers [80, 81].

Where it is necessary it can be combined with tubes and sheets (metal-foams attached to the solid structure using a co-sintering technique which is a thermal treatment, below the melting temperature of the main constituent material, that transforms a metallic or ceramic powder into a bulk material containing porosity), for flow separation and better heat transfer as seen in Figure 3.6e. Metal foams until recently have been used mainly in the aerospace, ship-building industries. Foam manufacturing costs have been decreasing lately and a range of applications including heat and mass transfer have entered the market. It is known that turbulence and dispersion enhances heat transfer and increases the performance and efficiency of the heat exchanger. Furthermore, flow paths through the foam are interconnected, which makes the flow available in all areas. As such, utilising the metal foam leads to smaller and lighter heat exchangers [82].

Figure 3.6e Metal-foam filled tubes [82].

The pressure drop is a function of permeability (K) of the metal foam which in turn depends on the pore density (ppi) and porosity (ε). Consequently, the pressure drop of single-phase flow through the pipe increases exponentially with pore density (i.e. the decrease of pore size).
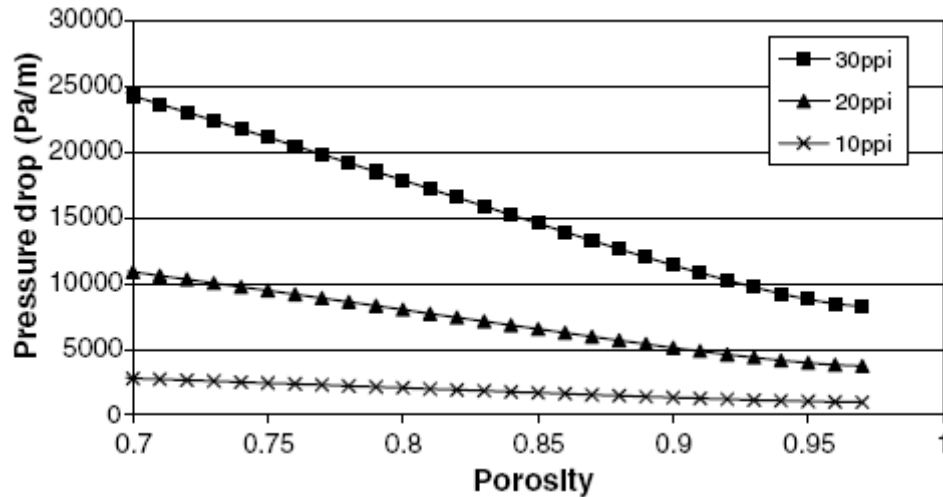
Figure 3.6f Variation of pressure drop with porosity [82].

Figure 3.6f shows the variation of pressure drop with the porosity at selected pore densities. As expected, the pressure drop increased with the decrease of porosity and increased in the pore density.

The presence of metal porous medium, i.e. copper, aluminium, inside a pipe causes a better thermal dispersion and also it increases the interface between the fluid and absorber. The overall thermal conductivity in this case is higher than that of the water. On the other hand, if a pipe is fully filled with a porous medium material, the disadvantage is the increase of the friction factor and significant pressure drop due to the porous material reducing the flow of the working fluid [83].

Another passive method that is extensively used to enhance heat transfer between the working liquid and the metal part of the collector is attained by using pulsating flows. This is because a non-uniform flow results in the disruption of the boundary layers [84].

A number of analytical, experimental investigations and findings have been reported in recent years. Generally pulsating flows consist of a steady flow part and an oscillating part. Oscillation changes the thickness of the thermal boundary layer and hence the thermal resistance, so the rate of heat transfer is altered [85].

Pulsating flows create turbulence which is considered to be an irregular movement of particles of the fluid. This produces eddies in the flow, and it causes boundary layer separation. A number of research studies have been conducted to investigate pulsating flow characteristics [86, 87].

There are several investigations in the literature concerned with the combination of porous medium in a forced convective flow system [88, 89]. However, due to the pressure drop and inertial effects, it is expected that a much higher heat transfer can be achieved by a pulsating flow through a pipe partially filled with a porous medium.

Forced convection in a system in which a fluid porous material occupies only a part of the passage has been the subject of numerous investigations [90]. Analytical solution studies showed an enhanced heat transfer in an annular duct partially filled with a porous medium of high permeability and conductivity.

Forced convection was numerically investigated in a developing region (area well inside the plates where viscous forces have taken place at the flow) of parallel-plate

ducts. A high-thermal conductivity porous substrate was attached to the inner wall of one plate as shown below in Figure 3.6g, in order to enhance the heat transfer characteristics of the flow under consideration [91].

Figure 3.6g presents a two dimensional isothermal parallel-plate channel. A porous insert of prescribed thickness was deposited at the inner wall of the lower plate. A sudden change in the boundary temperature occurred at the channel walls. At the entrance of the duct, the fluid velocity was kept at a value of U_o and the fluid temperature was kept at T_o
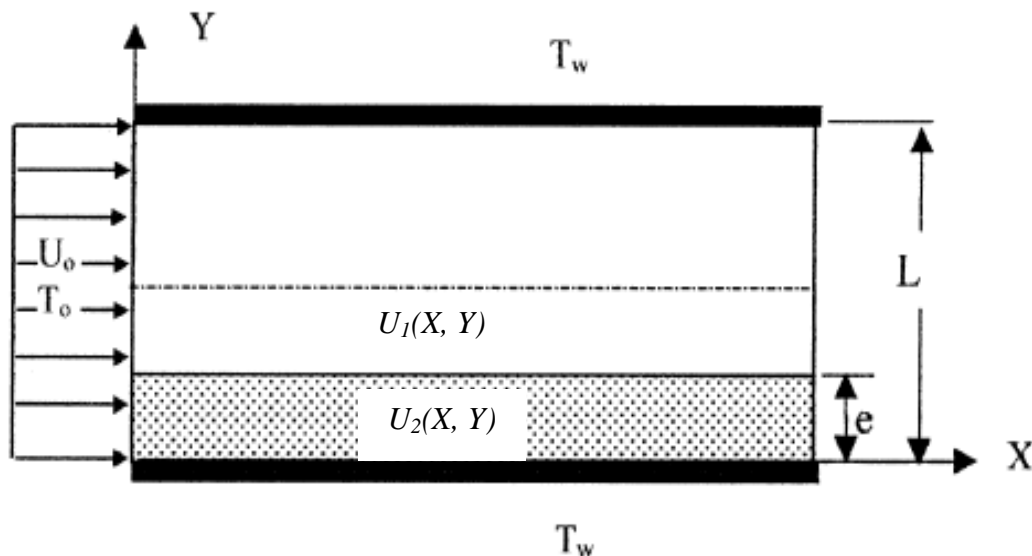
Figure 3.6g Diagram of the case under consideration [91].

It was assumed the porous medium was homogenous (evenly spaced along the length of the pipe) and saturated with fluid, with invariant thermal properties, and chemically stable. The fluid was homogenous, incompressible and in local thermal equilibrium with the solid part.

The effect of the porous substrate thickness on the axial velocity profile is shown in Figure 3.6h. It was clear that increasing porous layer thickness forced more fluid to escape to the clear region. It was also clear that the velocity distribution in the porous substrate was almost a uniform slug pattern except near the boundary at which the flow satisfied the no-slip boundary condition.
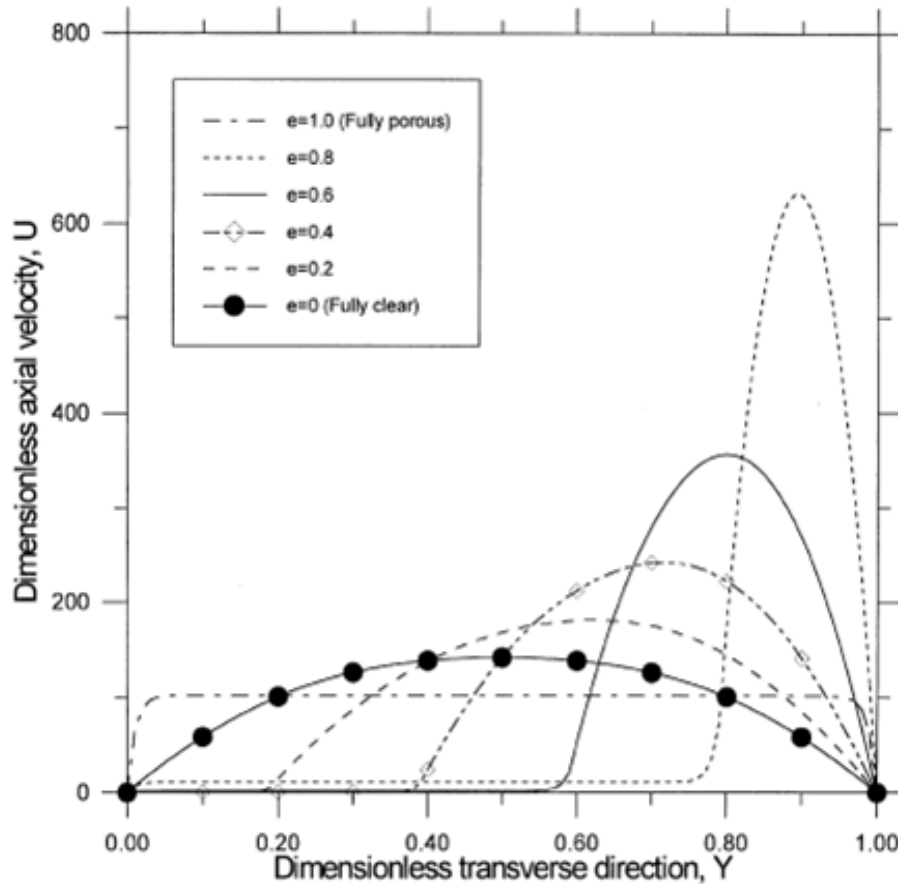
Figure 3.6h Effect of porous substrate thickness on the axial velocity profile [91].

It was concluded that heat transfer could be enhanced using higher thermal conduction ratio, decreasing Darcy number, and increasing the inertial coefficient. Higher thermal conductivity allowed more heat flow to be conducted to the fluid. Small Darcy

numbers or large values of microscopic inertial coefficient reduced the boundary layer thickness.

Generally, forced convection could be significantly enhanced by depositing porous substrate on heated walls, provided that high effective thermal conductivity and dense porous substrate were used.

3.7 Transmittance-Absorbptance Product ($\tau\alpha$)

Part of the radiation passing through the cover system is reflected back to it, while the rest is absorbed by the plate. In turn, the reflected radiation from the plate will be partially reflected at the cover system and returned back to the plate as illustrated in Figure 3.7a.

Incident solar

Cover

$(1-\alpha)\ \tau$

$(1-\alpha)^2 \tau\rho_d$

τ

$(1-\alpha)\ \tau\rho_d$

$(1-\alpha)^2 \tau\rho^2_d$

$\tau\alpha$ $(1-\alpha)\ \tau\alpha\rho_d$ $(1-\alpha)^2\ \tau\alpha\rho^2_d$
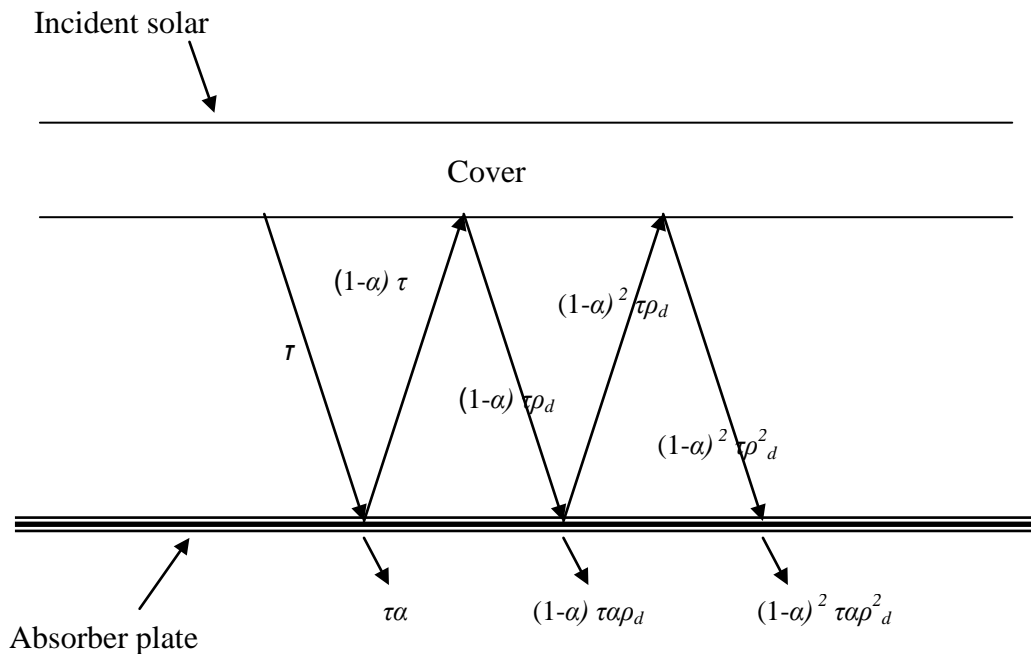
Absorber plate

Figure 3.7a Absorbed solar radiation under a cover system.

In Figure 3.7a, τ is the transmittance of the cover system at the desired angle, α is the angular absorbptance of the absorber plate and ρ_d refers to the reflectance of the cover system for diffuse radiation incident from the bottom side. It is assumed that the reflection from the absorber plate is diffuse and un-polarised.

3.8 Absorption of Solar Radiation

To predict the collector performance requires information of the absorbed solar energy by the collector absorber plate. The solar energy incident on a tilted collector consists of the beam radiation, the diffuse radiation and the ground-reflected radiation. Using the isotropic model [92] the absorbed radiation S on the absorber plate is:

$$S = I_b R_b (\tau\alpha)_b + I_d (\tau\alpha)_d \left(\frac{1+\cos\beta}{2}\right) + (I_b + I_d)(\tau\alpha)_g \rho_g \left(\frac{1+\cos\beta}{2}\right) \quad (3.8.1)$$

The terms $(1 + \cos\beta)/2$ and $(1 - \cos\beta)/2$ are the view factors from the collector to the sky and from the collector to the ground. The subscripts b, d, and g represent beam, diffuse and ground-reflected radiation, respectively.

In equation (3.8.1) I is the intensity of radiation on a horizontal surface, $(\tau\alpha)$ the transmittance absorbptance product that represents the effective absorbptance of the cover-plate system, β the collector slope, ρ_g the diffuse reflectance of ground and R_b the ratio of beam radiation on the tilted surface to that on a horizontal surface.

3.9 Energy Balance Equation of Flat Plate Collectors

The performance of a flat-plate solar collector in steady state can be described by an energy balance that indicates the distribution of incident solar energy into useful energy gain, thermal losses and optical losses. The useful gain from the collector Q_u is defined as the difference between the absorbed solar radiation and the thermal loss or the useful energy output of a collector:

$$Q_u = A_c[S - U_L(T_{pm} - T_a)] \qquad (3.9.1)$$

The first term is the absorbed solar energy and the second term represents the heat loss from the collector. The solar radiation absorbed by a collector per unit area of absorber S can be calculated using the optical properties of covers and a plate.

The thermal energy loss from the collector to the surroundings can be represented as the product of a heat transfer coefficient U_L times the difference between the mean absorber plate temperature T_{pm} and the ambient temperature T_a. A_c is the gross area of the collector (total area occupied by a collector).

The problem with equation 3.9.1 is that the mean absorber plate temperature is difficult to measure because it is a function of the collector design, the incident solar radiation and the conditions of the entering fluid. Therefore there is a need to express the useful energy gain in terms of parameters other than the mean absorber plate temperature. These parameters are well being presented and discussed later.

3.10 Heat Losses of the Collector

The solar energy absorbed by the absorber plate is distributed to useful gain and to thermal losses through the top, bottom and edges. Heat loss from a flat plate solar collector consists of top heat losses through cover systems and back and edge heat losses through back and edge insulation of the collector. Therefore the overall heat loss from the collector can be represented as:

$$Q_{loss} = U_L A_c (T_{pm} - T_a) \quad (3.10.1)$$

The collector overall loss coefficient U_L in the above equation is given by the sum of the top, back and edge losses:

$$U_L = U_t + U_b + U_e \quad (3.10.2)$$

3.11 Top Heat Losses of the Collector

The energy loss through the top is the result of convection and radiation between the parallel plates. The loss per unit area through the top is equal to the heat transfer from the absorber plate to the cover.

$$U_t = [\frac{q_{r,p-s}}{(T_p - T_a)} + \frac{1}{h_{c,p-c} + h_{r,p-c}} + \frac{1}{h_w + h_{r,c-a}}]^{-1} \quad (3.11.1)$$

The term $h_{c,p-c}$ is the convection coefficient between the plate and the cover where $h_{r,p-c}$ is the radiation coefficient from the plate to the cover and $h_{r,c-a}$ is the radiation

coefficient from the cover to the air. The net radiant energy transfer between the collector and the sky is signified by $q_{r,p\text{-}s}$. The term h_w is the wind convection coefficient and represents the convection heat loss from a flat plate collector to outside winds. T_a and T_p are the ambient and plate temperatures respectively. This is illustrated below in Figure 3.11a.
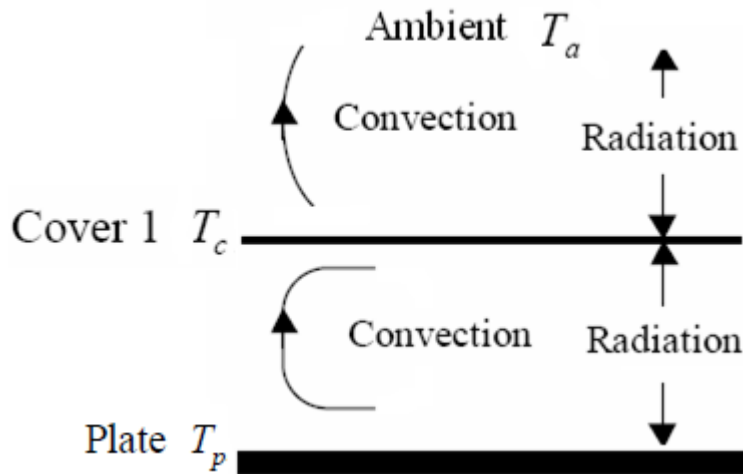
Figure 3.11a Heat transfer mechanisms through a collector with a single cover.

Free convection heat transfer data is correlated in terms of three dimensionless parameters, the Nusselt number Nu, the Rayleigh number Ra, and the Prandtl number Pr for the prediction of the top loss coefficient. The natural convection heat transfer coefficient h is related to three dimensionless parameters.

$$Nu = \frac{hL}{k} \qquad (3.11.2)$$

$$Ra = \frac{g\beta'\Delta T L^3}{v\alpha} \qquad (3.11.3)$$

where k is the thermal conductivity, L is the plate spacing, g the gravitational constant, β' is the volumetric coefficient of expansion of air and ΔT the temperature difference between plates.

$$Pr = \frac{v}{\alpha} \quad (3.11.4)$$

The terms v and α, are the kinematic viscosity and thermal diffusivity, respectively.

In a more recent experimental study [93], it was presented the relationship between the Nusselt number and Rayleigh number for tilt angle β from 0 to 75° as:

$$Nu = 1 + 1.44[1 - \frac{1708[\sin(1.8\beta)]^{1.6}}{Ra\cos\beta}][1 - \frac{1708}{Ra\cos\beta}]^+ + [(\frac{Ra\cos\beta}{5830})^{1/3} - 1] \quad (3.11.5)$$

3.12 Back and Edge Heat Losses of the Collector

The energy loss through the back of the collector is the outcome of the conduction through the back insulation and the convection and radiation heat transfer from the back of the collector to surroundings.

According to Duffie and Beckman the magnitudes of the thermal resistance of convection and radiation heat transfer are much smaller than that of conduction, and

therefore it can be assumed that all the thermal resistance from the back is due to the insulation [56]. The back heat loss, U_b, is then given by:

$$U_b = \frac{k}{L} \qquad (3.12.1)$$

where, k and L are the back insulation thermal conductivity and thickness, respectively.

The estimation of edge losses is complicated for most collectors; however the edge losses are so small that it is not necessary to predict them with great accuracy.

With the assumption of one-dimensional sideways heat flow around the perimeter of the collector, the edge losses based on the collector area A_c can be estimated by:

$$U_e = \frac{(UA)_{edge}}{A_c} \qquad (3.12.2)$$

The energy loss for a flat-plate collector without glazing through the top is given by:

$$Q_t = Q_c + Q_r = h_w A_p (T_{pm} - T_a) + \varepsilon_p \sigma A_p (T_{pm}^4 - T_a^4) \quad (3.12.3)$$

Heat is transferred by wind convection and radiation from the plate to ambient where subscripts c and r correspond to convection and radiation, respectively, h_w is the

wind convection coefficient, T_a the ambient temperature, ε_p the emittance of the absorber plate for infrared radiation and σ the Stefan-Boltzmann constant.
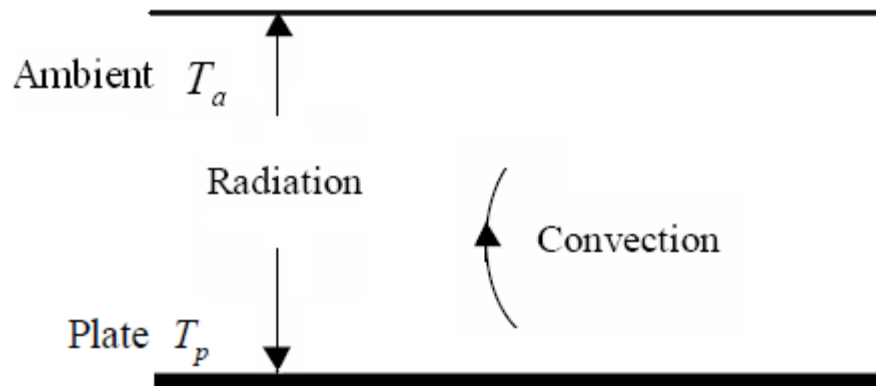
Figure 3.12a Top heat losses from the flat-plate solar collector without glazing.

3.13 Efficiency Factor of the Collector

The collector efficiency factor F' represents the temperature distribution along the absorber plate (fins) between the tubes.

The temperature distribution between two tubes can be derived with the assumption that the temperature gradient in the fin towards the flow direction is negligible. Figure 3.13a illustrates an absorber plate-tube configuration.

The distance between the tubes is W, the tube diameter is D and the inner diameter of the tube is D_i.

The absorber plate thickness is δ and T_b and T_f are the local base temperature and the fluid temperature, respectively.
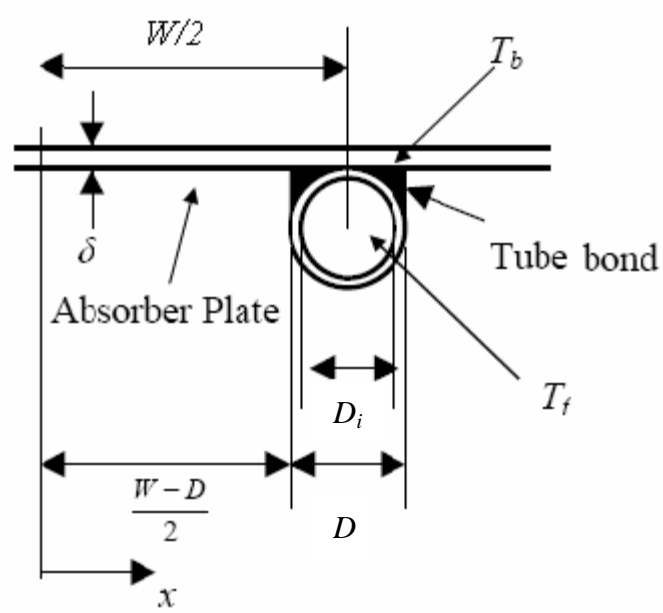
Figure 3.13a Fin and Tube dimensions.
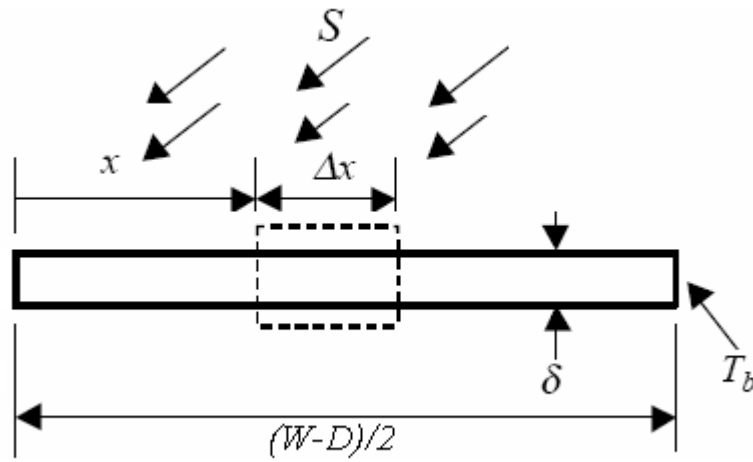
Figure 3.13b Energy balance on fin element.

The fin shown in Figure 3.13b is (*W-D*)/2 long and the temperature of the plate above the

tube is T_b. In Figure 3.13c an elemental region Δx and unit length in the flow direction is

shown.
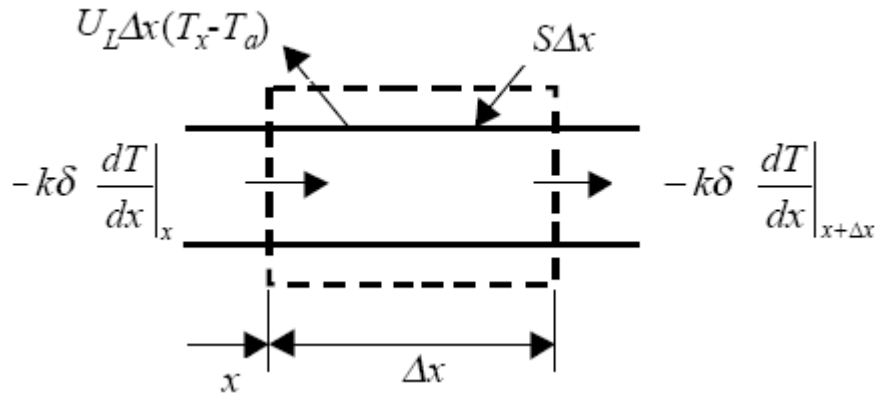
Figure 3.13c Energy balance on fin element.

By applying energy balance the governing equation for the fin can be derived:

$$\frac{d^2T}{dx^2} = \frac{U_L}{k\delta}(T - T_a - \frac{S}{U_L})$$
(3.13.1)

The two boundary conditions are the insulated side and the base temperature T_b.

$$\left.\frac{dT}{dx}\right|_{x=0} = 0 \quad \text{(3.13.1a)} \qquad\qquad \left.T\right|_{x=\frac{W-D}{2}} = T_b \quad \text{(3.13.1b)}$$

The energy conducted to the region of the tube per unit length in the flow direction is given by:

$$q'_{fin} = (W - D)F[S - U_L(T_b - T_a)] \qquad (3.13.2)$$

The function F is the standard fin efficiency for straight fins with rectangular profiles and is given by:

$$F = \frac{\tanh[m(W - D)/2]}{m(W - D)/2} \qquad (3.13.3)$$

where the parameter m is given by:

$$m = \sqrt{\frac{U_L}{k\delta}} \qquad (3.13.4)$$

The useful gain of the collector also includes the energy collected above the tube area which can be calculated by:

$$q'_{tube} = D[S - U_L(T_b - T_a)] \qquad (3.13.5)$$

In addition, the useful gain for the q'_u per unit length in the flow direction for the fin and tube (the sum of q'_{fin} and q'_{tube}) is given by:

$$q'_u = [(W - D)F + D][S - U_L(T_b - T_a)] \qquad (3.13.6)$$

Finally, the useful gain has to be passed to the working fluid, so the thermal resistance to the heat flow from the plate to the fluid results from the plate-tube bond

conductance and the tube-to-fluid convection heat transfer inside of the tubes. The useful gain per unit of length in the flow direction can be expressed as:

$$q'_u = \frac{T_b - T_f}{\dfrac{1}{h_{fi}\pi D_i} + \dfrac{1}{C_b}} \qquad (3.13.7)$$

where, D_i is the inner diameter of a tube, h_{fi} the forced-convection heat transfer coefficient inside of tubes, T_f the local fluid temperature and C_b the bond conductance. By eliminating T_b and by introducing the collector efficiency factor F' the expression for the useful gain is:

$$q'_u = WF'[S - U_L(T_f - T_a)] \qquad (3.13.8)$$

where the collector efficiency F' is given by:

$$F' = \frac{1/U_L}{W[\dfrac{1}{U_L[D + (W-D)]F} + \dfrac{1}{C_b} + \dfrac{1}{\pi D_i h_{fi}}]} \qquad (3.13.9)$$

The temperature of the working fluid is changing with a certain temperature profile. By applying the energy conservation on the system shown in Figure 3.13c and substituting q'_u from equation (3.13.8), then:

$$\frac{\dot{m}C_p dT_f}{dy} - nWF'[S - U_L(T_f - T_a)] = 0 \qquad (3.13.10)$$

where $\dot{m}$ is the total collector flow rate, n the number of tubes and T_f the temperature of fluid at any location y.

By assuming that that F' and U_L are independent of position the fluid temperature at any position y can be calculated from:

$$\frac{T_{fo} - T_a - S/U_L}{T_{fi} - T_a - S/U_L} = \exp(-\frac{U_L nWyF'}{\dot{m}C_p}) \qquad (3.13.11)$$

where nWy is the area of the collector A_c

$$\frac{T_{fo} - T_a - S/U_L}{T_{fi} - T_a - S/U_L} = \exp(-\frac{A_c U_L F'}{\dot{m}C_p}) \qquad (3.13.12)$$

$$T_{fo} = (T_{fi} - T_a - S/U_L)\exp(-\frac{A_c U_L F'}{\dot{m}C_p}) + \left(T_a + \frac{S}{U_L}\right) \qquad (3.13.13)$$
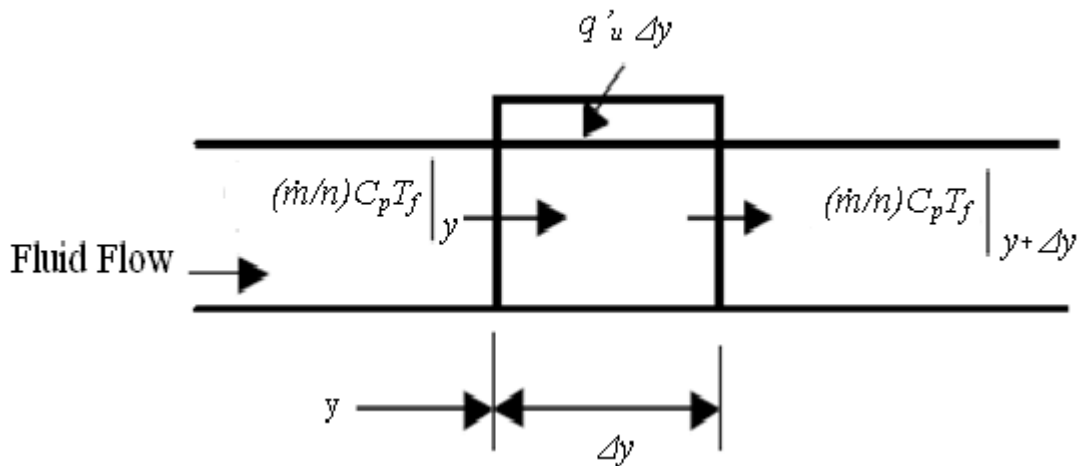
Figure 3.13d Energy balance on fluid element.

3.14 Heat Removal Factor of the Collector

To define a quantity that relates the actual useful energy gain of a collector to the maximum possible useful gain if the whole collector surface were at the fluid inlet temperature requires the introduction of the heat removal factor F_R is introduced which is defined as:

$$F_R = \frac{\dot{m}C_p(T_O - T_i)}{A_c[S - U_L(T_i - T_a)]}$$ (3.14.1)

The term T_o is the output temperature which can be determined using equation (3.13.11) by substituting tube length L for y. Then F_R can be expressed as:

$$F_R = \frac{\dot{m}C_p}{A_c U_L}[1 - \exp(\frac{A_c U_L F'}{\dot{m}C_p})]$$ (3.14.2)

Physically, the collector heat removal factor is equivalent to the effectiveness of a conventional heat exchanger. The collector heat removal factor times this maximum possible useful energy gain is equal to the actual useful energy gain Q_u when F_R and the modified overall heat transfer coefficient are used in equation 3.9.1, the actual useful energy gain Q_u is given by:

$$Q_u = A_C F_R[S - U_L(T_i - T_a)]$$ (3.14.3)

This is a very useful equation and applies to all flat plate collectors. The energy gain is now calculated as a function of the inlet fluid temperature, which is usually known, and not the mean plate temperature T_p.

3.15 Collector Efficiency η

An evaluation of collector performance is the collector efficiency η, which is defined as the ratio of the useful gain over a specified time period to the incident solar energy over the same period.

$$\eta_i = \frac{\int Q_u dt}{A_c \int G_T dt} \qquad \text{(3.15.1)}$$

The factor G_T is the irradiance on tilted plates and its value can be obtained from available charts. By replacing the actual useful gain Q_u, the instantaneous efficiency η_i can be rewritten as:

$$\eta_i = \frac{Q_u}{A_c G_T} = F_R(\tau\alpha) - F_R U_L \frac{(T_i - T_a)}{G_T} \qquad \text{(3.15.2)}$$

The absorbed energy is given by G_T $(\tau\alpha)$, where $(\tau\alpha)$ is the transmittance absorbptance product. The term F_R $(\tau\alpha)$ indicates how energy is absorbed by the collector and $F_R U_L$ indicates how energy is lost by the collector.

Another important aspect of collector testing is the determination of the effects of the angle of incidence of the radiation. To express the effects of the angle of incidence of the radiation on the thermal performance of the flat-plate solar collector, an incidence angle modifier $K_{\tau\alpha}$ is introduced.

A general expression for flat plate collectors has been recommended [94] for angular dependence of $K_{\tau\alpha}$:

$$K_{\tau\alpha} = 1 + b_0 \left(\frac{1}{\cos \vartheta} - 1 \right)$$ (3.15.3)

where ϑ is the angle of incidence of beam radiation and b_0 is a constant called the incident angle modifier coefficient, and is generally a negative number.

To guarantee that the collector can withstand high thermal loads, the highest temperature in the collector should be less than the melting point of the parts that is assembled from. Stagnation temperatures are the highest temperatures of the covers and absorber plate that can be obtained from the collector. They take place when the collector is not working, i.e. when the working fluid does not circulate. In this case, the useful gain from the collector is zero.

3.16 Formulation of the aim for this research study and Conclusions

The aim of this research study was to propose a novel design of a simple flat-plate unglazed collector without changing its original shape. This improved collector would be tested against an identical conventional collector in order to have a direct comparison at the same time. That way if results were improved then the same idea could be applied to any other system in the market since their geometry would not be changed.

This system could then be used in Mediterranean countries to provide dwelling with hot water. Due to relatively hot climate in the above region a large amount of solar water collectors are unglazed and use an "antifreeze" type solution or even water as a heat carrier. Further, the solar water heating devices are very often passive systems i.e. their operation is based on the flow of the heat carrier due to free convection.

The passive system built around a simple, low cost unglazed solar collector with a mesh made of a high conductivity metallic material (aluminium) and placed on the internal surface of the collector pipes for intensification of heat transfer will be studied in the framework of this research investigation. Such a technical solution could allow manufacturers to maintain the low cost of the production of solar collectors for application in the Southern Europe. However it is anticipated that expected intensification of the heat transfer in the collector noticeably would improve its performance.

Parameters described in this chapter, like the heat transfer coefficient, the Nusselt Number and other mathematical relations that can predict the performance of a collector, are important factors that this project can be based upon. From the work previous conducted by other researchers, and understanding the theory of thermodynamics and heat transfer techniques, the project work will be directly compared to those in order to verify the findings and ascertain its validity.

CHAPTER 4

CFD Background

Prior to building a test rig with a new solar water collector with improved performance it was necessary to obtain theoretical confirmation that using a metallic mesh insertion in the pipes of solar collectors would provide a positive effect on their performance. Such a preliminary investigation could be carried out by employing numerical investigations particularly based on CFD techniques. It was decided to investigate the effect of placing a metallic insertion inside a pipe, since collectors are formed by individual pipes. Hence the flow and heat transfer in this simplified scheme of a passive system was going to be investigated and then coupled to the experimental collector over the pipe length used in the CFD design.

4.1 Computational Fluid Dynamics (CFD)

Applied numerical analysis includes the solution of linear algebraic equations, ordinary and partial differential equations. Modelling of physical processes consist of the fluid flow, heat and mass transfer. The use of general-purpose computer codes comprises commercial computational fluid dynamics software.

Computational fluid dynamics (CFD) is concerned with the efficient numerical solution of the partial differential equations that describe fluid dynamics.

CFD techniques are used in many areas of engineering where fluid behaviour is the main element. Numerical analysis applied to fluid flow and heat transfer problems.

All CFD codes contain three main elements:

(1) A pre-processor which is used to input the problem geometry, generate the grid and define the flow parameters and the boundary conditions to the code.

(2) A flow solver which is used to solve the governing equations of the flow subject to the conditions provided. There are four different methods used as a flow solver: (i) finite difference method, (ii) finite element method, (iii) finite volume method, and (iv) the spectral method.

(3) A post-processor which is used to display the data and show the results in graphical and easy to read format.

4.2 Examples of Computational Fluid Dynamics applications

With the use of numerical models that can predict the physical performance of a design project, it is possible to find, optimised solutions without creating a large and expensive series of models.

The design of thermal equipment must focus on a combination of numerical and experimental techniques. A model for virtual prototyping of thermal equipment must be detailed enough in order to consider all the main physical phenomena that are taking place as well as giving results in a reasonable computational time [95].

Consequently, a compromise needs to be made between detailed simulations of CFDs models and a fast resolution. Both computers and computational algorithms

have been improved vastly in the last few years and therefore it is now feasible to analyse more complex geometries and designs within a reasonable computational time.

Numerous investigations in to solar thermosiphon systems have been conducted, but they are limited to a small range of heat exchanger configurations, flow visualisation and heat transfer. CFD models are even fewer in the case of flat-plate solar water collectors. In the 80's there was a boost in progress as a result of the increase of computing power. Initially, only low Rayleigh numbers and small aspect ratios were investigated.

More complicated studies, involving higher Ra numbers and aspect ratios, were investigated as more robust computing machines were developed. Later, the knowledge of flows was extended further by the numerical investigation of three-dimensional (3D) aspects.

The majority of the initial investigations were based on a model developed by Duffie and Beckman for flat plate solar collectors and this has been frequently used for design, calculations and the prediction of various systems. In this model the heat transfer is assumed to be one-dimensional from the thermal fluid to the ambient and the temperatures at the absorber plate and covers calculated at steady state conditions.

Tests on solar collectors under varying conditions over time have been presented using relations that give the characteristics of the collector by a Fourier transform of differential equations [96, 97].

Attempts had been made to develop models to describe the physical and geometrical complexity of the system more accurately. The models were fitted to a set

of measured data and the resulting collector parameters were compared. The total daily energy yield predicted by the models for a number of days of different weather conditions was calculated using a reference collector parameter set [98].

These models though are still limited to specific geometries and materials, and their wide-ranging to portray other trends such as phase change and radiative heat transfer is quite complicated. These models are currently being used by common simulation software packages such as TRNSYS and T-Sol 2.0.

Recently a one-dimensional transient numerical model for flat plate solar thermal devices was developed. This permitted the analysis of different configurations and components, such as multiple-glazing, transparent insulation, air-gaps, surface coatings, opaque insulation and energy accumulation in water or PCM internal stores. In order to obtain information of practical interest, the solar thermal devices were modelled following virtual testing procedures in accordance with the experimental test methods described by European and International standards [95].

Other theoretical investigations focused on vertical mantle tanks for solar domestic hot water systems. Differently designed mantle tanks have been evaluated using a transient three-dimensional CFD-model (CFX 4.1) [99, 100]. The results from the CFD-calculations were used to illustrate the thermal behaviour and the fluid dynamics in the mantle and in the inner tank. [101].

A three-dimensional numerical model was developed using the CFD numerical package FLUENT. An approximately half-scale experimental model was used to evaluate the flow patterns in the annular passageways and the heat transfer into the inner tank of a solar water system. Flow visualization was used to investigate

the flow structure. [102]. The numerical analysis indicated that although this heat exchanger configuration had good overall heat transfer, it did not provide an effective connection between the collector and the tank due to the failure to generate stratification in the tank.

The majority of the heat transfer occurred at the bottom section of the tank, rather than near the level between the inlet fluid temperature and the fluid inside the tank as shown by the shaded areas in Figure 4.2a. The poor distribution of heat input was due partially to the location of the inlet port near the bottom of the annular heat exchanger space. If the inlet port was displaced from the end of the annular space, shear induced recirculation flow regions would develop and it would degrade the stratification in the inner tank
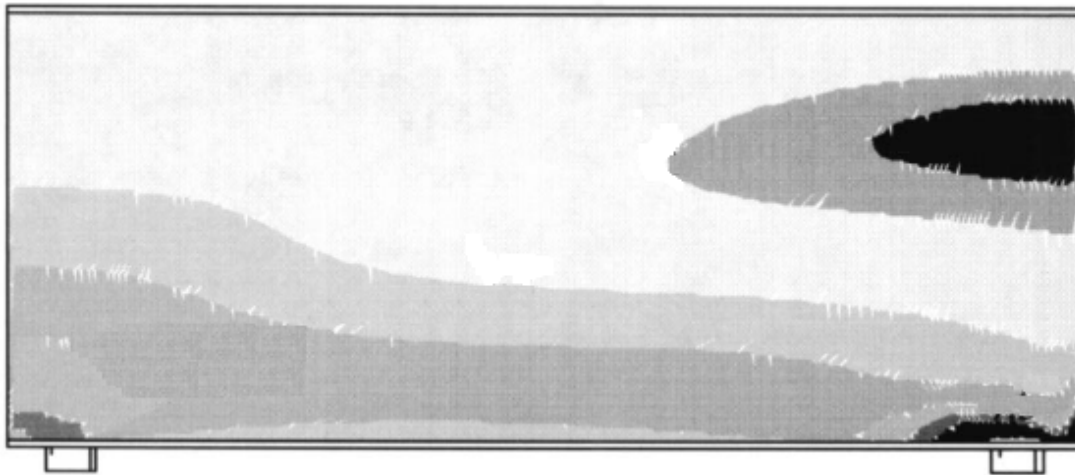
Figure 4.2a Temperature contours into the inner water tank.

A first approach to numerically examine Integrated Collector Systems was conducted by using a two and three-dimensional CFD model utilising the CFD-code FLUENT, neglecting the heat exchanger presence. The flow field inside the storage was examined using various turbulence models [103].

Two 3D numerical models were developed using the CFD package FLUENT 6.1. The first model was developed neglecting the heat exchanger. The presence of the heat exchanger was taken into account in the second model. The first model was solved for steady state and transient conditions. The computational grid consisted of about 91,922 cells.

The second model was solved always transiently, taking into account gravity forces. The grid used for the second model, with the attached heat exchanger. It consisted of about 157,000 cells. Both designs are illustrated in Figure 4.2b.

Transient solutions were taken, for service water flow rate 300 l/h, initial storage water temperature 60 $^{\circ}$C and inlet service water temperature 20 $^{\circ}$C.
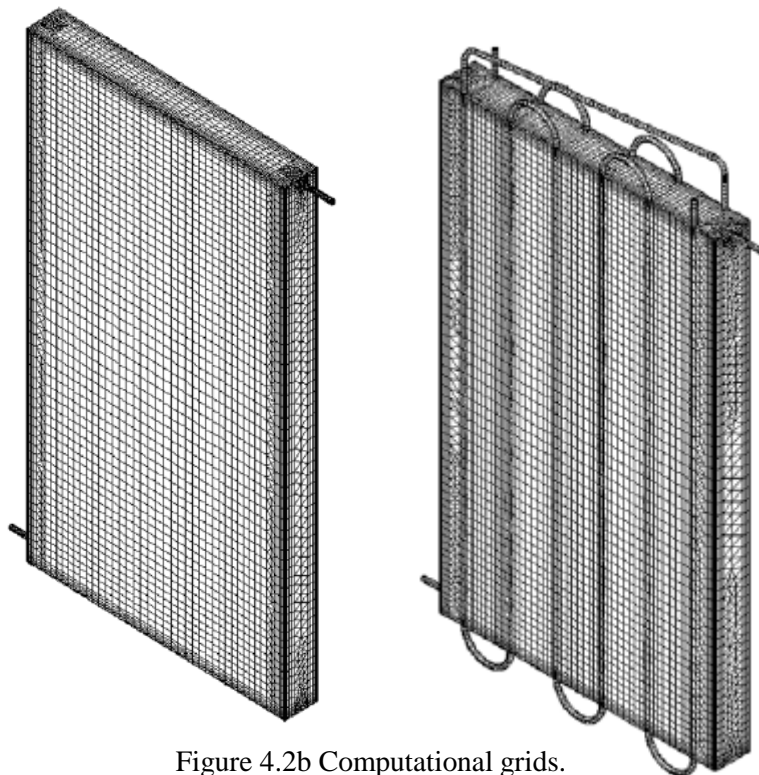
Figure 4.2b Computational grids.

All turbulence models (solution options depending on the type of flow laminar or turbulent) available in FLUENT were tested (variations of k–ε and k–ω, Reynolds stress model and Spallart–Almaras model), for steady state conditions, and the standard k–ω was proven as the most appropriate.

Studies of cavities has been broadened by variations that include different geometries, such as the effect of curved walls, addition of partitions and changes in the boundary conditions, such as spatially varying temperatures [104].

A comprehensive detailed study of the 2D CFD analysis compared with the results of experimental testing showed that the flow rising along the hot wall joins the flow descending down the cold wall and vice versa to make a complete loop along the walls. [105].

The mesh size is critical for CFD analysis, especially when dealing with natural convection [106]. This investigation found that the calculated convective heat transfer depends on the size of the grids by analyzing laminar flows of forced and natural convection over a flat plate. A finer grid distribution in CFD does not always lead to a more accurate solution when the constant viscosity turbulence model is used or when the first grid is in the sub-layer boundary with the other zero-equation turbulence models. Based on the theoretical analysis and numerical experimentation, the study suggested a universal first grid size of 0.005 m for natural convection air/flows and 0.1m for forced convection air flows.

Authors have analysed the laminar natural convection heat transfer inside a differentially heated shallow cavity with different Prandtl numbers [107]. Two-dimensional convective flows in shallow cavities with conducting horizontal

boundaries and driven by differential heating of the two vertical end walls, were studied numerically over a range of Rayleigh numbers and Prandtl numbers. As the Rayleigh number increased, nonlinearity first affected the flow structure in the turning regions near the ends of the cavity. This type of problems has been investigated by a combined computational and analytical approach. Numerical results confirmed predictions of low Prandtl number convection and at higher Prandtl numbers the nonlinear development of the flow with increasing Rayleigh number. The results also confirmed the development of thin boundary-layer structures near the walls of the cavity. In addition, the results for the Nusselt number determined the influence of convection in the end-zones on the lateral heat transfer across the cavity for a range of values of the Rayleigh number R.

A numerical study has been conducted, to examine the free convection inside an enclosure bounded by two isothermal wavy walls and two adiabatic straight walls. It was observed that the aspect ratio is the most important parameter affecting the heat and fluid flow and that higher heat transfer rate is obtained at lower aspect ratio for a certain value of Grashof number [108].

In natural convection heat transfer in porous enclosures, with global rising heat flux boundary conditions for different wave numbers and thermal stratification levels, it was indicated that local Nusselt numbers are very sensitive to thermal stratification [109].

The effect of stationary surface waves on the free convection induced by a horizontal uniformly heated surface in a porous medium has been investigated. Extensive computations presented for a wide range of wave amplitudes and phases, and some global heat transfer rates were given.

For all amplitudes and phases a thin near-wall boundary layer developed within the basic boundary layer as the distance downstream increased; an asymptotic analysis was given, which determines the structure of this layer [110].

An inclined, partially open, enclosure was investigated and it was demonstrated that the inclination angle inclination angle (ranged from 20° to 60°) affected the natural convection heat transfer. Two collectors were compared; one that had a wavy absorber and a second that had a flat absorber. The solution was performed assuming the isothermal boundary conditions of absorbers and covers of collectors [111]. Commercial software was used to simulate the laminar flow and thermal field. Natural convection heat transfer and fluid flow was strongly affected by the shape and inclination angle of the collector. This can be seen in Figure 4.2c.

Figure 4.2c Temperature contours in the examined collectors.

It was clear that both flow and temperature differences were affected by the geometry of the enclosure. Multiple cells were formed in the wavy enclosure. While main cells were obtained in the middle of the enclosure (darker shades), the small second cells were formed in the cavity part of wavy wall (darker shades). Meanwhile, other small cells were seen on the top of the wavy wall. In the case of the flat collector, there are two cells (darker shades) near the end walls. A long cell is formed at the middle of enclosure. In the cases examined, more heat transfer was obtained in the wavy collector than for the flat collector.

4.3 Governing equations of flow and heat transfer in passive solar collectors

For the finite-volume approach the integral form of the governing equations of heat and mass transfer processes are applied to the control volume of the cells, which make up the discretisational (computational) model of a continuous physical domain of the specific physical system under investigations. Normally the value at the centre of a cell is stored and the values at the faces are interpolated to give the values across the boundaries. It is also possible to obtain similar equations for the conservation of momentum and energy for each cell. From these equations it is then possible to create a set of simultaneous equations where either the value in the cell is equal to a boundary condition and/or a combination of the properties according to the discrete equations. Eventually, there would be a number of simultaneous equations equal to the number of independent discrete variables. These can be represented as a large matrix of algebraic equations which the computer then solves.

4.3.1 Laminar Flow Modelling

A CFD software package has to produce a prediction of fluid flow in a given situation with certain boundary conditions. To do this, the CFD software solves numerically the equations that govern the flow of fluids. These equations can be derived from the mass and momentum conservations principle.

Figure 4.3a shows a rectangular, two-dimensional patch of fluid ABCD, together with an assumed velocity distribution in terms of the velocity components u and v in the x- and y-directions respectively. Figure 4.3b shows a horizontal force acting on the fluid patch which caused by a normal stress, σ, and a shear stress, τ.

(a) Geometry and Velocities   (b) Forces in x- direction
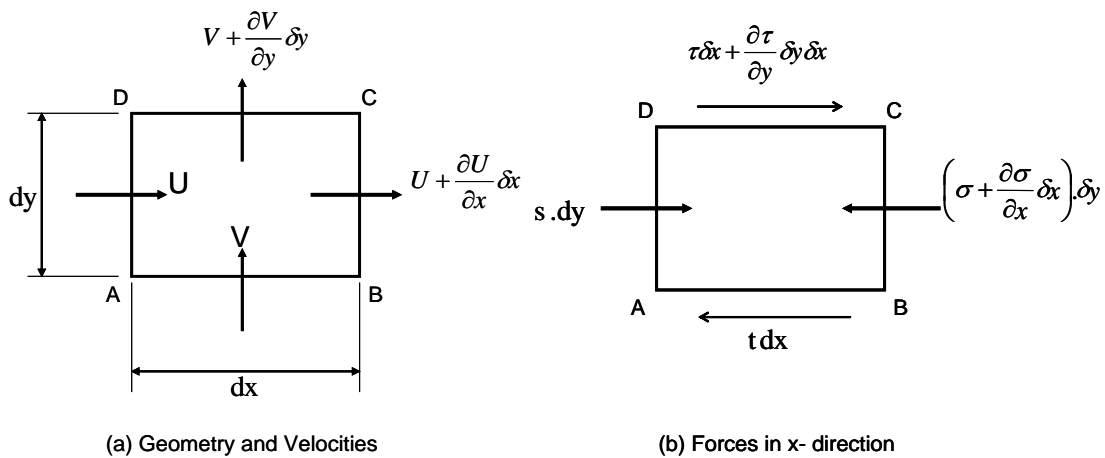
Figure 4.3a, b Flow in the control volume.

Mass continuity equation for the above case can be written as:

$$\frac{\partial u}{\partial x} + \frac{\partial v}{\partial y} = 0 \; ; \qquad\qquad (4.3.1)$$

Momentum equations (or Navier-Stokes equations) are as follows:

in the *x*-direction,

$$\rho \frac{\partial u}{\partial t} + \rho u \frac{\partial u}{\partial x} + \rho v \frac{\partial u}{\partial y} = -\frac{\partial p}{\partial x} + \frac{\partial}{\partial x}\left(\mu \frac{\partial u}{\partial x}\right) + \frac{\partial}{\partial y}\left(\mu \frac{\partial u}{\partial y}\right) + \rho g_x ; \qquad (4.3.2)$$

In the *y*-direction,

$$\rho \frac{\partial v}{\partial t} + \rho u \frac{\partial v}{\partial x} + \rho v \frac{\partial v}{\partial y} = -\frac{\partial p}{\partial x} + \frac{\partial}{\partial x}\left(\mu \frac{\partial v}{\partial x}\right) + \frac{\partial}{\partial y}\left(\mu \frac{\partial v}{\partial y}\right) + \rho g_y ; \qquad (4.3.3)$$

The pressure-based solver solves the flow problem in the coupled approach which obtains a robust and efficient single phase implementation for steady-state flows, with superior performance compared.

The coupled algorithm solves the momentum and pressure-based continuity equations together. The full implicit coupling is achieved through an implicit discretisation of pressure gradient terms in the momentum equations and an implicit discretisation of the face mass flux.

In the momentum equations, the pressure gradient for component *x* is of the form:

$$\sum_f p_f A_x = -\sum_j a^{u_x P} p_j \qquad (4.3.4)$$

where p_f and p_j is the pressure applied on a specified face f and j respectively, u_x is the *x* component of the flow velocity, $a^{u_x P}$ is the coefficient derived from the coefficients of the pressure interpolation.

Currently, very powerful and accurate CFD software packages are available to carry out numerical analysis of heat and mass transfer processes which take place in the wide range of engineering equipment. One of such leading CFD commercial

software is FLUENT based on the finite-volume numerical approach. This software was used in this study as an investigation tool.

4.3.2 Conclusions

After reviewing the limited CFD work conducted by other researches on heat transfer and on solar collectors, it was concluded that using a CFD package to design, analyse and predict the performance of a collector system it is dependable.

It was decided, after preliminary tests on CFD designs (using the FLUENT package mentioned above), to proceed this project with a simplified design mainly because the computing time needed to be kept to minimum since full scale designs would take very long to converge to a solution. Therefore an analysis would take place on a single tube and examine weather the heat transfer is increased, as it will be discussed on Chapter 5.

CHAPTER 5

CFD investigations of the effect of placing a metallic mesh in the channels of a passive solar collector model

CFD investigations of the effect of placing a metallic mesh inside the channel of the simplified passive solar collector scheme was carried out in this chapter employing CFD commercial software FLUENT which uses control volume numerical technique for solving the governing equations of flow and heat transfer. Numerical results obtained demonstrated that such a design would improve the heat transfer from the walls of channels to the liquid and therefore would result in the hot water production capacity of the solar collector.

5.1 Development of the Geometry of the simplified solar collector for CFD simulations

CFD modelling of a simplified solar collector was to be investigated by placing a metallic mesh inside the pipe of a simplified design of a passive system (free convection) which represented a segment of the solar collector operating in similar

conditions. Figure 5.1a illustrates the design used in CFD numerical investigations.

Figure 5.1a Designed geometry.

The model consisted of two vertical sections made of cylindrical pipes connected at both the top and bottom parts with adiabatic curved pipes to form the enclosed loop. The pipes on the left and right were used for heating and cooling the fluid, respectively. The model geometry is 350 mm high and the external diameter of

the pipes and the thickness of pipe walls are 10 and 1 mm, respectively. Two cases were investigated, namely without and with metallic mesh being placed inside the heating pipe. A sample of the mesh used in the experimental investigations is shown in Figure 5.1b.
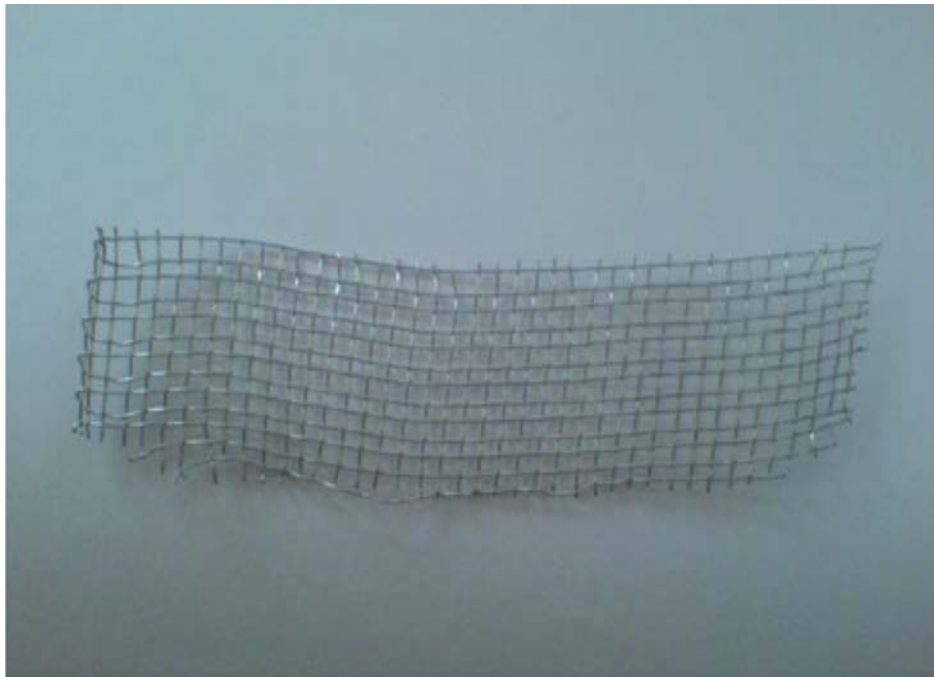
Figure 5.1b Aluminium mesh.

The full geometry and computational mesh for CFD simulations were created in the Gambit software, which is used as a pre-processor for the CFD solver and post-processor, namely FLUENT.

Figure 5.1c demonstrates the process of the creation of the simplified geometry of the metallic mesh for computational purposes. The geometry was a combination of circularly arranged rectangular bars rings and strips of the same shape. The rectangular shape has 1 mm × 1mm dimensions.

Figure 5.1d presents the complete geometry of the mesh in which there is 1.5 mm spacing between the circular bars and 2 mm spacing between rectangular strips and the above physical dimensions used to closely reflect the real geometry of the metallic mesh shown in Figure 5.1b.
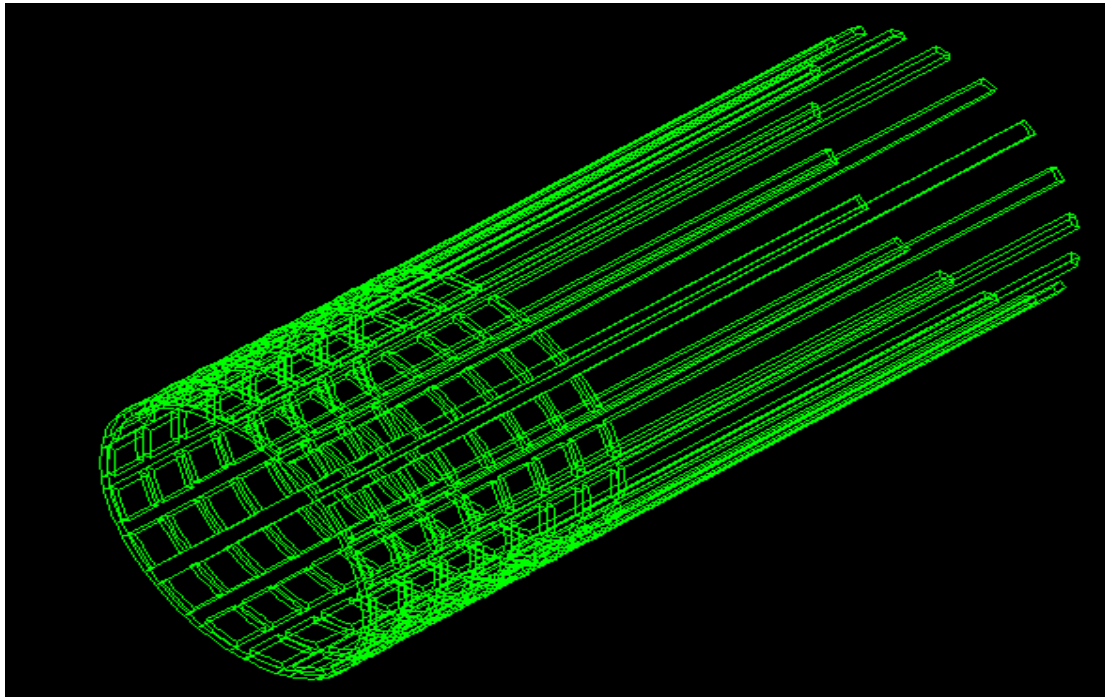
Figure 5.1c Procedure for creation of the geometry of the metallic mesh.
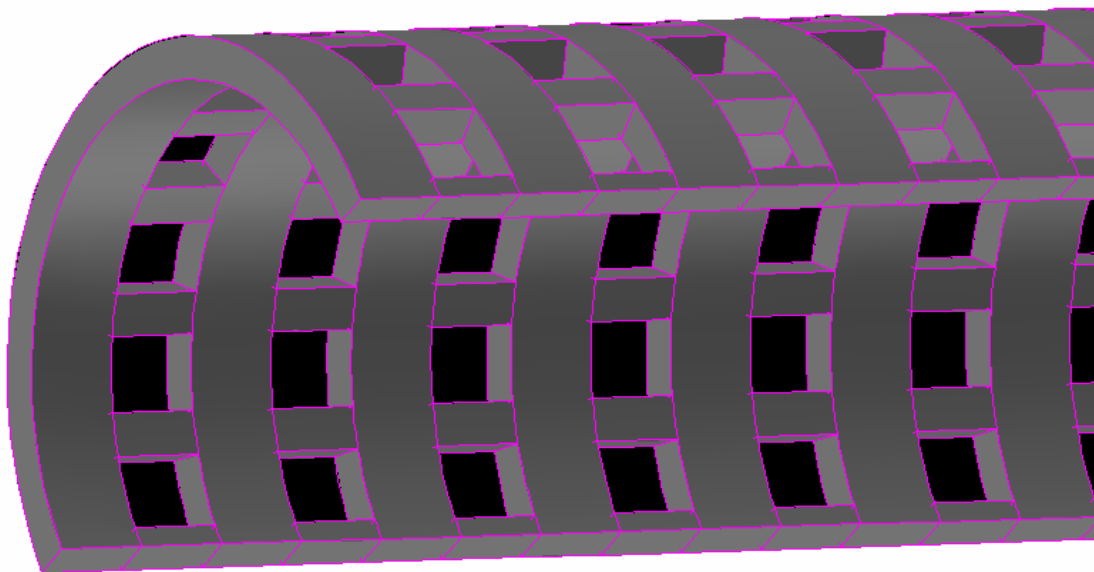
Figure 5.1d The created 3D geometry of the metallic mesh.

To describe the geometry of vertical and connection pipes, smooth cylinders of the relevant shape were used and Figure 5.1e and 5.1f demonstrate a section of one of the vertical pipes and the joint between the vertical and the connecting pipe, respectively. The top and bottom connecting pipes were created using a half of torroidal shape.
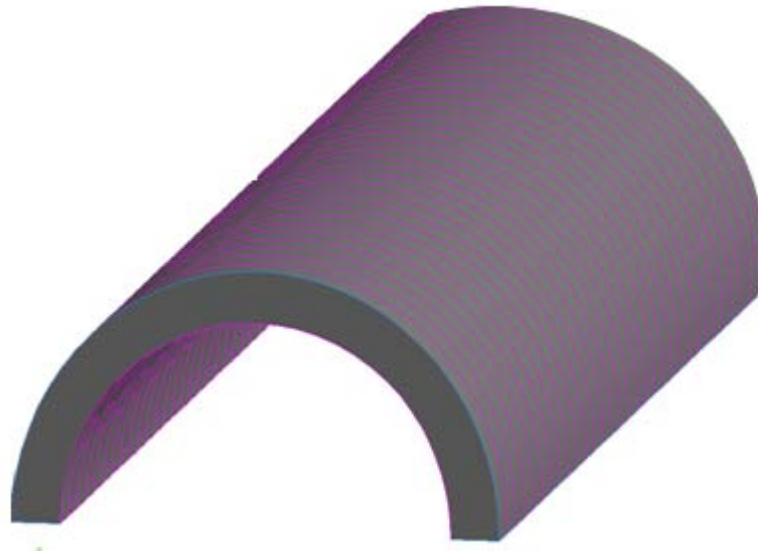
Figure 5.1e 3D geometry of vertical pipes.
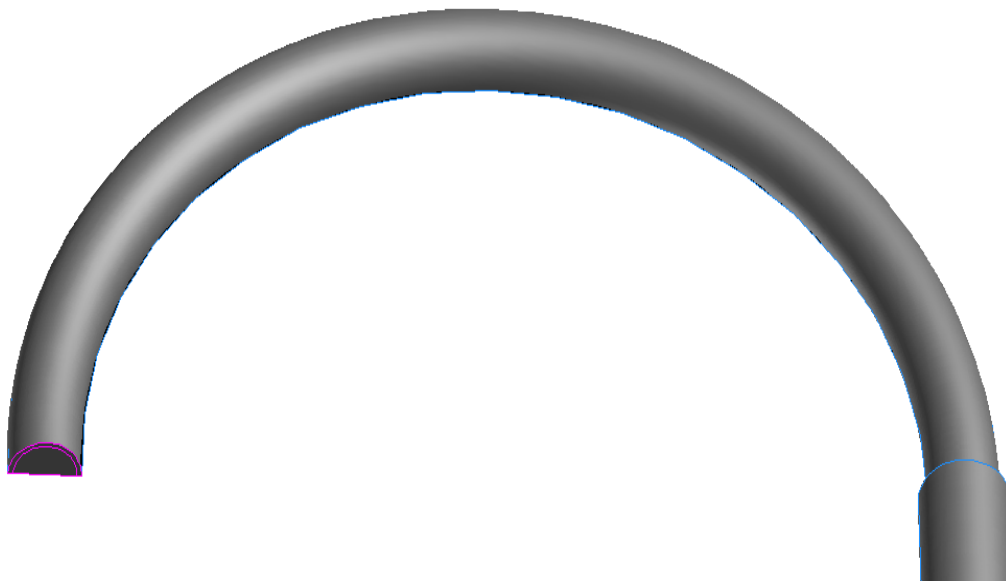
Figure 5.1f 3D geometry of the connecting pipes.

Finally, Figure 5.1g shows the geometry of the heating vertical pipe with the metallic mesh placed inside.
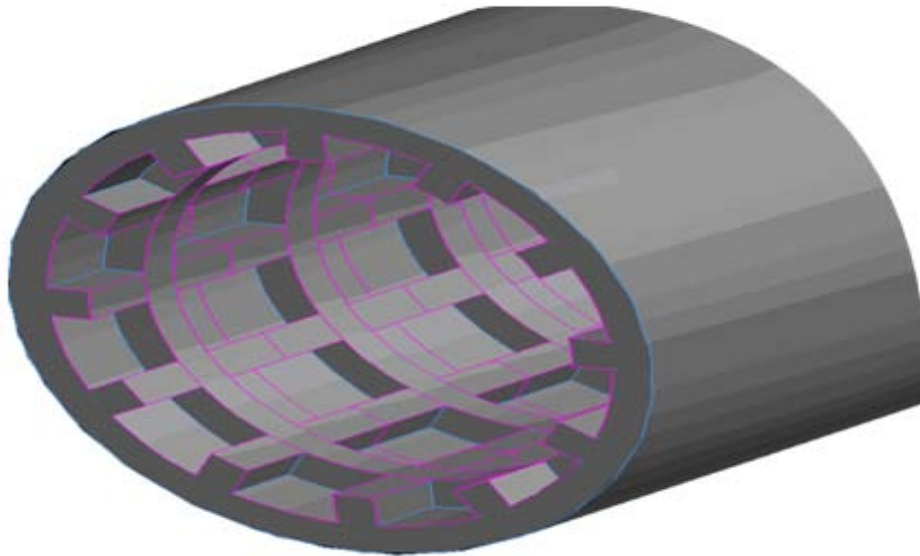
Figure 5.1g The full 3D geometry of the heating pipe.

A time consuming process while designing the proposed geometry was the creation and later meshing of the volume of water within the netted pipe. The difficulty occurred because of the complex shape of this particular volume of water. This was due to the large number of rectangles created at the internal surface of the pipe because of the presence of the net. That shape was then projected at the volume water. The computer package had difficulties in dealing with this profile, and therefore it was necessary to split the volume water into 35 smaller volumes before meshing took place.

In order to split the volume water from the whole netted pipe, a second cylinder was designed and used as a dicer. Using this technique, the volume water was split into two new different geometries that remained connected as there was a

common interface between them. This was made in order to ease the process of selecting and the meshing of the whole volume later on.

Figure 5.1h shows the half of the cross section of the water in one of the planes which is perpendicular to the axis of the heating pipe. Figure 5.1i illustrates details of the water domain in this pipe.
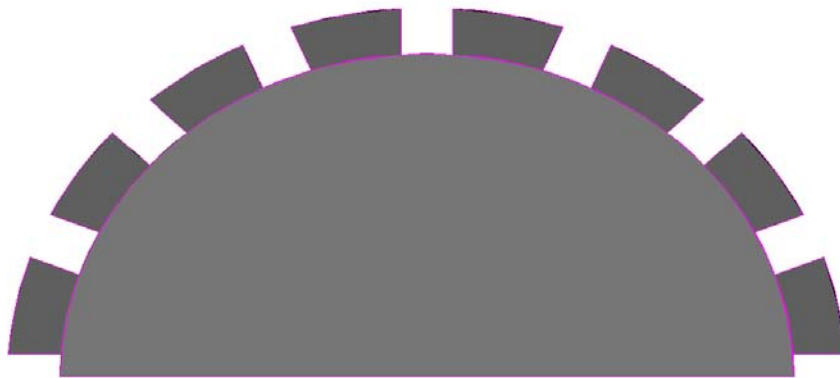
Figure 5.1h 3D geometry of the half of the cross section of the water.
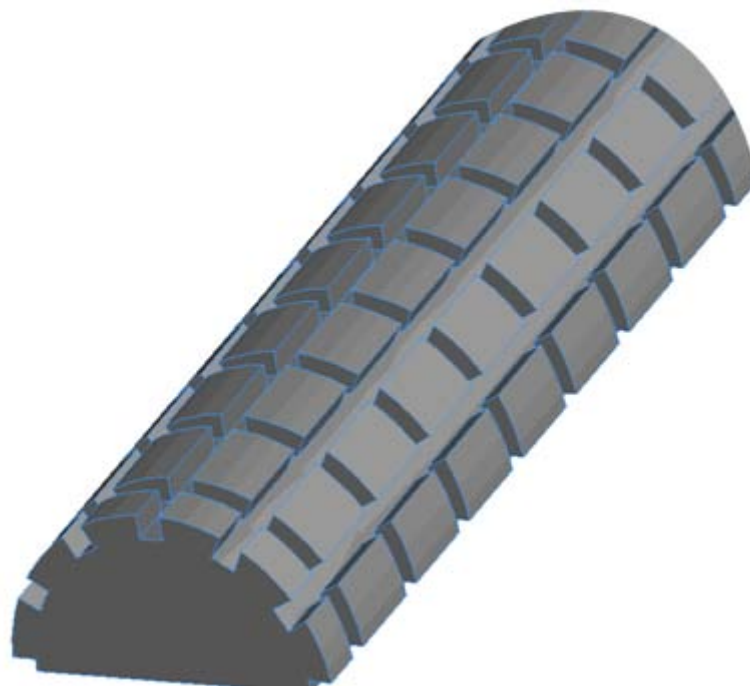
Figure 5.1i 3D geometry of the water domain in the heating pipe.

5.2 Computational mesh of the simplified solar collector for CFD simulations

Creation of an accurate computational mesh for the domain under investigation was of paramount importance in CFD simulations. The shape of control volumes should satisfy certain geometry requirements in order to eliminate irregularities in computational results.

The accuracy of numerical results in CFD modelling was mesh dependant: the finer mesh generally provides better results at the increased computational time. Therefore the size of the mesh in the domain should be gradually increased to such level that the further raise in the number of control volumes does not result in considerable changes in theoretical results produced.

Further using a regular computational mesh made of hexahedral control volumes also allows improving the accuracy of results and reducing the computational mesh. In this section, it was found that the rational number of hexahedral control volumes providing acceptable level of accuracy was about 27,000.

To use hexahedral control volumes it was necessary to split the whole domain into large number of smaller sub-volumes with simpler geometries. The section of the typical computational mesh for the fluid domain in the heating tube is shown in Figure 5.2a. Such a mesh was created by applying Quad-Map meshing scheme. In this scheme the face of the sub-volumes is first meshed using a regular quadrilateral grid.

The meshing element-scheme combination used for meshing the whole domain was Hex/Wedge – Cooper. Hex/Wedge scheme allowed the mesh to be composed primarily of hexahedral mesh elements, but included wedge (prism)

elements where appropriate. The Cooper volume meshing scheme swept the mesh node patterns of specified 'source' faces through the volume.
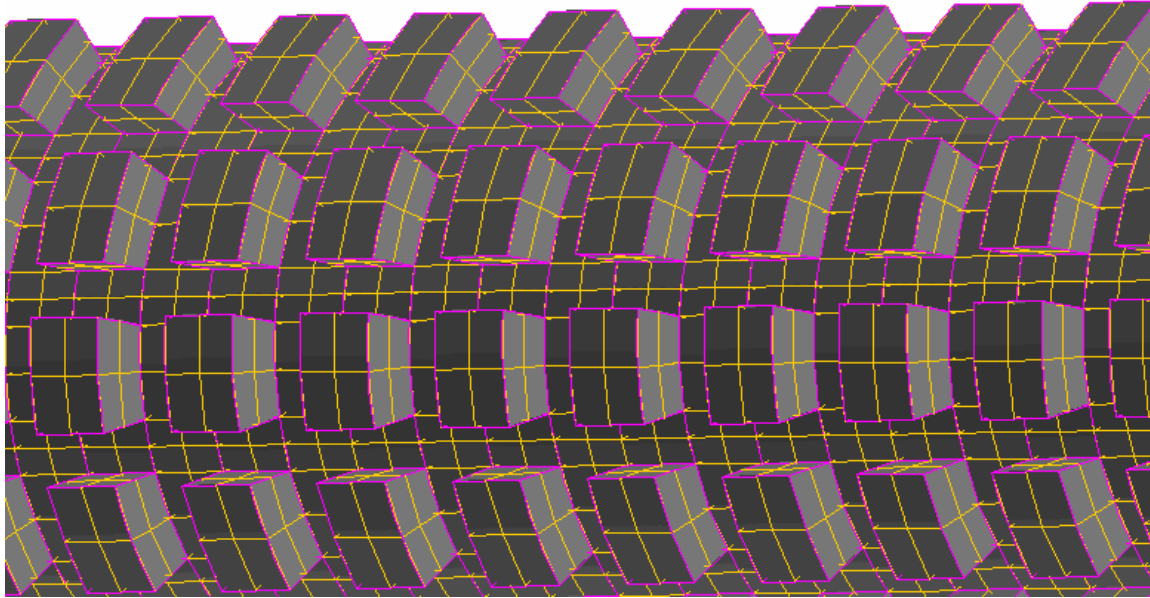
Figure 5.2a   Computational mesh for the fluid domain in the heating tube.

Figure 5.2b presents the Quad-Pave meshing scheme used to divide the cross-sectional area into computational elements which then was projected along the axis of pipes at certain intervals
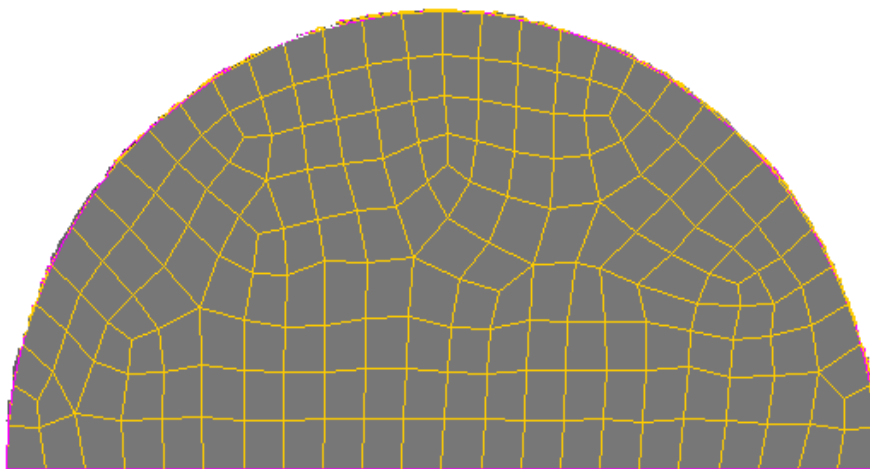
Figure 5.2b Quad-Pave meshing scheme for the cross-sectional area in the tubes.

The complete meshed volume for the section of the heating tube is illustrated below in Figure 5.2c.
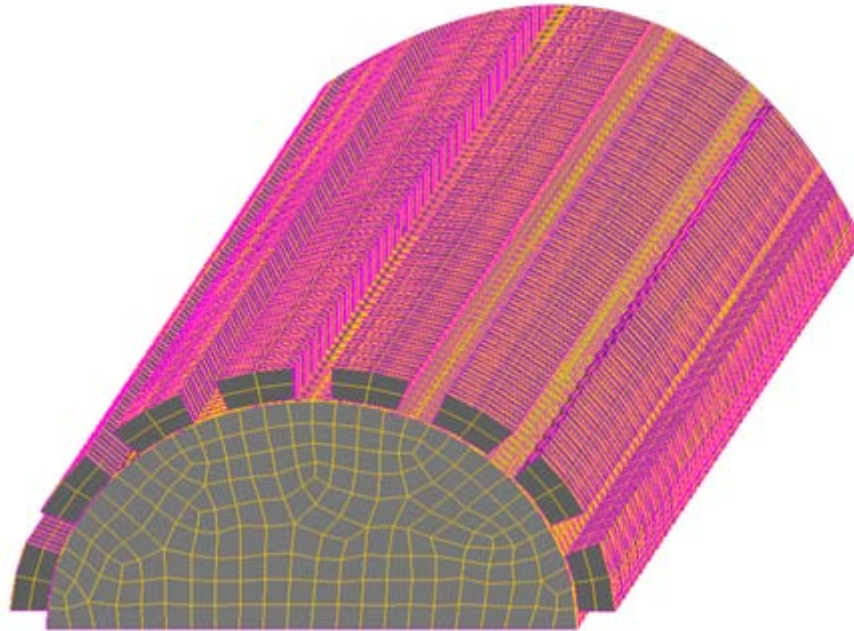
Figure 5.2c Computational mesh for the water domain in the heating tube.

In Figure 5.2c the yellow coloured lines represent the mesh and the purple e lines all the different volumes created after splitting the geometry of the volume of water with the net.

Using similar technique the "solid" domain was meshed including the volume of all pipes and that of the metallic mesh. The typical computational grid for the metallic mesh used inside the heating tube is presented below in Figure 5.2d.
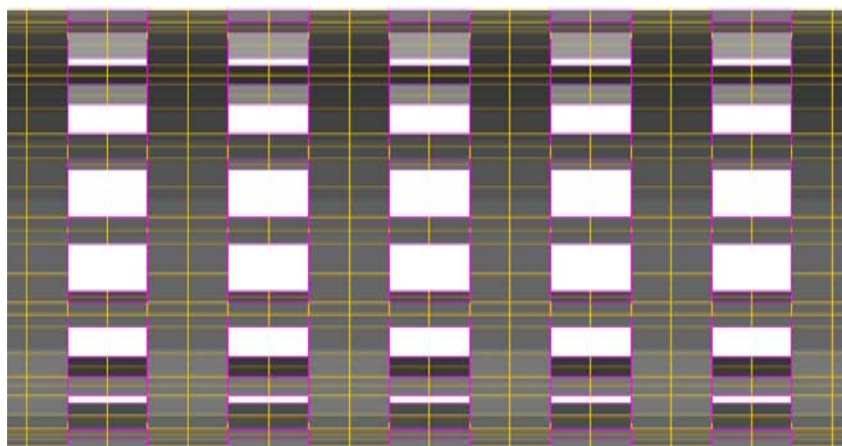
Figure 5.2d The computational grid of the metallic mesh insertion.

Since there was a symmetry plane in the created computational grid only half of the grid was used for CFD simulations as shown in in Figure 5.2e.
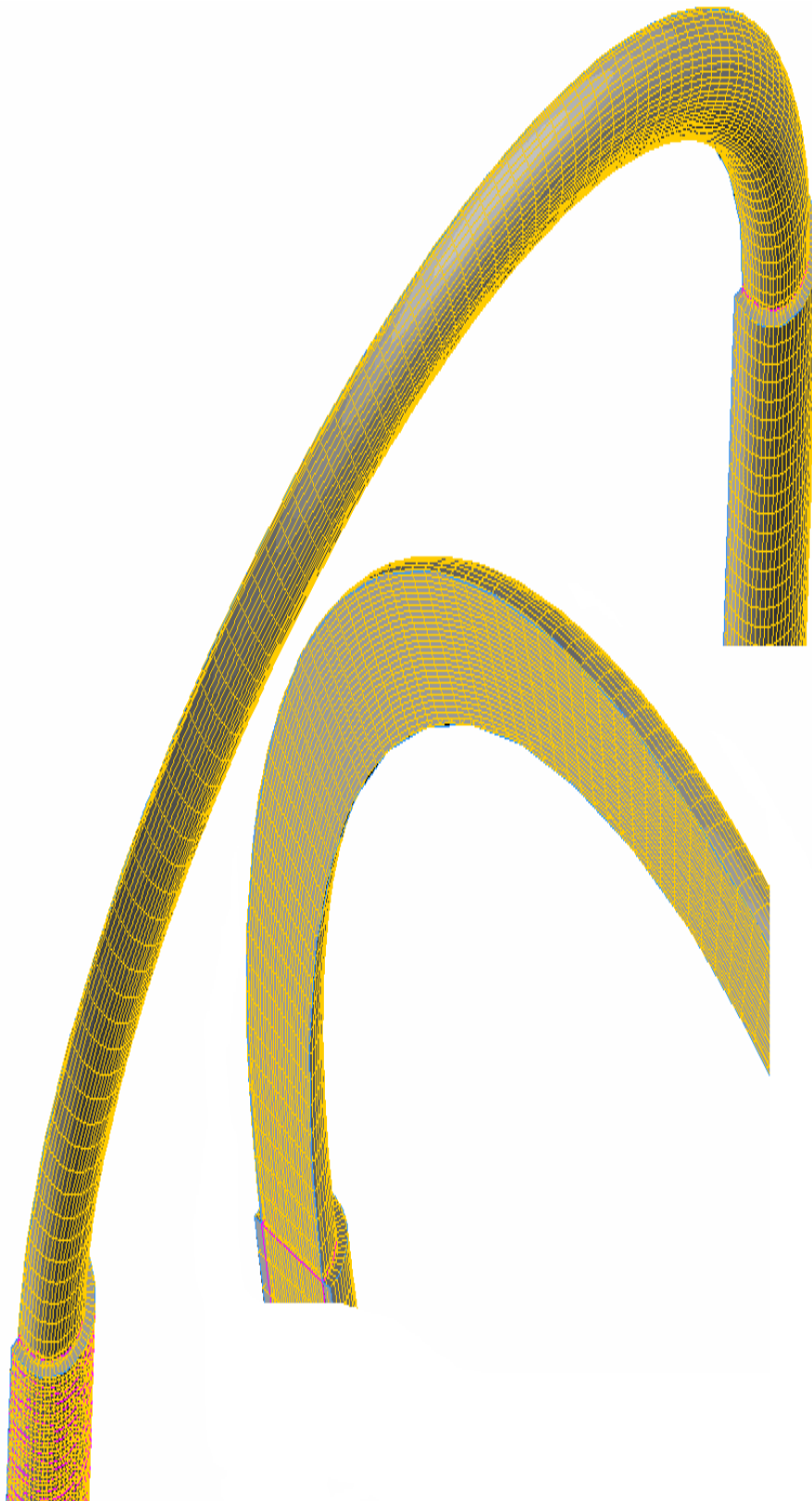
Figure 5.2e Sections of full computational grid used in numerical simulations.

As it was mentioned above, the total number of mesh cells created in the entire geometry was about 27.000 with density of the grid being greater in areas of large temperature and velocity gradients. Grid sensitivity tests (trial and approach) showed a variation of about 1% in the solution when the size of volumes increased or decreased by 10%.

In the pre-processor program GAMBIT any volume can be specified for a meshing operation, the shape and topological characteristics of the volume, the type of mesh scheme that can be applied to the volume can also be determined. To specify the meshing scheme, two parameters need to be specified: elements and type. The elements parameter defines the shape of the elements that are used to mesh the volume. The type parameter defines the meshing pattern of mesh elements in the volume. When a volume is specified on the Mesh Volumes form, GAMBIT automatically evaluates the volume with respect to its shape, topological characteristics and sets the scheme option buttons to reproduce a recommended volume meshing scheme.

The pre-processor software provided an option to check the quality of the computational mesh created in order to avoid the use of control volumes with high skewness which would very much affect the accuracy of the CFD solution and the optimal mesh used in these investigations passed such check as the levels of skewness were low in the range of 0.2- 0.3.

Another criterion to display the accuracy of the mesh is to set the volume element type, and specify the numbers of nodes associated with each of the volume element shapes. There are four volume element shapes available in GAMBIT: Hexahedron, Wedge, Tetrahedron and Pyramid.

Every volume element shape is associated with as many as five different node patterns. Each node pattern is characterised by the number of nodes in the pattern. The node patterns associated with each volume element shape are as follows:

Shape	Numbers of Nodes
Hexahedron	8, 20, 27
Wedge	6, 15, 18
Tetrahedron	4, 10
Pyramid	5, 13, 14

When you set a volume element type, GAMBIT applies the specified mesh node pattern to all volume elements of the specified shape i.e. when specify 18-node wedge volume elements, GAMBIT locates mesh nodes according to the 18-node pattern for all wedge volume elements produced in the subsequent volume meshing operation.

5.3 The CFD model set-up

After the completion of the computational grid the whole domain was split into different types of zones to specify the physical properties of materials of tubes, metallic mesh and also operational features of the model as well as boundary conditions applied. Additionally, since the symmetry plane has been used to halve the computational grid then flow, temperature and pressure gradients were set to be zero on this plane.

The properties of copper and aluminium were applied for tubes and metallic mesh insertion, respectively. The properties of liquid (water) were used for a liquid domain in the computational mesh. The properties of water were temperature-dependent and polynomial piecewise-linear functions were used to take into account the above dependence of water properties upon its temperature.

On the outer surface of the heating and cooling tubes the heat fluxes equivalent to 905 W/m^2 and -905 W/m^2 respectively, were specified in order to induce the free convection flow. This is illustrated below in Figure 5.3a where the red vertical pipe represents the heating region and the blue pipe is the cooling region. The two yellow semicircles were specified as adiabatic which meant that no heat flux was applied and there were no losses that region.
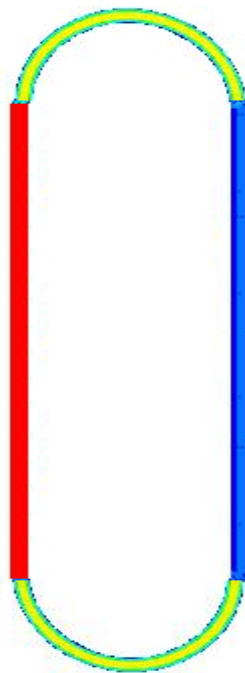
Figure 5.3a Colour scheme setting the boundary conditions.

The effect of gravity was taken into account along the vertical axis by specifying the negative acceleration value of 5.62 m/s^2 (cosine of 55$^\text{o}$ multiplied by the gravitational forces constant) since the solar collectors was assumed to be

inclined. The inclination angle was set to 55° which is the latitude of Durham, U.K. and this inclination was used in the experimental test rig. Both conventional (without metallic mesh insertion) simplified collector and the system under investigation were set to have initial temperature of 288 K.

The laminar flow model governing equations (4.3.1-4.3.3) were solved since flow velocities were very small. The Pressure-Velocity coupling scheme was used in these investigations because it was efficient for low velocity flows. Mass conservation (continuity) of the velocity field was achieved by solving a pressure equation (4.3.4). Since the governing equations mentioned above were nonlinear and coupled to one another, the solution process is iterative where the entire set of governing equations was solved repeatedly until the solution converged.

Since the free convectional flow was the case under investigation the time dependent solution technique was chosen. In FLUENT the time-dependent equations were discretised in both space and time. Sequential discretisation involved the integration of every term in the differential equations over a time step Δt.

The total computational time for both cases was about 35 minutes as the system reached a steady state where the plotted residuals did not vary any longer. At this moment results could be observed and analysed accordingly.

5.4 Analysis of CFD modelling results

This section presents some of the numerical results obtained from CFD modelling of a simplified model of a solar collector. Two cases were considered, namely the case of a solar collector with a conventional heating pipe and the case when the metallic mesh

insertion was placed inside the heating pipe as a proposed method of enhancing heat transfer.
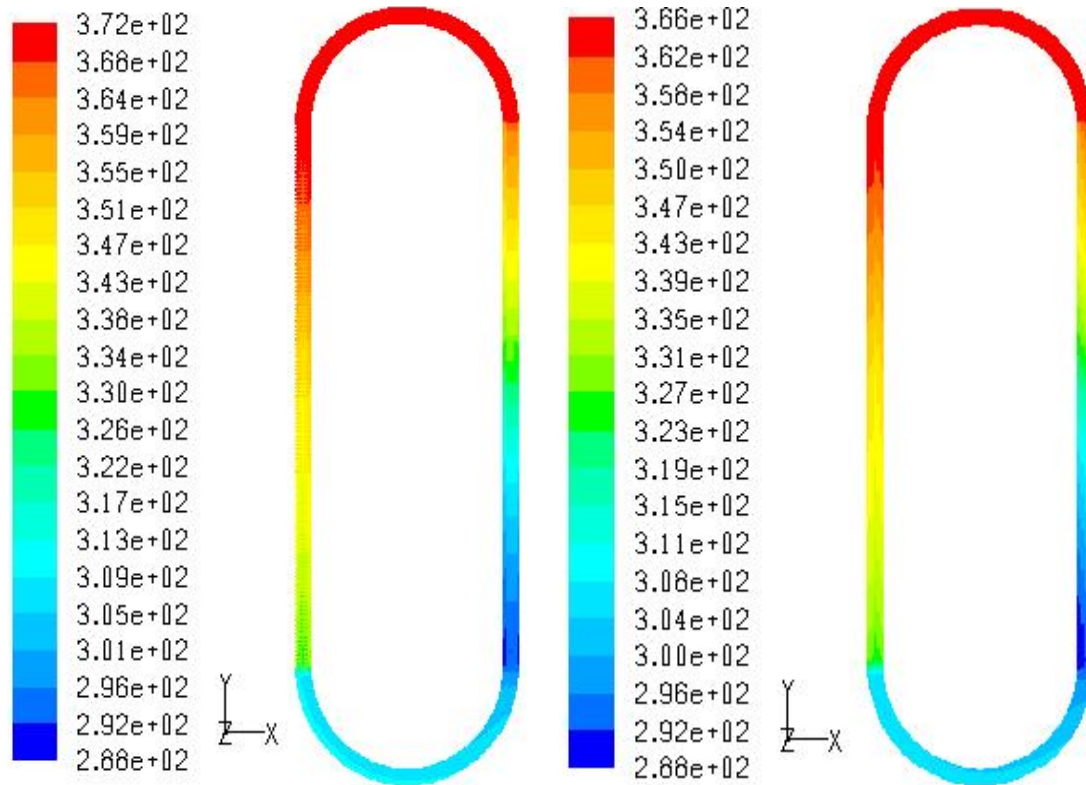
Figure 5.4a Temperature contours of both geometries (K).

Figure 5.4a presents the temperature contours for both the cases when steady-state operational conditions were achieved. The numerical results obtained, clearly demonstrate that the proposed design of the solar collector provides a considerable performance improvement.

In both cases, the identical boundary and initial conditions were applied as described the previous section. The left image in Figure 5.4a shows results for the simplified collector with the mesh insertion, while the right image presents the temperature contours for the conventional collector.

It can be seen that the working fluid is heated to the temperature 372 K which is 6 degrees higher compared to the maximum water temperature in the conventional solar collector. Considering the relatively small dimensions of both collectors the increase in temperature is quite significant. On the outer surface of the heating and cooling tubes the heat fluxes were equivalent to 905 W/m^2 and - 905 W/m^2 respectively. The power output Q of the designed collector with the metal mesh and the conventional was 78 W and 75 W respectively.

A graphical representation of the temperature rise in K along the length of the heating tube is shown in Figure 5.4b. The temperature T1(blue line) refers to the case with the mesh insertion and it can be seen that for such a design, the temperature increase in the heating tube is higher all along its length compared to that of a conventional collector displayed by the red line T2.
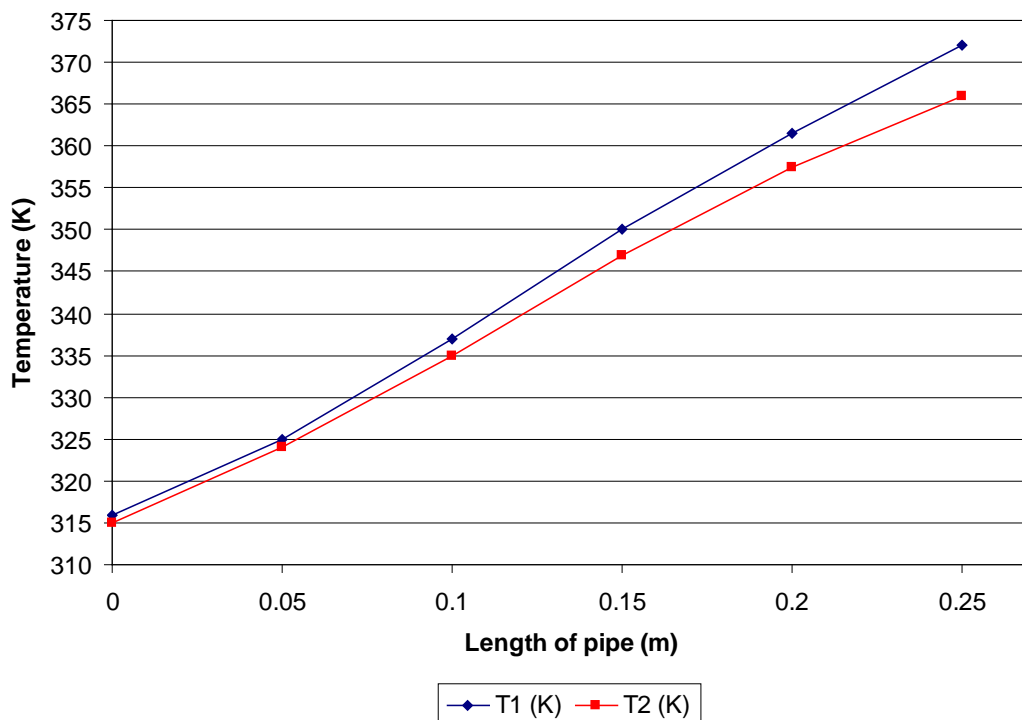
Figure 5.4b Temperature variation along the length of the heating pipes.

The variation of the water temperature in the section of the heating tube along its radius is demonstrated in Figure 5.4c (i) and it can be seen that the thickness of the near-wall layer of the fluid (water) or zone which has the high temperature is considerably greater for the case of the collector with metallic mesh insertion (image on the left).
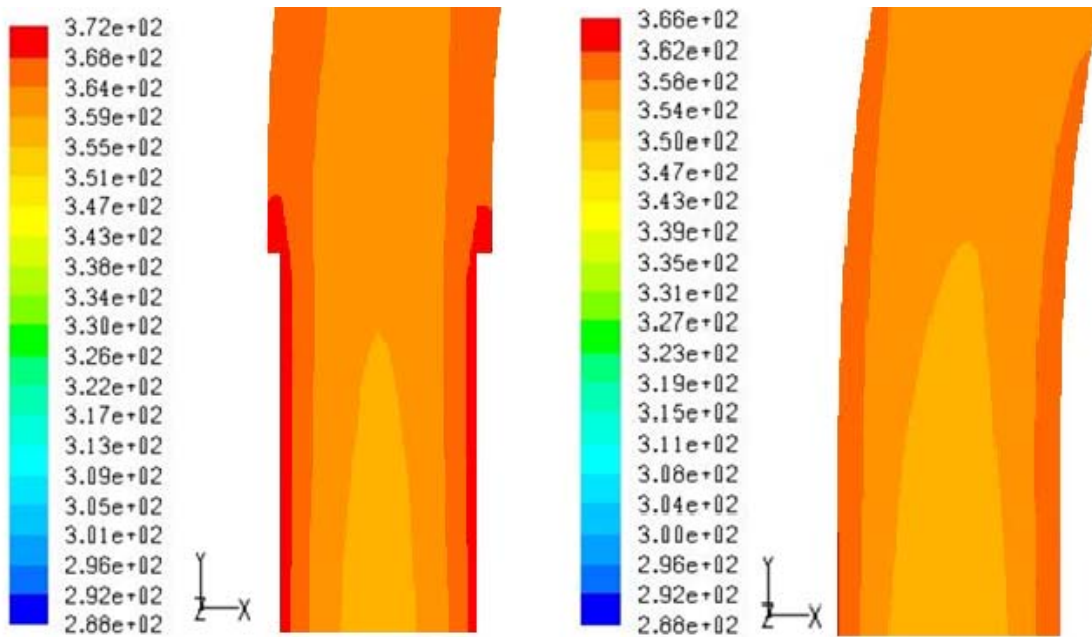
Figure 5.4c (i) Temperature contours at exit of the hot region.
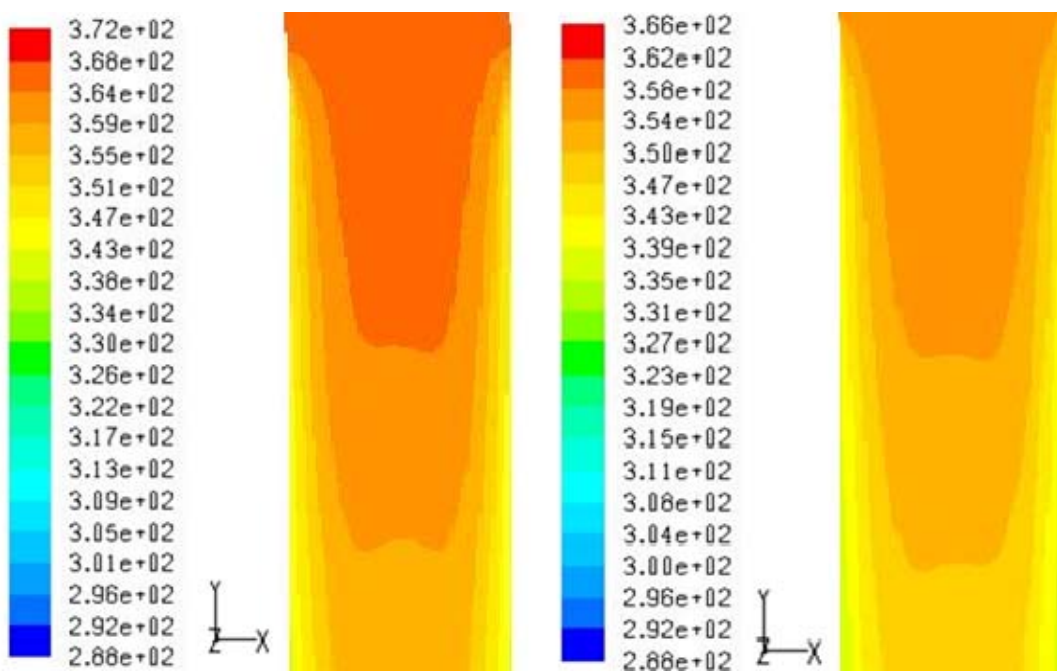
Figure 5.4c (ii) Temperature contours at the entrance of the cooling region.

The variation of the water temperature in the cooling tube along its radius is demonstrated in Figure 5.4c (ii). In the case of the conventional collector (image on the right) there is a domination of the lower temperature zone in the centre of the heating tube since the water entering has a lower temperature. The flow in the collector was induced by the density gradient, which in turn was caused by the
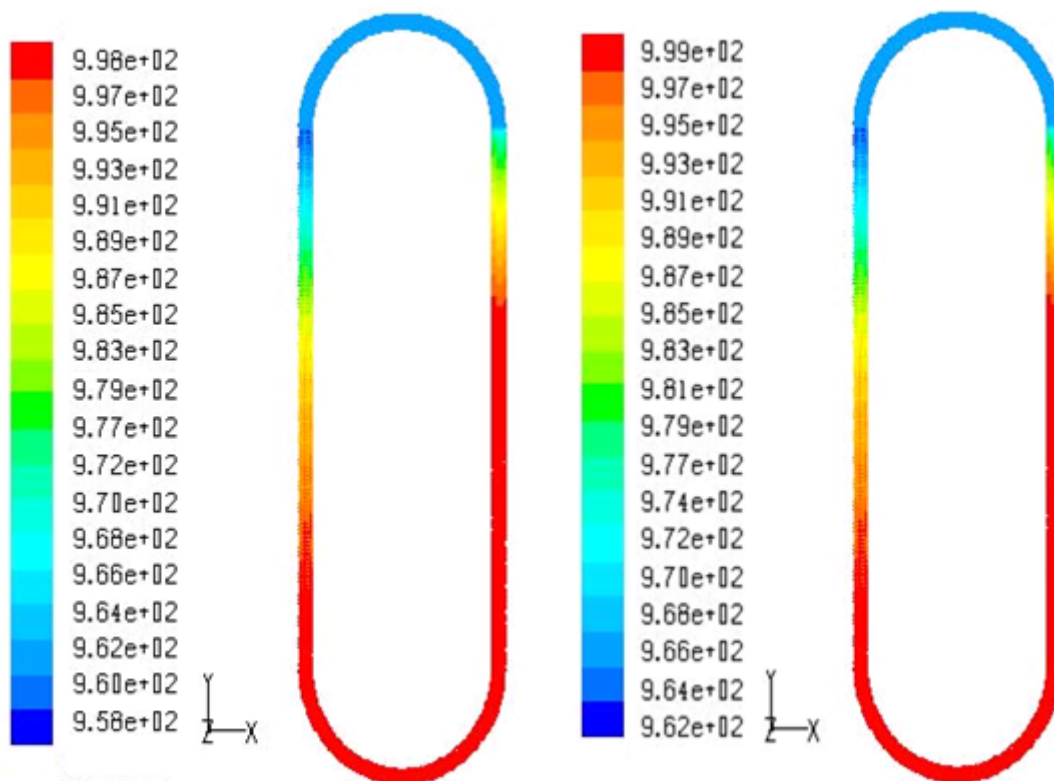
Figure 5.4d Density contours.

heating and cooling the working fluid. Figure 5.4d shows the typical variation of the density inside the collector. In both cases very similar patterns were obtained. It can be seen that for the given boundary conditions the density of water changes from 962.6 kg/ m³ at the top after heating process to 999 kg/ m³ at the bottom where the temperature is the lowest. In the in the design with the metal insertion case it varies between 958 kg/ m³ to 998 kg/ m³. Also from numerical results the water is cooled down more in the conventional design since higher water density results to a lower water temperature at the cooling tube.

The image on the left in Figure 5.4e shows velocity vectors V, in m/sec against its diameter D in mm, of the fluid flow in the symmetry plane for the convectional collector. The image on the right presents results for the proposed collector. Both images show the velocity vectors at the location where the fluid is leaving the heating tube. Results indicate that flow remains laminar for both cases though there was a small increase in the velocity at the centre of the heating pipe of the collector with metallic insertion,(does not exceed the velocity of the conventional design), due to the reduction in the cross-sectional area. At the pipe walls the velocity drops due to friction from the metallic insertion resulting to an overall velocity reduction along the pipe. The overall velocity then drops at the centre of the pipe after passing the zone where the metallic insertion is placed. The overall velocity flow rate is higher in the conventional scheme having 4.7 10^{-3} m/sec compared to 4.4 10^{-3} m/sec in the system with the metallic mesh.
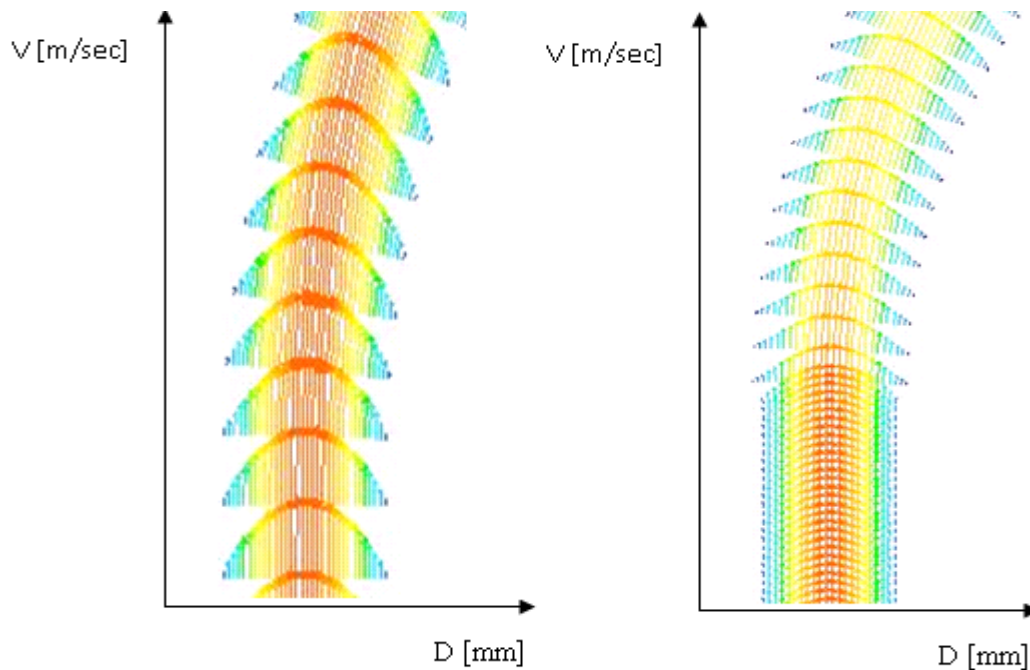
Figure 5.4e Blown up version of velocity vectors of both cases.

In order to validate the simulation findings it was essential to relate them to literature and hence the expression (5.4.1)[1] was used which is valid for constant surface heat flux. The output temperatures T_{out1} and T_{out2} were obtained for the collector with the metal insertion and the convectional collector, respectively. Data from the simulations was used in order to determine the output temperatures.

$$T_{out} = \frac{Q \cdot P}{(\dot{m} \cdot C_p)} + T_{ref} \qquad (5.4.1)$$

where Q is the heat flux in W/m^2, P is the perimeter of the pipe in mm^2, $\dot{m}$ in the mass flow rate in Kg/sec, C_p is the specific heat in J/Kg ^{o}C, T_{out} and T_{ref} are the output and average temperature of the system in ^{o}C, respectively. Table 5.4.a illustrates data obtained from simulation and other parameters from relevant charts i.e. C_p, to evaluate the CFD findings with the literature.

	Collector with metal mesh	Conventional Collector
Q(W/m^2)	905	905
P (mm)	31.15	31.15
T_{ref} (^{o}C)	341	336
$\dot{m}$ (Kg/sec)	$0.217 \cdot 10^{-3}$	$0.233 \cdot 10^{-3}$
C_p (J/Kg ^{o}C)	4190	4185

Table 5.4a Simulation data obtained for both cases.

Table 5.4a Simulation data obtained for both cases.

By placing the data to the expression (5.4.1) for the collector with the metallic mesh the output temperature T_{out1} was **372.2 ^{o}C** and for the conventional T_{out2} was **365.6 ^{o}C**. These results showed the accuracy of the CFD model since the values obtained were very close to the simulation ones **372 ^{o}C** and **366 ^{o}C** respectively (shown in Figure 5.4a).

---

[1] David P. de Witt expression.

Graph 5.4a illustrates the pressure drop along the length of section of tubes presented in Figure 5.4e. The red line represents the pressure drop in the conventional geometry and the black line is the pressure drop in the scheme using the mesh insertion. The pressure drop in the heating pipe for the given boundary conditions in both cases was relatively small, being about 3 and 7 Pa for the conventional design and the design with the metallic mesh insertion, respectively. Such low values of the pressure drop do not affect significantly the flow rates of the fluid and did not affect thermal performance of the both solar collectors. The point where the two graphs intersect is at the entrance of the hot region. The black line (representing the geometry with the mesh insertion) is of higher pressure magnitude since the temperature is this design is higher as pressure and temperature are directly related[2].
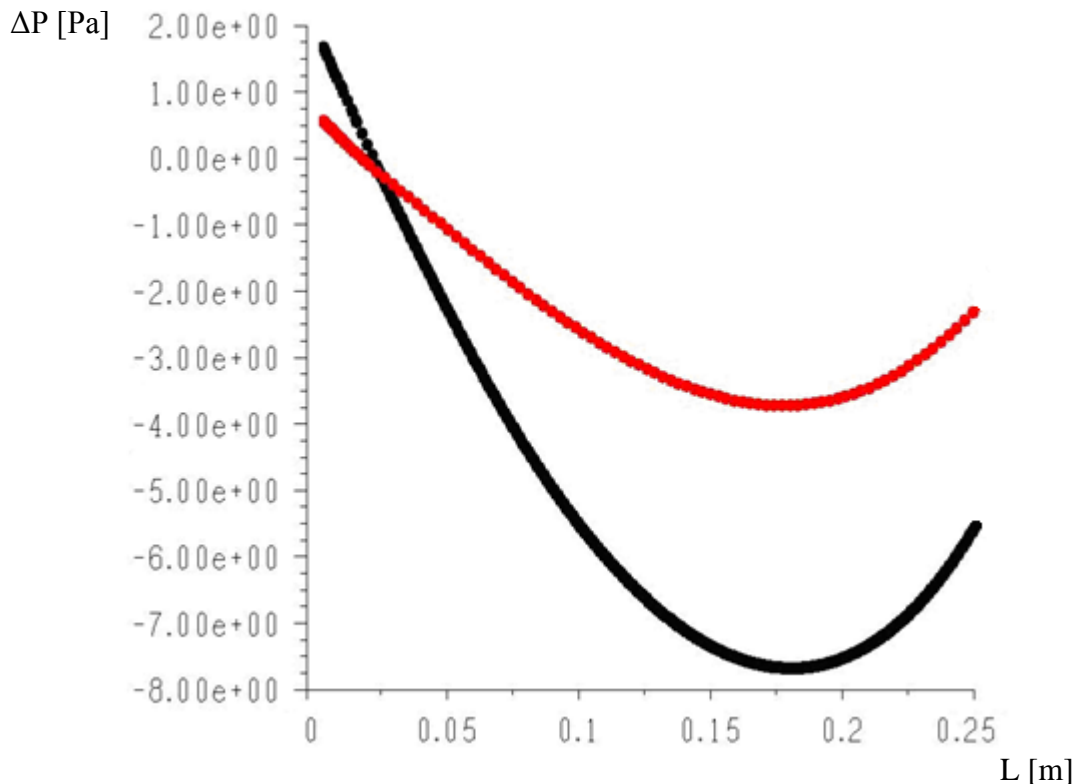
Graph 5.4a Pressure drop along the length of the pipes.

---

[2] Clausius- Clapeyron relation.

The operation of two geometries of the solar collector was CFD modelled as a function of the heat flux values on the heating and cooling tubes between 610 W/m^2 to 1070 W/m^2. The average heat transfer coefficient from solid domain to fluid in the heating pipe was determined from CFD simulations, see Table 5.4b.

Fluent uses the relation shown below in order to calculate the heat transfer coefficient of the examined geometry.

$$h = \frac{Q}{\left(T_w - T_{ref}\right)} \qquad (5.4.2)$$

where Q is the heat flux in W/m^2, T_w and T_{ref} are the temperature of the wall and a reference temperature, respectively.

It can be observed that the heat transfer value in the case of the collector with the metallic insertion was noticeably higher and the difference in heat transfer coefficients rises with increase of the heat flux applied.

Heat Flux (W/ m^2)	h Porous Case (W/m^2 K)	h Conventional Case (W/m^2 K)
1070	207.67	194.83
905	171.82	160.20
750	134.40	122.10
610	115.60	99.00

Table 5.4b Heat transfer coefficients (h) of the examined cases.

Further using results from CFD calculations the Rayleigh number (Ra) was determined, which is a measure of the strength of the heat transfer due to natural convection at the examined geometries. Using CFD simulations the heat transfer correlation was derived for different values of the heat flux applied on the surfaces of heating and cooling tubes.

Two different heat fluxes were used (1070 W/m^2 and 610 W/m^2) in order to accomplish this task. The Rayleigh number (*Ra*) is defined as shown below:

$$Ra = \frac{g\beta\Delta T L^3}{\nu\alpha}$$ (5.4.3)

Here *β* is the thermal expansion coefficient; *L* the length of the pipe, *v* the kinematic viscosity and *α* is the thermal diffusivity. The values of the (5.4.3) automatically change according to the change of temperature during the simulation process apart from the length L that remains constant.

Graph 5.4b presents the change in Rayleigh number along the heating tube for the collector with the mesh insertion (the curve in black line) and the conventional collector (the red line curve) for a heat flux value of 1070 W/m^2.
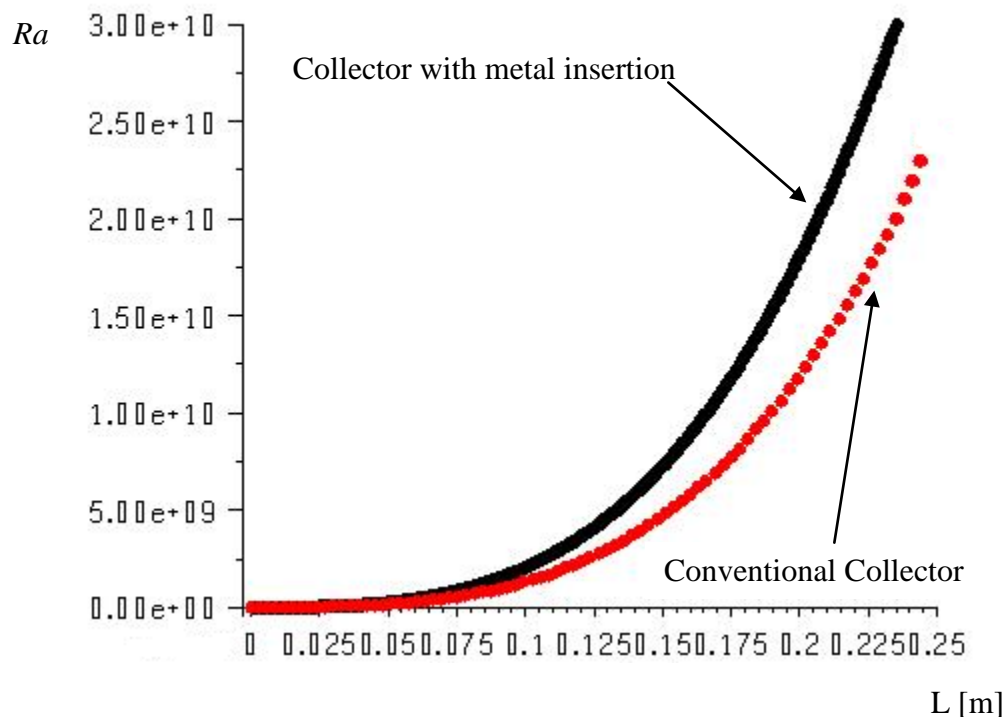
Graph 5.4b Rayleigh number representation against characteristic pipe length.

An identical graph was plotted as shown in Graph 5.4c for a heat flux of 610 W/m^2. The range of *Ra* number obtained in both cases suggested that the natural convection was the dominant mode of heat transfer.
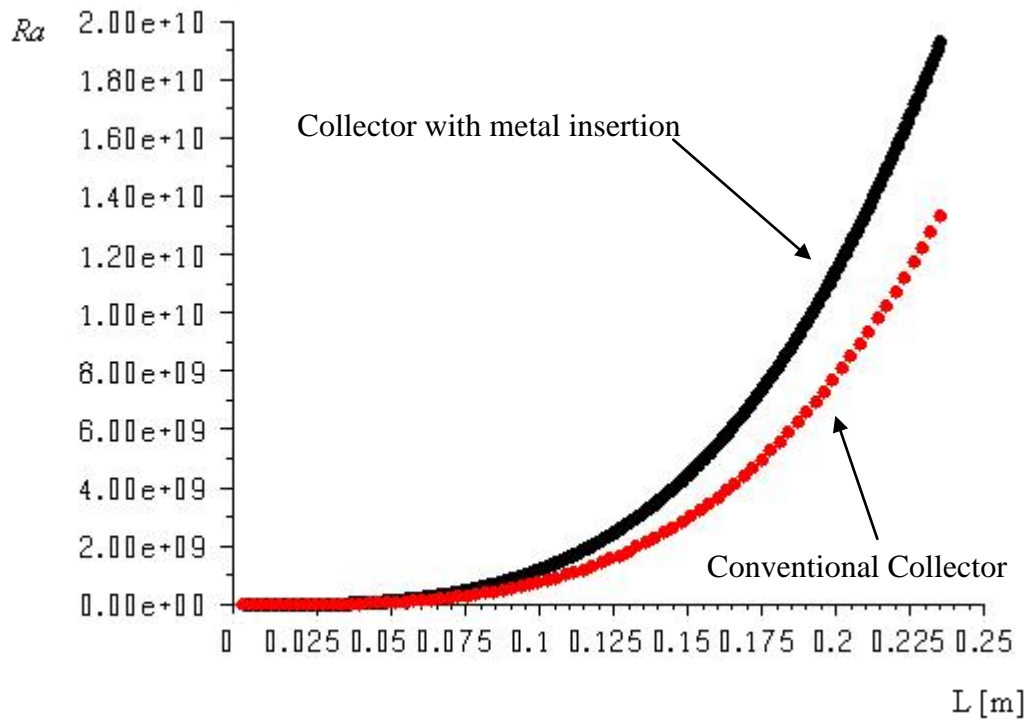
Graph 5.4c Rayleigh number representation against characteristic pipe length.

The heat transfer correlation relating Nusselt (*Nu*) and Rayleigh (*Ra*) numbers was sought in the following form:

$$Nu = c(Ra)^n \qquad (5.4.4)$$

Here *c* is the constant of proportionality and *n* is a variable determined by conditions on the constant heat flux surfaces or isothermal surfaces. This *n* coefficient was calculated and its average was used to calculate *c*.

The two parameters c and n were calculated by coupling equations in pairs as shown below:

$$Nu_1 = c(Ra_1)^n \qquad (5.4.5)$$

$$Nu_2 = c(Ra_2)^n \qquad (5.4.6)$$

$$n = \log_{\frac{Ra2}{Ra1}} \frac{Nu_2}{Nu_1} \qquad (5.4.7)$$

The n parameter was calculated for a range of Ra and Nu numbers as varied along the characteristic pipe length and its average was used to calculate c. The final correlation derived was for the heat fluxes of 1070 W/m^2 and 610 W/m^2 respectively:

$$Nu_{(1070)} = 0.013(Ra)^{0.285} \qquad (5.4.8)$$

$$Nu_{(610)} = 0.007(Ra)^{0.285} \qquad (5.4.9)$$

The value of n=0.285 suggested that conditions close to the isothermal ones were present on the surface of the geometry [112]. After the numerical solution was converged reaching the steady state and due to the presence of the aluminium mesh insertion it could be interpreted that the heat transferred to the fluid was uniform.

Equations (5.4.8) and (5.4.9) can be used to derive the Nu number in relation to Ra number under constant heat flux (from 610 W/m^2 to 1000 W/m^2). Also these two relations can be used to obtain other useful parameters that can predict the performance of a collector i.e. heat transfer coefficient h. Collectors are formed by individual tubes and therefore the above derived correlations can be applied to real systems to examine each of the collector's pipes individually over a characteristic

length. The values obtained from Fluent and those calculated from the correlations derived are listed below in the Table 5.4b.

1070 W/m^2			610 W/m^2		
Ra	*Nu*	*Nu calculated*	*Ra*	*Nu*	*Nu calculated*
2.5E+09	6.3	6.3	2E+09	3.3	3.1
5E+09	7.5	7.6	4E+09	4.0	3.8
7.5E+09	8.5	8.5	5E+09	4.3	4.0
1E+10	9.3	9.2	8E+09	4.5	4.6
1.5E+10	10.0	10.3	1.2E+10	4.8	5.1
Average values					
Ra	*Nu*	*Nu calculated*	*Ra*	*Nu*	*Nu calculated*
8E+09	**8.3**	**8.4**	**6.2E+09**	**4.2**	**4.3**

Table 5.4b *Nu* and *Ra* number relation.

Results showed that there was a very good agreement between *Nu* numbers obtained both from Fluent and the proposed correlation. Using the values from Table 5.4d a graph was plotted shown in Graph 5.4d. It displays the relation between the Nusselt number *Nu* and the Raleigh number *Ra*. It also illustrates the difference
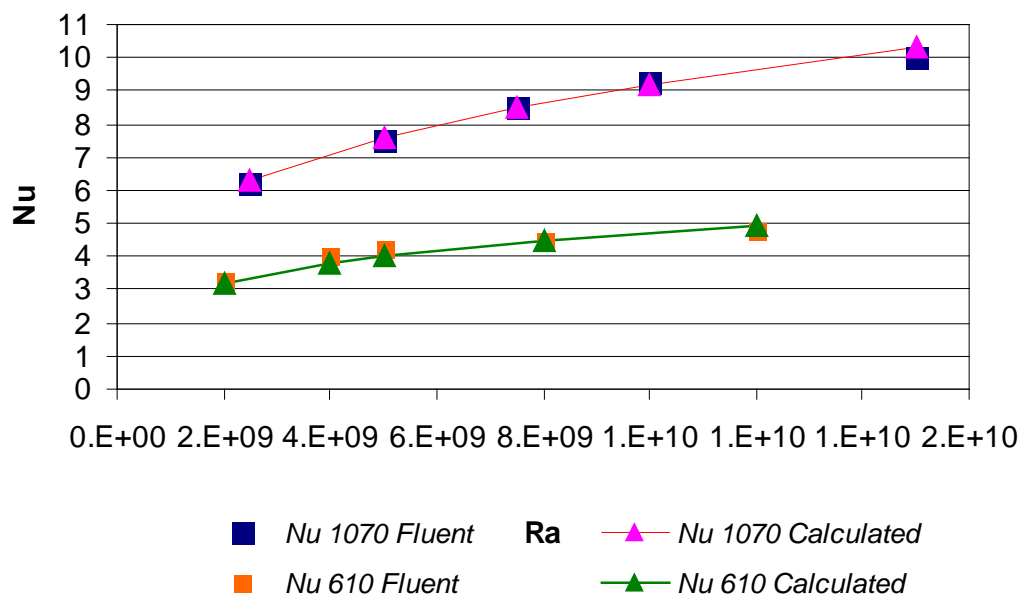
Graph 5.4d Rayleigh number as function of Nusselt number.

between the values of the *Nu* number obtained from the derived correlation and those from Fluent. The average *Nu* number ranges between **4.2** to **8.3** and the *Ra* number between **6.2·10⁹** to **8·10⁹** for heat fluxes between 610 W/m² to 1070 W/m² being in the range of the laminar flow. This was chosen to demonstrate the mechanism of the heat transfer intensification due to the presence of the metallic mesh insertion in the pipe.

An enlarged picture of flow structure within the pipe and the flow near-wall region is presented in Figure 5.4f.
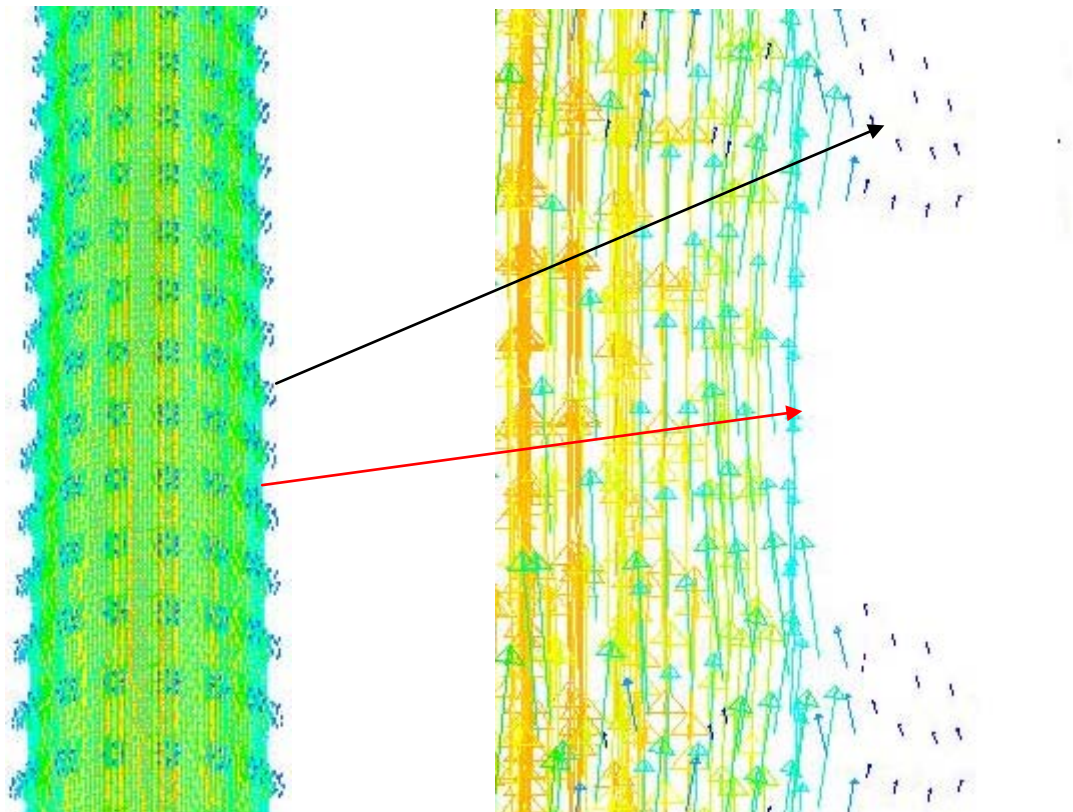
Figure 5.4f Velocity vectors inside the pipe with metallic mesh insertion.

The velocity vectors, illustrated by small coloured arrows, are shown in Figure 5.4f. The dark blue coloured arrows (lower velocity) located at the surface of the pipe at the areas without the metallic insertion as pointed out by the big black arrow. The

light blue arrows that represent a higher velocity are located in the region with porous material as pointed out by the big red arrow (higher velocity). The mesh insertion increased the heat transfer area assisted in the heat transfer from fluid layers near the wall to fluid (water) layers close to the centre of the heating tube.

Figure 5.4g illustrates a 3-D view of the velocity vectors (coloured arrows) inside the conventional pipe. The features of this laminar flow is presented with coloured vectors changing from shades of dark blue, corresponded to low velocities near the wall of the pipe. Shades of green, yellow and finally red corresponded to an increase of the velocity towards the centre of the pipe. Here due to the layer-by-layer motion the heat was transferred at a slower rate from the near wall zone in the direction toward the axis of the tube.
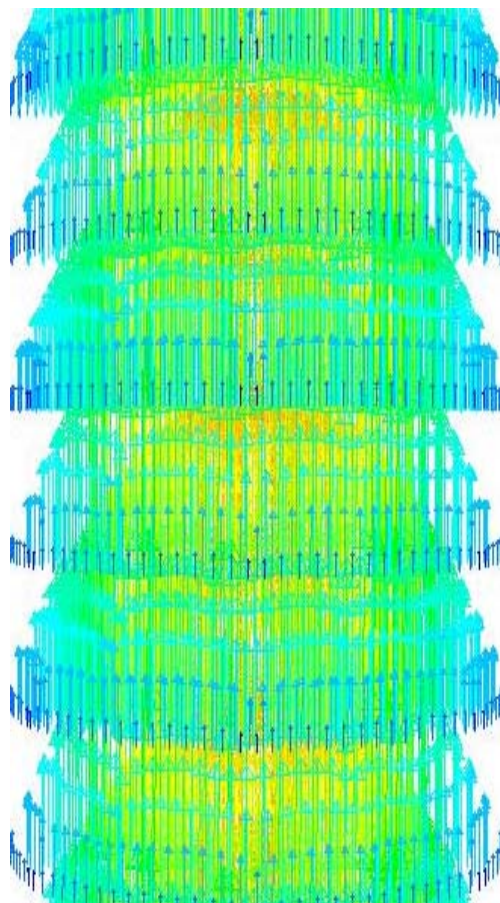
Figure 5.4g Velocity vectors inside the conventional pipe.

5.5 Related work

Initially, some other numerical approaches were conducted in order to simulate the effect of the presence of the metallic mesh inside the pipe.

Prior to designing the net inside the pipe the 'roughness' parameter along with the 'porous medium' option in CFD simulation package FLUENT was used to reflect the effect of the aluminium mesh insertion inside the copper pipe, as it is illustrated below in Figure 5.5a.

Copper pipe   Aluminium mesh

Volume water
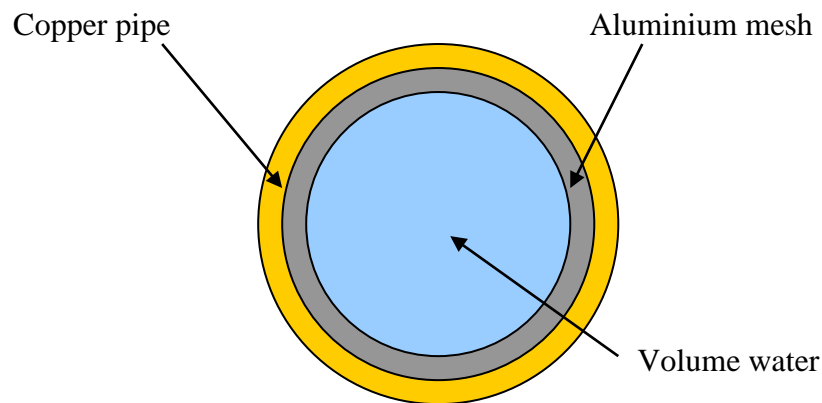
Figure 5.5a Cross-section of a pipe with aluminium mesh.

During numerical investigations different flow models including the turbulent models k-ε and k-ω models, were used since the regime of the flow (laminar or turbulent) could not be exactly determined initially.

Application of the roughness parameter and porous medium model in FLUENT did not succeeded (due to limitations of these models) in reflecting heat transfer intensification.

Additionally, an attempt to use more detailed design of the solar collector was tried as shown in Figure 5.5b which includes the absorber section. The design consisted of a copper pipe with radius (external) of 10 mm and a copper fin with width of 11 cm. This design was identical to that used in the experiments.
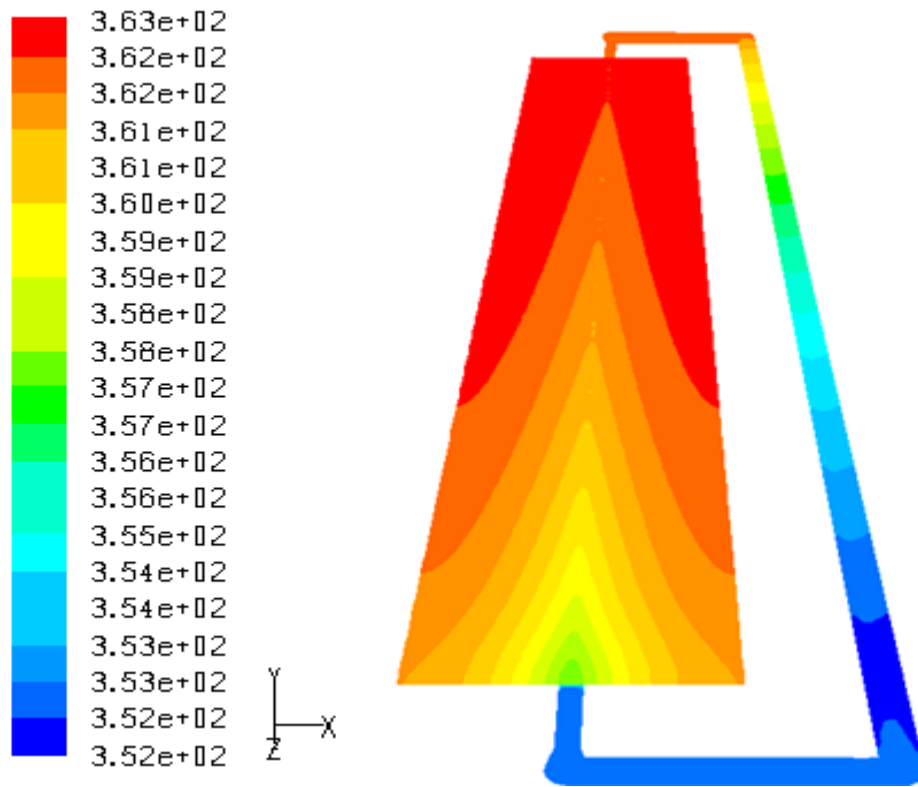
Figure 5.5b Simulated collector section.

The attempt described above was abandoned since it was determined that the design using a finned pipe would not affect the numerical results if the heat flux per unit area was increased on the pipe only reducing the overall computational time needed for the simulations.

Finally, a pipe which had regular turbulisation profiles on its internal wall was modelled as shown in Figure 5.5c. The depth of the profile was set to be 1 mm with a

pitch of 2 cm. The expectation was that such profiles would break the boundary layer and therefore improve the heat transfer to the fluid.

The main problem in this case was that very fine mesh was needed to carry out such CFD simulation to present the all features of the flow structure in the near-wall zone. The number of cells in the computational mesh created was 485,000 for 1m long tube requiring a significant amount of computational time to obtain the converged solution.
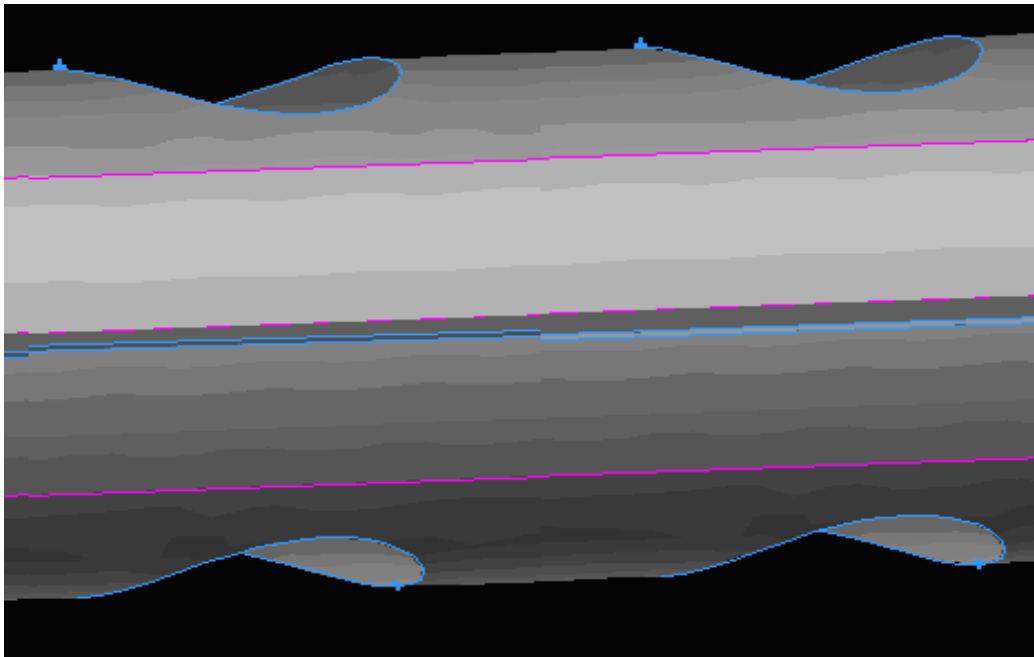
Figure 5.5c Profiled pipe design.

In Figure 5.5d the velocity vectors for the section of this design geometry can be observed. Overall, the results obtained from the simulations were encouraging. The presence of turbulisation profiles on the surface of the pipe affected the flow pattern of the liquid and had a positive effect on the heat transfer increase.

However, to achieve such a positive effect greater velocities than those typical in passive systems are needed.
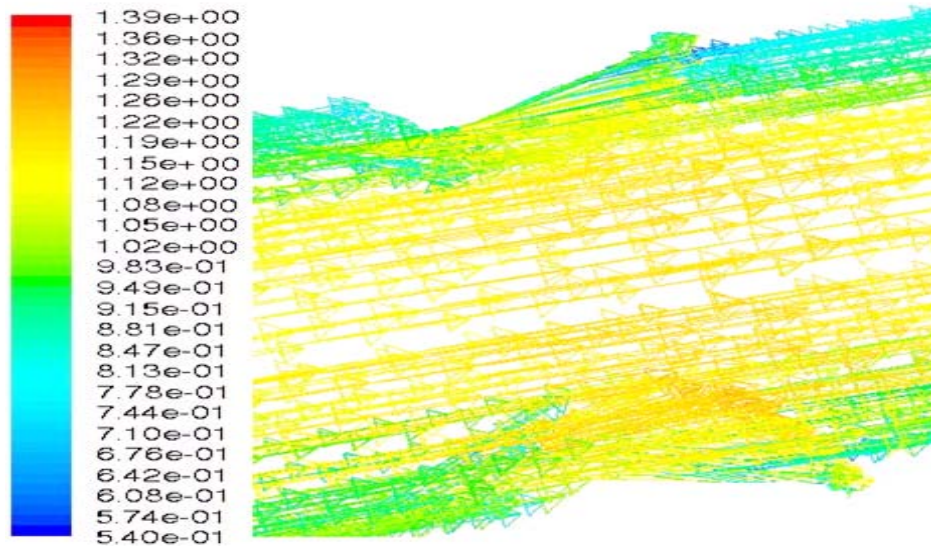
Figure 5.5d Velocity vectors in the profiled pipe design.

5.6 Conclusions

The analysis of the CFD model results, clearly demonstrated that the application of a metallic mesh insertion in the heating channels of passive solar collectors is an efficient way to intensify heat transfer from the heating surface to the working fluid and consequently improving the thermal performance of solar collectors.

The output temperatures obtained from simulations for the geometry with the metallic mesh and for the conventional were validated with literature which showed the accuracy of the CFD model.

Higher output temperature, *Nu* and *Ra* numbers and finally higher heat transfer coefficient *h* for the model with the metallic mesh compared to convectional, clearly displayed the benefits of using this heat transfer enhancement technique.

From the obtained expressions (5.4.8) and (5.4.9) the *Nu* number in relation to *Ra* number under constant heat flux (from 610 W/m^2 to 1000 W/m^2) can be derived for a pipe with a characteristic length of 0.25 m. These two relations can be used to obtain other useful parameters that can predict the performance of a collector i.e. heat transfer coefficient *h*.

The heat transfer correlations derived in this Chapter for the calculation of the heat transfer coefficient in the passive solar collectors with metallic mesh insertion could be used in lumped parameter models employed at the collector design stage. Since collectors are formed by individual tubes the derived correlations can be applied to a part of a real system in order to investigate whether the simulation results can be related to the experimental results as it will be discussed on Chapter 6.

CHAPTER 6

Experimental Work

6.1 Introduction

In solar water collectors, incident solar radiation is converted to heat and passed on to a working fluid such as water. Therefore effective heat transfer is important with the aim to assist energy conversion process.

As discussed on Chapter 3, research to demonstrate the sensitivity of the flow distribution to the collector's geometry and hydraulic resistance was conducted and also demonstrated that the geometry of channels could result to a non-uniform flow distribution in collector systems. The distribution of the flow can be approximately gauged by temperature measurements at various points of the collector.

Heat transfer enhancement in collectors can be achieved by affecting the boundary layer, which in effect provides a resistance to heat transfer, and by increasing

the heat transfer interface area. A variety of heat transfer enhancing techniques have been investigated and described in relevant literature [77, 78].

Heat transfer for natural or forced convections in a system with channels partially filled by a porous material has been the subject to numerous investigations. Research results showed the increased heat transfer in an annular duct partially filled with a porous medium with a high permeability and conductivity.

One of the aims of this study was to investigate experimentally the effect of placing aluminium net inside the channels of a simplified flat plate solar water collector for an application in Southern Europe.

6.2 Preliminary Experimental Setup

All the experiments took place in the Thermodynamics Lab in the Engineering Department at Durham University, over a period of 18 months. The experimental work involved tests conducted on the rig equipped with two types of unglazed solar collector panels and artificial insolation. The first type of the collector used was similar to a conventional design and the second had aluminium mesh inserted in all its pipes.

Each panel consisted of 4 sections which were in fact individual tubes with attached fins and these were 1.35 m long. The two central sections of the panel had copper pipes with aluminium alloy fins. The sections which were placed on each side of the panel have pipes and fins fully made of copper as shown in Figure 6.2a. All the pipes

had an external radius of 10 mm and fins are 110 mm in the width. The materials were provided by Sun Systems in Kavala, Greece.

Aluminium alloy fins and copper fins had a thickness of 1.5 and 0.5 mm, respectively. The finned pipes of the panel were connected at the top and bottom to a manifold.

Figure 6.2a Solar panel.

Each of the top manifolds were linked to the inlet of a cylindrical water jacket which dissipated heat produced by the collector panels. From the outlet of the water jacket the fluid was directed to the bottom manifold of the panel.

The absorption side of the panel was matt black painted. The collector panels were placed in separate wooden boxes with fibre glass insulation beneath as it is illustrated in Figure 6.2b.
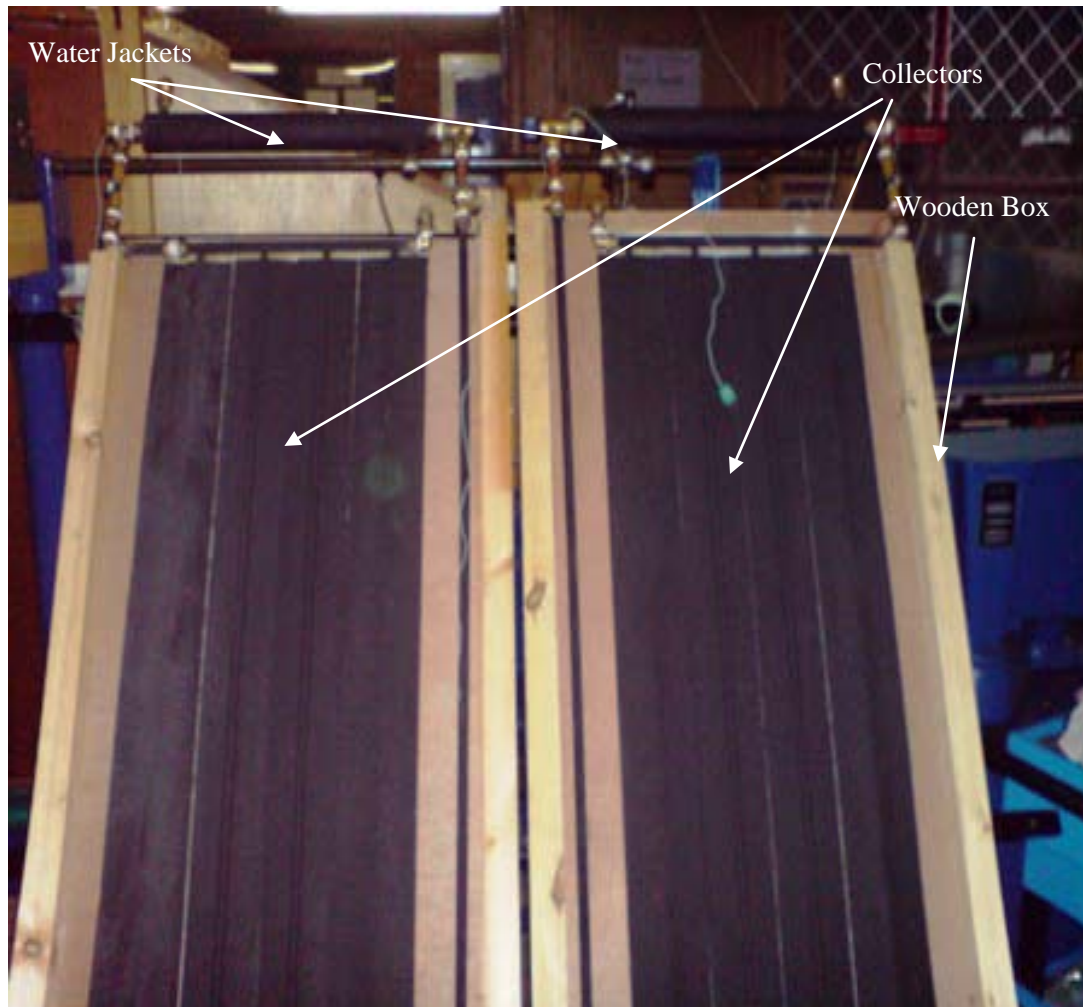
Figure 6.2b Painted collector panels placed in wooden boxes with fibre glass insulation.

The boxes were mounted side by side on the slopped metallic frame. An array of electrical bulbs was mounted above panels parallel to the wooden boxes to imitate insolation.

There were one hundred and ten 150 W halogen floodlights in the array evenly spaced over the area of 1.8 m^2, as seen in Figure 6.2c.

Figure 6.2c Array of halogen bulbs mounted above solar panels.

Halogen floodlights were split into three groups and the heat flux from bulbs could be controlled using a three phase electrical transformer manufactured by 'Zenith Electric Co.' London, U.K. illustrated below in Figure 6.2d.

Figure 6.2d A three phase electrical transformer.

The insertion used in one of the panels was made of an aluminium wire mesh which was folded and placed in each pipe to provide a reasonably even porosity along the length of the channel, shown in Figure 6.2e.

Figure 6.2e Porous medium inserted in a copper pipe.

A series of K-type thermocouples were fitted on each panel, measuring the temperature of the water in the collector at its inlet and outlet and there was an additional thermocouple which measured the temperature in the water jacket. All thermocouples were calibrated and the error deviation at measuring temperatures was around 0.05 ^{o} C. Therefore the thermocouple measurements were pretty accurate.

The water jacket in this case was used as a small water storage tank. Also a portable thermometer with a thermocouple used to measure the temperature of the surface of the panels at different locations. The flow rate of the fluid in the panels was determined using a turbine type flow sensors (manufactured by RS, Northands, U.K.) connected to an oscilloscope.
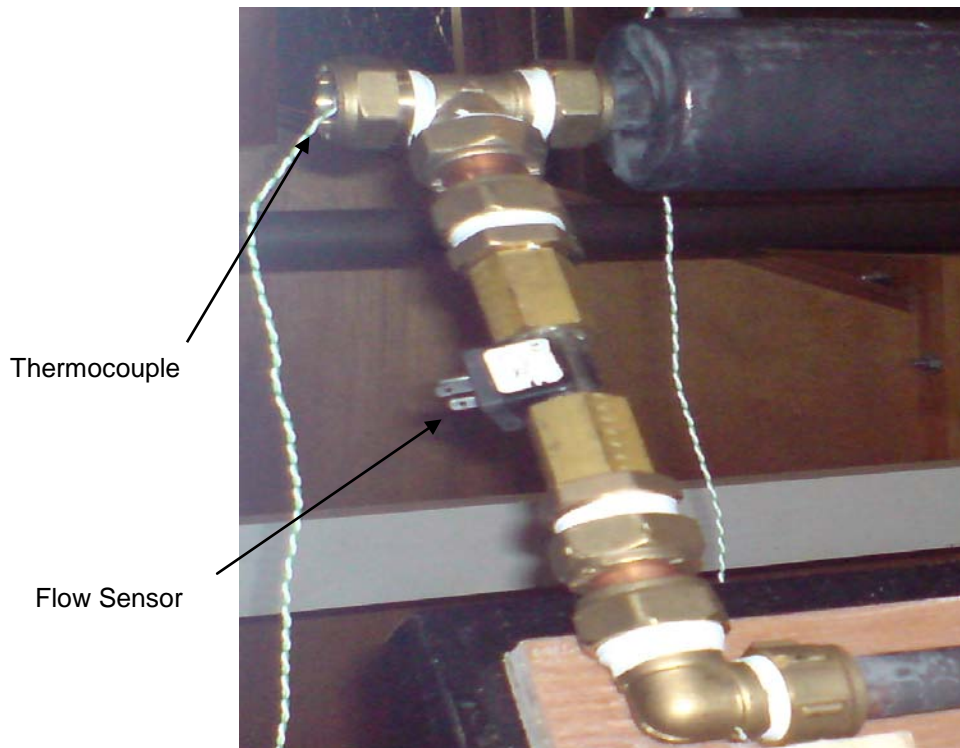
Figure 6.2f Flow sensor and thermocouple at the inlet of the water jacket.

The schematic diagram of the whole experimental test rig equipped with data measuring and recording devices is shown in Figure6.2g.
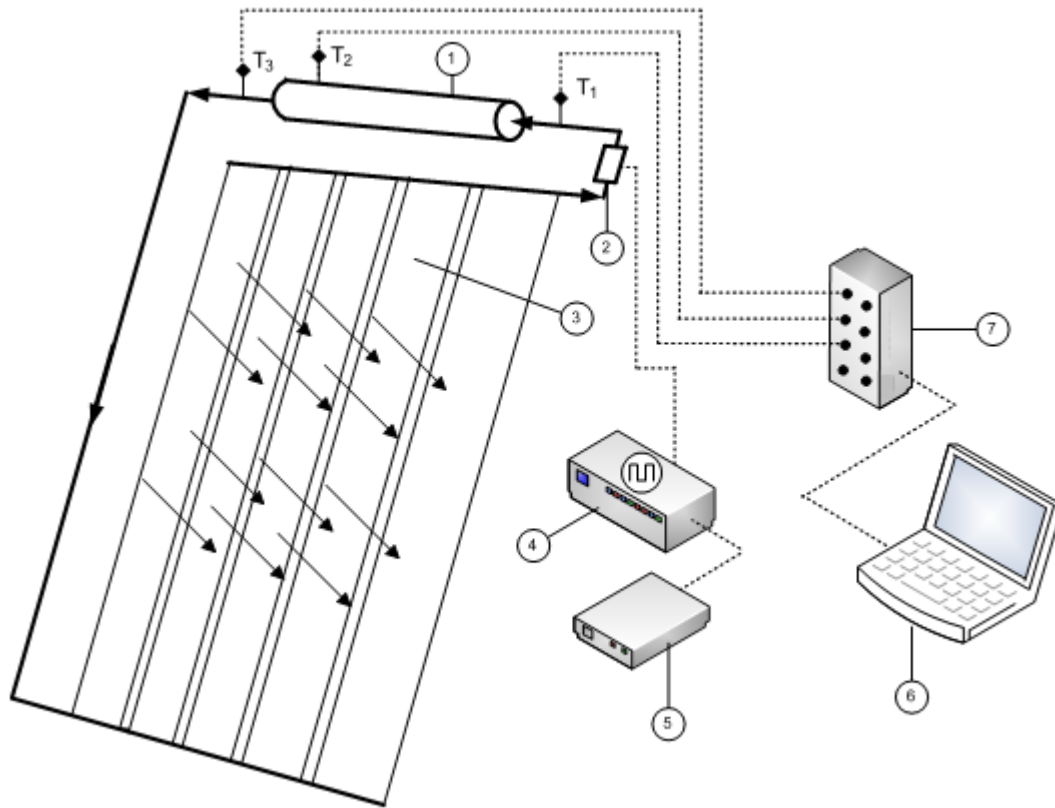
Figure 6.2g Schematic of the experimental Setup.

1-Water Jacket; 2-Flow sensor; 3-Flat plate collector; 4-Oscilloscope; 5-Power supply; 6-Laptop; 7-Data logger; T1, T2, T3 are thermocouples connected to the data logger that measured temperatures at the inlet, outlet and in the water jacket.

Three sets of experiments were conducted and the results obtained were averaged, even though the readings were pretty close in all the sets. Each test lasted for about 130 minutes and during the first 60 minutes a heat flux of 500 W/m^2 was applied and then this value was increased up to 700 W/m^2. The level of the heat flux was measured before the

commencement of the experiments using a pyranometer. The collector panels were filled up with water from the mains having a temperature of 15° C. The temperature values were recorded using a data logger illustrated below in Figure 6.2h.
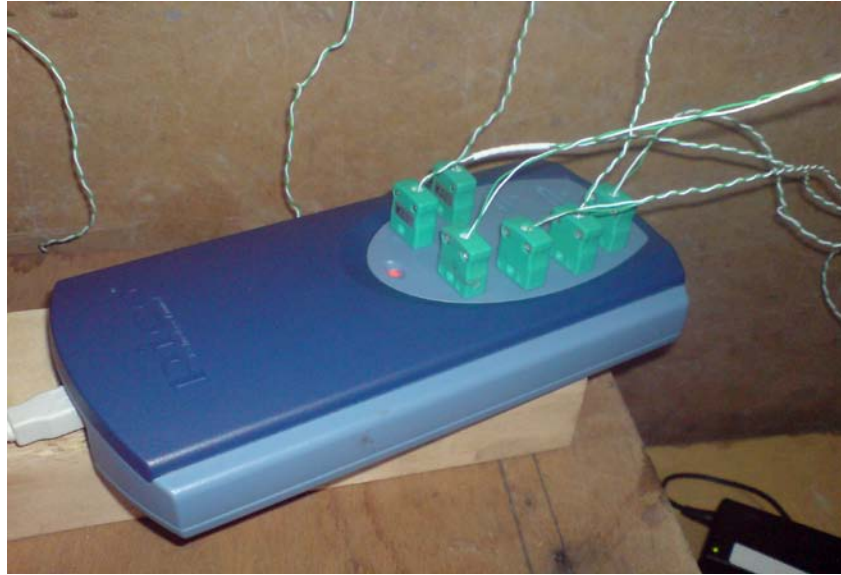
Figure 6.2h Data logger with thermocouples attached.

6.2.1 Results

The results obtained using the experimental setup described in the previous section were tabulated (see Appendix C1 and C2) and graphs plotted relating temperature variations versus time.

An error analysis was performed in all the experimental results, combining the 'least squares method' and the 'standard error of estimate' listed in the Appendix C12, where a measure of the scatter of the regression curve is supplied by an estimated value of a temperature T over time t.

Graph 6.2.1a illustrates the variation of the average temperatures of the water at the outlet of the conventional (Tout) and the porous medium ($Tout_p$) solar panels. It can be observed that the porous medium collector provided the higher water temperature in the outlet. As mentioned before, the sudden rise on both waveforms (Graph 6.2.1a) at the 60 minutes margin was due to the increase of the heat flux as intended to increase the radiation e and the response of the system to irradiation changes as it occurs in reality with the sun.
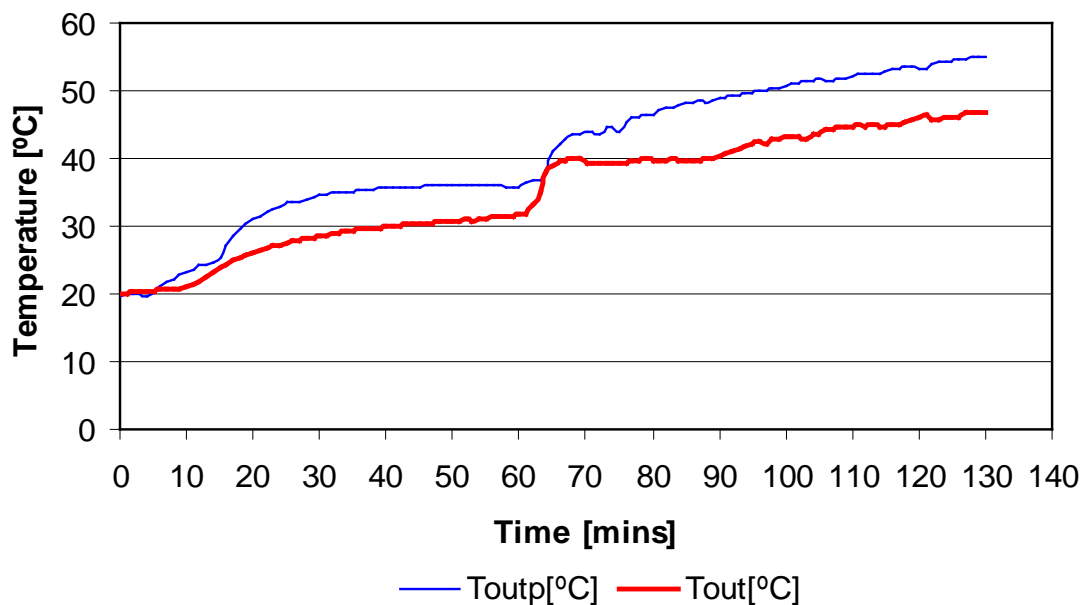
Graph 6.2.1a Temperature of the water in the outlet of solar panels as a function of time.

The temperature recorded at steady state, at the outlet of the panel with mesh insertion was 55.04 ^{o}C and for the conventional was 46.78 ^{o}C, resulting a remarkable difference in temperature of 8.26 ^{o}C. The averaged values recorded in this part of the experiment are listed in the Appendix C1. An error analysis using the 'standard error of estimate' method was applied to the experimental results that showed an error of ± 0.49

^{o}C on the recorded temperatures, well within the thermocouples calibration range of ($\pm$ 0.6 ^{o}C).

Graph 6.2.1b illustrates the temperature difference of the water stored inside the water jackets of the porous medium (T w tank $_p$) and the conventional one (T w tank). The averaged values recorded in this part of the experiment are listed in the Appendix C2. The temperature recorded when the system reached steady state, at the panel with the mesh insertion was 43.68 ^{o}C and at the conventional one was 37.15 ^{o}C, resulting a temperature difference of 6.53 ^{o}C. The error analysis performed upon the recorded temperatures, showed an error of $\pm$ 0.47 ^{o}C. It was concluded that the mass flow rate in the panel with the mesh insertion needed to be investigated in relation to the conventional panel in order to justify the temperature difference in the corresponding water jackets and at the collector's outlet.
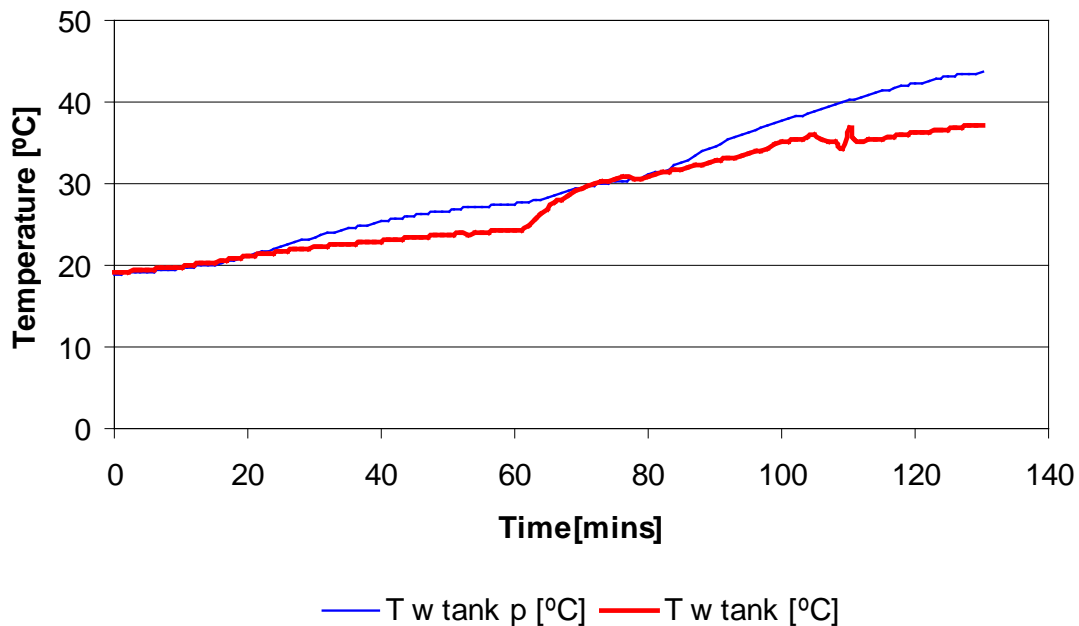
Graph 6.2.1b Temperature versus time in the water jackets.

Questions rose concerning the use of the mass flow sensor since it was observed that a considerable amount of heat dissipated across it, due to its construction material (plastic). There was also a suspicion about how accurate the flow rate measurements were, as the square wave showed on the oscilloscope, signifying there was water flowing, did not stay constant but kept flashing, even when the systems temperatures reached steady state.

6.3 Further Experimental Work

Following the observation made in the first set of experiments a few alterations took place at the experimental test rig in order to obtain more accurate results. The flow sensors were removed and replaced by copper pipes in both collectors. This would enable a better heat transfer as the plastic sensor prevented it in the first place. The manifolds were also removed and replaced by copper pipes joint together with compression fittings as shown in Figure 6.3a.

Figure 6.3a Manifold with thermocouples attached formed with compression fittings.

This would make experiments more flexible as the outlet temperature of every finned tube of the collectors could now be recorded using K-type thermocouples sealed inside the compression fittings, whereas before only the output temperature of each collector could be recorded.

The water jackets were insulated in order to have more accurate readings of the temperature rise in both collectors. The changes performed at the system can be seen in Figure 6.3b showing the new assembled manifold and the insulated water jackets.

Figure 6.3b Collector with thermocouples attached and insulated water jackets.

The downside of using compression fittings was that it would increase the hydraulic resistance in both collectors but there was not any other alternative in order to measure more accurately the temperatures of each finned tube. The compression fittings could possibly absorb part of the heat transferred to both systems but since there were positioned in both collectors, was not a case of affecting the performance of just one of the systems.

In Figure 6.3c a view of the whole experimental setup is illustrated, showing the simultaneous recording of data using two data loggers, a laptop and fourteen thermocouples, seven in each of the two collectors.
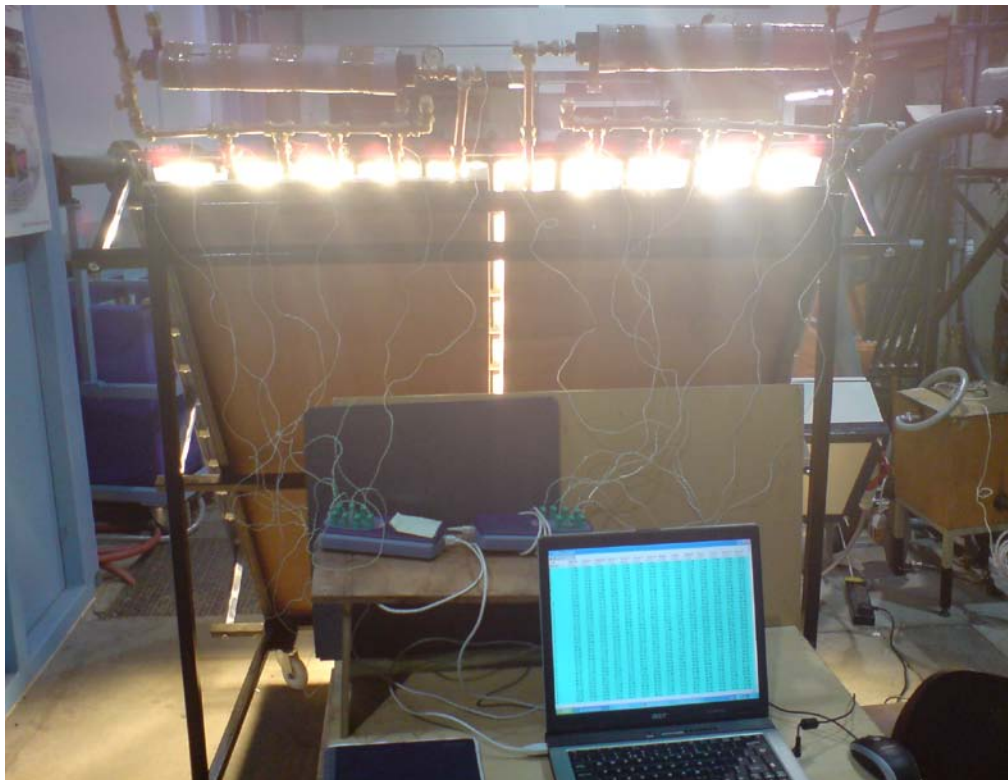
Figure 6.3c Complete experimental test rig.

The schematic diagram of the new experimental configuration and the devices for measuring and recording data is shown below in Figure6.3d.
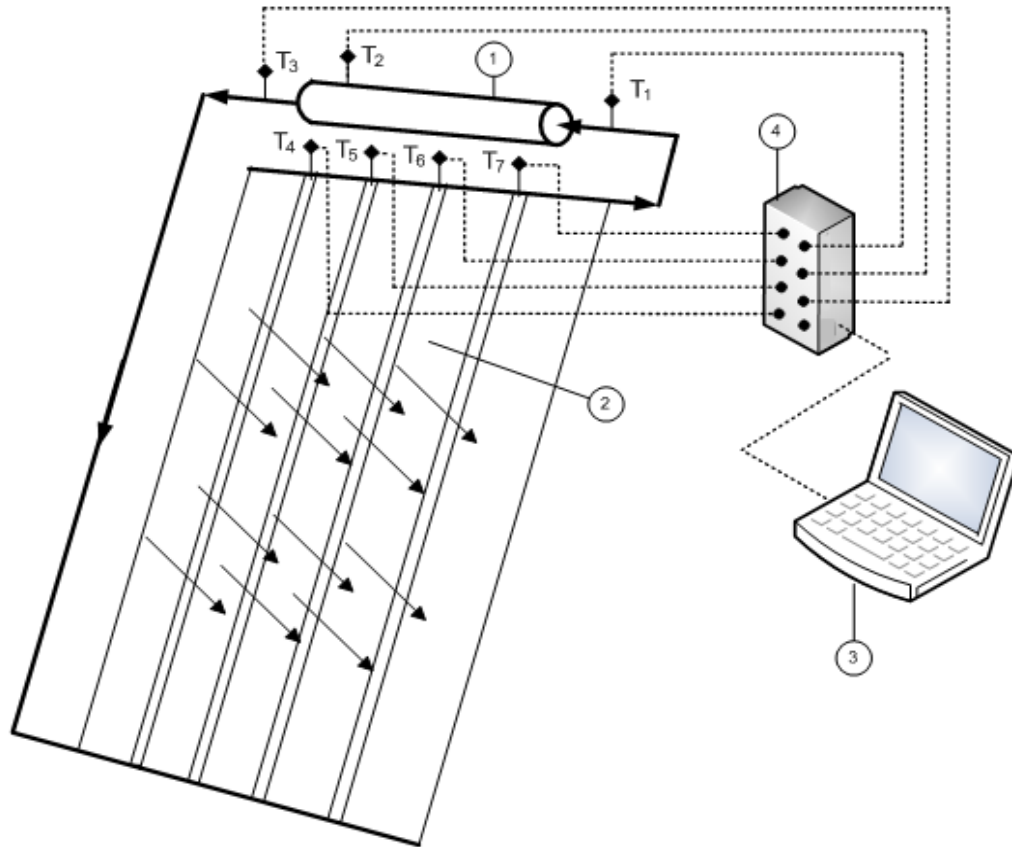
Figure 6.3d Schematic of the experimental Setup.

1-Water Jacket; 2-Flat plate collector; 3-Laptop; 4-Data logger;

T1, T3, T2, are thermocouples to measure temperatures at the inlet, outlet and in the water jacket respectively. T4 to T7 measured temperatures at the exit of each finned pipe. All thermocouples were connected to a data logger and the recorded temperatures were monitored via a laptop.

6.3.1 Results

The results obtained after modifications were carried out in this experimental setup, are listed in the Appendix C3, C4 and C5. Graphs were plotted to illustrate temperature variations versus time. In this set of experiments, the heat flux varied between 390 W/m^2 and 750 W/m^2. The heat flux started of at 390 W/m^2 for half an hour then changed to 490 W/m^2 for another half an hour. It was then raised to 610 W/m^2 for twenty minutes and further twenty minutes of 750 W/m^2.

The gradual increase of the heat flux was simply employed to create effects similar to the increase of the solar radiation as the sun rises higher during the day and more solar radiation strikes the earth. The Halogen bulbs were then switched off in order
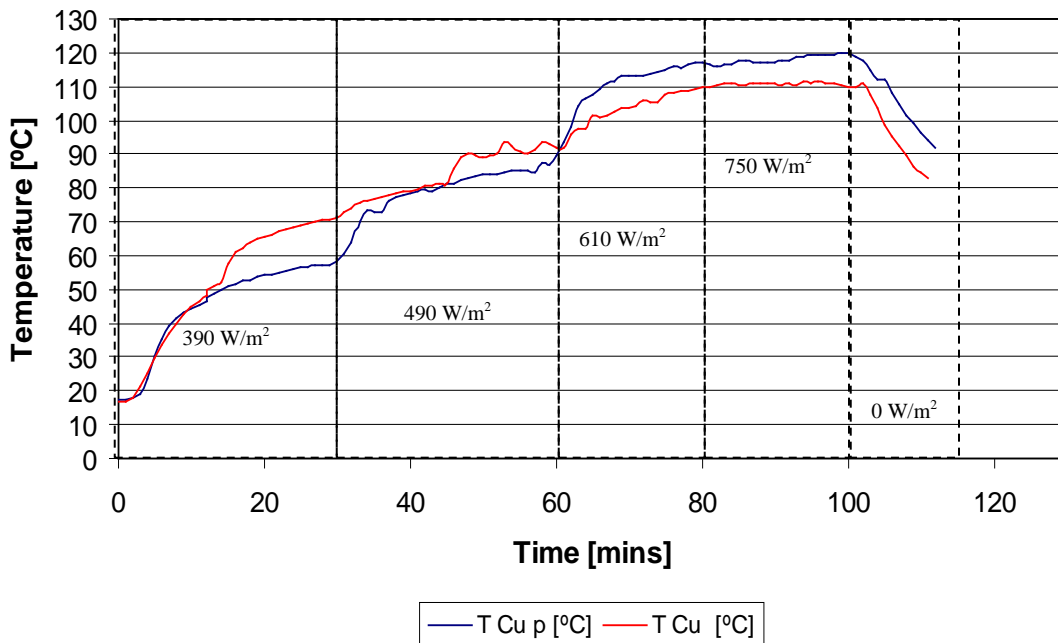
Graph 6.3.1a Temperature versus time at the outlet of the copper finned pipes.

to observe the response in each of the collectors under no heat flux conditions i.e. when a cloud blocks the sun's rays. Graph 6.3.1a above shows the variation of the average temperatures of the water at the outlet of the finned copper pipes in each of the two collectors under investigation.

It can be seen that up until the heat flux increased to 610 W/m^2 the temperature in the pipe with the metallic mesh is lower compared to the convectional collector due to the presence of the metallic mesh that absorb an amount of the heat flux provided.

In reality though a heat flux of 600W/m^2 and above appears from the early hours of the day [1] and can increase the collector's temperature really fast as seen on Graph 6.3.1a where the temperature rises approximately 25 ^{o}C in a space of 20 minutes.

The heat transfer process at the start of the experiment is slower in the pipes with metallic mesh since they attract part of the heat. The heat is then past to the liquid from the aluminium mesh and the water temperature increases above of the conventional finned copper pipes settling to a temperature difference of 10 ^{o}C.

As mentioned before an error analysis using the 'standard error of estimate' method was applied to the experimental results that showed an error of ±0.51 ^{o}C on the recorded temperatures, well within the thermocouples calibration range of (±0.6 ^{o}C).

At discharge when there is no heat flux, it can be seen that the copper pipes with porous medium can hold up more heat compared to the conventional and hence the higher temperature.

Graph 6.3.1b below shows the variation of the average temperatures of the water at the outlet of the finned aluminium pipes in each of the two collectors. The temperature difference in this case is also noticeable, about 6.5 $^{\circ}$C higher, 80 minutes into the experiment, at the porous medium finned aluminium pipe (T Al$_p$) compared to the conventional (T Al).

The error analysis performed upon the recorded temperatures, showed an error of ±0.52 $^{\circ}$C. The water temperature increased slower using porous medium inside the aluminium finned pipes, as part of the heat is attracted by the aluminium mesh at the commencement of the experiment. At discharge when there is no heat flux, can be observed that the aluminium pipes with porous medium can hold up more heat compared to the conventional and hence provide a higher temperature.
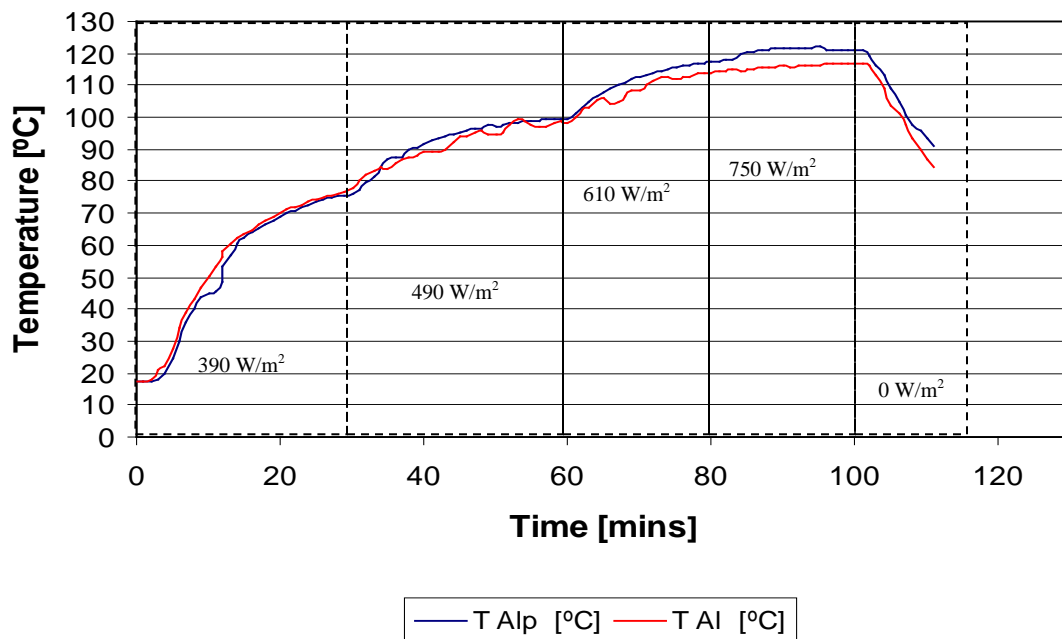
Graph 6.3.1b Temperature versus time at the outlet of the aluminium finned pipes.

Overall and since the aluminium fins withhold more heat due its thicker construction, under no heat flux conditions give a higher temperature to the liquid compared to the copper fins.

Graph 6.3.1c shows the temperature difference between the water stored inside the water jackets of the metallic mesh (T tank $_p$) and the conventional (T tank) solar panels. The temperature recorded when the system reached steady state, at the panel with the metallic mesh was about 50 ^{o}C and for the conventional one was 43 ^{o}C resulting to a temperature difference of 7 ^{o}C. The temperature in the porous medium tank increased above the convectional, 65 minutes into the experiment due to the presence of the metal mesh that withdrew some of the generated heat. The error analysis on the experimental results showed a $\pm$ 0.54 ^{o}C error on the recorded temperatures. At zero heat flux, the temperature inside the water tank with mesh remains higher for a few minutes, keeping the temperature about 6.5 ^{o}C higher compared to the conventional tank.
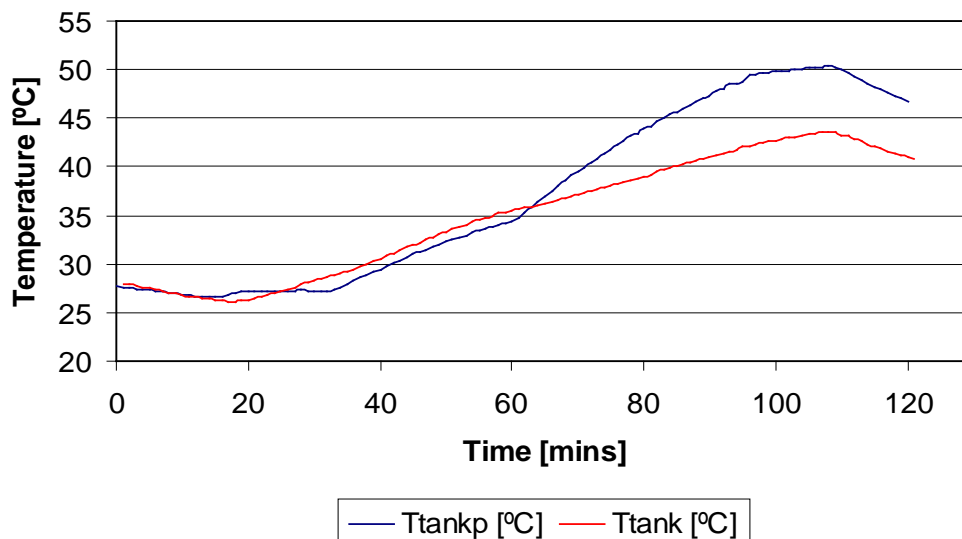
Graph 6.3.1c Temperature versus time in the water jackets.

The results in this experimental setup showed that the mesh inserted collector provided a higher water temperature compared to the conventional collector. It was then decided to convert the experimental test rig into a more practical system much similar to those used in the domestic sector.

6.4 Final Experimental Setup

Subsequently to the results obtained from the previous set of experiments it was necessary to transform the experimental test rig in order to acquire further water and collector's surface temperatures using a different experimental setup. The major change was to replace the water jackets by plastic water tanks, having a capacity of 15 litres. The new acquired plastic water tanks were drilled on either side along its length and a copper pipe was inserted. This can be seen below in Figure 6.4a.
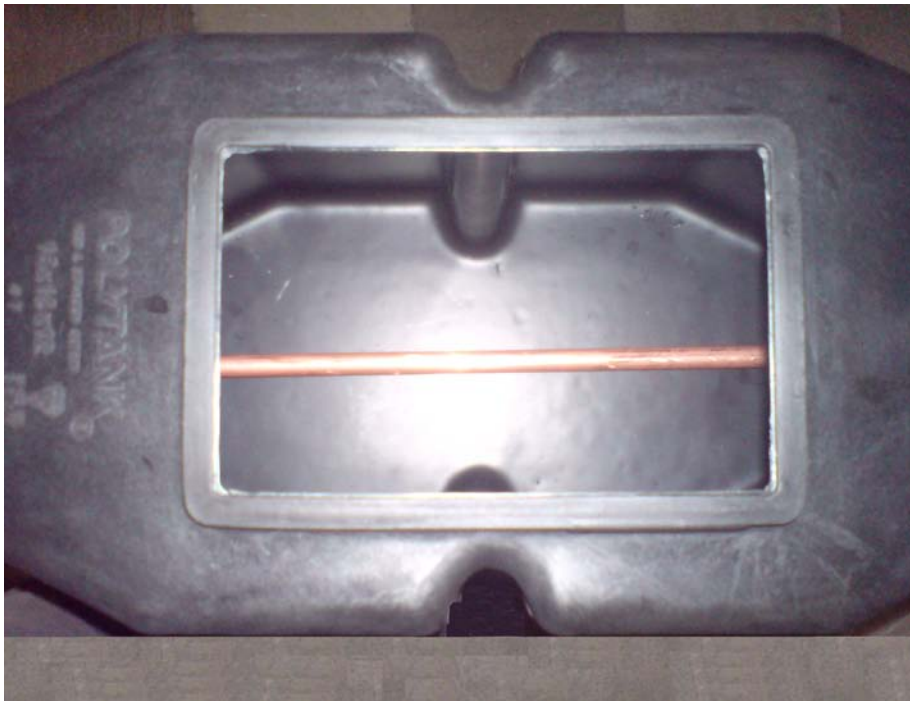
Figure 6.4a Top side view of water tank.

The pipe was positioned to act as a heat exchanger between the hot water flowing inside the copper pipe and the cold water stored inside the water tank. A metal extension was built at the top part of the metal frame and a wooden platform was attached to it in order to accommodate the water tanks. Thermocouples attached permanently on the surface of the collectors would measure and record its temperature accurately and instantaneously. The top manifolds were linked to the inlet of the water tank and from its outlet was directed to the bottom manifold of the panel as shown below in Figure 6.4b. The flow rate of the fluid in the panels was also needed to be determined since it would give more information concerning the behaviour of the fluid flow in each of the collectors. To reduce the overall heat losses, the water tanks and the copper pipes at its inlet were insulated using fibreglass 2cm thick enclosed in plastic cases shown in Figure 6.4c.

Figure 6.4b Water tanks connected to the collectors.
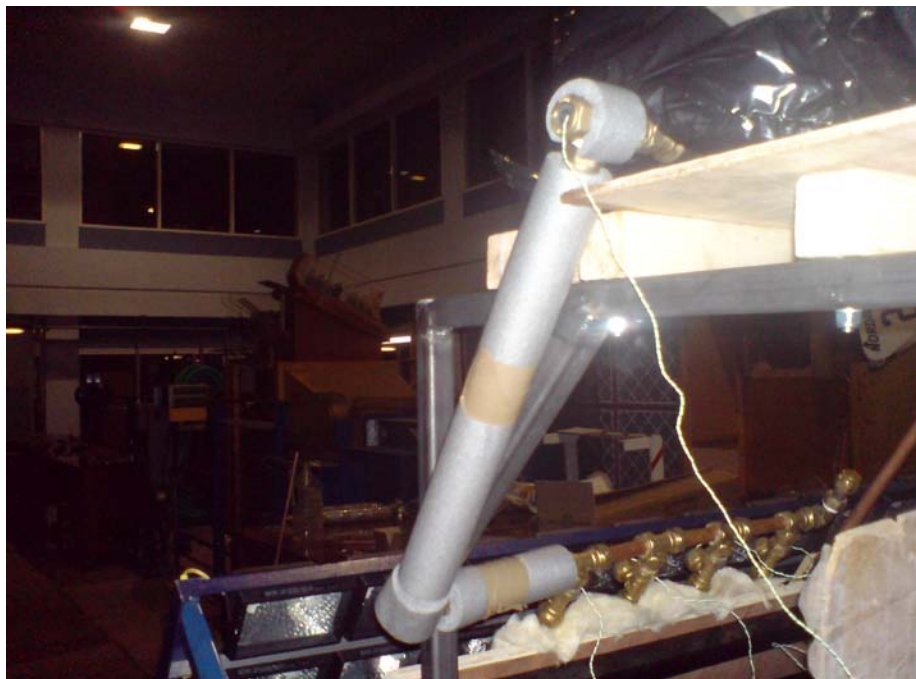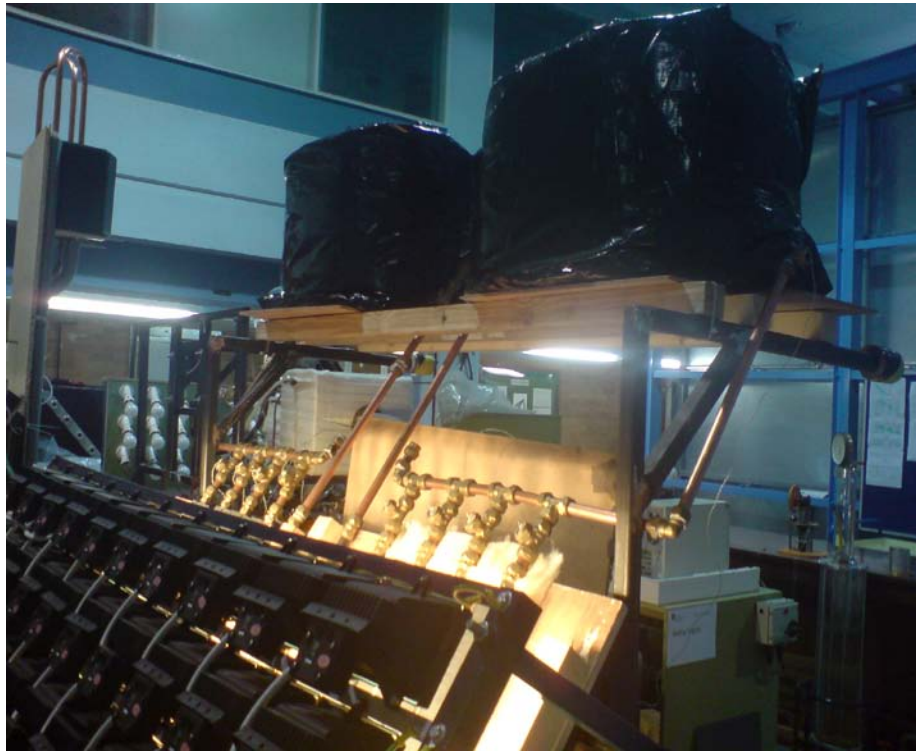
Figure 6.4c Insulated water tanks and copper pipes.

The final experimental setup's schematic diagram is presented in Figure 6.4d.
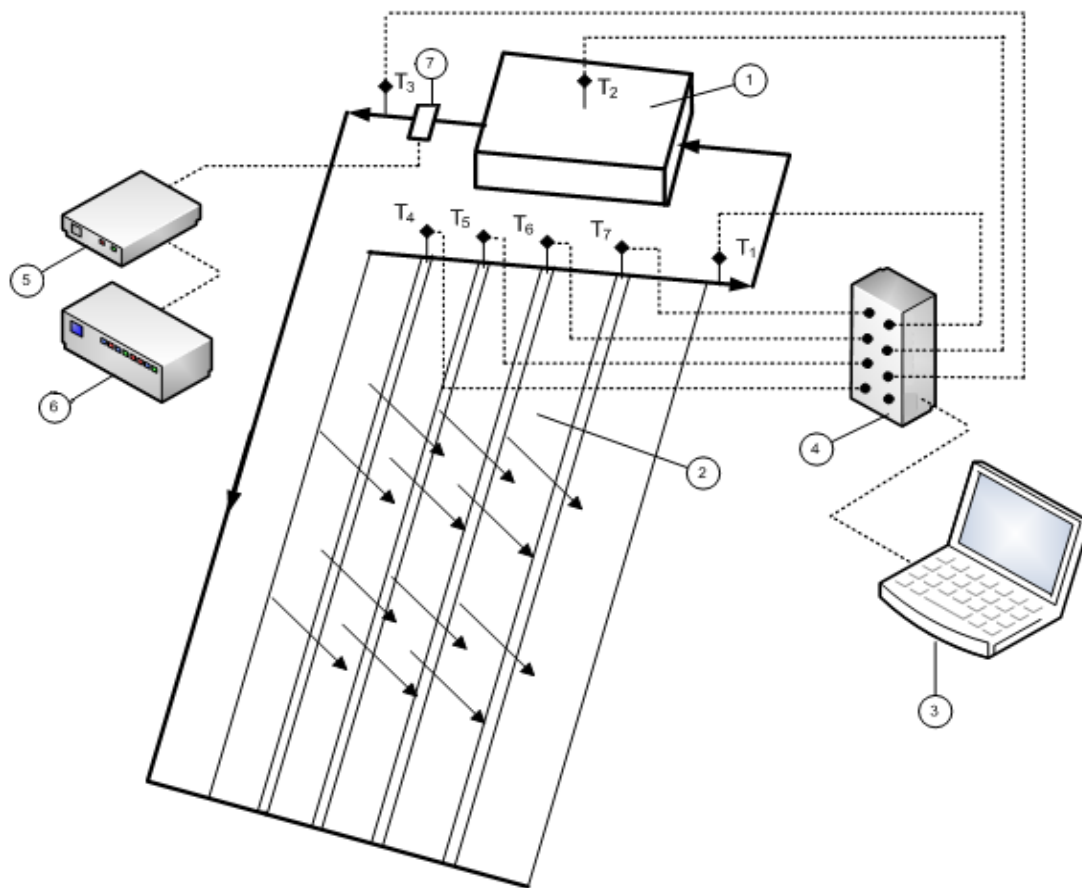
Figure 6.4d Schematic of the experimental setup.

1-Water Tank; 2-Flat plate collector; 3-Laptop; 4-Data logger; 5-Power supply; 6-Frequency meter; 7-Flow sensor /Pressure transducer.

T1, T2, T3, are thermocouples that measure the temperatures at the inlet, in the water tank and at the outlet respectively. T4 to T7 measure the temperatures at the exit of each finned pipe. All thermocouples were connected to a data logger and the temperatures were monitored via a laptop.

6.4.1 Pressure measurements

The pressure in both collectors was measured when the fluid was at rest and also in motion until it reached steady state. A pressure transducer manufactured in Leicester, U.K. by DRUCK, model PTX 1400 was connected at the top part of the collector as it is shown below in Figure 6.4e.

Figure 6.4e Pressure transducer.

The pressure transducer was connected to a power supply being set to 18 V and 0.4 mA. An 817 Ω resistor was connected in series with the transducer in order to measure the voltage drop across it. This would relate the recorded voltage drop to pressure, using an accurate multi-metre (FLUKE). The transducer was calibrated and an

initial voltage of 3.30 V represented the pressure inside the system at rest before the experiment started. From the manufacturer's specifications and by using the resistor of 817 Ω it was calculated that an increase of 0.523 V represented 1bar of pressure in the system. As the experiment progressed instant recording of pressure was visible till steady state was reached. The whole setup is illustrated in Figure 6.4f.
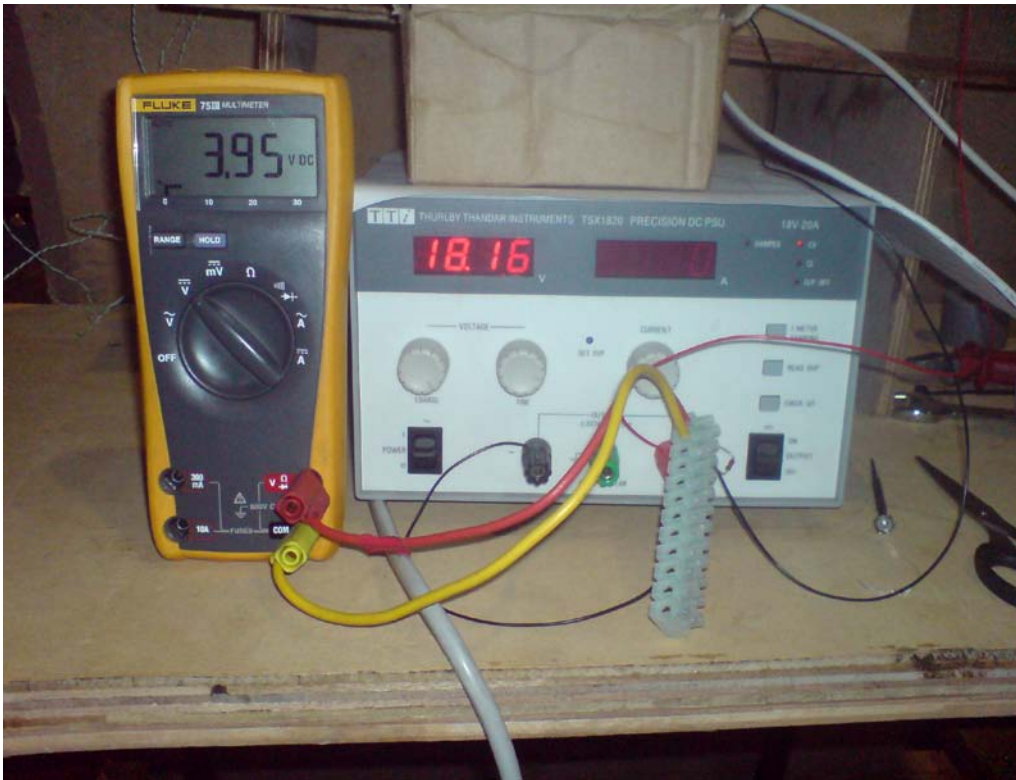
Figure 6.4f Pressure measurements experimental setup.

At steady state in the conventional collector, a voltage of 3.8 V was recorded that represented a pressure of 0.95 of a bar (gauge pressure) above the atmospheric pressure, that corresponds to a temperature of 119 ^{o}C. On the other hand a voltage of 3.96V in the collector with the metal mesh was recorded which represented a pressure of 1.26 bar

(gauge pressure) above the atmospheric pressure, that corresponds to a temperature of 125 ^{o}C. This justified the higher temperatures occurred in the collector having porous medium as higher pressure results to higher temperature in a closed system.

6.4.2 Mass flow rate measurements

The mass flow rate in both systems was determined by incorporating a low-flow positive displacement flow meter as it is illustrated below in Figure 6.4g. This had been proven to be a reliable and highly accurate volumetric method of measuring flow, as it has a high accuracy over a wide range of viscosities and flow rates. This flow sensor repeatedly entrapped the fluid to measure its flow. That is accomplished using rotating parts that form moving seals between each other and the flow meter body. Rotation can be sensed mechanically or by detecting the movement of a rotating part. When more fluid is flowing, the rotating parts turn relatively faster. The electronic transmitter reads the

Figure 6.4g Mass Flow meter.

signal generated by the rotation to determine the flow of the fluid. The whole process of entrapment and release of the fluid from the sensor is illustrated below in Figure 6.4h.
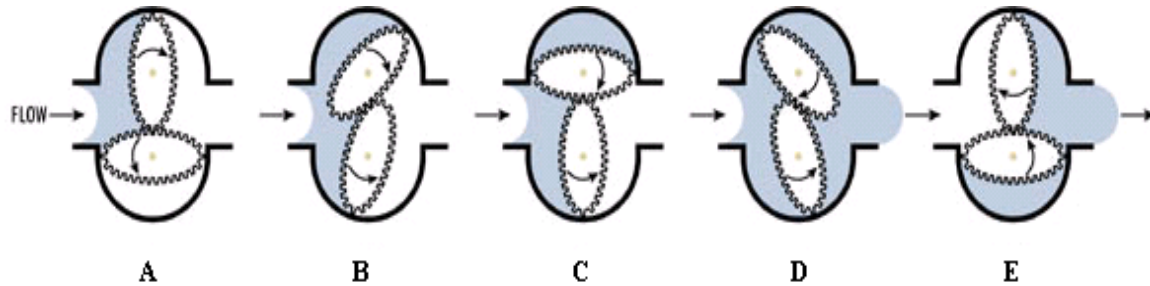
Figure 6.4h Mass Flow meter operating steps.

Prior to the installation of the flow meter to the system it was calibrated by connecting it to the water mains and via a measuring tube, a power supply and a digital frequency meter as shown in Figure 6.4i. The mass flow rate was measured for various frequencies.
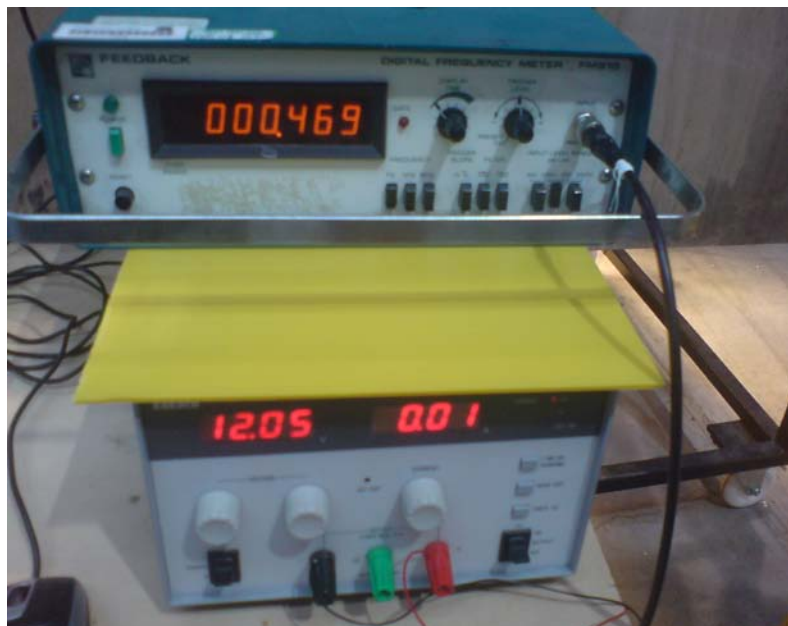
Figure 6.4i Power supply and digital frequency meter.

The data collected during the calibration process was plotted, as illustrated below in Graph 6.4a.

$$y = 1.4812x \qquad R^2 = 0.9983$$
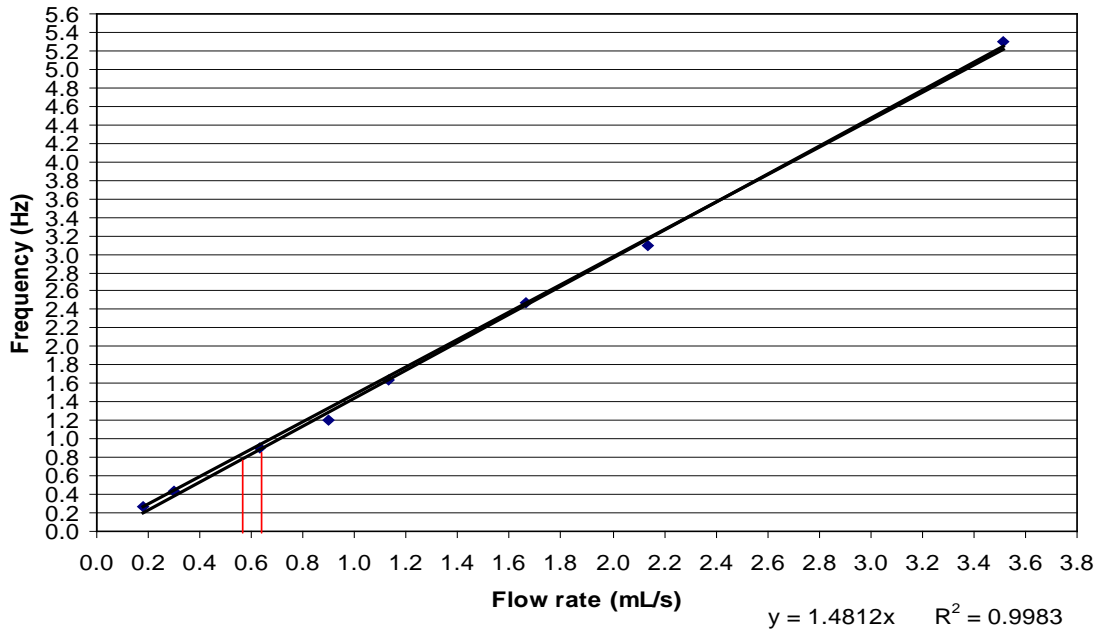
Graph 6.4a Frequency vs. flow rate.

After calibration took place, the sensor was connected to the system as shown in Figure 6.4a and experiments commenced. It was important to obtain an accurate mass flow rate since it would prove, into certain extend, that could affect the output temperature of both collectors.

The two red lines in Graph 6.4a illustrate the two different flow rates, for a heat flux of 905 W/m^2. For the convectional collector was 0.62ml/sec and for the one with the metal mesh was 0.58 ml/sec.

The difference between the two flow rates was not significant. It was calculated that the flow rate of 0.58 ml/sec would only increase the temperature of the conventional collector by 1.7 $^{\circ}$C.

6.4.3 Surface temperature measurements

A series of K-type thermocouples were attached onto the surface of each of the panels so more accurate and instantaneous temperature readings could be recorded. The thermocouples were placed as pairs in each of the finned pipes as shown in Figure 6.4j below.

Figure 6.4j Surface temperature measurements setup.

All thermocouples were positioned half way along the length of each of the panels. One thermocouple was placed on the fin to measure the fin temperature and the second at the joint between the pipe and the fin to measure the so called base temperature T_b important factor for further analysis of the system i.e. the heat transfer coefficient h.

6.4.4 Results

Measurements available in the Appendix C6 and C7 show that the surface temperature of the collector utilising porous medium was lower to the conventional collector proving that there is a better heat transfers. Two cases were examined for two different heat fluxes 610 W/m^2 and 1070 W/m^2 which covered the upper and lower limit of heat fluxes used in the experiments.
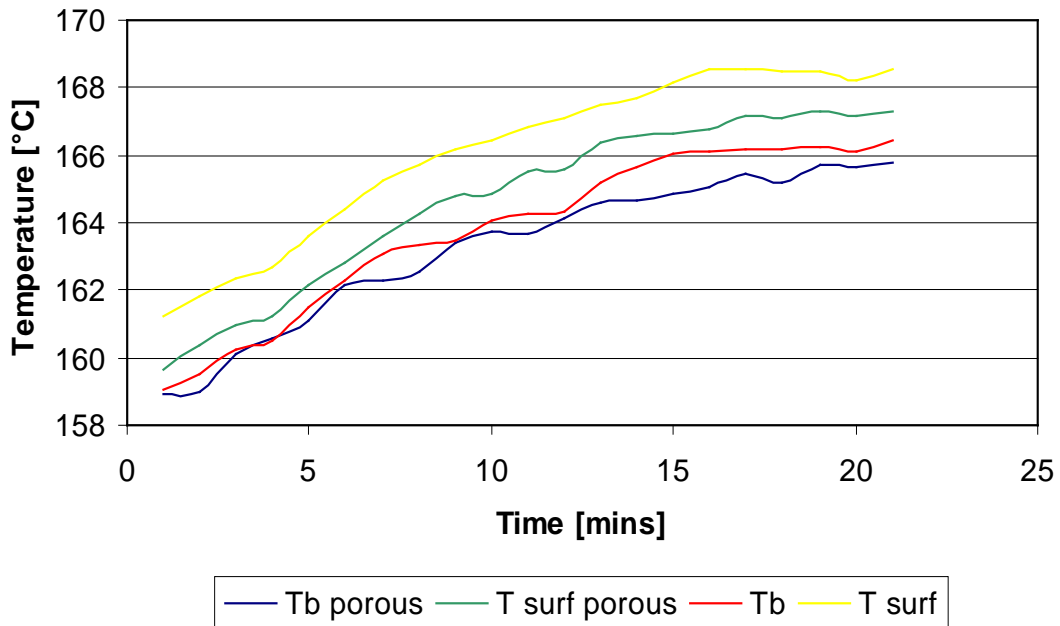
Graph 6.4.4a Temperature versus time at the surface of the collectors.

Graph 6.4.4a illustrates the variation of the surface and base (the point where fin is attached to the pipe) temperatures of the two collectors under investigation using a heat flux of 1070 W/m^2. The data displayed was recorded at the point where the temperatures reached a steady state. The error analysis on the experimental results showed a $\pm$ 0.34 ^{o}C error on the recorded surface temperatures. Tb and Tsurf porous are the base and surface temperatures respectively of the collector utilising porous medium. For the conventional collector Tb and Tsurf are the base and surface temperatures respectively.

The second case examined is shown on Graph 6.4.4b that demonstrates the same effect as in the previous case using a heat flux of 610 W/m^2. The error analysis performed upon the recorded temperatures, showed an error of $\pm$0.37 ^{o}C.
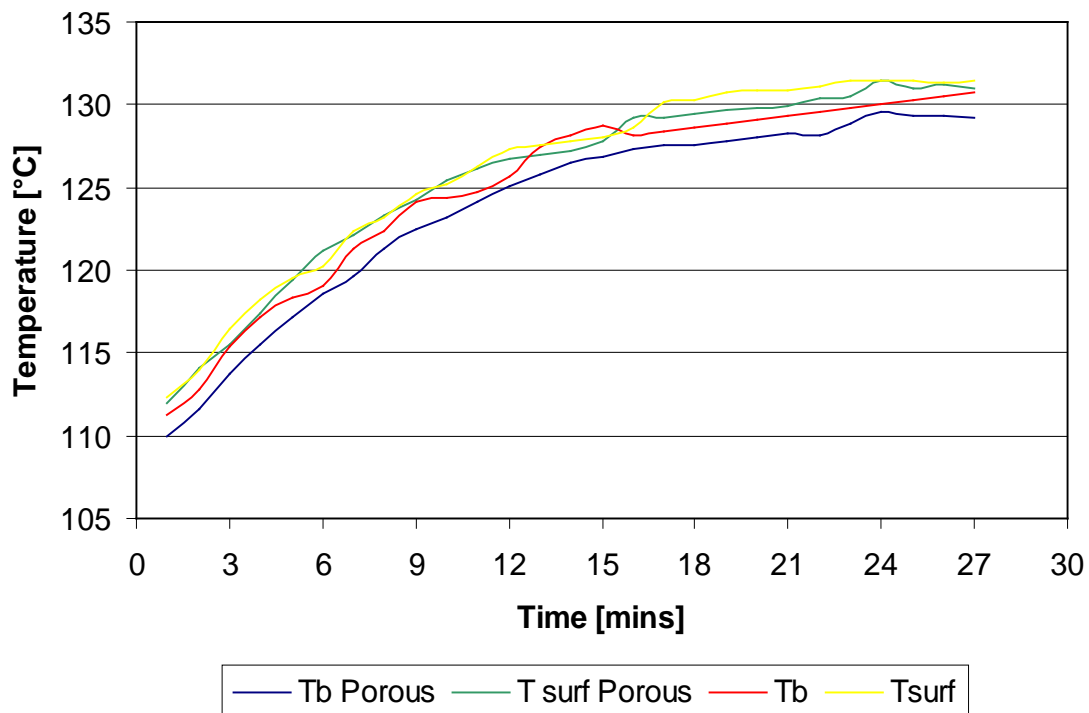
Graph 6.4.4b Temperature versus time at the surface of the collectors.

From the recorded data the local Rayleigh number for each case was calculated from:

$$Ra = \frac{g\beta\Delta T D^3}{v\alpha}$$
(6.4.1)

where g is the gravitational force, β is the thermal expansion coefficient, ΔT is the wall and ambient temperature, D is the diameter of the pipe, v the kinematic viscosity and α is the thermal diffusivity. Table 6.4.4a displays the obtained Ra number for both cases under investigation and for two different heat fluxes.

Heat Flux (W/ m²)	(Ra) Porous Case	(Ra) Conventional Case
1070	$3.4 \cdot 10^7$	$3.3 \cdot 10^7$
610	$1.2 \cdot 10^7$	$1.1 \cdot 10^7$

Table 6.4.4a Local Rayleigh number (R) of the examined cases.

The results showed that the convective forces are dominant in both geometries as they are well in the range of the free convection limits. A higher Ra number was obtained for the case with porous medium. The difference between the two was not great since for the characteristic length the diameter D of the pipe was used, which meant it was measured at a slice (locally) of the pipe but still it was higher.

The heat transfer coefficient was also obtained from the expression:

$$h = \frac{Q}{\left(T_b - T_{fref}\right)}$$
(6.4.2)

where Q is the heat flux in W/m², T_b is the temperature at the joint of the fin and pipe and T_{fref} is the fluid reference temperature in °C.

Table 6.4.4b displays the values obtained for heat transfer coefficient h in both cases under investigation and for two different heat fluxes. Results showed that there was a higher heat transfer coefficient in the collector with porous medium, supporting further the investigation so far.

Heat Flux (W/ m^2)	h Porous Case (W/m^2 C)	h Conventional Case (W/m^2 C)
1070	375	334
610	196	179

Table 6.4.4b Heat transfer coefficient (h) of the examined cases.

From the findings so far a relation could be made between the experimental results and the results obtained by the simulations. Hence the average Ra and Nu number for the porous cases could be obtained over a characteristic pipe length and then compared to the findings of Table 5.4b and the expressions (5.4.8) and (5.4.9). The average Ra number could be obtained from the expression (6.4.3).

$$Ra = \frac{C_p \rho^2 g \beta (\Delta T) L^3}{\kappa \mu} \qquad (6.4.3)$$

where C_p is the specific heat of the water, ρ is the density of the water, g is the gravitational force at (55° inclination), β is the thermal expansion coefficient, ΔT is the temperature difference between the outer pipe surface and the water temperature at the pipe wall, L is the characteristic length of the pipe, κ is the thermal conductivity and μ the dynamic viscosity.The average Ra number was obtained for the heat fluxes of 1070 W/m^2 and 610 W/m^2 as exploited on Chapter 5 in the simulation cases.

The data used to obtain the Rayleigh numbers is listed on Table 6.4.4c. The water properties were taken from charts for the average temperatures of 152°C and 121°C generated by 1070 W/m^2 and 610 W/m^2 respectively.

	1070 W/m^2	610 W/m^2
C_p (J/Kg ^{o}C)	4316	4246
ρ (Kg/m^3)	915	943
g (m/s^2)	5.62	5.62
β(1/^{o}C)	$1.03 \cdot 10^{-3}$	$0.88 \cdot 10^{-3}$
ΔT(^{o}C)	3.0	3.2
L(m)	0.25	0.25
κ(W/m^2 ^{o}C)	$0.682 \cdot 10^{-3}$	$0.683 \cdot 10^{-3}$
μ(Kg/m·sec)	$0.18 \cdot 10^{-3}$	$0.23 \cdot 10^{-3}$

Table 6.4.4c Data for the *Ra* number.

The average *Ra* numbers obtained for the heat flux of 1070 W/m^2 and 610 W/m^2 was **7.95·10^9** and **6.14 ·10^9** respectively, showing a good agreement to the simulations findings which were **8·10^9** and **6.2 ·10^9** for the heat flux of 1070 W/m^2 and 610 W/m^2 respectively. The average *Nu* numbers could be determined in relation to *Ra* numbers using the expressions (5.4.8) and (5.4.9) on Chapter 5:

$$Nu_{(1070)} = 0.013(Ra)^{0.285} \qquad (5.4.8)$$

$$Nu_{(610)} = 0.007(Ra)^{0.285} \qquad (5.4.9)$$

The resulting *Nu* numbers obtained was **8.61** and **4.32** for the heat flux of 1070 W/m^2 and 610 W/m^2 respectively showing a good agreement to the simulations results

which were **8.4** and **4.3**. The above findings show an agreement between the numerical studies conducted on Chapter 5 and the experimental in the current chapter.

This final experiment started having a heat flux of 490 W/m^2, changing approximately every forty seven minutes to 610 W/m^2 then rose to 750 W/m^2 and finally to 905 W/m^2. The halogen bulbs were then switched off in order to observe the response of both collectors under no heat flux conditions. The experiment terminated when the temperatures on both collectors decreased considerably.

Graph 6.4.4c shows the variation of the average temperatures of the water (Appendix C8) at the exit of the finned copper pipes in each of the two collectors under investigation. The error analysis performed upon the recorded temperatures, showed an error of ±0.46 $^{\text{o}}$C.
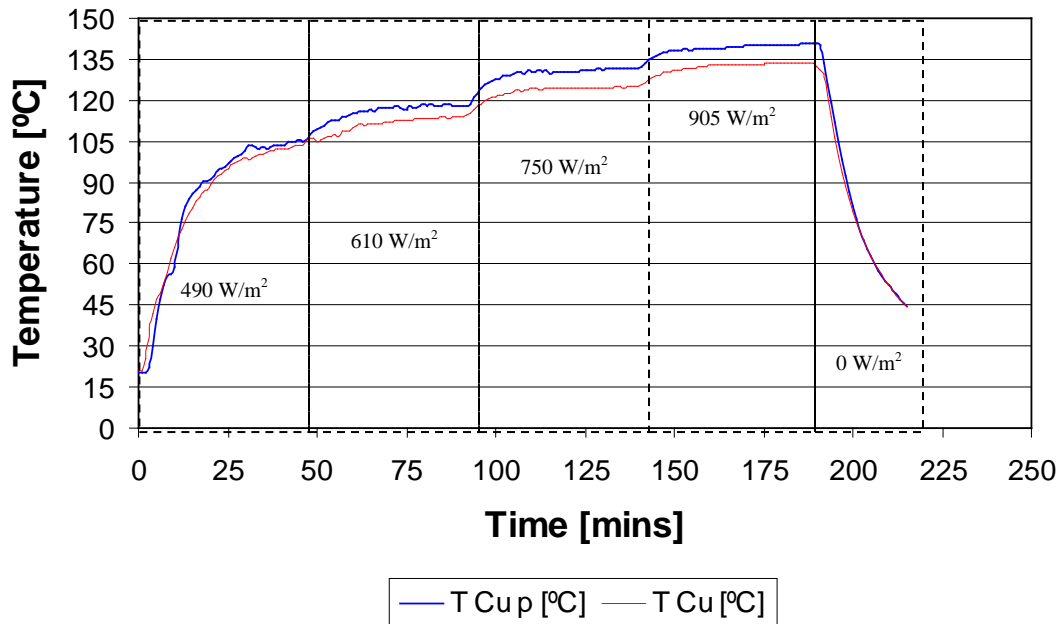
Graph 6.4.4c Temperature versus time at the exit of the copper finned pipes

A temperature of 7 $^{\circ}$C higher was attained for the porous medium copper finned pipes (T Cu$_p$) compared to the conventional (T Cu).For the first twenty minutes the water temperature builds up slower in the pipes with porous medium since much of the heat is drawn by the aluminium mesh at the start of the experiment. The heat is then past to liquid from the aluminium net and the water temperature increases above the conventional finned copper pipes.

At discharge when there is no heat flux, and for about twenty minutes, it can be seen that the copper pipes with porous medium can hold up more heat compared to the conventional until both system reach almost the same temperature the last fifteen minutes of the experiment. Graph 6.4.4d shows the variation of the average temperatures of the water at the outlet of the finned aluminium pipes in each of the two collectors. Data is listed in the Appendix C9.
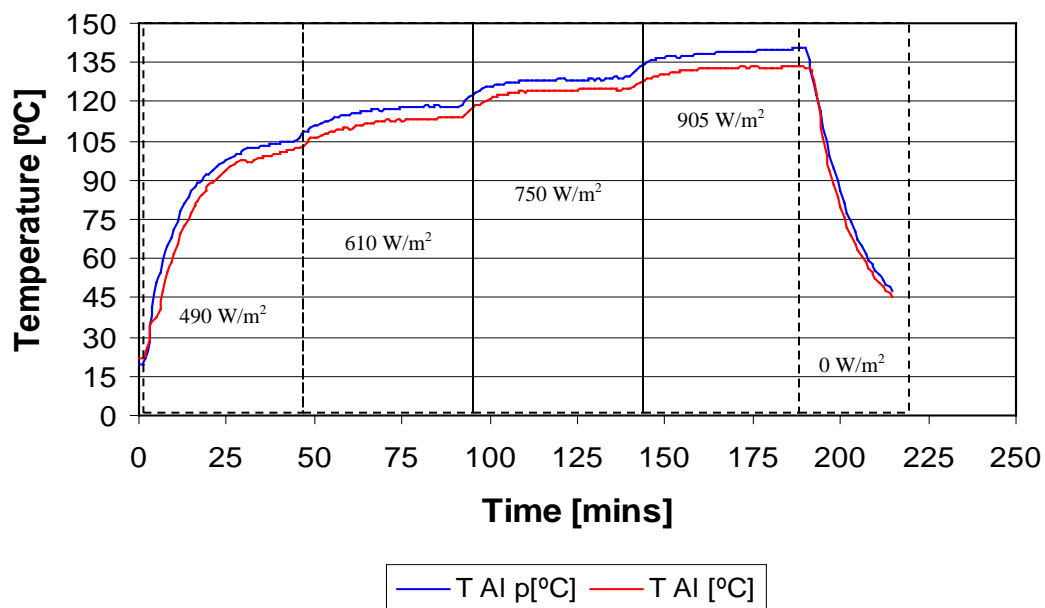
Graph 6.4.4d Temperature versus time at the outlet of the aluminium finned pipes.

A temperature of 7.5 ^{o}C higher was obtained for the porous medium aluminium finned pipes (T Al $_p$) compared to the conventional (T Al). The error analysis on the experimental results showed a ±0.44 ^{o}C error on the recorded temperatures. The temperature difference is also greater at lower heat fluxes as can be noticed on the graph.

Graph 6.4.4e shows the temperature of the water at the inlet of the water tanks of the porous medium (T input wt $_p$) and the conventional (T input wt) one. Data listed in the Appendix C10. The error analysis performed on the experimental results showed a ± 0.6 ^{o}C error on the recorded temperatures.
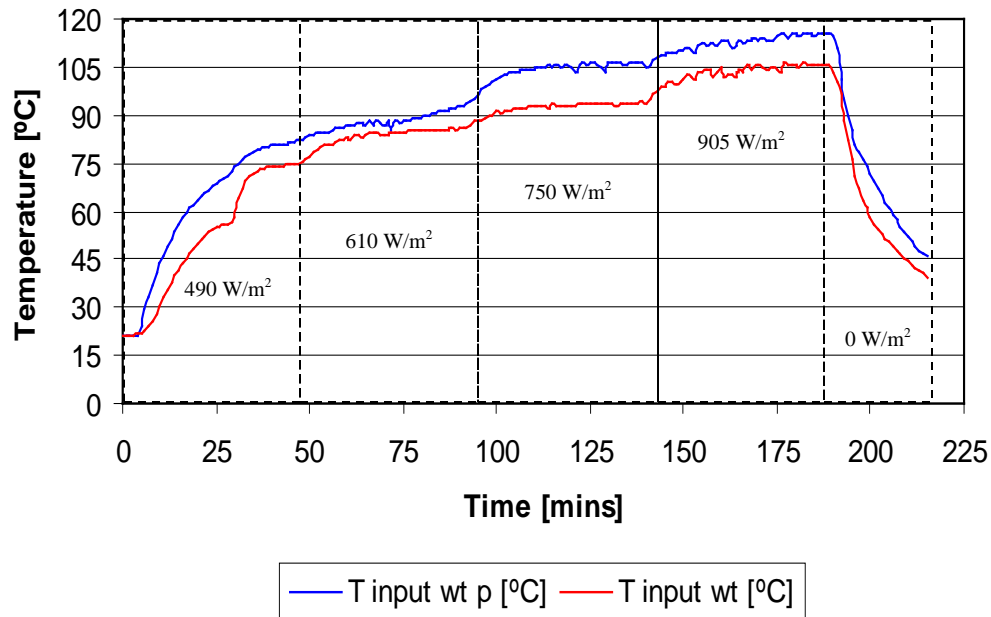
Graph 6.4.4e Temperature versus time at the inlet of the water tanks.

The pattern of the waveforms, showing once again a better performance of the collector that utilised the aluminium porous material.

The temperatures recorded on the water tank inlet in both of the collectors at the point shown below in Figure 6.4k.

As it can be seen that all the piping and compression fittings from the collector's outlet to the water tank's inlet was insulated in order to minimise heat loses.
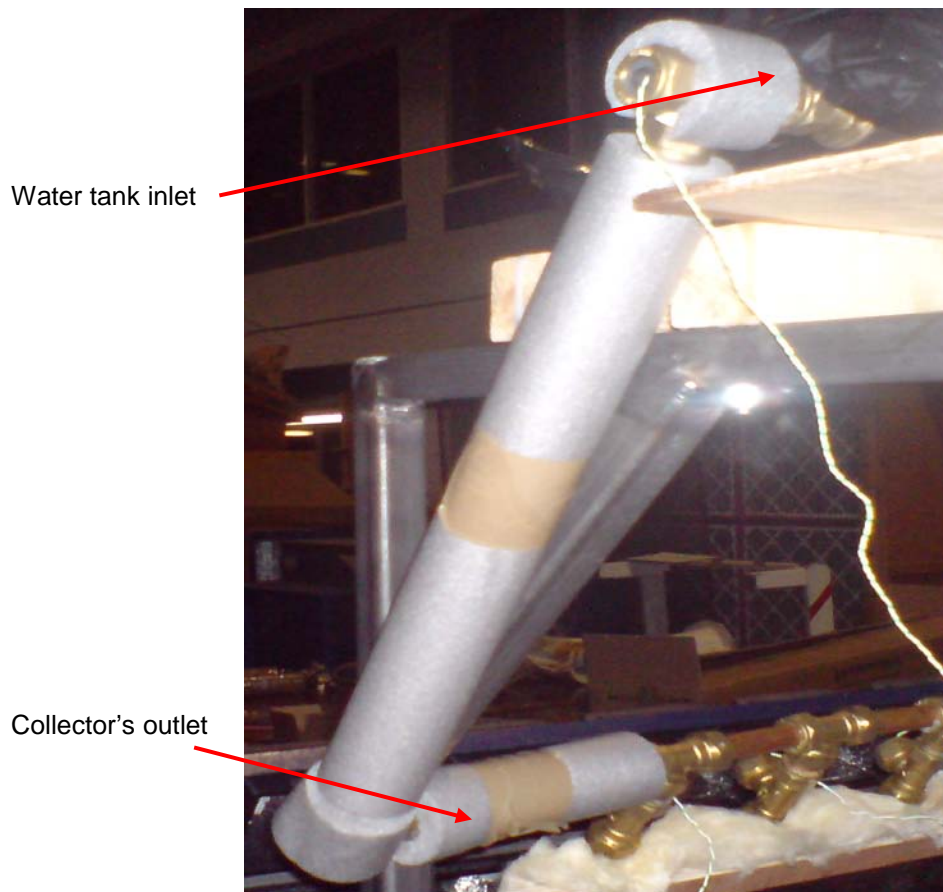
Figure 6.4k Temperature measurements at the inlet of water tank.

This experiment proved that there was a better heat transfer using porous medium as the temperature difference between the two collectors at the water tank inlet for two different heat fluxes i.e. 750 W/m^2 and 905 W/m^2 on average was 10.5 ^{o}C higher for the

collector utilised porous medium. There were also periods during the experiments that the temperature difference between the two graphs reached to 16 $^{\circ}$C as shown on Graph 6.4.4e.

Hence it was concluded that it was beneficial having porous inserted in the channels of the collector but also having in all the piping of the system. Probably it could be advantageous to utilise porous medium from the collector all the way to the domestic appliances since it could provide a better heat transfer. The pipes though need to be very well insulated. Graph 6.4.4f shows the temperature difference between the water inside the tank of the porous medium (T wt $_p$) and the conventional (T wt). Data is listed in the Appendix C11. The error analysis on the experimental results showed a ±0.44 $^{\circ}$C error on the recorded temperatures.
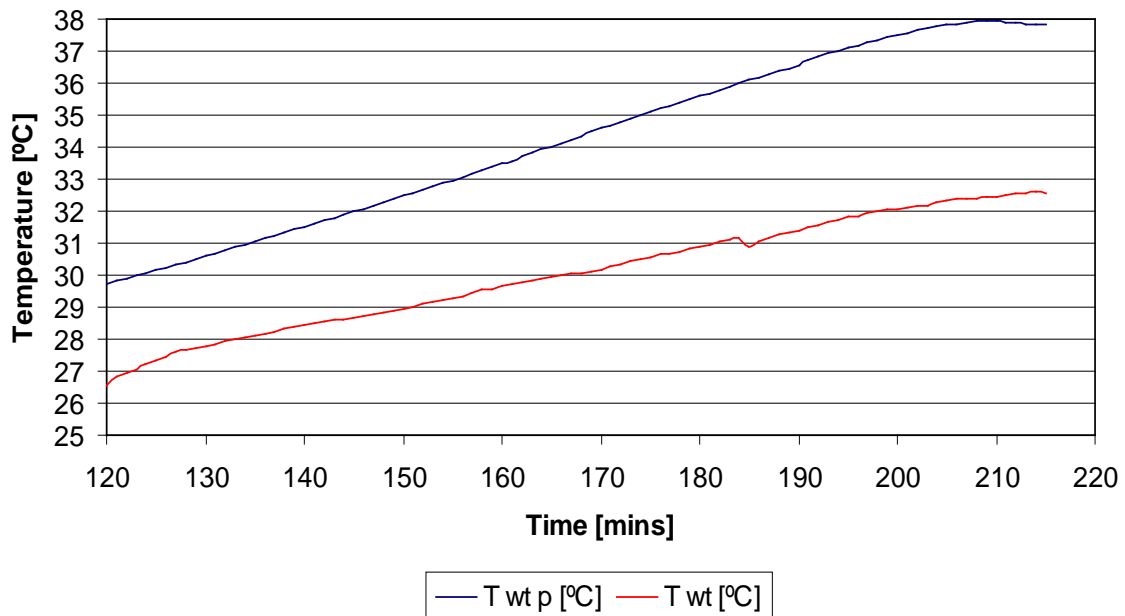
Graph 6.4.4f Temperature versus time inside the water tanks.

Both tanks were filled up with 8 litres of water in order to cool down the water flowing inside the collectors.

The temperatures recorded two hours into the experiment as it was when temperature started to increase inside the water tanks. The amount of the hot water flowing inside the collector heat exchanger needed more time to heat up the 8 litres of water stored in the tank compared to previous experiments where the amount of water stored in the water jackets was 1.5 litres.

As it can be observed in the Graph 6.4.4f at about 180 minutes of operation the temperature inside the water tank with the porous medium was about 36 ^{o}C and for the conventional 31 ^{o}C resulting to a temperature difference of 5 ^{o}C. From this point onwards and when there was no heat flux, could also be seen that the temperature inside the water tank with porous medium remains higher for a significant amount of time, maintaining a relatively constant temperature difference of about 5.5 ^{o}C higher compared to the conventional one.

6.5 Conclusions

On the whole, the experimental results showed that the metallic mesh inserted in the collector, provided a higher water temperature compared to the conventional collector and it is the presence of the aluminium mesh inside the channels that distributes heat more evenly. The error analysis performed in all the experimental data verified the accuracy of the findings.

It was apparent that using partially filled porous mesh in the pipes the heat transfer area increased. The roughness of the aluminium net created a thermal diffusion at the boundary layer that could make the collector more efficient. The experimental results are supporting the theoretical findings obtained during CFD simulations.

The average *Ra* and *Nu* numbers obtained for the heat flux of 1070 W/m^2 and 610 W/m^2 were higher in the collector that utilised the aluminium mesh, compared to the conventional and in both cases they showed a good agreement to the simulations findings, determined from the expressions (5.4.8) and (5.4.9) on Chapter 5.

It was then important to utilise a lumped parameters model that would assess the findings from the numerical and experimental work so far. This would enable a further theoretical study, using mathematical formulae. This is discussed and analysed in the following Chapter 7.

CHAPTER 7

Development of a Lumped Parameter Model for Estimation of Solar Collector Performance

A lumped parameter mathematical model is a useful instrument to be used for rapid determination of design dimensions and operational performance of solar collectors at the designing stage. Such a model which incorporates data from relevant CFD and experimental investigations can provide an acceptable accuracy in predictions and be used as an effective design tool. This chapter describes the developed of lumped parameter model and demonstrates its practical application.

7.1 Lumped parameter model for the calculation of the performance of a solar collector

The theoretical background and some equations relevant to the development of the lumped parameter model were presented earlier in Chapter 3. The energy conservation

equation is the governing equation in the lumped parameter model. Considering Figure 7.1a, the energy of the working fluid entering the pipe at a distance y, plus the useful gain q'_u of the tube and fin will be equal to energy gained at distance y+Δy:
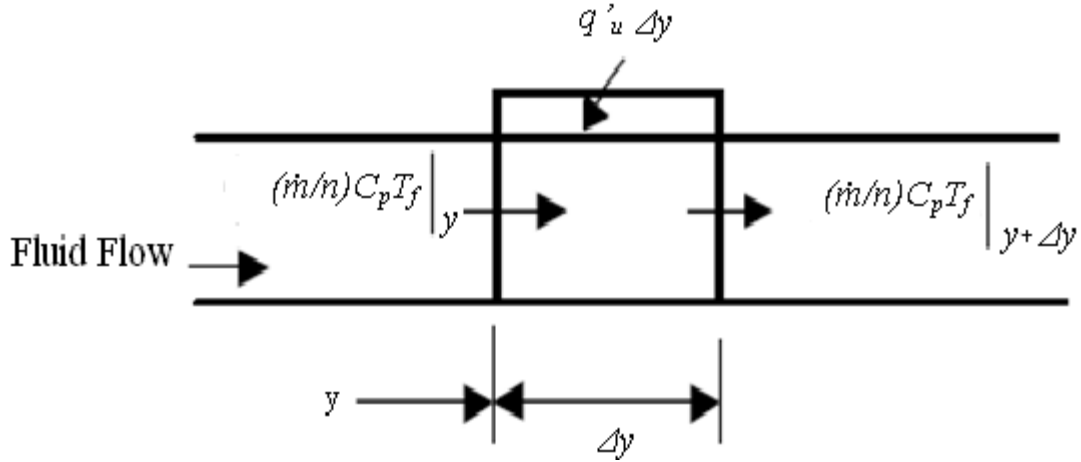
Figure 7.1a Energy balance on fluid element.

$$\left(\frac{\dot{m}}{n}\right)CpT_f\Big|_y + \Delta y q'_u = \left(\frac{\dot{m}}{n}\right)CpT_f\Big|_{y+\Delta y} \qquad (7.1.1)$$

or

$$\left(\frac{\dot{m}}{n}\right)CpT_f\Big|_y - \left(\frac{\dot{m}}{n}\right)CpT_f\Big|_{y+\Delta y} + \Delta y q'_u = 0 \qquad (7.1.2)$$

If n is taken as a common factor then equation (7.1.2) can be re-arranged as

$$\not{n}\left(\frac{\dot{m}}{\not{n}}\right)CpT_f\Big|_y - \not{n}\left(\frac{\dot{m}}{\not{n}}\right)CpT_f\Big|_{y+\Delta y} + n\Delta y q'_u = 0 \qquad (7.1.3)$$

or

$$\dot{m}CpT_f\Big|_y - \dot{m}CpT_f\Big|_{y+\Delta y} + n\Delta y q'_u = 0 \qquad (7.1.4)$$

174

Dividing all elements of the equation (7.1.4) by Δy the following equation is obtained:

$$\left(\frac{\dot{m}}{\Delta y}\right)CpT_f\Big|_y - \left(\frac{\dot{m}}{\Delta y}\right)CpT_f\Big|_{y+\Delta y} + \frac{n\Delta y q'_u}{\Delta y} = 0 \qquad (7.1.5)$$

The first term of the equation (7.1.5) could be neglected since the value of Δy is very small. The parameters Δy and T_f can considered as dy and dT_f, respectively, since the temperature rise of the liquid flowed in such a small distance inside the pipe would be insignificant. Following these assumptions equation (7.1.5) can be written as:

$$-\dot{m}Cp\frac{dT_f}{dy} + nq'_u = 0 \qquad (7.1.6)$$

or

$$\dot{m}Cp\frac{dT_f}{dy} - nq'_u = 0 \qquad (7.1.7)$$

and finally

$$\dot{m}Cp\frac{dT_f}{dy} = nq'_u \qquad (7.1.8)$$

Using equation (3.13.8) in Chapter 3 q'_u is given by:

$$q'_u = WF'[S - U_L(T_f - T_a)]$$

Combining (3.13.8) to (7.1.7) gives:

$$\dot{m}Cp\frac{dT_f}{dy} - nWF'\left[S - U_L\left(T_f - T_\alpha\right)\right] = 0 \qquad (7.1.9)$$

Dividing both terms of (7.1.9) by the term $\dot{m}Cp$ we obtain:

$$\left(\frac{\dot{m}Cp}{\dot{m}Cp}\right)\frac{dT_f}{dy} - n\left(\frac{WF'}{\dot{m}Cp}\right)\left[S - U_L\left(T_f - T_\alpha\right)\right] = 0 \qquad (7.1.10)$$

or

$$\frac{dT_f}{dy} - n\left(\frac{WF'}{\dot{m}Cp}\right)\left[S - U_L\left(T_f - T_\alpha\right)\right] = 0 \qquad (7.1.11)$$

Rewriting (7.1.11) and performing the multiplications between the elements of the equation:

$$\frac{dT_f}{dy} + n\left(\frac{WF'}{\dot{m}Cp}\right)\left[-S + U_L\left(T_f - T_\alpha\right)\right] = 0 \qquad (7.1.12)$$

or

$$\frac{dT_f}{dy} + nWF'\left[-\frac{S}{\dot{m}Cp} + \frac{U_L T_f}{\dot{m}Cp} - \frac{U_L T_\alpha}{\dot{m}Cp}\right] = 0 \qquad (7.1.13)$$

Re-arranging the above equation we obtain

$$\frac{dT_f}{dy} + nWF'\left[\frac{U_L}{\dot{m}Cp}\left(-\frac{S}{U_L} + T_f - T_\alpha\right)\right] = 0 \qquad (7.1.14)$$

or

$$\frac{dT_f}{dy} = -nWF'\left[\frac{U_L}{\dot{m}Cp}\left(-\frac{S}{U_L} + T_f - T_\alpha\right)\right] \qquad (7.1.15)$$

But since:

$$d\left(-\frac{S}{U_L} + T_f - T_\alpha\right) = \left(-\frac{S}{U_L} + T_f - T_\alpha\right)dT_f \qquad (7.1.16)$$

176

The right hand side of (7.1.6) can be rewritten as:

$$d\left(-\frac{S}{U_L}+T_f-T_\alpha\right)=\left[\left(-\frac{S}{U_L}\right)'+\left(T_f\right)'-\left(T_\alpha\right)'\right]dT_f \quad (7.1.17)$$

The dotted elements of the right hand side of (7.1.7) means that they will be differentiated.

Since we differentiate T_f then all the constant elements will be equal to zero as (7.1.8) illustrates:

$$d\left(-\frac{S}{U_L}+T_f-T_\alpha\right)=(0+1-0)dT_f \quad (7.1.18)$$

Finally:

$$d\left(-\frac{S}{U_L}+T_f-T_\alpha\right)=dT_f \quad (7.1.19)$$

By substituting (7.1.19) into (7.1.15) the equation takes the following form:

$$\frac{d}{dy}\left(-\frac{S}{U_L}+T_f-T_\alpha\right)=\frac{-nWF'U_L}{\dot{m}Cp}\left(-\frac{S}{U_L}+T_f-T_\alpha\right) \quad (7.1.20)$$

Equation (7.1.20) can be re-written as

$$d\left(-\frac{S}{U_L}+T_f-T_\alpha\right)=\frac{-nWF'U_L}{\dot{m}Cp}\left(-\frac{S}{U_L}+T_f-T_\alpha\right)dy \quad (7.1.21)$$

or

$$\frac{d\left(-\frac{S}{U_L}+T_f-T_\alpha\right)}{\left(-\frac{S}{U_L}+T_f-T_\alpha\right)}=\frac{-nWF'U_L}{\dot{m}Cp}dy \quad (7.1.22)$$

177

By integrating both sides of the equation (7.1.22):

$$\int_{Tfi}^{Tfo} \frac{d\left(-\dfrac{S}{U_L}+T_f-T_\alpha\right)}{\left(-\dfrac{S}{U_L}+T_f-T_\alpha\right)} = \frac{-nWF'U_L}{\dot{m}Cp}\int_0^L dy \qquad (7.1.23)$$

or

$$\ln\left|-\frac{S}{U_L}+T_f-T_\alpha\right|_{T_{fi}}^{T_{fo}} = \left(\frac{-nWF'U_L}{\dot{m}Cp}\right)L \qquad (7.1.24)$$

But $nWL = A_c$ (the area of the collector) and therefore:

$$\ln\left|-\frac{S}{U_L}+T_{fo}-T_\alpha\right|-\ln\left|-\frac{S}{U_L}+T_{fi}-T_\alpha\right| = \frac{-A_cF'U_L}{\dot{m}Cp} \qquad (7.1.25)$$

By taking the exponential of both sides of the equation (7.1.25), it results in:

$$\ln\frac{\left|-\dfrac{S}{U_L}+T_{fo}-T_\alpha\right|}{\left|-\dfrac{S}{U_L}+T_{fi}-T_\alpha\right|} = \frac{-A_cF'U_L}{\dot{m}Cp} \qquad (7.1.26)$$

or

$$\frac{\left[-\dfrac{S}{U_L}+T_{fo}-T_\alpha\right]}{\left[-\dfrac{S}{U_L}+T_{fi}-T_\alpha\right]} = \exp\left(\frac{-A_cF'U_L}{\dot{m}Cp}\right) \qquad (7.1.27)$$

And finally:

$$\frac{\left[T_{fo} - T_{\alpha} - \dfrac{S}{U_L}\right]}{\left[T_{fi} - T_{\alpha} - \dfrac{S}{U_L}\right]} = \frac{1}{\exp\left(\dfrac{A_c F' U_L}{\dot{m} C p}\right)} \qquad (7.1.28)$$

From equation (7.1.28) it is possible to determine T_{fo} as a function of design parameters of the collector and operational conditions:

$$T_{fo} = \left(T_{\alpha} + \frac{S}{U_L}\right) - \left[\left(-T_{fi} + T_{\alpha} + \frac{S}{U_L}\right)\frac{1}{\exp\left(\dfrac{A_c F' U_L}{\dot{m} C p}\right)}\right] \qquad (7.1.29)$$

In open literature there is no a general analytical equation for calculation of the parameter F' as function of heat transfer coefficient and the overall heat losses coefficient.

This dependence usually presented in the form of tables or charts. The tabulated data from the literature was used to derive a general equation in the form of $F'=f(h_f, U_L)$.

An example of the tabulated data is shown in Table 7.1a. Combination of three values of heat transfer coefficient, h_{fi} (100, 300 and 1000 W/m^{2}C) and of U_L (2, 4 and 8 W/m^{2}C) were used to derive the general equation that could cover a wide range of flow regimes (laminar and turbulent). Data listed in Table 7.1a present results found by Duffie and Beckman.

h_f (W/m^{2}C)	U_L (W/m^{2}C)	F'
100	2	0.930
100	4	0.865
100	8	0.765

h_f (W/m^{2}C)	U_L (W/m^{2}C)	F'
300	2	0.970
300	4	0.940
300	8	0.890

h_f (W/m^{2}C)	U_L (W/m^{2}C)	F'
1000	2	0.985
1000	4	0.970
1000	8	0.945

Table 7.1a Data of h, U_L and F'.

Five new parameters, namely *X, Y, Z, B,* and *C* were introduced to be used in the generalised equation:

$$X = 7 - U_L \; (4) \quad (7.1.30) \qquad Y = (9 - h_{fi})/100 \quad (7.1.31)$$

Parameters *X* and *Y* refer to the series of values of the heat loss coefficient U_L and the heat transfer coefficient h_{fi}, respectively.

The collector efficiency factor is given as:

$$F' = \frac{1/U_L}{W\left[\dfrac{1}{U_L[D + (W - D)]F} + \dfrac{1}{C_b} + \dfrac{1}{\pi D_i h_{fi}}\right]} \quad (7.1.32)$$

In order to define F' for wide range of h_f and U_L values a new generalised equation was introduced in the following form:

$$F' = Z + \sum_{i=0}^{X} B + i^2 \cdot C \qquad (7.1.33)$$

where Z, B, and C are:

$$Z = 9.45 \cdot 10^{-1} - \sum_{i=0}^{X} 10^{-4} + i^4 \cdot 11.66 \cdot 10^{-6} \qquad (7.1.34)$$

$$B = 5.99 \cdot 10^{-3} - \sum_{j=0}^{Y} 10^{-5} + j^4 \cdot 11.05 \cdot 10^{-7} \qquad (7.1.35)$$

$$C = 3.4 \cdot 10^{-5} - \sum_{j=0}^{Y} 10^{-6} + j^4 \cdot 1.8 \cdot 10^{-8} \qquad (7.1.36)$$

The above equation was checked against charts presented in Appendix D which display different values of F' versus tube spacing and various overall heat loss coefficient values and Equation (7.1.33) very closely predicts the value of F'.

7.2 Validation of the developed lumped parameter model using experimental data

Experimental results obtained during tests in both the conventional solar collector and the collector with metallic mesh insertion is used in this section to validate the developed lumped parameter model.

Parameters shown on Table 7.2a obtained from experiments (bold data) for the conventional and the porous medium collectors. Combined together with data obtained from charts, were both used to calculate theoretically the temperature of the water in the outlet part of the collector section T_{fo} using equation (7.1.29) in order to cross examine the experimental results to the theoretical techniques employed.

Variables	Conventional Collector	Porous Collector
W (m)	0.11	0.11
D (m)	0.01	0.01
S (W/m²)	905	905
U_L (W/m² °C)	6.55	6.55
T_b °C	**149.6**	**148.7**
T_a °C	18	18
k (W/m °C)	400	400
d (m)	0.0005	0.0001
Di (m)	0.008	0.007
m	5.7	5.7
T_{fi} °C	**65.6**	**81.7**
A_c (m²)	0.64	0.64
$\dot{m}$ (mg/s)	**0.62**	**0.58**
Cp (J/Kg °C)	4230	4240

Table 7.2a: Data for the conventional and porous collector.

In Table 7.2a, W is the width of the fin, D is the external diameter of the pipes, S is the solar heat flux, U_L is the collector overall loss coefficient, T_b is the base temperature at the joint of fin and tube, T_{fref} is the fluid reference temperature T_a is the ambient temperature, k is the thermal conductivity of the metal, d is the thickness of the fin. D_i is the internal diameter of the pipe, $m = \sqrt{\dfrac{U_L}{k\delta}}$, T_{fi} is the temperature of the working fluid at the inlet, Ac is the area of the collector, $\dot{m}$ is the volumetric flow rate, and Cp is the specific heat of the working fluid.

The function F which is the standard fin efficiency for straight fins with rectangular profile was obtained from (3.13.3) for both collectors having a value of **0.974**.

For the Conventional Collector:

The useful gain q'_u for the tube and fin per unit length in the flow direction was calculated using equation (3.13.6) for both copper and aluminium finned pipes having a value of **7.29**. The thermal resistance to heat flows from the plate to the fluid resulted from the plate-tube bond conductance and the tube-to-fluid convection heat transfer inside of tubes.

Reynolds number Re was calculated as:

$$Re = \frac{4\dot{m}}{\pi D \mu} \quad (7.2.1)$$

The dynamic viscosity (μ) was taken from charts for 133°C.

In equation (7.2.1) $\dot{m}$ is the total collector flow rate (0.62ml/sec), D (0.01m) is the diameter of the pipe, μ is the dynamic viscosity ($0.209 \cdot 10^{-3}$ Kg/ms).

The value of the Re number calculated was **377** which represented a laminar flow (since Reynolds found that for a flow in a pipe it did not matter which of the parameters $\dot{m}$ or D varied in this dimensionless group, as long as Re was less than approximately 2300, the flow is laminar) .

The collector efficiency factor F' calculated was **0.873**. F' contains the value of the local heat transfer coefficient h obtained in experiment and equal to **238** W/m^{2}C.

Finally, the theoretical water outlet temperature was calculated from (7.1.29) and was equal to **133.4 °C** which was very close to the one found in the experiments (**133 °C**).

For the Porous Medium Collector:

The useful gain q'_u for the tube and fin per unit length in the flow direction was determined for both copper and aluminium finned pipes and was equal to **7.45**.

Reynolds number *Re* was calculated for the water temperature of 140°C as found in the experiments. In this case the values of $\dot{m}$ was 0.58ml/sec, *D* was 0.01m and μ was $0.197 \cdot 10^{-3}$ Kg/ms. The value of *Re* number calculated was **373** which corresponds to a laminar flow.

The collector efficiency factor *F'* obtained was **0.885**. *F'* was calculated for the value of the local heat transfer coefficient *h* equal to **266** W/m²C (from the experiments).

The theoretical output temperature was calculated from (7.1.29) was **139.5 °C** which was very close to the one found in the experiments (**140 °C**).

From the findings so far the average *Ra* and *Nu* number for the porous and conventional cases could be obtained over a characteristic pipe length. The average *Ra* number could be obtained from the expression (6.4.3).

$$Ra = \frac{C_p \rho^2 g \beta (\Delta T) L^3}{\kappa \mu} \qquad (6.4.3)$$

where C_p is the specific heat of the water, ρ is the density of the water, g is the gravitational force at (55° inclination), β is the thermal expansion coefficient, ΔT is the temperature difference between the outer pipe surface and the water temperature at the pipe wall, L is the characteristic length of the pipe, κ is the thermal conductivity and μ the dynamic viscosity.The average Ra number was obtained for the heat flux of 905 W/m^2.

The data used to obtain the Rayleigh numbers is listed on Table 7.2b. The water properties were taken from charts for the temperatures of 140°C (porous medium collector) and 133°C (conventional collector).

	Conventional Collector	Porous medium Collector
C_p (J/Kg ^oC)	4270	4286
ρ (Kg/m^3)	930	922
g (m/s^2)	5.62	5.62
β(1/^oC)	$0.93 \cdot 10^{-3}$	$0.97 \cdot 10^{-3}$
ΔT (^oC)	3.0	3.2
L(m)	0.25	0.25
κ(W/m^2 ^oC)	$0.684 \cdot 10^{-3}$	$0.683 \cdot 10^{-3}$
μ(Kg/m·sec)	$0.208 \cdot 10^{-3}$	$0.197 \cdot 10^{-3}$

Table 7.2b Data for the Ra numbers.

The average Ra numbers obtained for the convectional collector and for the porous medium collector was $\mathbf{6.35 \cdot 10^9}$ and $\mathbf{7.38 \cdot 10^9}$ respectively.

As with equations (5.4.8) and (5.4.9) obtained on Chapter 5 from simulations and validated by the literature, the average Nu number determined in relation to Ra number for the porous medium case for a heat flux of 905 W/m^2 given by the expression (7.2.2):

$$Nu_{(905)} = 0.0107(Ra)^{0.285} \qquad (7.2.2)$$

The *Nu* number obtained for the collector utilising the metallic mesh was **6.91** and for the conventional collector was **5.75.**

To summarise all the findings in this chapter, Table 7.2c was created and illustrates all the results for both collectors.

Variables	Porous medium Collector	Conventional Collector
h_f *(local heat transfer coefficient)*	266 W/m^{2}C	238 W/m^{2}C
F' (collector efficiency factor)	0.885	0.873
Re (Reynolds number)	373	377
T_{fout} *(Output water temperature)*	139.5 ^{o}C	133.4 ^{o}C
Ra number	7.38·10^9	6.35·10^9
Nu number	6.91	5.75

Table 7.2c Parameters of the porous medium and the conventional collector.

It can be observed that the collector with the metallic insertion material has greater values of *F'*, T_{fout} and h_f which indicates the enhancement in the heat transfer in the collector. The *Nu* and *Ra* numbers are greater in the case of the porous medium collector supporting the enhancement of the convective heat transfer. The output temperature T_{fout}, based on the model created by Duffie and Beckman, obtained in both cases from (7.1.29) is approximately ±0.3^{o}C accurate.

7.3 Conclusions

The experimental results validated by the lumped parameter model and demonstrated that can accurately predict the performance of the collector and therefore can be used in the designing process.

Similarly to the expressions (5.4.8) and (5.4.9) obtained from simulations, validated by the literature and by using experimental results, the average *Nu* number

determined in relation to *Ra* number for the porous medium case for a heat flux of 905 W/m^2 given by the expression (7.2.2).

A comparison of the findings was made using Table 7.2c showing clearly the positive effect of the utilisation of the aluminium net inside the pipes of the collector section.

CHAPTER 8

Conclusions and Recommendations

8.1   Introduction

Different techniques and methods have been applied for many years with the aim to improve the efficiency of flat plate solar water collectors. The purpose of this study was to investigate the theory behind solar water collectors and the potential techniques available in to order to find novel ways to enhance its performance. The main focus was on the passive flat-plate collectors which are commonly used in Mediterranean region.

An experimental test rig was created with the aim to examine how the heat transfer intensification technique using partial porous medium in the form of the aluminium net mesh insertion could be applied in a real system and if it would be feasible for practical applications.

The use of Computational Fluid Dynamics (CFD) was a very important tool in this project to obtained detailed numerical data on heat and mass flow transfer in the proposed design solution.

The heat transfer enhancement method considered in this thesis was tested experimentally and numerically and a lumped parameter model was developed using data from CFD and experimental tests to predict the performance of the proposed solar collector for a rapid design process.

8.2   Conclusions

Research has been conducted with the aim of enhancing the heat transfer in a passive flat plate solar water collector using a cost effective technique that could be easily applied in a typical (conventional) flat plate collector without changing or redesigning its shape.

The literature review performed in this work suggested that previously designed models as described in Chapter 2 achieved the increase in the efficiency of the collectors by using relatively expensive design solutions which in some cases made the product bulky, heavier and therefore difficult to install and exploit. This could result in putting off customers from buying solar collectors and use renewable energy technologies especially in the current economic crisis conditions. Furthermore the highest efficiency was achieved in the cases where the convection heat transfer was enhanced by the means of fins within the pipes.

Computational Fluid Dynamics (CFD) modeling and experimental work demonstrated an increase in the water temperature in the solar collector with the aluminum mesh insertion by **7°C** in comparison to the conventional one. The findings were validated with the literature for their accuracy by the means of using a lumped parameters model and existing mathematical expressions.

Parameters such as Rayleigh *(Ra)* and Nusselt *(Nu)* numbers obtained and the results showed that existence of a laminar flow that had a dominant convective heat transfer mechanism in the case of the collector with the metal insertion.

The average *Ra* numbers calculated using experimental data, for the heat flux of 1070 W/m^2 and 610 W/m^2 was **7.95·10^9** and **6.14 ·10^9** respectively, showing a good agreement to the simulations findings which were **8·10^9** and **6.2 ·10^9** and for the heat flux of 1070 W/m^2 and 610 W/m^2 respectively.

The resulting *Nu* numbers obtained experimentally was **8.6** and **4.3** for the heat flux of 1070 W/m^2 and 610 W/m^2 respectively showing a good agreement to the CFD results which were **8.3** and **4.2** and to the ones calculated which were **8.4** and **4.3** respectively.

The presence of the aluminium mesh insertion enhanced the convective heat transfer in the conventional collectors on average by **9.3%** (CFD findings) and by **10 %** (experimental investigations). Such technique provided a higher temperature at the outlet of the solar collector that increased by **9.2%**.

There was an agreement between experimental findings and results from the lumped parameter model. The output temperature calculated in part of the conventional collector section was **133.4 °C** which was very close to the experimental of **133 °C**. In part of the collector section with the aluminium mesh insertion, the calculated output temperature was **139.5 °C**, which was very close to the experimental one of **140 °C**. An error analysis was performed in all experiments to evaluate its accuracy, the calibration techniques and the manufacturing specifications of the apparatus used in the experimental test rig.

The three important correlations, listed below, that relate the Rayleigh *(Ra)* and the Nusselt *(Nu)* numbers, obtained for different heat fluxes, can be used on collector's finned pipes **0.25m** long, in order to predict and determine the heat transfer coefficient *h*.

$$Nu_{(1070)} = 0.013(Ra)^{0.285} \qquad (5.4.8)$$

$$Nu_{(905)} = 0.0107(Ra)^{0.285} \qquad (7.2.2)$$

$$Nu_{(610)} = 0.007(Ra)^{0.285} \qquad (5.4.9)$$

Although a simplified CFD model was used, it was directly compared to the experimental setup, since the findings in both cases were cross-examined over the same characteristic length (0.25). Both numerical and experimental tests were in good agreement that the aluminium metal insertion considerably increased the output water temperature in the collector.

Such technique would allow the reduction of the solar collector area and its associated manufacturing costs. The presence of the aluminium mesh inside the channels increases the heat transfer and also changes the flow pattern in such a way which increases heat transfer from fluid present in the near-wall zone to the internal layers of the water.

Finally the lumped parameter model of the solar collector was developed which can be used to determine the thermal performance of the solar collector. This model can be also used in the rapid designing process. The developed lumped parameter model was tested on the solar collector design used in the experiments.

Overall conclusion from the research work undertaken is that using such a low cost modification in a design, using a metallic mesh insertion, considerably improves the performance of the solar collector.

8.3   Recommendations

Extending the work covered in this thesis, improvements and modifications could be made in the experimental test rig in order to further enhance the effect of porous medium insertions in solar collectors. The following improvements could be performed in four main areas:

1)   Modify collectors by removing all compression fittings in order to make the system more efficient. It could also be useful to extend the piping from the collector's outlet to the water tanks in order to investigate the benefit of having porous medium in all the piping of the system.

2)   Another modification to carry out would be creation of pulsating flow to investigate its effect on the thermal performance of the collector with metallic insertions. This can be investigated both experimentally and theoretically (using CFD modeling on an identical to the experiments collector section).

3)   Reduction of heat losses from the system by using more advance thermal insulation of all components of the system. Further work could be contacted upon the aluminium net inserted inside the pipes. This can be accomplished by folding the net in order to have two or three turns or even to a spiral shaped profile that could probably contribute more heat to the working fluid. Also the application of metallic foams of different porosities.

4)   The lumped parameter model should be modified in order to take into account features of the design of porous medium insertion and heat transfer at the pulsating flow.

The proposed future research will improve existing knowledge on solar collectors and enhance their performance.

CHAPTER 9

References

1. Duffie, J. A., and W. A. Beckman, Solar Engineering of Thermal Processes, John Wiley and Sons, New York, 1991.

2. United States, Department of Energy, Solar energy technologies Program http://www1.eere.energy.gov/solar/solar_time_1767-1800.html

3. California solar centre, http://www.californiasolarcenter.org/history_pv.html

4. Ken Butti, John Perlin A Golden Thread, Published by Van Nostrand Reinhold Company, 1980.

5. Charles Smith, History of Solar Energy Revisiting, Past Solar Power Technology Review, 1995.

6. The Kentucky Solar Partnership, http://www.kysolar.org/

7. International Energy Agency of Solar Heating and Cooling Programme, Data-Annual Report 2001.

8. S. Kalogirou, Solar thermal collectors and applications, Progress in Energy and Combustion Science 30, 231–295, 2004.

9. U.S. Department of Energy - Energy Efficiency and Renewable Energy Solar Energy Technologies Program. http://www1.eere.energy.gov/solar/

10. International Standard, ISO 9806-1, Test methods for Solar Collector's Thermal performance of glazed liquid heating collectors, 1996.

11. Mahjouri F, Stiteler R, Walker A, Evacuated-Tube Heat-Pipe Solar Collectors National Renewable Energy Laboratory, 2004.

12. Innovators in Solar, INS-SOLAR, http://www.ins-solar.com/index.html

13. George Simons, Joe McCabe, California Research and Development, Energy Research and Development Division, 2005.

14. Solar Thermal Technology Department Sandia National Laboratories Albuquerque. http://solstice.crest.org/renewables.

15. G. W. Treadwell, Low-Temperature Performance Comparisons of Parabolic -Trough and Flat-Plate Collectors Based on Typical Meteorological Year Data, Sandia National Labs, Report 1979.

16. Hans Muller, Franz Tried, Institute Of Technical Thermodynamics, (DLR), power point presentation, Stuttgart, Germany.

17. L F. Caslake, D J. Connolly, V Menon, CM. Duncanson, R Rojas and J Tavakoli, Disinfection of Contaminated Water by Using Solar Irradiation, Appl. Environ Microbiol.70, 1145–1150, 2004.

18. Amnon Einav, Solar Energy Research and Development Achievements in Israel and Their Practical Significance Sol. Energy Eng. Volume 126, 92, 2004.

19. P.Konttinen, R.Kilpib, P.D.Lund, Micro structural analysis of selective CyAl2O3yAl solar absorber surfaces, Thin Solid Films 425, 24–30, 2002.

20. P. Konttinen, P.D. Lund, Mechanically manufactured selective solar Absorber surfaces Solar Energy Materials & Solar Cells 79, 273–283, 2003.

21. Qi-Chu Zhang, M S Hadavi, K-D Lee and Y G Shen, 2Zr–ZrO2 Cermet solar coatings designed by modelling calculations and deposited by dc magnetron sputtering. J. Phys. D: Appl. Phys. 36, 2003.

22. Qi-Chu Zhang, Metal–AlN Cermet solar selective coatings deposited by direct current magnetron sputtering technology J. Phys. D, Appl. Phys. 31 1998.

23. S Suzer, F. Kadirgan, H.M. Sohmen, A.J. Werherilt, I.E. Ture, Spectroscopic characterization of Al_2O_3-Ni selective absorbers for solar collectors, Solar Energy Materials and Solar Cells, Vol. 52, 55-60, 1998.

24. F. Kadirgan, M. Sohmen, Development of Black Cobalt Selective Absorber on Copper for Solar Collectors, Turk J Chem 23, 345-351, 1999.

25. E. Wackelgard F. Kadirgan, M. Sohmen, Electrochemical Characterization of Al2O3-Ni Thin Film Selective Surface on Aluminium, Turk J Chem 23, 381 -391, 1999.

26. J. J. Zybert and D. R. McKenzie Colloidally deposited high-temperature solar selective surfaces Applied Optics Vol. 20, No. 23, 1981.

27. B. Norton, Anatomy of a solar collector: Developments in Materials, Components and Efficiency Improvements in Solar Thermal Collector Systems, Volume 7, 32-35, 2006.

28. O.P Agnihotri., B.K Gupta. Solar Selective Surfaces, Wiley Series, New Delhi, 1981.

29. G. M. Choudhury, Selective Surface for efficient Solar Thermal Conversion, Bangladesh Renewable Energy Newsletter, Vol. 1, No.2, 1-3, 2000.

30. D Poulikakos Conduction heat transfer, Prentice Hall, Englewood Cliffs, NJ, 1994.

31. K. S. Kohli, K. N. Chopra, R. Hradaynath, An Efficient Optical Window for Flat-Plate Solar Energy Collectors, J. Optics (Paris), Vol. 10, 1979.

32. S. Furbo and L. Jivan Shah, Thermal advantages for solar heating systems with a glass cover with antireflection surfaces, Volume 74, 513-523, 2003.

33. Thomas A. Hofmann, Monika Kursawe, Antireflective Coating on Float Glass for Solar Collectors Glass Processing Days, 2001.

34. G. Jorgensena, S. Brunoldb, M. Köhlc, P. Nostelld, H. Oversloote, A. Roosd, Durability testing of antireflection coatings for solar applications National Renewable Energy Laboratory, Annual Meeting and Exhibition, 1999.

35. K. Maatouk, M. Shigenao, K. Atsuki, B. Masud, Flat-Plate Solar Collector Performance with Coated and Uncoated Glass Cover, Heat Transfer Engineering, Vol. 27, 46-53, 2006.

36. Close DJ, Solar air heaters. For low and moderate temperature applications. Solar Energy 7, 117–124, 1963.

37. CL Gupta, HP Garg. Performance studies on solar air heaters, Solar Energy 11, 25–31. 1967.

38. KS Ong, A finite-difference method to evaluate the thermal performance of a solar water heater Solar Energy 18, 181–191, 1974.

39. KS Ong, An improved computer program for the thermal performance of a solar water heater. Solar Energy 18, 183–191, 1976.

40. G Morrison, JE Braun System modelling and operation characteristics of thermosyphon solar water heaters. Solar Energy 34, 389–405, 1985.

41. Schmidt C, Goetzberger A, Schmid J. Test results and evaluation of integrated collector storage systems with transparent insulation. Solar Energy 41, 487–94, 1988.

42. J.E Hay, D.C. McKay, Estimating solar irradiance on inclined surfaces: a review and assessment of methodologies. J. Solar Energy 3, 203-240, 1985.

43. D. Faiman and A. Zemel, Low-profile solar water heaters: the mirror booster problem revisited, solar energy, Vol.40, 385-390, 1988.

44. V. K Agarwal and D. C Larson, Calculation of the Top Loss Coefficient of a Flat-Plate Collector, Solar Energy Vol. 27, 69-71, 1981.

45. D.G. Gomes, N. Fico JR. Experimental study of energy loss in solar energy collectors Instituto Tecnológico de Aeronáutica,São José dos Campos, SP, Brazil, Journal of Solar Energy Engineering Volume 126, 1101-1105, 2004.

46. R. A. Bajura and E. H. Jones. Flow distributions in manifolds. J. Fluids Eng. Trans. ASME 98, 654-655, 1976.

47. V. Weitbrecht, D. Lehmann and A. Richter, Flow distribution in solar collectors with laminar flow conditions Solar Energy Vol. 73, 433–441, 2002.

48. A. Rabl, Active Solar Collectors and Their Applications. Oxford University Press, New York, 1985.

49. El-Nashar A. M. The effect of dust accumulation on the performance of evacuated tube collectors. Solar Energy Volume 53, 105-115, 1994.

50. S. Biryuikov, D. Faiman and A. Goldfeld, An Optical System for the Quantitative Study of Particulate Contamination on Solar Collector Surfaces Solar Energy Vol. 66, 371-378, 1999.

51. A. Goetzberger, J. Dengler, M. Rommel, and V. Wittwer, The bifacial absorber collector: a new highly efficient flat plate collector, International Solar Energy Society, USA, 1212-1217, 1991.

52. N.K. Groenhout, G.L. Morrison and M. Behnia, Design of Advanced Solar Water Heaters, Proc. ANZSES Solar 2000 Conf, 295–303, 2000.

53. S. Janjai, A. Esper and W. Mühlbauer, Modelling the performance of a large area plastic solar collector, Volume 21, 363-376, 2000.

54. K. Sopian, M. Syahri, S. Abdullah, M. Y. Othman and B. Yatim, Performance of a non-metallic unglazed solar water heater with integrated storage system, Volume 29, 1421-1430, 2004.

55. H.D. Ammari and Y.L. Nimir, Experimental and theoretical evaluation of the performance of a tar solar water heater, Energy Conversion and Management 44, 3037–3055, 2003.

56. V. Kienzlen, J.M. Gordon and J.F Kreider, The reverse flat plate collector: A stationary, non evacuated, low-technology, medium-temperature solar collector, J. Solar Energy Engineering, Vol. 110, 23-30, 1988.

57. I. Tanishita, Recent development of solar water heaters in Japan, Proceedings of the UN Conference on New Sources of. Energy 5, Rome, 102, 1964.

58. S.C. Kaushik, R. Kumar, H.P. Garg, J. Prakash, Transient analysis of a triangular built-in-storage solar water heater under winter conditions. Heat Recovery System CHP 14, 337–341, 1994.

59. H.A. de Beijer, Product development in solar water heating, Renewable Energy 15 201-204, 1998.

60. D. Faiman, H. Hazan and I. Laufer, Reducing the Heat Loss at Night From Solar Water Heaters of the Integrated Collector Storage Variety Solar Energy Vol. 71, 87–93, 2001.

61. S. L. Abreu and S. Colle An experimental study of two-phase closed thermosyphons for compact solar domestic hot-water systems, Volume 76, 141-145, 2004.

62. M. Smyth, P. McGarrigle, P.C. Eames, B. Norton, Experimental comparison of alternative convection suppression arrangements for concentrating integral collector storage solar water heaters, Solar Energy, Volume 78, 223-233, 2005.

63. H. Al-Madani, The performance of a cylindrical solar water heater, Renewable Energy 31 1751–1763, 2006.

64. H. A Zondag, D. W. De Vries, W van Helden, The Thermal and Electrical Yield of a PV-Thermal Collector, Solar Energy Vol. 72, 113–128, 2002.

65. M. Bakker, K. J. Strootman and M Jong. Photovoltaic Thermal Panels, Renewable and Competitive. ECN report ECN-C-03-103, 2003.

66. H. P. Garg , R. S. Adhikari, Performance analysis of a hybrid photovoltaic/thermal (PV/T) collector with integrated CPC troughs. John Wiley & Sons, Ltd. Vol. 15, 1295-1304, 1999.

67. Y. Tripanagnostopoulos, M. Souliotis , R. Battisti , A. Corrado. Energy, cost and results of PV and hybrid PV/T solar systems. University of Patras. John Wiley Vol. 13, 235 – 250, 2005.

68. Y. Morita, T. Fujisawa, T. Tani, Moment performance of photovoltaic/thermal hybrid panel. Scripta Technica, Electr Eng Japan, 133, 43-51, 2000.

69. B. Robles-Ocampo, E. Ruı´z-Vasquezb, H. Canseco-Sanchez, R.C. Cornejo-Meza G. Trapaga-Martınez, F.J. Garcıa-Rodrigueza, J. Gonzalez-Hernandez, Y.V. Vorobiev, Photovoltaic/thermal solar hybrid system with bifacial PV module and transparent plane collector, Solar Energy Materials & Solar Cells Vol. 91, 1966–1971, 2007.

70. G.F Jones and N. Lior, Flow distribution in manifold solar collectors with negligible buoyancy effects. Solar Energy 52, 289–300, 1994.

71. Solar Thermal Tech. Sandia National Labs: http://solstice.crest.org/renewable

72. V. Weitbrecht, D. Lehmann, A. Richter, Flow distribution in solar collectors with laminar flow conditions, Solar Energy Volume 73, 433-441, 2002.

73. J. Fan, L. J. Shah and S. Furbo, Flow distribution in a solar collector panel with horizontally inclined absorber strips. Solar Energy, Vol.81, 1501-1511 2007.

74. N. Molero Villar, J.M. Cejudo Lopez, F. Domınguez Munoz, E. Rodrıguez Garcıa, A. Carrillo Andres, Numerical 3-D heat flux simulations on flat plate solar collectors, Solar Energy 83, 1086–1092, 2009.

75. X. A Wang and L. G Wu, Analysis and performance of flat plate solar collector arrays. Solar Energy 45, 71–78, 1990.

76. A. Campo, Quick identification of gases for enhancing heat transfer in turbulent pipe flow using standard correlation equations. Applied Thermal Engineering Vol. 25, 2029-2038, 2003.

77. R. L. Webb, Principles of Enhanced Heat Transfer, Wiley, N.Y. 1994.

78. A.E. Bergles Techniques to enhance heat transfer. W.M. Rosehnow et al. Handbook of Heat Transfer, McGraw-Hill, N.Y. 1998.

79. R. K. Dash and K. N. Mehta Casson fluid flow in a pipe filled with a homogeneous porous medium, Int. J. Eng Sci. Vol. 34, 1145-1156, 1996.

80. S. Mahjoob, K. Vafai, A synthesis of fluid and thermal transport models for metal foam heat exchangers, International Journal of Heat and Mass Transfer 51, 3701–3711, 2008.

81. L. Tianjian, Ultralight porous metals: from fundamentals to applications Acta Mechanica Sinica, Chinese J. Mech. 18, 457–479 (2002).

82. W. Lu a, C.Y. Zhao S.A. Tassou, Thermal analysis on metal-foam filled heat exchangers. Part I: Metal-foam filled pipes, International Journal of Heat and Mass Transfer 49, 2751–2761, 2006.

83. G. Zhixiong Pulsating flow and heat transfer in a pipe partially filled with porous medium. Int. J. Heat Mass Transfer Vol. 40, 4209-4218, 1997.

84. E. P. Orda, and K Mahkamov, Development of Low-tech Solar Thermal Water Pumps for Use in Developing Countries Journal of Solar Energy Engineering. Volume 126, 768-773, 2004.

85. H. Yapici, G. Basturk, N. Kayatas, S. Yalcin, Numerical study on transient local entropy generation in pulsating turbulent flow through an externally heated pipe. Sadhana Vol. 30, 2005.

86. S. Ray, B. Unsal, F. Durst, O. Ertunc, O. A. Bayoumi, Mass flow rate controlled fully developed laminar pulsating pipe flows. Journal of Fluid Engineering, Vol. 127, 625–648, 2005.

87. T. Moschandreou, M.Zamir, Heat transfer in a tube with pulsating flow and constant heat flux, Int. J. Heat Mass Transfer 32, 923-934, 1997.

88. A Hadim, Forced convection in a porous channel with localized heat sources, Journal of Heat Transfer 116, 465–472, 1994.

89. S. Y. Kim, B. H. Kang, J. M Hyun, Heat transfer from pulsating flow in a channel filled with porous media. J. Heat Mass Transfer 37, 2025–2033, 1994.

90. D. Poulikakos and M. Kazmierczak, Forced convection in a duct partially filled with porous material. ASME J. Heat Transfer 109, 653–662, 1987.

91. M.K. Alkam, M.A. Al-Nimr, M.O. Hamdan, Enhancing heat transfer in parallel-plate channels by using porous inserts, International Journal of Heat and Mass Transfer 44 931-938, 2001.

92. B. Y. H. Liu and R. C. Jordan, The Inter-relationship and Characteristic Distribution of Direct, Diffuse, and Total Solar Radiation, Solar Energy, Vol. 4, 1-19, 1960.

93. T. E Hollands, G. D. Raithby, and L Lonicek, Free Convection Heat Transfer Across Inclined Air Layers, Journal of Heat Transfer, Vol. 98, 189-201, 1976.

94. A. F. Souka and H.Safwat, Optimum Orientations for the Double Exposure Flat-Plate Collector and Its Reflector," Solar Energy, Vol. 10, 1966.

95. J. Cadafalch, A detailed numerical model for flat plate solar thermal devices, Universitat Politècnica de Catalunya, Solar Energy (UPC), 2008.

96. W. Kamminga, Experiences of a solar collector test method using Fourier transfer functions. International Journal of Heat Mass Transfer 28, 1393–1404, 1995.

97. P. Isakson, Solar collector model for testing and simulation. Final report for BFR project Nr. 900280-1, Building Services Engineering, Royal Institute of Technology, Stockholm, 1995.

98. J. Schnieders, Comparison of the energy yield predictions of stationary and dynamic solar collector models and the models' accuracy in the description of a vacuum tube collector. Solar Energy 61, 179–190, 1997.

99. L J Shah and S. Furbo, Correlation of experimental and theoretical heat transfer in mantle tanks used in low flow SDHW systems, Solar Energy Vol. 64, 245–256, 1998.

100. A. Nasr, G. L. Morrison and M. Behnia, Flow development and heat transfer characteristics in a concentric heat exchanger with application to solar thermosyphon systems. Proceedings 5th Australian Natural Convection Workshop, Sydney, Australia, 31–34, 1996.

101. E. Hahne, Y. Chen, Numerical study of flow and heat transfer characteristics in hot water stores, Solar Energy 64, 9–18, 1998.

102. Morrison G. L., Nasr A., Behnia M. and Rosengarten G Performance of horizontal mantle heat exchangers in solar water heating systems. Proceeding ISES Solar World Congress, Taejon, Korea 2, 149–158, 1997.

103. K.P. Gertzos, Y.G. Caouris, Experimental and computational study of the developed flow field in a flat plate integrated collector storage (ICS) solar device with recirculation, Experimental Thermal and Fluid Science 31, 1133–1145, 2007.

104. D. Amaresh and D. M. Kumar, Laminar natural convection in an inclined complicated cavity with spatially variable wall temperature, Int. J Heat Mass Transfer 48, 3833–3854, 2005.

105. Y. Yang, Laminar natural convective flow in inclined rectangular glazing cavities. CEERE, University of Massachusetts, Department of Mechanical Engineering and Industrial Engineering, January 2002.

106. Z. Zhai and C. Chen, Numerical determination and treatment of convective heat transfer coefficient in coupled building energy simulation, Build Environ 39, 1001–1009, 2004.

107. P. Wang and P. G. Daniels, Numerical study of thermal convection in shallow cavities with conducting boundaries, Inf. J. Heat Mass Transfer. Vol. 37, 387-399, 1994.

108. S. Mahmud, P.K. Das, N. Hyder, A.K.M.S. Islam. Free convection heat transfer in an enclosure with vertical wavy walls, International Journal of Thermal Science 41, 440–6, 2002.

109. B.V.R. Kumar, Shalini. Natural convection in a thermally stratified wavy vertical porous enclosure, Numerical Heat Transfer, 43, 753–776, 2003.

110. D.A.S. Rees and I. Pop Free convection induced by a horizontal wavy surface in a porous medium, Fluid Dynamics Research, Volume 14, 151-166, 1994.

111. Y Varola, F. Hakan A. Oztop, A comparative numerical study on natural convection in inclined wavy and flat-plate solar collectors, Building and Environment 43, 1535–1544, 2008.

112. A. Bejan, Convection Heat Transfer, Wiley, New York, 161-179, 1993.

113. A.E. Bergles, J.S. Brown, and W.D. Srdder, Heat Transfer Performance of Internally Finned Tubes, American Society of Mechanical Engineers, N.Y, ASME Vol. 71, Heat Transfer 31, 1971.

114. D. Chouclhary and S.V. Patankar, Analysis of Developing Laminar Flow and Heat Transfer in Tubes with Radial Internal Fins, ASME National Heat Transfer Conference, 57-63, 1985.

115. M. Huq and Aziz-ul Huq Measurements of Heat Transfer In An Experimental Internally Finned Tube, Int. Comm. Heat Mass Transfer, Vol. 25, 619-630, 1998

116. M.H. Hu and Y.P. Chang, Laminar Flow in Internally Finned Tubes under Constant and uniform Heat Flux, Journal of Heat Transfer 95, 332, 1973.

117. C.D. Ho, T.C. Chen, Collector efficiency improvement of recyclic double-pass sheet-and- tube solar water heaters with internal fins attached, Renewable Energy Vol. 33 655–664, 2008.

APPENDIX A

Open and Closed Loop Passive Systems

Passive systems move domestic water or a heat-transfer fluid through the system without pumps. These systems are usually less expensive than active systems, but are also generally less efficient due to slower liquid flow rates through the system. Thermosyphon system is an example of Open Loop Passive System. It is based on natural convection to circulate water through the solar absorber and to the tank. The tank is located above the collector. As water in the collector heats, it becomes lighter and naturally rises into the tank above. Meanwhile, cooler water in the tank flows downwards into the solar collector, causing circulation throughout the system.

Open Loop Passive System
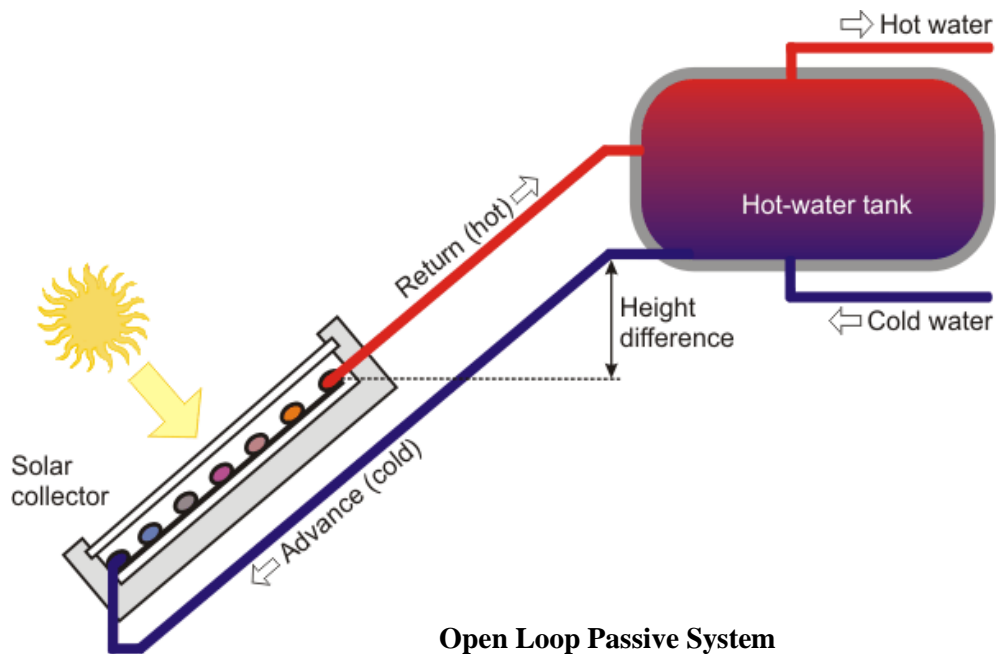
Open and Closed Loop Active Systems

Closed loop systems use pumps to transfer the fluid (usually a glycol-water antifreeze mixture) through the solar water heater. Heat exchangers transfer the heat from the fluid to the water that is stored in tanks. Thick walled heat exchangers prevent the mixture from the domestic water. Closed-loop systems are popular in areas with low temperatures because they offer good antifreeze protection. However, glycol antifreeze systems are more expensive to purchase and install and the glycol must be checked every year and replaced every few. Open-loop active systems use pumps to circulate domestic water through the collectors. This design is efficient and lowers operating costs but it is not appropriate if water is hard or acidic because corrosion will damage the system. Open-loop active systems are popular in regions that do not experience freezing temperatures.

Closed Loop Active System
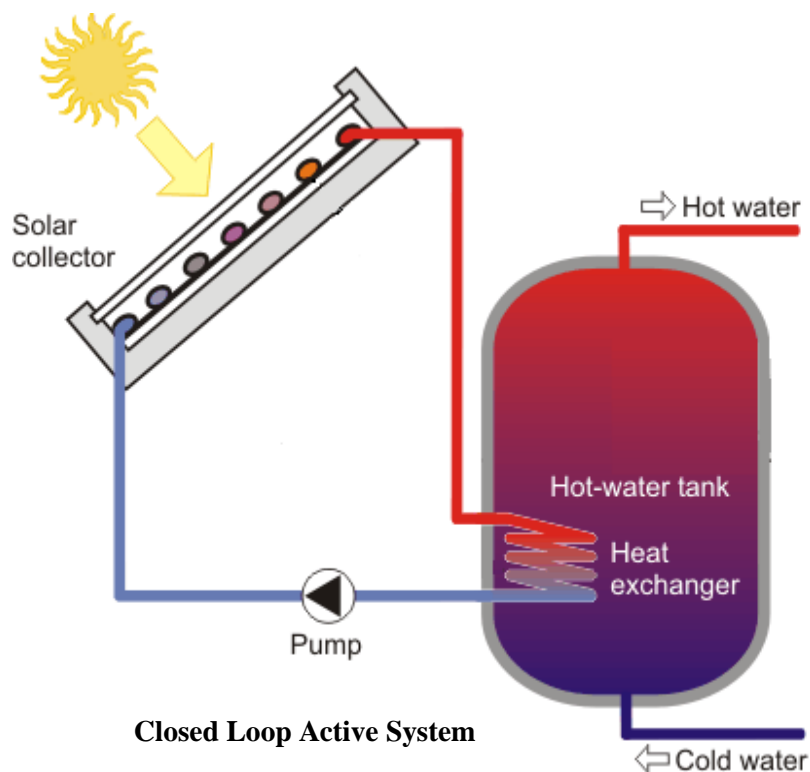
Batch water heaters

Batch water heaters, also known as 'breadboxes' are very simple passive systems for heating water using solar energy and have been used since the early 1900's. Batch systems consist of black storage tanks contained within an insulated box that has a transparent cover. Cold water is added to the hot water stored in the tanks whenever hot water is removed. Modern batch systems are used as preheating systems, where the water is then heated further by conventional gas, electric or wood systems. To retain the heat within the water, the system requires insulated covering to be placed over the glazing at night to prevent the heat being lost to the environment.
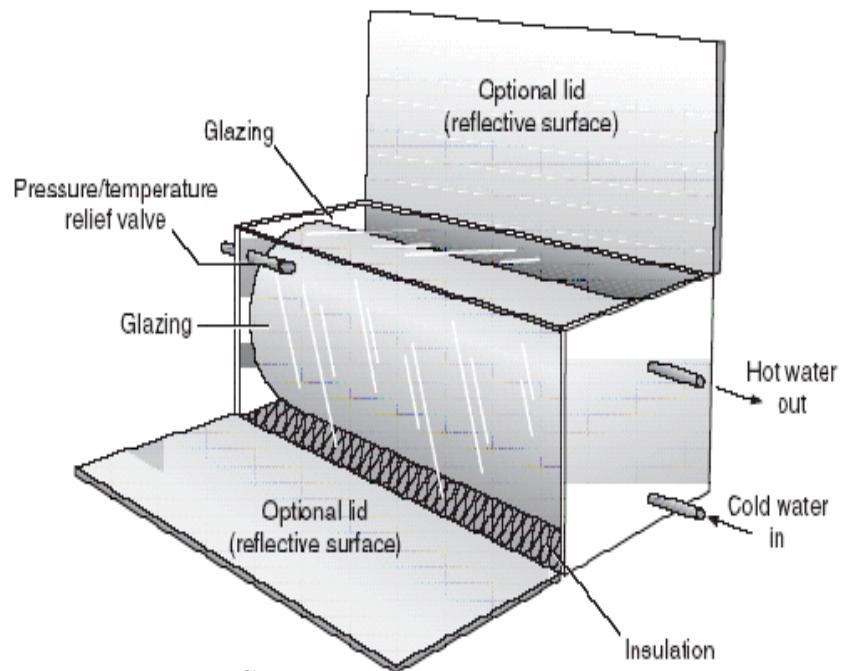
Batch Collector

Source of information and figures in the APPENDIX A: Canadian Renewable Energy Network (CanRen).

APPENDIX B

Insolation Measurements

Varial	Area			Corner Voltage			Middle Voltage			Corner	Middle	Average
Voltage	Lamps	Columns	Rows	Lamp	Column	Row	Lamp	Column	Row	Insolation		
%	m^2	m^2	m^2	Volts	Volts	Volts	Volts	Volts	Volts	W/m^2	W/m^2	W/m^2
20	0.964	0.717	0.181	0.04	0.04	0.04	0.05	0.05	0.05	12	15	14
30	0.964	0.717	0.181	0.185	0.185	0.8	0.23	0.23	0.23	73	69	71
40	0.964	0.717	0.181	0.38	0.41	0.55	0.57	0.59	0.51	122	172	147
50	0.964	0.717	0.181	0.74	0.78	0.92	1.21	1.15	1.19	232	355	294
55	0.964	0.717	0.181	1.12	1.09	1.02	1.52	1.44	1.5	330	446	388
60	0.964	0.717	0.181	1.25	1.37	1.38	2.01	1.87	2.06	393	588	490
65	0.964	0.717	0.181	1.6	1.58	1.8	2.42	2.46	2.47	484	732	608
70	0.964	0.717	0.181	1.9	1.94	2.23	3.08	3.01	3.02	584	914	749
72	0.964	0.717	0.181	2.29	2.4	2.91	3.1	3.28	3.34	718	958	838
75	0.964	0.717	0.181	2.38	2.53	2.82	3.67	3.4	3.55	744	1066	905
78	0.964	0.717	0.181	2.84	2.99	3.61	3.99	3.84	4.05	892	1181	1037
80	0.964	0.717	0.181	2.8	2.81	3.23	4.35	4.28	4.06	854	1288	1071
82	0.964	0.717	0.181	3.23	3.38	4.05	4.2	4.37	4.41	1010	1286	1148

APPENDIX C1

Time [mins]	Toutp [ºC]	Tout [ºC]
0	19.82	20.06
1	19.83	20.15
2	19.87	20.23
3	19.88	20.30
4	19.65	20.40
5	20.48	20.50
6	21.24	20.55
7	21.76	20.60
8	22.16	20.62
9	22.75	20.70
10	23.21	20.90
11	23.70	21.28
12	24.12	21.80
13	24.44	22.43
14	24.81	23.09
15	25.34	23.76
16	27.01	24.37
17	28.69	24.89
18	29.69	25.36
19	30.27	25.77
20	30.90	26.14
21	31.43	26.46
22	32.15	26.75
23	32.48	27.03
24	32.76	27.30
25	33.50	27.55
26	33.63	27.79
27	33.74	28.01
28	33.96	28.21
29	34.17	28.39
30	34.49	28.56
31	34.76	28.71
32	34.96	28.82
33	35.03	28.98
34	34.91	29.13
35	35.11	29.29
36	35.21	29.47
37	35.28	29.53
38	35.41	29.65
39	35.56	29.72
40	35.61	29.85
41	35.59	29.94
42	35.63	30.05
43	35.66	30.18
44	35.75	30.24
45	35.88	30.31
46	36.01	30.39
47	36.06	30.47

Time [mins]	Toutp [ºC]	Tout [ºC]
48	36.15	30.59
49	36.10	30.66
50	36.06	30.78
51	36.23	30.89
52	36.12	31.00
53	36.18	30.63
54	35.93	31.10
55	35.92	31.20
56	35.96	31.28
57	35.96	31.40
58	35.87	31.47
59	35.78	31.55
60	35.84	31.62
61	36.39	31.92
62	36.87	33.10
63	36.70	35.09
64	38.36	37.69
65	41.20	38.94
66	42.32	39.54
67	43.00	39.77
68	43.40	39.84
69	43.51	39.86
70	43.83	39.28
71	43.89	39.12
72	43.74	39.16
73	44.61	39.11
74	44.75	39.13
75	44.08	39.28
76	45.51	39.39
77	45.91	39.61
78	46.07	39.80
79	46.41	39.98
80	46.42	39.82
81	47.25	39.62
82	47.47	39.55
83	47.66	39.87
84	47.86	39.81
85	48.05	39.79
86	48.25	39.81
87	48.44	39.72
88	48.36	40.04
89	48.56	40.17
90	48.75	40.35
91	48.95	40.74
92	49.14	41.16
93	49.34	41.34
94	49.53	41.77

Time [mins]	Toutp [ºC]	Tout [ºC]
95	49.73	42.09
96	49.92	42.45
97	50.12	42.29
98	50.32	42.73
99	50.51	42.87
100	50.71	43.18
101	50.90	43.10
102	51.10	43.14
103	51.29	42.86
104	51.49	43.45
105	51.68	43.75
106	51.34	44.20
107	51.54	44.45
108	51.73	44.61
109	51.93	44.80
110	52.12	44.79
111	52.39	44.83
112	52.59	44.61
113	52.46	44.90
114	52.66	44.82
115	52.85	44.82
116	53.05	45.03
117	53.24	45.10
118	53.44	45.51
119	53.63	45.80
120	53.17	46.06
121	53.37	46.28
122	53.93	45.83
123	54.13	45.78
124	54.32	46.07
125	54.45	46.10
126	54.58	46.00
127	54.71	46.72
128	54.84	46.70
129	54.97	46.76
130	55.04	46.78

APPENDIX C2

Time [mins]	T w tank p [ºC]	T w tank [ºC]
0	18.98	19.20
1	18.99	19.20
2	19.03	19.25
3	19.07	19.30
4	19.13	19.37
5	19.16	19.44
6	19.24	19.52
7	19.32	19.60
8	19.38	19.65
9	19.51	19.73
10	19.59	19.83
11	19.68	19.95
12	19.79	20.06
13	19.89	20.17
14	20.01	20.29
15	20.14	20.42
16	20.27	20.56
17	20.43	20.70
18	20.64	20.83
19	20.88	20.96
20	21.11	21.10
21	21.34	21.23
22	21.59	21.35
23	21.84	21.45
24	22.08	21.57
25	22.32	21.69
26	22.56	21.80
27	22.79	21.89
28	23.02	21.98
29	23.24	22.06
30	23.47	22.15
31	23.68	22.27
32	23.89	22.41
33	24.09	22.45
34	24.29	22.52
35	24.48	22.61
36	24.64	22.69
37	24.83	22.76
38	24.99	22.84
39	25.16	22.92
40	25.32	22.99
41	25.47	23.07
42	25.62	23.15
43	25.76	23.23
44	25.90	23.31
45	26.04	23.41
46	26.17	23.45
47	26.30	23.53

Time [mins]	T w tank p [ºC]	T w tank [ºC]
48	26.43	23.60
49	26.56	23.67
50	26.68	23.75
51	26.78	23.82
52	26.89	23.89
53	27.13	23.83
54	27.09	24.02
55	27.22	24.08
56	27.26	24.14
57	27.35	24.21
58	27.43	24.28
59	27.49	24.32
60	27.56	24.35
61	27.64	24.42
62	27.78	24.82
63	27.95	25.60
64	28.04	26.23
65	28.33	26.83
66	28.59	27.72
67	28.88	28.07
68	29.12	28.65
69	29.29	29.19
70	29.48	29.45
71	29.65	29.83
72	29.78	29.95
73	29.97	30.15
74	30.14	30.32
75	30.17	30.69
76	30.32	30.85
77	30.37	31.00
78	30.49	30.63
79	30.69	30.67
80	31.08	30.88
81	31.43	31.05
82	31.55	31.30
83	31.85	31.54
84	32.19	31.67
85	32.53	31.78
86	32.98	31.90
87	33.42	32.17
88	34.06	32.32
89	34.30	32.52
90	34.67	32.89
91	34.99	33.00
92	35.29	33.07
93	35.58	33.25
94	35.88	33.46

Time [mins]	T w tank p [ºC]	T w tank [ºC]
95	36.24	33.65
96	36.45	33.97
97	36.74	34.12
98	37.06	34.19
99	37.32	34.74
100	37.61	35.11
101	37.87	35.27
102	38.16	35.39
103	38.40	35.53
104	38.64	35.83
105	38.91	36.06
106	39.12	35.46
107	39.34	35.07
108	39.60	35.25
109	39.87	34.18
110	40.18	36.73
111	40.41	35.43
112	40.63	35.21
113	40.90	35.34
114	41.13	35.44
115	41.31	35.54
116	41.52	35.68
117	41.71	35.82
118	41.88	35.93
119	42.04	36.04
120	42.27	36.15
121	42.42	36.25
122	42.58	36.34
123	42.83	36.45
124	42.98	36.56
125	43.09	36.67
126	43.23	36.78
127	43.31	36.94
128	43.45	37.01
129	43.52	37.02
130	43.68	37.15

APPENDIX C3

Time [mins]	T Cu p [ºC]	T Cu [ºC]
0	17.30	17.03
1	17.29	17.01
2	17.72	17.88
3	19.16	21.06
4	23.71	25.40
5	30.06	29.61
6	35.49	33.80
7	39.07	36.79
8	41.31	39.54
9	43.06	42.33
10	44.46	44.61
11	45.25	46.56
12	46.37	48.36
13	47.42	49.65
14	48.65	50.75
15	49.84	52.18
16	50.91	58.00
17	51.71	61.16
18	52.41	62.44
19	52.93	63.76
20	53.55	64.81
21	54.17	65.70
22	54.62	66.38
23	55.06	67.06
24	55.60	67.72
25	56.08	68.39
26	56.41	68.96
27	56.70	69.41
28	57.13	69.90
29	57.18	70.35
30	57.00	70.75
31	58.47	71.27
32	60.73	72.58
33	63.82	74.23
34	69.96	75.43
35	73.50	76.34
36	72.86	76.70
37	72.98	77.20
38	76.23	77.90
39	77.32	78.42
40	77.74	78.80
41	78.57	79.23
42	79.27	79.84
43	79.52	80.51
44	79.27	80.83
45	80.34	81.30
46	81.41	81.45
47	81.05	85.78

Time [mins]	T Cu p [ºC]	T Cu [ºC]
48	82.12	89.17
49	82.68	90.03
50	83.60	89.43
51	84.12	89.14
52	83.92	89.44
53	83.87	90.40
54	84.85	93.51
55	85.22	92.53
56	85.27	90.89
57	84.93	89.95
58	84.68	91.10
59	87.56	93.55
60	87.08	93.16
61	89.46	92.05
62	93.49	91.66
63	97.79	95.69
64	104.31	97.61
65	106.47	97.71
66	107.69	101.16
67	109.53	100.73
68	110.85	101.53
69	111.51	102.65
70	113.19	103.48
71	113.28	103.82
72	113.21	104.27
73	113.30	105.67
74	113.95	105.29
75	114.42	105.47
76	115.03	107.42
77	115.84	108.36
78	115.57	108.53
79	116.35	108.97
80	116.92	109.15
81	117.07	109.86
82	116.45	109.98
83	116.02	110.63
84	116.79	111.08
85	116.75	110.97
86	117.61	110.56
87	117.71	110.29
88	117.34	110.79
89	117.06	110.67
90	117.14	110.89
91	117.26	110.87
92	117.64	110.35
93	117.73	111.08
94	118.54	110.54

Time [mins]	T Cu p [ºC]	T Cu [ºC]
95	118.87	111.32
96	119.38	111.02
97	119.42	111.58
98	119.25	111.21
99	119.54	111.08
100	119.75	110.42
101	119.80	110.02
102	118.90	110.06
103	117.82	110.77
104	114.65	107.42
105	111.83	103.45
106	111.89	98.36
107	108.22	95.24
108	104.65	92.68
109	101.43	89.67
110	98.93	86.46
111	96.28	84.43
112	93.88	82.23
113	91.77	80.68

APPENDIX C4

Time [mins]	T Al p [ºC]	T Al [ºC]
0	17.56	17.35
1	17.56	17.34
2	17.65	17.89
3	17.95	20.79
4	19.83	22.14
5	24.30	27.36
6	30.11	34.23
7	35.74	38.76
8	40.28	42.93
9	43.56	46.95
10	45.17	50.37
11	45.27	53.51
12	48.78	56.35
13	53.09	58.41
14	56.90	60.21
15	60.21	62.37
16	62.57	63.77
17	64.07	64.89
18	65.46	66.42
19	66.64	67.84
20	67.74	69.09
21	68.81	70.15
22	69.91	71.03
23	70.81	71.95
24	71.91	72.73
25	72.68	73.56
26	73.44	74.34
27	74.17	74.91
28	74.82	75.59
29	75.22	76.30
30	75.62	76.63
31	76.22	78.08
32	77.28	80.23
33	79.92	81.95
34	81.51	83.30
35	84.38	84.29
36	86.96	83.99
37	87.51	85.61
38	87.24	87.01
39	89.68	87.60
40	90.68	88.16
41	91.38	89.34
42	92.79	89.22
43	93.27	89.34
44	94.07	89.86
45	94.92	92.14
46	95.33	94.21
47	95.77	93.81

Time [mins]	T Al p [ºC]	T Al [ºC]
48	96.33	95.47
49	96.67	95.75
50	97.43	94.92
51	97.28	94.95
52	97.49	95.55
53	98.01	97.88
54	98.45	99.19
55	98.72	98.81
56	98.58	97.60
57	98.69	97.08
58	99.25	97.04
59	99.24	98.45
60	99.25	98.65
61	99.33	97.99
62	100.97	100.19
63	102.91	102.72
64	104.82	103.10
65	106.42	105.65
66	107.70	105.95
67	108.98	104.12
68	109.96	104.91
69	110.99	106.58
70	111.88	108.28
71	112.65	108.21
72	113.43	109.95
73	113.91	111.35
74	114.44	112.69
75	115.13	112.49
76	115.74	112.07
77	116.09	112.38
78	116.33	112.79
79	116.70	113.64
80	117.10	113.88
81	117.36	114.01
82	117.54	114.16
83	117.87	114.68
84	118.05	115.18
85	120.86	114.64
86	121.11	115.21
87	121.35	115.19
88	121.84	115.33
89	122.09	115.75
90	122.30	115.92
91	122.45	116.02
92	122.55	115.74
93	122.54	116.10
94	122.45	116.26

Time [mins]	T Al p [ºC]	T Al [ºC]
95	122.40	116.50
96	122.92	116.03
97	121.95	116.93
98	121.67	116.89
99	121.77	116.69
100	121.94	116.67
101	122.14	116.78
102	122.16	116.66
103	120.23	116.01
104	117.27	113.33
105	114.12	108.79
106	109.83	103.45
107	105.58	101.45
108	101.65	97.39
109	98.88	93.41
110	96.87	90.09
111	94.52	86.83
112	92.28	84.31

APPENDIX C5

Time [mins]	Ttankp [ºC]	Ttank [ºC]
0	27.65	27.98
1	27.61	27.90
2	27.53	27.74
3	27.45	27.60
4	27.36	27.49
5	27.28	27.35
6	27.20	27.23
7	27.12	27.07
8	27.04	26.93
9	26.95	26.79
10	26.87	26.67
11	26.80	26.55
12	26.72	26.47
13	26.65	26.38
14	26.59	26.31
15	26.54	26.23
16	26.55	26.16
17	26.80	26.11
18	27.01	26.24
19	27.16	26.35
20	27.11	26.51
21	27.12	26.67
22	27.13	26.84
23	27.19	27.02
24	27.15	27.19
25	27.12	27.42
26	27.11	27.64
27	27.10	27.85
28	27.28	28.06
29	27.10	28.30
30	27.13	28.49
31	27.15	28.70
32	27.21	28.89
33	27.35	29.04
34	27.54	29.23
35	27.87	29.46
36	28.22	29.70
37	28.57	29.96
38	28.80	30.24
39	29.13	30.52
40	29.43	30.78
41	29.73	31.06
42	30.09	31.36
43	30.36	31.70
44	30.65	31.98
45	30.98	32.22
46	31.28	32.50
47	31.51	32.76

Time [mins]	T Al p [ºC]	T Al [ºC]
48	31.79	33.02
49	32.05	33.30
50	32.33	33.59
51	32.52	33.81
52	32.76	34.06
53	32.98	34.35
54	33.20	34.57
55	33.42	34.75
56	33.62	34.98
57	33.78	35.20
58	33.94	35.32
59	34.17	35.46
60	34.36	35.63
61	34.68	35.77
62	35.26	35.92
63	35.90	36.06
64	36.36	36.24
65	36.87	36.35
66	37.42	36.54
67	38.02	36.73
68	38.54	36.89
69	39.11	37.14
70	39.52	37.33
71	39.90	37.45
72	40.42	37.66
73	40.84	37.86
74	41.28	38.07
75	41.74	38.28
76	42.21	38.49
77	42.71	38.67
78	43.13	38.83
79	43.48	39.03
80	43.87	39.22
81	44.15	39.47
82	44.60	39.66
83	45.01	39.90
84	45.35	40.06
85	45.65	40.25
86	45.98	40.45
87	46.30	40.67
88	46.68	40.79
89	46.99	40.99
90	47.35	41.17
91	47.79	41.31
92	47.96	41.49
93	48.52	41.69
94	48.58	42.14

Time [mins]	T Al p [ºC]	T Al [ºC]
95	48.82	42.15
96	49.46	42.33
97	49.53	42.44
98	49.68	42.60
99	49.73	42.73
100	49.79	42.82
101	49.84	42.96
102	49.90	43.06
103	49.95	43.26
104	50.01	43.41
105	50.15	43.46
106	50.24	43.51
107	50.29	43.51
108	50.36	43.56
109	50.29	43.28
110	50.06	43.13
111	49.65	42.87
112	49.27	42.59
113	48.89	42.34
114	48.55	42.06
115	48.22	41.85
116	47.91	41.58
117	47.60	41.36
118	47.33	41.23
119	47.06	40.95
120	46.78	40.87

APPENDIX C6

Time [mins]	Tb p [ºC]	T surf p [ºC]	Tb [ºC]	T surf [ºC]
0	158.90	159.65	159.09	161.22
1	159.02	160.38	159.54	161.83
2	160.13	160.97	160.25	162.38
3	160.59	161.23	160.54	162.67
4	161.13	162.13	161.48	163.61
5	162.14	162.80	162.28	164.41
6	162.27	163.62	163.10	165.23
7	162.55	164.24	163.37	165.73
8	163.40	164.78	163.45	166.19
9	163.74	164.89	164.08	166.44
10	163.70	165.52	164.25	166.84
11	164.13	165.60	164.31	167.13
12	164.59	166.35	165.16	167.52
13	164.64	166.58	165.62	167.72
14	164.85	166.64	166.07	168.17
15	165.08	166.79	166.13	168.55
16	165.47	167.16	166.16	168.57
17	165.17	167.11	166.17	168.51
18	165.70	167.32	166.21	168.47
19	165.68	167.16	166.14	168.22
20	165.75	167.28	166.45	168.58

APPENDIX C7

Time [mins]	Tb p [ºC]	T surf p [ºC]	Tb [ºC]	T surf [ºC]
1	109.98	112.02	111.26	112.38
2	111.63	114.12	112.82	113.94
3	113.72	115.51	115.39	116.51
4	115.50	117.45	117.13	118.25
5	117.17	119.37	118.36	119.48
6	118.59	121.20	119.10	120.22
7	119.64	122.09	121.27	122.39
8	121.28	123.29	122.36	123.21
9	122.44	124.21	124.11	124.56
10	123.22	125.45	124.40	125.25
11	124.17	126.09	124.69	126.28
12	125.02	126.75	125.72	127.31
13	125.80	127.01	127.39	127.54
14	126.48	127.24	128.14	127.77
15	126.90	127.84	128.70	128.00
16	127.29	129.25	128.16	128.67
17	127.54	129.23	128.39	130.11
18	127.61	129.41	128.62	130.32
19	127.80	129.72	128.85	130.71
20	127.99	129.84	129.08	130.87
21	128.23	129.96	129.31	130.88
22	128.11	130.44	129.54	131.11
23	128.80	130.53	129.77	131.40
24	129.55	131.50	130.00	131.46
25	129.36	131.02	130.23	131.42
26	129.36	131.22	130.46	131.39
27	129.16	130.98	130.69	131.47

APPENDIX C8

Time [mins]	T Cu p [ºC]	T Cu [ºC]
0	20.00	21.18
1	20.00	21.09
2	20.12	25.64
3	22.50	36.17
4	30.37	42.05
5	39.93	46.92
6	47.34	48.89
7	52.23	52.93
8	55.60	57.24
9	56.01	62.22
10	58.77	66.10
11	69.09	69.87
12	76.81	72.77
13	81.06	75.70
14	83.77	78.49
15	85.91	80.27
16	86.80	82.94
17	88.63	84.36
18	90.19	86.58
19	90.28	87.28
20	91.31	89.37
21	92.59	90.94
22	94.03	92.14
23	94.92	93.32
24	95.81	94.53
25	96.66	95.07
26	97.52	96.10
27	99.02	96.78
28	99.56	97.51
29	100.51	98.53
30	101.83	98.89
31	103.24	98.17
32	103.25	99.12
33	102.57	99.29
34	102.40	100.12
35	102.57	100.25
36	102.31	100.58
37	102.97	101.21
38	103.72	101.78
39	103.78	102.17
40	103.68	102.11
41	103.74	102.25
42	104.48	102.40
43	104.78	102.90
44	104.82	103.43
45	105.14	103.46
46	105.05	103.75
47	105.26	105.14

Time [mins]	T Cu p [ºC]	T Cu [ºC]
48	107.53	105.80
49	108.49	106.00
50	109.50	104.61
51	110.15	105.31
52	110.66	106.04
53	111.80	106.47
54	112.35	106.82
55	112.95	107.41
56	112.82	107.05
57	114.08	108.54
58	113.93	108.68
59	114.67	108.84
60	115.00	109.85
61	115.42	110.51
62	115.78	111.03
63	115.93	110.59
64	115.88	111.11
65	116.33	111.25
66	116.25	111.64
67	117.03	111.32
68	117.05	111.61
69	117.35	112.05
70	117.43	112.03
71	117.30	112.16
72	117.89	112.79
73	117.03	112.45
74	116.85	112.57
75	116.90	112.95
76	117.73	112.97
77	117.30	112.96
78	117.50	113.49
79	117.69	113.28
80	118.36	113.03
81	117.87	113.35
82	118.36	113.19
83	117.63	113.53
84	117.98	113.46
85	118.10	113.75
86	118.30	113.67
87	118.43	113.30
88	118.03	114.12
89	117.87	113.82
90	117.96	114.22
91	118.03	113.82
92	117.88	114.40
93	118.81	115.13
94	121.19	116.36

Time [mins]	T Cu p [ºC]	T Cu [ºC]
95	122.54	117.85
96	124.33	118.85
97	125.60	119.63
98	126.30	120.22
99	127.28	120.88
100	127.74	121.25
101	128.02	121.79
102	128.98	122.05
103	128.93	122.67
104	129.18	122.77
105	129.57	123.30
106	130.07	123.49
107	130.12	123.35
108	129.85	123.90
109	130.72	123.87
110	130.20	124.33
111	130.60	124.17
112	130.81	124.11
113	130.58	124.07
114	130.70	124.28
115	129.98	124.16
116	130.44	124.48
117	130.18	124.44
118	130.57	124.52
119	130.28	124.38
120	130.32	124.43
121	130.47	124.22
122	130.63	124.33
123	130.28	124.41
124	130.81	124.46
125	130.98	124.51
126	131.01	124.55
127	131.16	124.60
128	131.08	124.67
129	131.39	124.72
130	131.26	124.76
131	131.56	124.63
132	131.45	124.68
133	131.42	124.73
134	131.39	124.94
135	131.66	124.83
136	131.79	124.50
137	131.58	125.10
138	131.73	124.92
139	131.89	124.98
140	131.84	124.96
141	132.34	125.85

Time [mins]	T Cu p [ºC]	T Cu [ºC]
142	133.47	126.72
143	135.00	127.82
144	135.90	128.69
145	136.57	129.31
146	137.03	129.28
147	137.41	130.10
148	137.63	130.39
149	138.01	130.35
150	138.19	130.78
151	138.25	131.11
152	138.22	131.31
153	138.55	131.54
154	138.53	131.77
155	138.32	131.84
156	138.59	131.96
157	138.70	132.23
158	138.81	132.52
159	138.88	132.56
160	139.02	132.75
161	139.13	132.79
162	139.10	132.82
163	139.10	132.86
164	139.19	132.89
165	139.35	132.93
166	139.41	132.96
167	139.61	132.99
168	139.64	133.03
169	139.65	133.06
170	139.90	133.10
171	140.01	133.13
172	139.98	133.16
173	140.04	133.20
174	139.95	133.23
175	139.94	133.27
176	140.09	133.30
177	140.16	133.33
178	140.19	133.37
179	140.24	133.40
180	139.98	133.44
181	140.15	133.47
182	140.08	133.50
183	140.09	133.54
184	140.19	133.57
185	140.49	133.61
186	140.51	133.63
187	140.68	133.66
188	140.63	133.85

Time [mins]	T Cu p [ºC]	T Cu [ºC]
189	140.62	133.87
190	140.71	132.05
191	140.18	131.29
192	133.45	129.64
193	125.85	121.93
194	119.00	113.70
195	111.92	106.36
196	104.84	99.52
197	98.26	93.49
198	92.13	88.16
199	86.34	83.61
200	81.13	79.34
201	76.50	75.45
202	72.36	71.97
203	68.65	68.73
204	65.44	65.68
205	62.65	62.98
206	60.14	60.52
207	57.88	58.22
208	55.79	56.02
209	53.86	54.00
210	52.08	52.14
211	50.44	50.42
212	48.89	48.79
213	47.45	47.25
214	46.09	45.89
215	44.80	44.63

APPENDIX C9

Time [mins]	T Al p [ºC]	T Al [ºC]
0	19.78	21.59
1	19.77	21.57
2	22.09	22.70
3	27.96	30.90
4	41.31	36.31
5	50.42	37.61
6	54.83	40.83
7	59.55	47.66
8	64.50	54.54
9	67.71	58.42
10	70.85	61.76
11	74.40	65.34
12	77.92	69.44
13	81.37	72.34
14	83.81	75.39
15	85.75	77.70
16	87.20	80.54
17	88.85	82.34
18	90.22	84.26
19	91.86	86.25
20	92.54	87.90
21	94.06	89.32
22	95.35	90.46
23	96.38	91.64
24	97.14	93.13
25	97.99	93.91
26	98.76	94.93
27	99.58	95.81
28	100.08	96.78
29	100.39	97.55
30	101.61	97.89
31	102.71	97.20
32	102.33	97.17
33	102.34	97.54
34	102.72	98.05
35	103.12	98.62
36	103.38	98.93
37	103.25	99.22
38	103.68	99.43
39	103.55	99.96
40	104.07	100.17
41	104.54	100.49
42	104.59	101.09
43	104.52	101.31
44	104.95	101.46
45	105.23	102.01
46	106.23	102.08
47	108.25	103.03

Time [mins]	T Al p [ºC]	T Al [ºC]
48	108.79	104.72
49	109.85	106.28
50	110.65	105.97
51	110.96	106.53
52	112.10	106.90
53	112.25	107.45
54	112.65	107.81
55	113.32	108.57
56	113.72	108.78
57	114.26	109.18
58	114.66	109.23
59	114.69	109.94
60	115.00	109.65
61	115.33	110.18
62	115.49	111.19
63	115.97	111.21
64	116.15	111.32
65	116.78	111.62
66	116.61	111.89
67	116.82	111.98
68	116.96	112.24
69	116.71	112.41
70	117.32	112.71
71	117.22	112.91
72	117.54	112.47
73	117.03	112.85
74	117.30	113.25
75	117.68	112.76
76	117.96	113.06
77	118.02	113.29
78	118.11	113.32
79	117.72	113.51
80	117.95	113.37
81	118.14	113.32
82	118.37	113.57
83	118.30	113.51
84	118.16	113.67
85	118.38	113.50
86	117.85	113.71
87	118.05	114.02
88	118.28	113.78
89	118.06	114.10
90	118.00	114.13
91	118.27	114.32
92	118.52	114.16
93	120.28	115.10
94	121.61	116.50

Time [mins]	T Al p [ºC]	T Al [ºC]
95	122.45	117.59
96	123.35	118.44
97	124.06	119.07
98	124.83	119.89
99	125.49	120.55
100	125.79	120.94
101	126.05	121.70
102	126.31	122.15
103	126.46	122.44
104	126.91	122.76
105	127.13	122.81
106	127.30	123.11
107	127.58	123.32
108	127.55	123.71
109	127.89	123.85
110	127.95	123.64
111	127.77	124.00
112	128.34	124.04
113	127.80	124.36
114	128.32	124.08
115	128.06	124.20
116	128.07	124.11
117	128.42	124.26
118	128.10	124.22
119	128.16	124.25
120	128.55	124.24
121	128.55	124.51
122	128.49	124.45
123	128.32	124.60
124	128.05	124.24
125	128.18	124.54
126	128.19	124.69
127	128.21	124.66
128	128.31	125.00
129	128.71	124.76
130	128.32	124.78
131	128.76	124.63
132	128.44	124.71
133	128.71	124.79
134	128.81	124.75
135	128.75	124.75
136	129.30	124.72
137	129.10	124.59
138	129.15	124.73
139	129.51	124.84
140	129.78	124.71
141	131.09	125.53

Time [mins]	T Al p [ºC]	T Al [ºC]
142	132.17	126.62
143	133.91	127.56
144	134.47	128.23
145	135.20	128.86
146	135.71	129.25
147	136.16	129.87
148	136.40	129.91
149	136.77	130.41
150	137.00	130.53
151	137.24	130.72
152	137.49	131.01
153	137.27	131.23
154	137.08	131.38
155	137.41	131.67
156	137.59	131.71
157	137.58	131.85
158	137.87	132.16
159	137.98	132.39
160	138.05	132.63
161	138.01	132.63
162	138.26	132.55
163	138.36	132.78
164	138.42	132.78
165	138.80	132.81
166	138.93	132.73
167	139.08	132.94
168	138.94	132.87
169	139.10	133.01
170	139.12	133.04
171	139.24	133.11
172	139.27	133.28
173	139.25	133.02
174	139.35	133.20
175	139.36	133.27
176	139.42	133.23
177	139.90	133.19
178	139.87	133.16
179	139.84	133.14
180	139.66	133.16
181	139.87	133.17
182	139.84	133.14
183	139.55	133.17
184	140.01	133.35
185	140.20	133.34
186	140.08	133.43
187	140.71	133.48
188	140.38	133.55

Time [mins]	T Al p [ºC]	T Al [ºC]
189	140.49	133.56
190	140.41	133.01
191	136.32	132.83
192	129.45	131.65
193	122.89	123.62
194	116.07	114.95
195	110.22	106.63
196	104.62	99.57
197	99.52	93.53
198	94.79	88.26
199	90.15	83.54
200	85.59	79.30
201	81.48	75.50
202	77.60	71.99
203	73.92	68.82
204	70.58	65.92
205	67.55	63.28
206	64.72	60.80
207	62.10	58.50
208	59.72	56.39
209	57.52	54.45
210	55.50	52.65
211	53.65	50.96
212	51.93	49.40
213	50.34	47.95
214	48.87	46.64
215	47.44	45.37

APPENDIX C10

Time [mins]	T input wt [ºC]	T input wt [ºC]
0	20.96	21.39
1	20.96	21.38
2	20.98	21.37
3	21.02	21.40
4	21.15	21.57
5	24.40	21.97
6	29.37	22.89
7	33.40	24.29
8	37.04	25.97
9	40.49	28.10
10	43.47	30.45
11	46.17	32.92
12	48.82	35.30
13	51.38	37.61
14	53.77	39.80
15	55.90	41.83
16	57.82	43.71
17	59.43	45.53
18	60.88	47.16
19	62.17	48.64
20	63.51	49.92
21	64.68	51.25
22	65.74	52.33
23	66.63	53.32
24	67.60	54.21
25	68.37	54.93
26	69.15	55.42
27	69.82	55.85
28	70.81	56.15
29	72.11	56.25
30	74.16	58.20
31	75.00	64.48
32	76.08	67.48
33	77.04	69.22
34	77.88	70.76
35	78.43	71.50
36	79.05	72.33
37	79.52	72.92
38	79.87	73.52
39	80.21	74.15
40	80.41	74.01
41	80.68	74.05
42	80.88	73.89
43	81.05	74.07
44	81.09	74.40
45	81.38	74.52
46	81.58	74.58
47	81.90	75.08

Time [mins]	T input wt p [ºC]	T input wt [ºC]
48	82.54	75.67
49	83.14	76.27
50	83.76	77.15
51	84.15	78.45
52	84.52	78.92
53	84.43	79.78
54	84.31	80.49
55	84.78	80.90
56	84.99	80.90
57	86.02	81.78
58	86.24	82.24
59	86.40	82.08
60	86.78	82.87
61	86.73	82.61
62	87.00	83.52
63	87.23	83.50
64	87.26	83.00
65	86.63	83.65
66	88.02	84.18
67	87.02	84.25
68	88.38	84.61
69	87.22	84.08
70	86.66	84.12
71	88.41	83.83
72	85.39	84.40
73	88.46	84.63
74	87.73	84.76
75	88.29	84.73
76	88.19	84.46
77	88.39	85.19
78	88.71	85.12
79	89.19	85.09
80	89.31	85.04
81	89.66	85.39
82	90.07	85.13
83	90.31	85.12
84	90.87	85.19
85	91.22	85.17
86	91.17	85.60
87	91.30	85.43
88	92.00	85.94
89	92.41	85.58
90	92.93	86.20
91	93.15	85.78
92	93.53	85.89
93	94.56	86.89
94	95.39	88.09

Time [mins]	T input wt p [ºC]	T input wt [ºC]
95	96.71	87.99
96	97.76	88.59
97	98.87	89.31
98	99.74	89.49
99	100.62	89.87
100	101.19	91.02
101	101.79	90.51
102	102.47	91.54
103	102.65	91.64
104	103.15	91.69
105	103.59	91.80
106	103.67	91.86
107	104.09	92.05
108	104.30	92.45
109	104.25	92.55
110	104.40	93.18
111	104.64	92.46
112	104.69	92.76
113	104.88	92.71
114	105.33	92.42
115	105.24	93.35
116	105.49	93.15
117	105.26	93.08
118	105.33	92.58
119	105.48	92.92
120	104.83	93.06
121	103.41	93.13
122	105.68	93.29
123	106.22	93.63
124	105.57	93.56
125	106.10	93.52
126	106.36	93.51
127	105.76	93.29
128	104.95	93.58
129	103.77	93.93
130	106.22	93.35
131	106.72	93.49
132	106.04	93.17
133	106.61	93.65
134	105.91	93.74
135	105.99	93.39
136	106.50	93.77
137	106.21	93.68
138	106.79	93.83
139	106.46	94.15
140	104.56	93.82
141	105.61	95.02

Time [mins]	T input wt p [ºC]	T input wt [ºC]
142	107.50	96.89
143	107.90	97.20
144	108.33	98.93
145	108.99	98.99
146	109.49	100.07
147	109.75	100.41
148	109.29	99.98
149	109.86	100.68
150	110.23	101.00
151	110.61	102.39
152	109.82	102.15
153	109.49	101.24
154	112.05	103.25
155	112.18	103.10
156	111.74	103.94
157	112.70	104.35
158	112.58	102.17
159	111.36	103.62
160	113.22	104.57
161	113.14	101.80
162	113.05	102.37
163	110.67	102.99
164	112.07	101.65
165	113.22	104.28
166	112.10	103.58
167	113.31	105.49
168	113.57	103.85
169	114.09	104.66
170	113.52	105.59
171	114.07	104.86
172	113.42	104.31
173	113.55	104.39
174	113.05	104.69
175	114.36	104.42
176	115.13	103.74
177	115.12	106.29
178	114.10	105.76
179	115.30	106.01
180	115.78	105.93
181	114.67	105.07
182	115.35	106.05
183	115.34	105.77
184	115.16	105.53
185	114.86	105.62
186	115.58	105.56
187	115.43	105.31
188	115.49	105.37

Time [mins]	T input wt p [ºC]	T input wt [ºC]
189	115.46	105.32
190	114.42	103.64
191	110.66	100.04
192	101.02	96.61
193	95.32	88.05
194	89.86	82.16
195	85.04	76.42
196	81.08	71.15
197	78.16	66.92
198	76.28	63.58
199	73.87	61.00
200	71.52	58.08
201	69.28	55.83
202	67.14	54.38
203	64.98	53.01
204	62.82	51.64
205	60.77	50.30
206	58.82	49.04
207	57.01	47.79
208	55.21	46.60
209	53.54	45.43
210	52.00	44.30
211	50.54	43.24
212	49.17	42.27
213	47.91	41.26
214	46.77	40.39
215	45.70	39.58

APPENDIX C11

Time [mins]	T input wt [ºC]	T input wt [ºC]
120	29.72	26.53
121	29.81	26.82
122	29.90	26.94
123	29.99	27.07
124	30.07	27.22
125	30.15	27.34
126	30.23	27.47
127	30.32	27.60
128	30.40	27.68
129	30.50	27.74
130	30.59	27.80
131	30.69	27.86
132	30.78	27.92
133	30.87	27.99
134	30.96	28.04
135	31.05	28.10
136	31.14	28.17
137	31.23	28.25
138	31.33	28.31
139	31.42	28.37
140	31.52	28.43
141	31.62	28.48
142	31.71	28.54
143	31.80	28.59
144	31.89	28.62
145	31.98	28.67
146	32.08	28.73
147	32.17	28.78
148	32.27	28.82
149	32.37	28.87
150	32.48	28.93
151	32.58	29.01
152	32.68	29.09
153	32.78	29.16
154	32.88	29.24
155	32.97	29.30
156	33.07	29.36
157	33.17	29.45
158	33.27	29.53
159	33.37	29.58
160	33.48	29.64
161	33.58	29.70
162	33.70	29.76
163	33.81	29.83
164	33.92	29.89
165	34.02	29.93
166	34.13	29.98
167	34.24	30.03

Time [mins]	T input wt p [ºC]	T input wt [ºC]
168	34.24	30.08
169	34.36	30.13
170	34.48	30.19
171	34.59	30.27
172	34.69	30.36
173	34.80	30.44
174	34.90	30.51
175	35.00	30.58
176	35.10	30.64
177	35.20	30.69
178	35.30	30.75
179	35.39	30.81
180	35.49	30.88
181	35.59	30.97
182	35.69	31.05
183	35.78	31.12
184	35.88	31.19
185	35.99	30.89
186	36.09	31.05
187	36.19	31.16
188	36.28	31.26
189	36.38	31.35
190	36.47	31.41
191	36.58	31.48
192	36.71	31.57
193	36.83	31.65
194	36.92	31.73
195	37.00	31.85
196	37.10	31.85
197	37.19	31.94
198	37.27	32.00
199	37.35	32.06
200	37.42	32.07
201	37.50	32.10
202	37.58	32.14
203	37.65	32.19
204	37.71	32.27
205	37.77	32.34
206	37.82	32.38
207	37.86	32.40
208	37.89	32.41
209	37.93	32.43
210	37.97	32.46
211	37.92	32.49
212	37.91	32.53
213	37.89	32.56
214	37.86	32.59
215	37.84	32.61

APPENDIX C12

The least square method that fits a set of sample points is given by:

$$T=a+bt+cx^2 \qquad \text{(C12.1)}$$

Where, T is the temperature, t is the time and a, b, c are determined from the normal equations:

$$\sum T = na + b\sum t + c\sum t^2$$

$$\sum T \cdot t = a\sum t + b\sum t^2 + c\sum t^3$$

$$\sum T \cdot t^2 = a\sum t^2 + b\sum t^3 + c\sum t^4$$

where n is the number of sample points used.

The three equations listed above, obtained by summing both sides of equation (C12.1) after multiplying successively by 1, x, x^2 respectively.

If we let T_{est} denote the estimated value of temperature T, for a given value of time t, as obtained from the regression curve of T on t, then a measure of the scatter about regression curve is supplied by the quantity[1]:

$$Error = \sqrt{\frac{\sum (T-T_{est})^2}{n}}$$

Which is called the standard error of estimate of T on t.

---

[1] Schaum's :Probability and Statistics, Chapter 8

APPENDIX D1
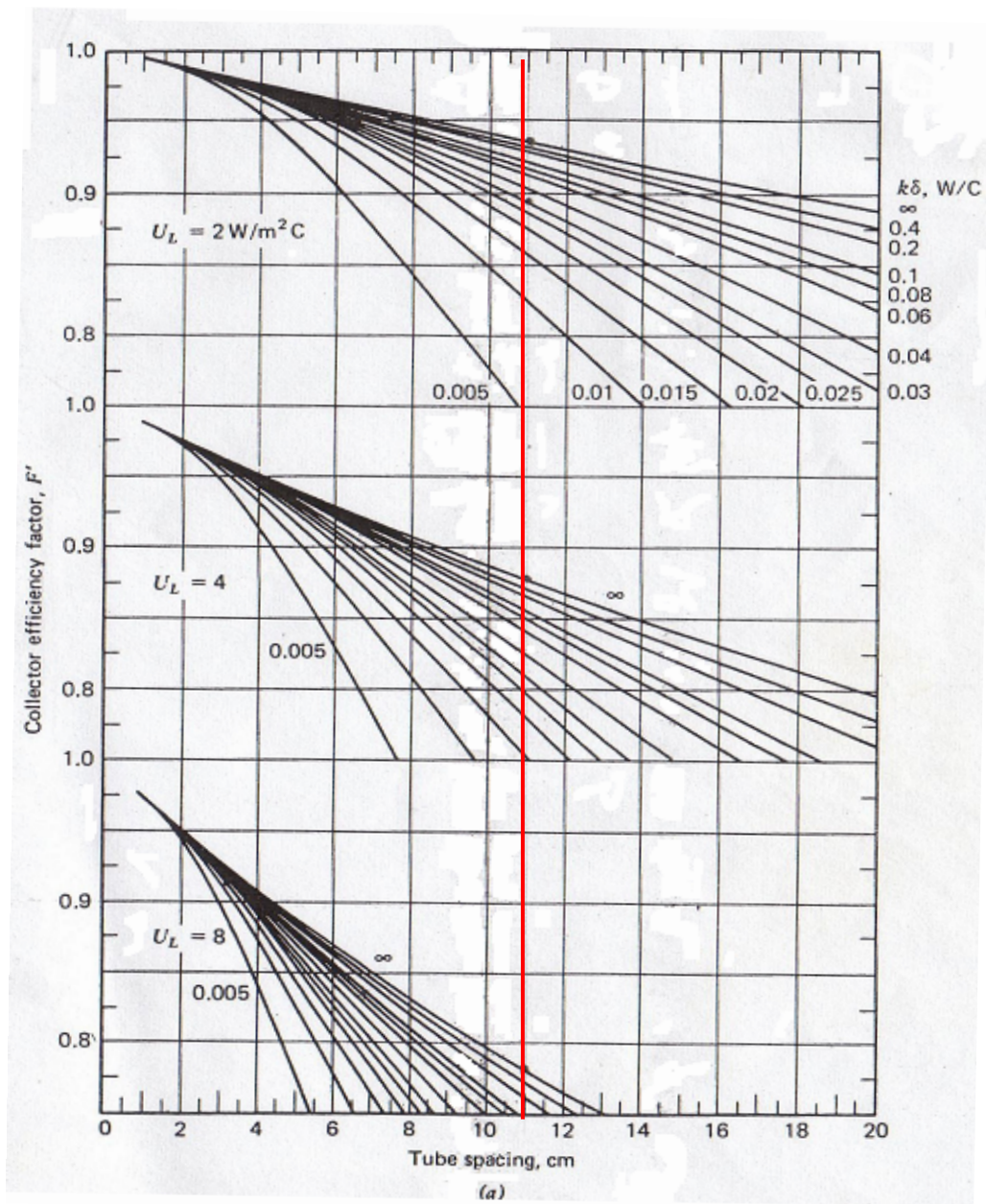
Collector Efficiency Factor F' vs. tube spacing for 10mm diameter tubes & for $h=100$ W/m^2.

APPENDIX D2
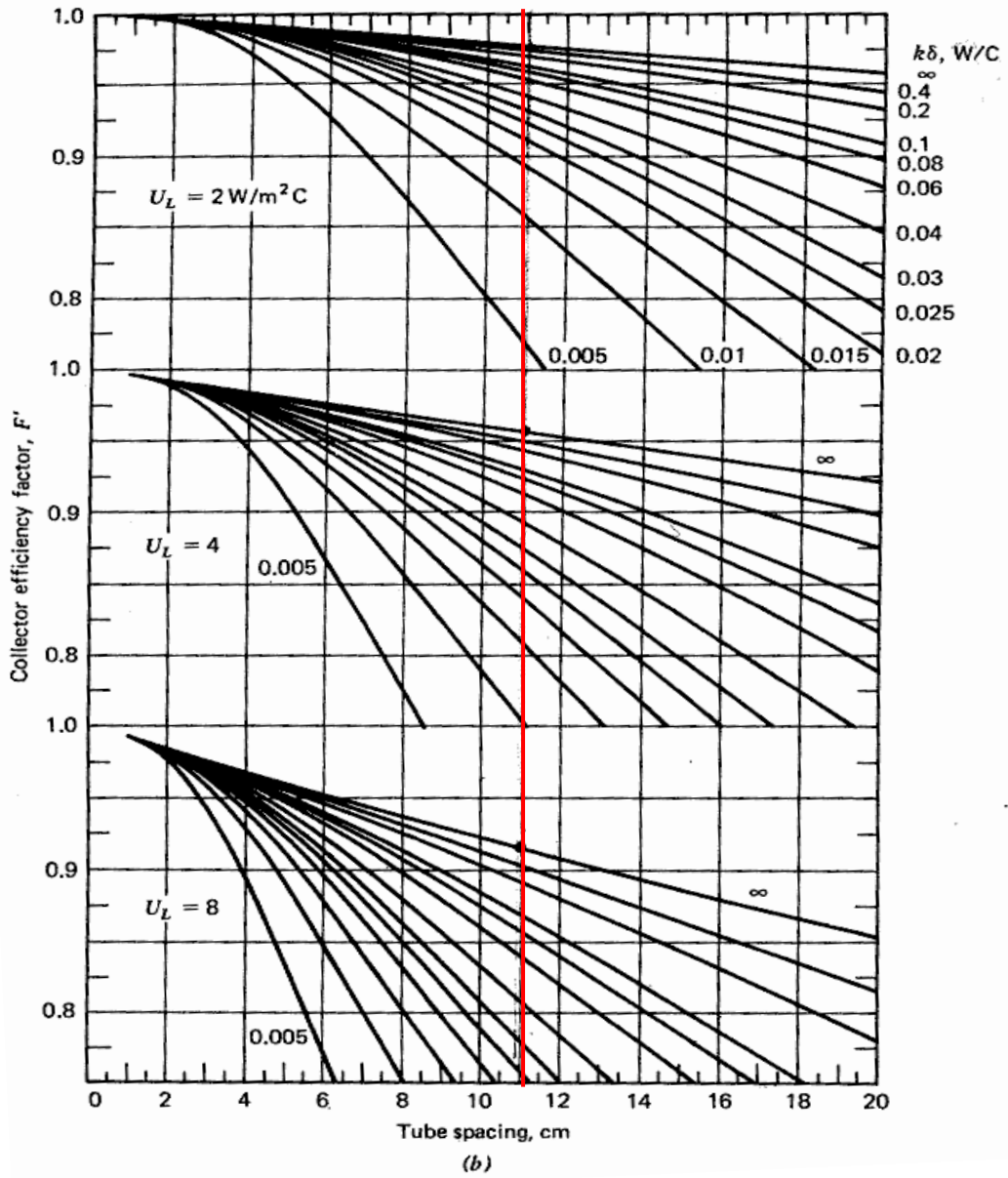
Collector Efficiency Factor F' vs. tube spacing for 10mm diameter tubes & for h=300 W/m^2.

APPENDIX D3
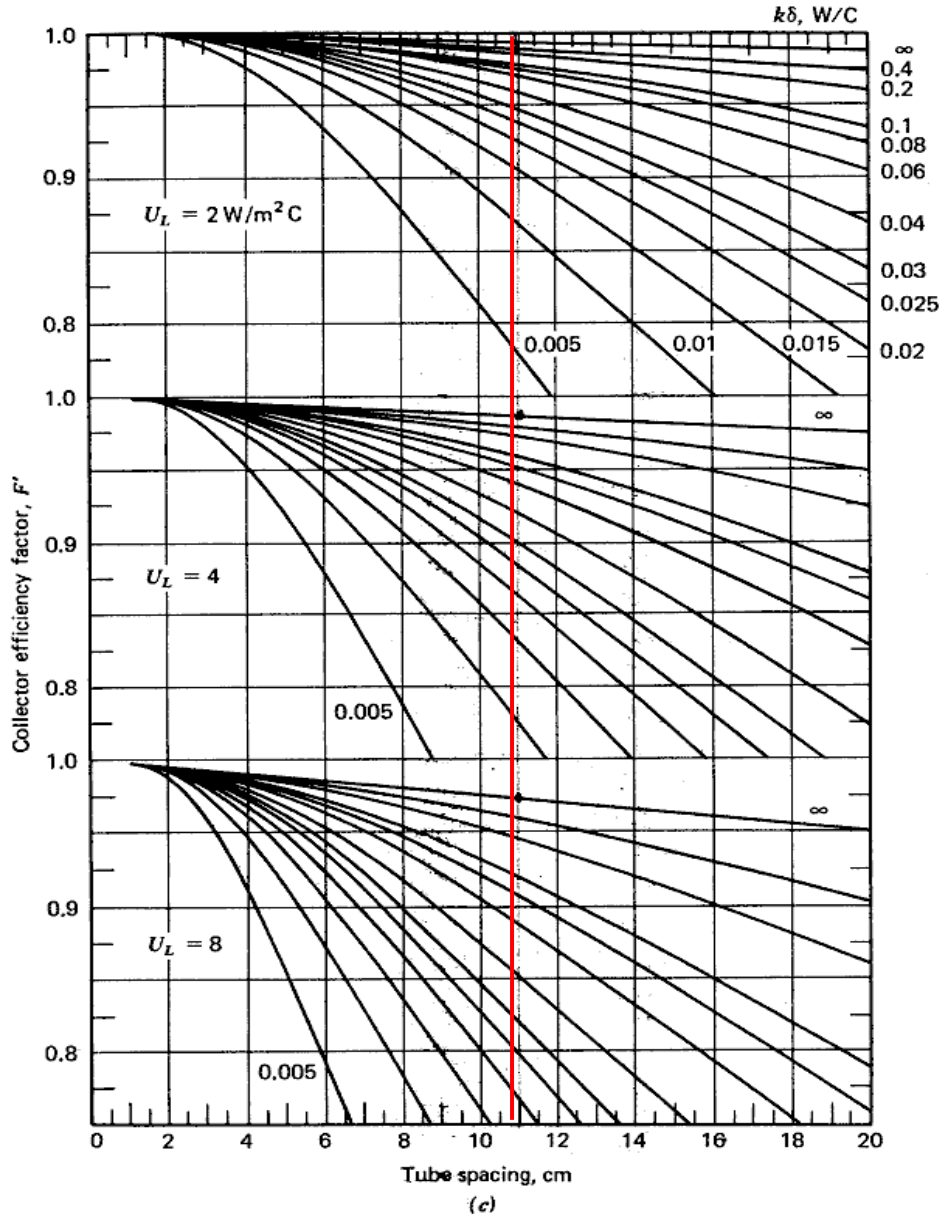
Collector Efficiency Factor *F'* vs. tube spacing for 10mm diameter tubes & for *h*=1000 W/m^2.

APPENDIX E1

Halogen Floodlight 150w Black

Manufactured by:

Ningbo Start Electrical Co., Ltd. China.

Utilises a:

150 watt, THLS R7s 78mm Tungsten Halogen Lamp, 220-240V. Max. Fusing: 5A.

2100 lumen.

APPENDIX E2

Manufacturer: Christian Bürkert GmbH & Co. Germany.

Type 8071 - Positive Displacement Low Flow Sensor 0.5 - 50 l/h.

APPENDIX E3

Manufacturer: Pico Technology, Cambridgeshire, U.K.

Type: USB TC-08 Thermocouple Data Logger.

PicoLog Data Acquisition Software was used to record data at the experiments.

Temperatures were measured using K-type Thermocouples by Pico.

- Diameter: 1.5 mm
- Temperature Range: -75 to +250 °C

APPENDIX E4

Brass Compression Fittings Supplied from: Skrew-Fix, Gateshead, U.K

Type: Yorkshire Kuterlite 618, diameter of 10mm and 15mm.

Type: Yorkshire Kuterlite 615, diameter 15mm.